THÈSE

Présentée en vue d'obtenir le grade de

DOCTEURE

En : Chimie théorique, physique, analytique

Par

Raafa AL KADERI

Doctorat de l'Université de Lille délivré par IMT Nord Europe

Titre de la thèse :

Emission of particles and volatile organic compounds from urban railway friction braking

Soutenue le 11 septembre 2025

Aurélien SAULOT	PR	LaMCoS, INSA Lyon	Président
Pascal FLAMENT	PR	LPCA, Université du Littoral-Côte d'Opale	Rapporteur
Aurélie CHARRON	CR HDR	UMRESTTE, Université Gustave Eiffel	Rapportrice
Boris VANSEVENANT	IR Docteur	EASE, Université Gustave Eiffel	Examinateur
Alexandre TOMAS	PR	CERI EE, IMT Nord Europe	Directeur de thèse
Yannick DESPLANQUES	PR	LaMcube, Centrale Lille	Co-Directeur de thèse
Esperanza PERDRIX	MCF	CERI EE, IMT Nord Europe	Encadrante
Alexandre MEGE-REVIL	MCF	LaMcube, Centrale Lille	Encadrant
Karine PAJOT	Docteure	Alstom SA	Membre invitée

Laboratoires d'accueil : CERI EE, IMT Nord Europe & LaMcube, Centrale Lille

École doctorale SMRE 104 (ULille, UPHF, Centrale Lille, Chimie Lille, IMT Nord Europe)

Abstract

Air quality is a major public health concern worldwide. Rail transportation is rightly recognized as one of the greener and CO_2-efficient mobility solutions. However, enclosed railway stations often experience degraded air quality, raising significant concerns about non-exhaust emissions. The aim of this thesis is to determine the physicochemical characteristics and origin of the particulate matter (PM) emitted during braking and collected as a function of their size, and to characterize volatile organic compounds (VOCs) emissions, under different braking conditions, using realistic 8-hour-long pathways that simulate a commuting train. The essays were conducted in a reduced-scale tribometer designed in LaMcube based on thermal and thermomechanical scaling factors.

The first part of this work investigates the effect of the braking energy by conducting the program under two different braking loads, representing normal and heavy pathways of a commuting train line. Measurement uncertainties for PM and VOCs were treated through the use of duplicate test samples and multiple sampling devices, ensuring consistency and reliability of the results. The physicochemical characteristics of braking emitted particles were examined, with a focus on size distribution and chemical composition. The analysis revealed significant contributions from iron, barium, and calcium. The potential origins of PM, including brake pads and discs, were examined by identifying tracer metals to estimate the contributions of pad and disc wear to emissions. Furthermore, the relationship between average PM emissions and wear was assessed by comparing the consistency between material mass and volume loss and the measured particle mass emissions. Finally, the relationship between real-time VOC emissions and braking operating conditions during the heavy pathway was investigated. The results demonstrated that braking contact temperature and speed are key factors influencing VOC release, with the extent of their impact depending on the specific type of VOC.

The second part of the thesis examines the effect of modifying the brake system on emissions. The first modification focused on the brake pad design by varying the curing process during manufacturing, resulting mainly in variations in rigidity and thermal expansion without changing the material formulation. This modification resulted in noticeable changes in PM emissions, with the rigid pad material producing the highest emissions, followed by the reference, and then the soft pad, while VOC emissions remained relatively unaffected. The second modification concerned the system scale. Although the full scale is closer to reality, the reduced scale offers more controlled conditions, enabling a better observation of the phenomena generated by mechanical braking. The effect of the downscaling on the tribology and wear had been previously studied, but not the effect on emissions. In this study, braking tests at both scales exhibited emitted particles with the same physical and chemical characteristics.

Key words: Emissions, braking, particles, volatile organic compounds

Résumé

La qualité de l'air est une préoccupation majeure de santé publique à l'échelle mondiale. Le transport ferroviaire est à juste titre reconnu comme l'une des solutions de mobilité les plus écologiques et efficaces en matière d'émissions de CO_2. Cependant, les gares ferroviaires souterraines présentent souvent une qualité de l'air dégradée, soulevant d'importantes préoccupations concernant les émissions non liées à l'échappement. Cette thèse vise à déterminer les caractéristiques physico-chimiques et l'origine des particules (PM) collectées selon leur taille, et à caractériser les émissions de composés organiques volatils (COV) dans différentes conditions de freinage, en utilisant un protocole réaliste de 8 heures d'exploitation journalière d'un train de banlieue. Les essais ont été menés sur un tribomètre à échelle réduite, la réduction d'échelle développée au laboratoire LaMcube se basant sur des facteurs thermiques et thermo-mécaniques.

La première partie de ce travail étudie l'effet de l'énergie de freinage en menant les essais selon deux niveaux de sollicitation, représentant des scénarios d'exploitations normale et intensive d'une ligne de train de banlieue. Les incertitudes de mesure pour les PM et les COV ont été traitées par le doublement des essais et l'utilisation de dispositifs de prélèvement multiples, assurant la cohérence et la fiabilité des résultats. Les caractéristiques physico-chimiques des particules issues du freinage ont été examinées, en se concentrant sur la distribution granulométrique et la composition chimique. L'analyse a révélé une contribution significative du fer, du baryum et du calcium. L'origine potentielle des PM, incluant les garnitures et les disques de frein, a été évaluée à l'aide d'éléments traceurs pour estimer leurs contributions respectives à l'usure. De plus, la relation entre les émissions moyennes de PM et l'usure a été examinée en comparant les pertes de masse et de volume des matériaux avec les émissions particulaires mesurées. Finalement, la relation entre les émissions instantanées de COV et les conditions de fonctionnement du frein pour l'exploitation intensive du train a été explorée. Les résultats montrent que la température de contact et la vitesse influencent fortement l'émission de COV, l'ampleur des effets dépendant du type de composé.

La seconde partie de la thèse examine l'effet de modification du système de freinage sur les émissions. La première modification a concerné le design des plaquettes de frein, en variant le processus de cuisson lors de leur fabrication, ce qui a essentiellement induit des variations de rigidité et de dilatation thermique sans avoir modifier la formulation des matériaux. Cette modification entraîne des changements notables dans les émissions de particules : le matériau le plus rigide génère le plus d'émissions, suivi du matériau de référence, puis du matériau le plus souple, tandis que les émissions de COV restent relativement stables. La deuxième modification concernait l'échelle du système. Bien que la pleine échelle soit plus proche de la réalité, l'échelle réduite offre des conditions plus contrôlées, permettant une meilleure observation des phénomènes générés par le freinage mécanique. L'effet de la réduction d'échelle sur la tribologie et l'usure avait été précédemment étudié, mais pas l'effet sur les émissions. Dans cette étude, les tests de freinage aux deux échelles ont montré des particules émises avec les mêmes caractéristiques physiques et chimiques.

Mots clés : Émissions, freinage, particules, composés organiques volatils

Introduction et Contexte

La pollution de l'air demeure le principal risque environnemental pour la santé en Europe, contribuant de manière significative aux maladies respiratoires et cardiovasculaires, aux cancers et à la mortalité prématurée. Parmi les différentes sources de pollution, les transports jouent un rôle critique — non seulement par la combustion de carburants, mais aussi, de plus en plus, à travers des processus non liés à l'échappement tels que l'usure des freins et des pneus. Historiquement, la recherche et la réglementation se sont concentrées principalement sur les émissions d'échappement. Cependant, avec la montée en puissance des véhicules électriques, y compris les trains électriques, l'attention s'est progressivement portée sur les impacts encore peu étudiés mais importants des émissions non liées à l'échappement.

Bien que les trains électriques soient généralement perçus comme bénéfiques pour l'environnement en raison de l'absence d'émissions à l'échappement, ils contribuent néanmoins de manière significative à la pollution de l'air, notamment dans les environnements clos tels que les systèmes ferroviaires souterrains. Le freinage mécanique génère de grandes quantités de matières particulaires (PM) et de composés organiques volatils (COV) par friction entre les plaquettes de frein et les disques. Ces émissions, souvent appelées particules d'usure aéroportées (PUA), s'accumulent dans des espaces confinés où la ventilation est limitée, ce qui soulève de sérieuses préoccupations sanitaires pour les usagers quotidiens, le personnel des transports et les populations urbaines environnantes.

L'exposition à ces particules, souvent fines, voire ultrafines, ainsi qu'aux composés gazeux associés a été liée au stress oxydatif, à l'inflammation et à d'autres effets biologiques. Il est important de souligner que, bien que les émissions de PM aient été largement étudiées, les COV restent encore mal caractérisés, en particulier dans les environnements ferroviaires. Leur composition, leur évolution temporelle, leurs mécanismes d'émission et leurs interactions avec les processus atmosphériques ne sont pas encore entièrement compris. Ce manque de connaissances freine le développement de stratégies de réduction efficaces et limite notre capacité à évaluer la charge environnementale réelle des systèmes ferroviaires électriques.

Motivation de la Recherche et Objectifs

Cette thèse répond à la nécessité urgente de caractériser en détail les émissions de particules (PM) et de composés organiques volatils (COV) générées par les systèmes de freinage ferroviaires. Son objectif principal est d'étudier comment les conditions de freinage et la configuration des systèmes influencent la génération et le comportement de ces polluants. Plus précisément, elle examine les effets de :

- la sévérité du freinage (freinage normal vs freinage intensif),
- la conception des plaquettes de frein, incluant leur rigidité et la géométrie des rainures,
- les propriétés thermiques et mécaniques des matériaux (influencées par les procédés de cuisson),
- l'échelle du système d'essai (à pleine échelle vs à échelle réduite).

L'objectif global est de mettre en évidence les transformations physico-chimiques qui se produisent durant le freinage, de caractériser la dynamique des émissions de polluants et de quantifier les facteurs d'émission dans des scénarios de freinage représentatifs.

Pour y parvenir, l'étude combine des mesures en temps réel et hors ligne, développe une méthode optimisée d'échantillonnage des COV, et évalue la représentativité des essais à échelle réduite par rapport

aux systèmes à pleine échelle. Ce travail propose également un cadre méthodologique systématique permettant de relier les mécanismes d'usure au comportement des émissions, en fournissant les premiers facteurs d'émission détaillés pour les COV dans des conditions de freinage contrôlées en environnement ferroviaire.

Approche Méthodologique

Afin de garantir la précision et la reproductibilité des résultats, les expériences ont été menées à l'aide de systèmes de freinage à la fois à pleine échelle et à échelle réduite. Le banc d'essai à pleine échelle, exploité en collaboration avec Alstom-Flertex, a permis de simuler des séquences réelles de freinage de métro en utilisant des composants de frein industriels soumis à des pressions et vitesses opérationnelles.

Le tribomètre à échelle réduite, issu de la thèse de Joseph Frangieh (2025), a quant à lui été soigneusement calibré pour reproduire l'environnement thermomécanique du freinage à pleine échelle, tout en offrant une plus grande flexibilité et un meilleur contrôle sur les variables d'essai.

Instrumentation et Analyses

Un ensemble d'instruments de pointe a été mobilisé pour analyser à la fois les émissions particulaires et les espèces gazeuses :

- L'analyse de la masse et de la taille des particules au moyen de porte-filtres et d'impacteurs en cascade,
- L'analyse élémentaire par plasma à couplage inductif (ICP), la quantification du carbone organique et élémentaire (OC/EC), et la microscopie électronique à balayage avec spectroscopie EDX (SEM-EDX),
- L'étude du comportement thermique et de la dégradation des plaquettes de frein à l'aide d'une analyse thermogravimétrique couplée à la spectroscopie infrarouge (TGA-FTIR),
- La spéciation des composés gazeux par chromatographie en phase gazeuse couplée à la spectrométrie de masse (GC-MS) et chromatographie liquide haute performance (HPLC),
- La surveillance en temps réel des COV par spectrométrie de masse à transfert de protons (PTR-MS).

Des protocoles rigoureux ont été appliqués pour minimiser les risques de contamination, et l'ensemble des tests a été répété afin d'évaluer l'incertitude des mesures et la répétabilité des résultats.

Principaux Résultats sur la Sévérité du Freinage

Les résultats de cette thèse démontrent que les émissions de particules (PM) et de composés organiques volatils (COV) provenant des systèmes de freinage ferroviaires sont fortement sensibles aux paramètres de freinage, à la conception des plaquettes et à l'échelle des essais. Parmi toutes les variables étudiées, la sévérité du freinage est apparue comme le facteur le plus influent. En conditions de freinage intensif, caractérisées par un apport énergétique plus élevé et une température d'interface accrue, les émissions de PM ont considérablement augmenté. En particulier, les concentrations de particules en suspension totale (TSP) ont été multipliées par un facteur allant de 6 à 11 par rapport à un freinage normal.

La distribution granulométrique des PM est restée de type unimodal dans tous les scénarios, avec un pic dominant autour de 1 µm. Cela suggère un mécanisme uniforme de détachement des particules, probablement dû à une abrasion thermo-mécanique, indépendamment du niveau d'énergie appliqué. Les distributions ont également révélé que les particules submicroniques, les plus susceptibles d'être inhalées profondément dans les poumons, représentaient une part significative de la masse totale.

Les mesures temporelles des particules ont montré un pic d'émission rapide au début du freinage, cohérent avec des contacts de friction intenses initiaux et la fragmentation des aspérités de surface. À mesure que le freinage se poursuivait, les niveaux de PM diminuaient, probablement en raison d'une stabilisation des surfaces et d'une accommodation thermique. En revanche, les COV ont suivi une dynamique temporelle différente. Les mesures en temps réel par PTR-MS ont révélé que les émissions de COV augmentaient généralement tout au long de l'événement de freinage, atteignant souvent leur maximum à la fin ou peu après. Ce décalage s'explique par la décomposition thermique des composés organiques présents dans la plaquette, comme les liants et les élastomères, qui se dégradent progressivement à mesure que la température augmente à l'interface de friction.

Les analyses hors ligne des COV ont confirmé la présence de composés dangereux, notamment des aldéhydes (acétaldéhyde, formaldéhyde), des cétones (propanone), des phénols et divers hydrocarbures aromatiques polycycliques (HAP). Nombre de ces substances sont reconnues comme irritantes ou cancérogènes, ce qui soulève des préoccupations quant à l'exposition chronique des usagers et du personnel dans les environnements de transport souterrains. L'analyse TGA-FTIR des plaquettes de frein a confirmé un processus de décomposition en plusieurs phases, au cours duquel les composants organiques de la matrice se dégradent à différentes plages de température, libérant des sous-produits gazeux à l'origine des COV.

La réponse des différents COV aux paramètres de freinage était variable. Par exemple, l'acroléine a montré une forte dépendance à la température, avec une augmentation marquée en cas de freinage intensif, tandis que des composés aromatiques comme le toluène et le benzène étaient plus corrélés à l'énergie totale du freinage. Fait intéressant, à des puissances de freinage très élevées, les émissions de COV diminuaient parfois, suggérant que des pressions de contact accrues pourraient réduire l'échappement des gaz en resserrant l'interface entre la plaquette et le disque.

Influence de la Conception des Plaquettes de Frein et de l'Échelle du Système

La conception des plaquettes a également eu un impact significatif sur le comportement des émissions. Les plaquettes rigides, en raison de leur module d'élasticité plus élevé et de leur meilleure conductivité thermique, ont généré 2 à 3 fois plus de particules en suspension totale (TSP) que les plaquettes plus souples dans des conditions de test identiques. Toutefois, les distributions granulométriques des particules sont restées similaires entre les différents types de plaquettes, ce qui indique que la rigidité influence davantage la quantité totale d'émissions que le mécanisme de formation des particules. Les plaquettes rainurées ont présenté des tendances d'émission particulières, probablement liées à des modifications du flux d'air et des schémas de microcontacts à l'interface, pouvant soit favoriser, soit limiter l'échappement des particules et des gaz selon la dynamique du freinage.

Sur le plan de la composition chimique, les émissions de PM étaient systématiquement dominées par le fer (Fe), reflet de la contribution commune du disque en fonte et de la plaquette. Des éléments secondaires tels que le baryum (Ba), le calcium (Ca) et l'aluminium (Al) étaient également présents de manière significative. Les fractions submicroniques conservaient une proportion importante de ces

métaux, ce qui indique que les particules fines sont non seulement de petite taille physique, mais aussi chimiquement représentatives des matériaux sources. La teneur en carbone organique des particules émises diminuait fortement lors des freinages intensifs, ce qui témoigne d'une volatilisation des composés organiques à des températures élevées. Cette observation est corroborée par l'analyse de fermeture massique, qui montre que les oxydes métalliques et les composés carbonés constituent la majorité de la masse particulaire.

À l'inverse, les émissions de COV semblaient moins sensibles à la rigidité des plaquettes, renforçant l'hypothèse selon laquelle les émissions gazeuses proviennent principalement de la dégradation thermique des matériaux, plutôt que de l'usure mécanique. Bien que tous les types de plaquettes aient émis des COV, les différences de concentration totale et de composition restaient faibles, en particulier en conditions de freinage normal. La constance des émissions de COV malgré les variations de propriétés mécaniques souligne l'importance de cibler les comportements thermiques et les processus de décomposition lors de la conception de matériaux à faibles émissions.

Un autre résultat clé de cette étude est la validation des essais à échelle réduite pour l'étude des émissions. En ce qui concerne les particules, les tests à échelle réduite et à pleine échelle ont produit des résultats très comparables en termes de facteurs d'émission, de profils chimiques et de distributions granulométriques. Ce constat confirme l'intérêt des bancs d'essai contrôlés en laboratoire pour mener des études répétables et économiquement viables sur l'usure des freins. Pour les COV, les tests à échelle réduite se sont révélés encore plus avantageux, offrant une interférence de fond plus faible et une meilleure clarté des signaux. Toutefois, les essais à pleine échelle restent indispensables pour valider la pertinence en conditions réelles et prendre en compte des variables complexes telles que la ventilation, la température ambiante et la contamination extérieure.

Développement de la Méthode d'Échantillonnage des COV

Une innovation majeure de cette thèse réside dans le développement d'un protocole d'échantillonnage des composés organiques volatils (COV) spécifiquement adapté aux essais d'usure des freins. Les méthodes traditionnelles de mesure des COV souffrent de plusieurs limitations, telles que la contamination des échantillons, un faible taux de récupération, et l'incapacité à isoler les gaz issus spécifiquement du freinage.

Cette étude a introduit:

- Des protocoles de correction des blancs et des entrées d'air pour éliminer les bruits de fond,
- Une analyse conjointe des phases gazeuse et particulaire,
- Une vérification croisée par détection hors ligne et en temps réel.

Cette nouvelle approche a permis d'établir pour la première fois des facteurs d'émission quantitatifs des COV liés au freinage ferroviaire, ainsi que l'identification de plus de 40 composés individuels, incluant des carbonyles, des composés aromatiques et des semi-volatils. Ces avancées méthodologiques jettent les bases d'une standardisation des évaluations de COV dans la recherche sur les transports.

Conclusion et Perspectives

Cette thèse présente une investigation approfondie des émissions générées par les systèmes de freinage ferroviaires, en s'intéressant à la fois aux particules et aux composés organiques volatils. Elle identifie les variables clés — la sévérité du freinage, la rigidité des matériaux, et l'échelle d'essai — qui influencent la production de polluants, tout en offrant des éléments de compréhension sur les mécanismes physico-chimiques impliqués.

Elle introduit également un protocole robuste de mesure des COV, permettant à de futurs travaux de recherche de s'appuyer sur ces résultats avec plus de précision et de fiabilité.

Les perspectives de recherche incluent :

- L'extension des études sur les COV à des environnements réels d'exploitation avec des horaires de train dynamiques,
- L'exploration de formulations alternatives de plaquettes pour réduire les émissions,
- L'étude de la formation de polluants secondaires issus de l'oxydation des COV,
- La réalisation d'évaluations toxicologiques des espèces émises afin d'évaluer les risques pour la santé publique.

Dans l'ensemble, ce travail fait progresser notre compréhension des émissions non liées à la combustion dans le secteur ferroviaire et offre des bases concrètes pour concevoir des systèmes de mobilité urbaine plus propres et plus sûrs.

Table of Contents

Acknowledgments VI
List of figures VII
List of tables XII
List of appendices XIV
List of abbreviations XV
Introduction 1
Chapter 1: Review of particulate and gaseous emissions from urban railway braking 3
1.1 Air quality 3
1.1.1 Overview of Main PM Sources in Europe 3
1.1.2 Impact of non-exhaust emissions 4
1.2 Exposure and health effects 5
1.3 Brake system 7
1.3.1 Braking phenomena 7
1.3.2 Wear and tribological circuit 7
1.3.3 Factors affecting emissions 11
1.4 PM in railway transports 14
1.4.1 PM concentrations 14
1.4.2 PM properties 18
1.4.3 PM sources in railway transport 21
1.5 Gases in railway transports 22
1.5.1 Gas concentrations 22
1.5.2 Gas sources in railway transport 23
1.6 Mitigation strategies 24
1.7 Conclusions of the bibliographic study 24
1.8 Framework 25
1.8.1 BREAQ project 25
1.8.2 Thesis Objectives 25
Chapter 2: Experimental setups and methods 27
2.1 Materials 27
2.1.1 Braking disc 27
2.1.2 Pad 27
2.2 Full-scale brake system 27

2.3 Reduced-scale brake system 29
2.4 Test protocols 33
2.4.1 Pathways 33
2.4.1.1 Normal pathway (NP) 33
2.4.1.2 Heavy pathway (HP) 34
2.4.2 Background measurements 35
2.4.2.1 Particle background characterization in reduced scale setup 35
2.4.2.2 Assessment of airflow dynamics and indoor air infiltration in the full-scale setup 35
2.4.3 Bedding 37
2.4.4 Summary of the tests performed at both scales 38
2.5 Physical measurements during the tests 38
2.5.1 Temperature measurement 38
2.5.2 Pad and disc wear measurements 39
2.6 Experimental set-up for PM and VOC measurement at reduced scale 39
2.6.1 Experimental set-up for PM measurement at reduced scale 41
2.6.1.1 Sampling of PM for off-line analysis at reduced scale 41
2.6.1.2 Particle mass concentration and uncertainties 43
2.6.1.3 Online PM measurement at reduced scale 45
2.6.1.4 Summary of PM measurements at reduced scale 46
2.6.2 Experimental set-up for VOC measurements at reduced scale 47
2.6.2.1 Off-line VOC measurement at reduced scale 47
2.6.2.2 Online VOC measurement at reduced scale 47
2.6.2.3 Summary of VOC measurements at reduced scale 49
2.7 Experimental set-up for PM and VOC measurement at full scale 49
2.8 Offline analytical techniques and procedures 50
2.8.1 Elemental analysis of particles by ICP-MS and ICP-AES 50
2.8.1.1 Experimental methods 50
2.8.1.2 Validation of the analytical method 51
2.8.1.3 Estimation of the chemical speciation of the elements 55
2.8.1.4 Methodology of source apportionment based on the metal analysis of particles 57
2.8.2 Thermo-optical analysis of particulate carbon 58
2.8.3 Microscopic observation of particles 60
2.8.4 Determination of volatile carbonyl compounds by HPLC-UV 60

2.8.4.1 Uncertainties 61
2.8.4.2 Blank assessment 61
2.8.5 Determination of VOC by TD-GC-MS-FID 63
2.8.5.1 Quantitative analysis 64
2.8.5.2 Laboratory calibration 65
2.8.5.3 Blanks assessment 65
2.8.6 Pad thermogravimetric analysis by TGA-FTIR 66
Chapter 3: Effect of braking severity on emissions at the reduced scale bench 67
3.1 Average emissions for the normal and heavy pathways 67
3.1.1 Average and maximum temperatures recorded during the normal and heavy pathways 67
3.1.2 Average mass concentrations of Total suspended particles (TSP), sampled using filtration and impaction, during the normal and heavy pathways 68
3.1.2.1 TSP average mass concentrations of replicates across different sampling supports 68
3.1.2.2 Mass size distributions for NP and HP 69
3.1.3 Physico-chemical characterization of the pad and disc materials 71
3.1.3.1 Chemical analysis of pad and disc by ICP-MS/AES 71
3.1.3.2 Identification of pad and disc metal tracers 72
3.1.4 Average elemental composition of the emitted TSP 72
3.1.4.1 Repetition consistency of elemental composition of TSP from NP & HP 72
3.1.4.2 Mass closure & elemental composition of TSP from NP & HP 73
3.1.5 Submicron particle composition from the 3-stage impactor 76
3.1.5.1 Consistency of metallic composition using different sampling supports 77
3.1.5.2 Mass closure & elemental composition of submicronic particles from NP & HP 77
3.1.5.3 Effect of severity of braking on total carbon emissions 80
3.1.5.4 Mass size distribution of major elements under NP & HP from the 14-stage impactor. 82
3.1.6 Wear and emissions characteristics in normal vs heavy pathways 85
3.1.6.1 Effect of braking severity on the metal enrichment of TSP 85
3.1.6.2 Consistency of overall wear (mg/km) and emissions (mg/km) 87
3.1.6.3 Particle formation in the heavy pathway 91
3.1.6.4 Comparison of submicronic particle emissions between normal and heavy pathways . 92
3.1.7 Average emissions of Volatile Organic Compounds 95
3.1.7.1 Carbonyl compounds sampled on DNPH cartridges 95
3.1.7.2 Other VOCs sampled on Tenax cartridges 96

3.1.7.3 VOC emissions from the pad using TGA-FTIR 100
3.1.7.4 Synthesis of the VOCs identified in integrated samples 101
3.2 Dynamics of the emissions 103
3.2.1 TVOC emission trends under normal and heavy braking conditions using PID analysis 103
3.2.1.1 Peak selection 103
3.2.1.2 PID dynamics during NP 103
3.2.1.3 PID dynamics during HP 104
3.2.1.4 Effect of braking power on TVOC emissions 105
3.2.2 VOC emission dynamics during braking events: Time-resolved analysis using Proton Transfer Reaction–Mass Spectrometry (PTR-MS) 106
3.2.2.1 Choice of compounds 106
3.2.2.2 Backgrounds of the major VOCs 110
3.2.2.3 Overview of VOC emissions and temperature evolution with time 110
3.2.2.4 Repeatability of VOC emissions across round trips 112
3.2.2.5 Temporal behavior and source classification of VOC 113
3.2.2.6 Correlations between VOCs and braking parameters 118
3.2.2.7 Emission behavior under single braking application 122
3.2.2.8 Emission behaviors under multiple braking applications 124
Chapter 4: Modification of the pad design and brake system 128
4.1 Effect of the brake pad design 128
4.1.1 Average mass concentrations from NP using the modified pads 129
4.1.1.1 TSP average mass concentrations of replicates across different sampling supports ... 129
4.1.1.2. Mass size distributions of particles related to pad designs 129
4.1.2 Average elemental composition of the emitted TSP from NP using the modified pads 130
4.1.2.1 Repetition consistency of elemental composition in TSP from NP1 and NP2 across the modified pads 130
4.1.2.2 Mass closure and elemental composition of TSP from NP1 & NP2 using modified pads 131
4.1.3 Submicron particle composition from the 3-stage impactor using the modified pads 133
4.1.3.1 Mass closure and elemental composition of submicronic particles from NP1 & NP2 using various brake pads 133
4.1.3.2 Effect of pad rigidity on carbon emissions and disc wear contribution in submicronic particles 135
4.1.3.3 Effect of pad grooves on carbon emissions in submicronic particles 136

4.1.4 Mass size distribution of major elements using rigid pad from the 14-stage impactor 139
4.1.5 Scanning Electron Microscopy (SEM) observations of particles emitted from grooved pad under braking application 141
4.1.6 Average emissions of VOCs 143
4.1.6.1 Effect of pad rigidity and pad design on TVOC 143
4.1.6.2 Carbonyl emissions 143
4.2 Effect of the scale brake system 146
4.2.1 Mean to change the scales 146
4.2.2 Emission factors under normal and heavy pathways at both test scales 147
4.2.3 Particle mass size distribution 148
4.2.4 Chemical composition and scale comparison of brake particles under HP 148
4.2.5 Estimation and comparison of pad and disc contributions to brake particle emissions across full and reduced scales 150
4.2.6 VOC analysis 151
Chapter 5: Conclusions and perspectives 153
5.1 Conclusions 153
5.2 Perspectives 155
References 156
Appendices 168

Acknowledgments

I would like to express my gratitude to the Alstom Group, coordinator of the ADEME BREAQ Project, for the scientific and industrial collaboration, with special gratitude to Alstom Flertex for providing access to their testing facilities. I extend my warmest thanks to Karine Pajot for her exemplary project management and her understanding of the project's challenges.

I am deeply grateful to my directors and supervisors, each of whom added their spark to this PhD. Alexandre Tomas, for his reassuring presence throughout the ups and downs of this journey. Yannick Desplanques, whose ability to make sense of tribology never failed. Esperanza Perdrix, for her patience and support whenever my brain hit a red light. Alexandre Mege-Revil, for always offering just the right critique. And, Laurent Alleman, whose insightful thoughts, besides his good humor, made every meeting both productive and enjoyable. It was an honor to have such a brilliant and perceptive supervisory team. Your guidance, especially during the final stretch, helped pull the thesis over the finish line. Thank you all for your kindness and support throughout this journey.

I would also like to thank all the staff at CERI EE, especially Marina Jamar, whose quick and clever solutions to every VOC issue were invaluable. Thanks to Isabelle Fronval and Laurence Depelchin, who managed full conversations about DNPH analysis despite my very limited French, giving me hope that I might actually survive the language! And to Bruno Malet, many thanks, not only for his priceless help with ICP analyses, but also for the countless filters he patiently weighed throughout my PhD. I am also thankful to all the LaMcube staff for their warm welcome, and especially to Joseph Frangieh, Asma Grira, and Laurent Coustenoble, who shared long experimental days in the lab and transformed intense days into successful teamwork. To my colleagues in Douai and Lille who became friends during my PhD—you made this journey not only educational but also much more bearable, filled with laughter along the way.

To my dear friends, my second family here abroad, who made Douai feel like home, thanks for being my pillars and source of encouragement. I am deeply grateful for your support and for believing in me during the challenging times.

Last but certainly not least, I would like to express my profound gratitude to my family, especially my parents and sisters. Thank you for your unconditional support. No matter the distance, I always felt your love and encouragement, and you were closer to me than ever when I needed it most.

Finally, thanks to everyone who helped me, directly or indirectly, scientifically or personally, in surviving this journey.

List of figures

Figure 1.1 Population exposure to $PM_{2.5}$ and PM_{10} exceeding the WHO guidelines (Chang et al., 2021) ... 3
Figure 1.2 Contribution (%) of different transport sectors to total emissions of PM_{10} and $PM_{2.5}$ in Europe (*EEA*, 2019) ... 4
Figure 1.3 Sources of railway emissions (*UBA*, 2020) ... 5
Figure 1.4 Representation of the ability of PM to penetrate the respiratory system according to their size (Guarnieri & Balmes, 2014) ... 6
Figure 1.5 Railway disc brake - Alstom Flertex full-scale test bench ... 7
Figure 1.6 Physico-chemical phenomena involved in the contact (Vakis et al., 2018) ... 8
Figure 1.7 Tribological circuit (Renouf & Saulot, 2015) ... 9
Figure 1.8 Third body (Desplanques & Degallaix, 2010) ... 10
Figure 1.9 Competition of the source flow and wear flow as functions of the mass Mi of the third body (Fillot et al., 2007) ... 11
Figure 1.10 Yearly PM_{10} concentrations in 2022 in different Parisian subway stations and near the Paris ring road in Porte d'Auteuil (modified from (RATP, 2023)) ... 14
Figure 1.11 Mean particle emission rates for different braking materials adapted from (Abbasi et al., 2012) ... 18
Figure 2.1 Full scale test bench at Alstom Flertex. The blue arrows indicate the trajectory of the inlet air; the red arrows refer to the trajectory of the outlet air. In the photography of room 1, the door of the cabin is open to show the dynamometer inside. This door is closed for safety when tests are performed. ... 28
Figure 2.2 Pads in full scale ... 28
Figure 2.3 Disc-pad assembly at full scale. ... 29
Figure 2.4 LaMcube test room ... 29
Figure 2.5 Thermal properties of soft (in red), rigid (in green) and reference (in blue) pad materials:(a) thermal diffusivity, (b) thermal conductivity in both normal (in dark) and tangential (in light) directions, and (c) specific heat capacity (Frangieh, et al., 2025). ... 31
Figure 2.6 Designs of the reduced-scale pads "reference", "rigid" and "soft" (left) and of the reduced-scale pad "grooved" (right). ... 31
Figure 2.7 Reduced-scale enclosure of the disc-pad system. ... 32
Figure 2.8 Overall scheme of the experimental set-up at reduced scale. ... 33
Figure 2.9 Braking conditions during one way of a round trip of the normal pathway (Frangieh 2025) ... 34
Figure 2.10 Mechanical brake applications in the normal pathway ... 34
Figure 2.11 PM temporal profile of total particle number concentration measured by FMPS in a blank sample ... 35
Figure 2.12 Schematic of airflow and emission sampling in the full-scale dynamometer setup, with the red arrow indicating a positive indoor air flow rate and the green arrow indicating a negative indoor air flow rate. ... 36
Figure 2.13 Ratio of the volumetric flow rate of indoor air to outlet air in function of the disc speed. A positive ratio means that indoor air penetrates into the cabin. A negative one means that no indoor air enters the cabin but that some cabin air escapes to the workshop. ... 36

Figure 2.14 Thermocouples: red dots in the disc, orange dots in the pads, blue dot in the enclosure, and green dot at the exit, shown at reduced scale (detail of Figure 2.8) 39
Figure 2.15 Reduced-scale emission measurement instrumentation 40
Figure 2.16 Scheme of the filter holder and the 3-stage and 14-stage impactors with their respective sampling air flow rates 42
Figure 2.17 Simplified diagram of PTR-MS (adapted from Amann et al., 2010) 48
Figure 2.18 PTR-MS set up during sampling 48
Figure 2.19 Position of the sampling system in the dynamometer facility at full scale 49
Figure 2.20 Full scale emission measurement instrumentation 50
Figure 2.21 Simple cause and effect diagram to identify factors related to accuracy and precision (Lamaison 2006) 53
Figure 2.22 Quartz filter (blank) showing the punch ready for carbon analysis 59
Figure 2.23 Particles captured on filters using the 3-stage impactor with aerodynamic diameters of (a) >10 µm, (b) 2.6-10 µm, (c) 1-2.6 µm and backup filter <1 µm. 60
Figure 2.24 Schematic diagram of the High-Performance Liquid Chromatography (HPLC) system (Czaplicki, 2013) 61
Figure 2.25 Schematic diagram of the TD-GC-MS-FID 64
Figure 2.26 Concentrations of selected compounds in 8 h and 1 h blank samples 66
Figure 3.1 Mass size distribution of the emitted particles for the normal pathway (a), and (b) superimposition of the normal and heavy pathway using a reference pad and the cast iron disc 70
Figure 3.2 Comparison of the metal concentrations in the emitted TSP between the 2 repetitions of the normal pathway (a) and heavy pathway (b) using the reference pad 73
Figure 3.3 Mass closure and chemical composition of particulate emissions (NP1 and NP2) 74
Figure 3.4 Metal content in TSP for NP1 & NP2 using the reference pad 74
Figure 3.5 Mass closure and chemical composition of particulate emissions (HP1 and HP2) 75
Figure 3.6 Metal concentration in TSP for HP1 & HP2 using the reference pad 76
Figure 3.7 Mass closure and chemical composition of submicronic (PM1) particulate emissions (NP1 and NP2) 77
Figure 3.8 Metal content in submicronic particles for NP1 & NP2 using the reference pad 78
Figure 3.9 Mass closure and chemical composition of submicronic particulate emissions (HP1 and HP2) 78
Figure 3.10 Metal concentrations in submicronic particles for HP1 & HP2 using the reference pad 80
Figure 3.11 Total carbon emissions with the reference brake pad: (a) carbon concentration in submicronic particulate matter collected during NP and HP braking pathways; (b) weight percentage of total carbon content in submicronic particulate emissions collected on the backup filter for NP and HP 81
Figure 3.12 TC content in PM10 samples under different braking protocols for NAO 1 and NAO 2 (Alves et al., 2021) 82
Figure 3.13 Particle mass concentration size distribution of selected metals during NP1 84
Figure 3.14 Volumetric wear loss (Thesis of Frangieh, 2025) 88
Figure 3.15 Calculation method of emissions factors based on wear volume and emission mass 89
Figure 3.16 Surface observations using SEM on worn surfaces of the pads: (a) pad surface after NP2, (b) close up of the stored particles on the pad, (c) pad surface after HP2, (d) close up of stored particles on the pad (Frangieh, 2025) 91
Figure 3.17 Surface observations using SEM on disc worn surfaces after (a) NP, and (b) HP2 (Frangieh, 2025) 94

Figure 3.18 Mass concentrations of carbonyls using DNPH-HPLC/UV with the reference pad for (a) NP and (b) HP 95
Figure 3.19 Zoomed TIC from GC/MS analysis of NP1 test outlet in red and NP2 test outlet in black 97
Figure 3.20 Zoomed TIC from GC/MS analysis of HP1 test outlet in red and HP2 test outlet in black..... 97
Figure 3.21 Zoomed TIC from GC/MS analysis of NP2, test outlet in black and test inlet in red..... 98
Figure 3.22 Zoomed TIC from GC/MS analysis of HP2 test outlet in black and HP2 test inlet in red 99
Figure 3.23 2D and 3D FTIR mapping of evolved gases during thermal degradation of the pad in oxygen atmosphere 101
Figure 3.24 Yellow stars mark the peaks selected where the TVOC (ppb) values exceed baseline fluctuations observed in blank samples. Only peaks surpassing the background fluctuations are selected 103
Figure 3.25 The evolution of the PID signal throughout the NP1, with the exit enclosure temperature superimposed 104
Figure 3.26 The evolution of the PID signal throughout the HP1, with the mean temperature at 2 mm from the surface of the pad and the disc 105
Figure 3.27 Effect of braking force using the reference pad by comparing the average TVOC concentration measured by PID of NP in blue and HP in orange..... 106
Figure 3.28 Example of PTR-MS compound signals (a) exhibiting a baseline increase with no variation during braking, and (b) with zero concentration throughout the test 107
Figure 3.29 Examples of PTR-MS compound signals exhibiting strong increase from the baseline during braking throughout the test 107
Figure 3.30 Background measurements were conducted for 50 min prior to the test, focusing on the major compounds. These measurements used pure air (Alpha Gas 1) with disc rotation inside the enclosure 110
Figure 3.31 The upper panel shows particle emissions measured by OPS and FMPS; the middle panel presents the emissions of the sum of selected VOCs measured by PTR-MS (intermittent measurements); and the bottom panel shows the temperature evolution of the pad and disc, measured 2 mm from their surfaces. 111
Figure 3.32 Time-resolved profiles of TVOC concentrations measured by PTR-MS (top panel) and the corresponding disc rotational speed and applied force (bottom panel) during three consecutive return rounds 112
Figure 3.33 Dynamic emissions of the major VOCs measured by PTR-MS and braking parameters (pad and disc temperature, normal and tangential force, and speed) during a typical braking event 113
Figure 3.34 Major VOCs distribution throughout the whole heavy pathway 114
Figure 3.35 Braking profiles of (a) m41_frag.C3H4.H^+ and (b) m59_C3H6O.H^+ concentrations (top panel) and their corresponding disc rotational speed and applied force (bottom panel)..... 115
Figure 3.36 Time evolution of pad temperatures (average and maximum) and ambient temperatures (enclosure and exit) in relation to the evolution of m41_frag.C3H4.H^+ during the transition from the second to the third round trip..... 116
Figure 3.37 Measurement of m57_frag.C4H8.H^+ (a) background (b) Time-resolved profiles of m57_frag.C4H8.H^+ concentrations (top panel) and the corresponding disc rotational speed and applied force (bottom panel) during three consecutive return rounds 118
Figure 3.38 Relationship between total VOC concentrations measured by PTR-MS and braking parameters under single braking conditions..... 118

Figure 3.39 Relationship between dissipated energy and m42_C2H3N.H^+ (acetonitrile), m79_C6H6.H^+ (benzene), and m93_C7H8.H^+ (toluene) across the round trips with single braking application 119
Figure 3.40 Relationship between maximum disc temperature and m57_C3H4O.H^+ (acrolein) across the round trips with single braking application 119
Figure 3.41 Relationship between total VOC emissions and braking parameters under single braking conditions (with averaged intervals) 120
Figure 3.42 Influence of maximum braking power, force components, and initial speed on Total VOC emissions during single braking applications 121
Figure 3.43 Influence of maximum braking power, tangential force on m57_C3H4O.H^+ (acrolein) during single braking applications 122
Figure 3.44 Heatmap representation of VOC concentration (ppb) per PTR-MS mass as a function of relative time of a single station. The blue line indicates the total VOC concentration (right y-axis). Each horizontal line corresponds to a specific PTR-MS mass, with darker shading indicating higher VOC concentration. The plot illustrates the dynamic release and subsequent decline of individual VOC masses and total VOCs over the course of the measurement 122
Figure 3.45 Distribution of VOC concentration (ppb) per PTR-MS mass measured at the peak of the braking event. The horizontal bars represent the molar ratio of each VOC ion at one station 123
Figure 3.46 VOC emissions during the second round trip under single braking scenarios for the HP: (a) one step and (b) two steps 124
Figure 3.47 VOC emissions under various braking scenarios for the HP: (a) single braking application, (b) two consecutive braking applications, and (c) three consecutive braking applications 125
Figure 3.48 Correlation of particle number concentration and major VOC emissions with braking parameters and disc temperature during multiple braking application 126
Figure 3.49 Time-resolved particle size distribution and number concentration within FMPS and OPS measurements during a multiple braking application 127
Figure 4.1 Mass size distribution of the (a) soft, (b) rigid, and (c) superimposition of the 3 pads 130
Figure 4.2 Comparison of the metal concentration between the 2 repetitions of the normal pathway using the (a) soft pad, (b) rigid pad, and (c) grooved pad 131
Figure 4.3 Mass closure and chemical composition of TSP of NP1 and NP2 using: (a) soft pad, (b) rigid pad, and (c) grooved pad 132
Figure 4.4 Metal content of TSP for NP1 & NP2 using: (a) soft pad, (b) rigid pad, (c) grooved pad 133
Figure 4.5 Mass closure and chemical composition of submicronic particles of NP1 and NP2 using: (a) soft pad, (b) rigid pad, (c) grooved pad 134
Figure 4.6 Metal content of submicronic particles for NP1 & NP2 using: (a) soft pad, (b) rigid pad, and (c) grooved pad 135
Figure 4.7 Percentage of total carbon content in normal pathways using the soft, reference, and rigid pad collected on the backup filter (submicron particles) 136
Figure 4.8 Percentage of total carbon content in submicron particles for normal pathways using the reference and the grooved pads 137
Figure 4.9 Particle mass concentration size distribution of selected metals using the rigid pad during the normal pathway 2 140
Figure 4.10 Surface observations using SEM on filter-collected particles from one braking event using grooved pad: (a) overall view, (b) magnified view of marked region 1, (c) magnified view of marked region 2 141

Figure 4.11 Surface observations using SEM on filter-collected particles from one braking event using grooved pad 142
Figure 4.12 Surface observations using SEM on filter-collected particles from one braking event using grooved pad: (a) SEM-SE (b) SEM-BSE, (c) magnified view of marked region 1, (d) magnified view of marked region 2 142
Figure 4.13 Effect of pad rigidity and design on TVOC concentration measured by PID during normal pathway 143
Figure 4.14 Mass Concentrations of the carbonyls for the Normal Pathway with the soft pad (a) and with the rigid pad (b) using DNPH-HPLC/UV 144
Figure 4.15 (a) Comparison of carbonyls from different pads, and (b) zoom in on the compounds with concentrations less than 0.4 µg/m^3 146
Figure 4.16 Particle mass size distribution of HP and NP at full scale 148
Figure 4.17 The chemical composition of particles collected during the third-round-trip of the HP at full scale, comparing TSP collected with a filter holder and PM1 collected with the 3-stage impactor 149
Figure 4.18 Comparison of TSP metal composition between full and reduced scales: linearity in µg/mg and µg/m^3 149
Figure 4.19 Pad and disc contributions to full-scale emissions under HP: (a) TSP, (b) PM1 151
Figure 4.20 Comparison of VOC concentrations measured at the inlet, outlet, and indoor environments during HP 152

List of tables

Table 1.1 Composition of pads 12
Table 1.2 $PM_{2.5}$ concentrations measurements in µg/m^3 in staff areas (Chang et al., 2021) 15
Table 1.3 Comparison of indoor/outdoor ratios of PM concentrations (PM1, $PM_{2.5}$, and PM_{10}) across various cities 16
Table 1.4 Average PM_{10} concentration levels in metro and subway environments worldwide 16
Table 1.5 Average $PM_{2.5}$ concentration levels in metro and subway environments worldwide 17
Table 1.6 Average PM_1 concentration levels in metro and subway environments worldwide 17
Table 1.7 Iron in $PM_{2.5}$ 18
Table 1.8 Summary of metals identified in subway particulate matter by various studies 19
Table 1.9 Comparison of $PM_{2.5}$ metallic content between above-ground and underground stations 19
Table 1.10 Element concentrations found in emitted brake wear dust adapted from (Grigoratos & Martini, 2015) 20
Table 1.11 Reported peak particle sizes and braking conditions in various studies 21
Table 1.12 VOC concentrations in railway stations worldwide 23
Table 2.1 Main components of the braking pad formulation. 27
Table 2.2 Physical parameters: Compression modulus, thermal expansion and density 30
Table 2.3 Carbon weight content in pad materials 31
Table 2.4 Conditions for the bedding of disc and pads. 37
Table 2.5 Summary of the tests performed at both scales 38
Table 2.6 Isokinetic PM sampling in the reduced-scale experimental set-up 41
Table 2.7 Effective particle size classes (aerodynamic diameters) of the modified 3-stage impactors (Appendix 2) 42
Table 2.8 Particle size classes (aerodynamic diameters) of the 14-stage impactor 43
Table 2.9 Summary of particle measurements at reduced scale 46
Table 2.10 Summary of VOC measurements at reduced scale 49
Table 2.11 Isokinetic PM sampling in the full-scale experimental set-up. 50
Table 2.12 Oxide forms, molar masses, and conversions used for metal-to-oxide calculations 55
Table 2.13 Total oxygen percentage varying with iron oxide 56
Table 2.14 LD of HPLC/UV for carbonyl compounds in air and detection in blank samples 63
Table 2.15 GC oven temperature program 64
Table 2.16 Compounds found in the 1-hour blanks 65
Table 3.1 Average and maximal temperatures for normal (NP) and heavy pathways (HP) 67
Table 3.2 Mass concentration in [µg/m3] by the three sampling methods (Filter Holder, 3-stage, and 14-stage impactors) across four test scenarios (NP1 and NP2 in blue, HP1 and HP2 in orange) 68
Table 3.3 Pressure drop across all sampling supports 69
Table 3.4 Pad and disc weight content of elements analyzed by ICP-MS/AES 71
Table 3.5 Ratios of metallic elements between brake pad and disc: pad-to-disc and disc-to-pad fractions (yellow cells: pad tracers, blue cells: disc tracers) 72
Table 3.6 Tracer ratio in TSP of NP2 to NP1 (yellow cells: pad tracers, blue cells: disc tracers) 75
Table 3.7 Tracer ratio in TSP [µg/m3] of HP2 to HP1 (yellow cells: pad tracers, blue cells: disc tracers) 76
Table 3.8 Ionic concentrations measured in backup filter samples from the normal pathways 78

Table 3.9 Ionic concentrations measured in backup filter samples from the heavy pathways 79
Table 3.10 Tracer ratio in submicronic particles of HP2 to HP1 (yellow cells: pad tracers, blue cells: disc tracers) 80
Table 3.11 Braking protocols and corresponding TC wt% in PM10 samples for NAO1 and NAO2 under varying conditions (Alves et al., 2021) 82
Table 3.12 Effect of braking severity on the metal enrichment of TSP, through the HP-to-NP ratios of the metal weight contents (µg metal per mg TSP) (yellow cells: pad tracers, blue cells: disc tracers) 85
Table 3.13 Relative mass contributions to TSP of the pad and disc, estimation based on metal tracers. . 86
Table 3.14 Pad and disc mass concentrations to TSP, estimation based on metal tracers. 86
Table 3.15 The overall mass wear rate (mg/km) and the emission factors (mg/km) of TSP for NP and HP for the reduced scale..... 89
Table 3.16 Disc wear and tracer element emission ratios (HP to NP) 90
Table 3.17 Pad wear and tracer element emission ratios (HP to NP) 91
Table 3.18 Effect of energy braking severity on the metal enrichment of submicronic particles (yellow cells: pad tracers, blue cells: disc tracers) 93
Table 3.19 Quantified VOCs with retention times, probabilities, and concentrations under normal and heavy braking conditions 99
Table 3.20 Compounds detected in braking tests in comparison with the literature 102
Table 3.21 Comparison of PTR-MS vs DNPH measurements of some compounds during HP 108
Table 3.22 List of VOC compounds detected by PTR-MS from braking during HP, compounds highlighted in orange represent the major VOCs..... 109
Table 3.23 Classification of major compounds based on braking and disc rotation influence..... 114
Table 4.1 Consistency of mass concentration in µg/m3 of the sampling supports and test repetitions . 129
Table 4.2 Carbon content in brake wear particles: %TC detected from various brake pad types and sampling conditions 138
Table 4.3 Rigid tests emissions..... 145
Table 4.4 TSP emission factors [µg/km] for NP and HP at full and reduced scale benches..... 147
Table 4.5 Heavy pathway varying parameters for reduced and full scales..... 147
Table 4.6 Calculated relative mass contributions of the pad and disc to TSP and PM1, based on each metal tracer, for NP and HP routes at full scale. 150
Table 4.7 Normalized pad and disc contributions for NP and HP across both scales 151

List of appendices

Appendix 1 Transfer function of the tribometer at LaMcube 169
Appendix 2 Cut-off aerodynamic diameters of the 3-stage impactor 183
Appendix 3 Validation of the mineralization protocol using certified reference materials (Table A3.1 & Table A3.2) 186
Appendix 4 Evaluation of blanks and limits of detection & quantification (Table A4.1 & Table A4.2) 187
Appendix 5 Evaluation of the method: accuracy and intermediate precision (Table A5.1, Table A5.2, Table A5.3 & Table A5.4) 188
Appendix 6 X-ray diffraction analysis of disc and pad 190
Appendix 7 Masses collected using 14-stage impactor 192
Appendix 8 TSP Metal concentrations and weight content during NP and HP using the reference pad (Table A8.1 & Table A8.2) 193
Appendix 9 Fraction Metal concentrations and weight content during NP1 and NP2 using the reference pad (Table A9.1 & Table A9.2) 197
Appendix 10 Fraction Metal concentrations and weight content during NP1 and NP2 using the reference pad (Table A10.1 & Table A10.2) 201
Appendix 11 Results of the source apportionment based on the metal analysis of particles: application to NP and HP routes for the reference pad and disc 205
Appendix 12 Pad & disc mass fractions calculated by the metal tracers' method in particles collected by the 3-stage impactor tracers 207
Appendix 13 Chromatograms (Figure A13.1, Figure A13.2, Figure A13.3, Figure A13.4, Figure A13.5, Figure A13.6, Figure A13.7, Figure A13.8 & Figure A13.9) 209
Appendix 14 TSP using different sampling supports across different pads 213
Appendix 15 Sum of metals from the tests using different sampling devices 214
Appendix 16 Metal concentrations and weight content during NP using the modified pads (Table A16.1 & Table A16.2) 216
Appendix 17 Fraction Metal concentrations and weight content during NP using the modified pads (Table A17.1, Table A17.2 & Table A17.3) 220
Appendix 18 Mass size distribution of rigid pad 226
Appendix 19 Particle number size distribution 227
Appendix 20 Valorization of thesis work 234

List of abbreviations

AES	Atomic Emission Spectroscopy
Av	Average
AWP	Airborne Wear Particles
BWP	Brake Wear Particles
CRM	Certified reference materials
CV	Coefficient of variation
DLPI	Dekati Low Pressure Impactor
DNPH	Dinitrophenylhydrazine
EC	Elemental Carbon
EF	Emission factors
EU	European Union
FESEM	Field Emission Scanning Electron Microscopy
FID	Flame ionization detection
FMPS	Fast Mobility Particle Sizer
FTIR	Fourier transform infrared
GC	Gas chromatography
GCU	Gas calibration unit
GL	Lamellar-Graphite
HP	Normal Pathway
HPLC	High-pressure liquid chromatography
ICP	Inductively-Coupled Plasma
IE	Ionization energies
LD	Limit of detection
LQ	Limit of quantification
MS	Mass spectrometry
NAO	Non-asbestos organic
NIST	National Institute of Standards and Technology

NP	Heavy Pathway
OC	Organic Carbon
OPS	Optical Particle Sizer
PID	Photoionization Detector
PM	Particulate Matter
PMx	Particulate Matter with an aerodynamic diameter less than x µm
PSD	Platform Screen Doors
PTFE	Polytetrafluoroethylene
PTR	Proton Transfer Reaction
QC	Quality control
Qe	Environment flow
Qi	Internal flows
Qi	Quadruple interface
Qr	Recirculation flow
Qs	Source flows
Qw	Wear flow
Rt	Retention Time
SD	Standard deviation
SEM	Scanning electron microscopy
SVOCs	Semi-volatile organic compounds
TC	Total carbon
TD	Thermal desorption
TEM	Transmission electron microscopy
TGA	Thermogravimetric analysis
TIC	Total Ion Chromatogram
ToF	Time of Flight
TSP	Total Suspended Particles
UIC	International Union of Railways
UV	Ultraviolet

VOC	Volatile Organic Compound
WHO	World Health Organization
wt	Weight content

Introduction

Air pollution is considered the single most significant environmental health risk in Europe (Grigoratos et al., 2023). Pollutants can come from natural sources, such as volcanic eruptions and wildfires, or human-made sources, such as transportation, industrial processes, and agriculture. Besides, at a wider scale, atmospheric aerosol loading is known to have an influence on rainfall, local climate, and ultimately on climate change, leading Richardson et al. to confirm that air pollution is one of the nine Planetary Boundaries (Richardson et al., 2023). Moreover, in the same Planetary Boundaries framework, particulate matter (PM) and volatile organic compounds (VOCs) also contribute to the novel entities' boundary.

Pollution arising from transportation has a significant impact on air quality and can contribute to health problems such as respiratory diseases, heart diseases, and cancer. It can also have negative environmental impacts, including contributing to climate change, acid rain, and water pollution. Until now, most studies on pollutant emissions from transport have focused mainly on exhaust car emissions from internal combustion engines. Since the development of electric cars, studies have increasingly centered on non-exhaust car emissions caused by material degradation.

Recently, studies (Xu & Hao, 2017; Yang et al., 2023) have focused on non-exhaust railway emissions. Trains can emit various pollutants, such as PM, VOCs, and other gases, which can cause respiratory problems and harm ecosystems. This pollution may be a significant concern in areas with large numbers of trains or railway stations, such as urban areas.

Although trains using electrical power are assumed to be more environmentally friendly mobility systems, they can degrade air quality since significant amounts of airborne wear particles (AWP) are generated from mechanical friction processes between different components of the vehicles, such as the brake disc–pad contact and the wheel-rail contact. This pollution is particularly pronounced in underground railway places, where generated AWP can accumulate in very high concentrations (Lee, 2020), posing public health issues.

Indeed, several toxicological studies suggested that AWP can cause oxidative stress (Daellenbach et al., 2020; Karlsson et al., 2005; Vinzents et al., 2005) . It was proposed that not only the total mass of released wear has a significant effect, but the particle quantity (number of particles released), their size, morphology, and their chemical composition require further attention when their biological effects are addressed (Conca et al., 2022; Plachá et al., 2017). For example, it is well known that hazardous compounds (such as antimony trisulfide) are released into the environment (Malachova et al., 2016; Von Uexküll et al., 2005). VOC emissions such as carbonyls or hydrocarbons are also expected to worsen air quality. However, much less attention has been given to them and the number of research investigations is very limited (Yang et al., 2023).

Therefore, it is urgent to characterize more precisely the detailed emissions (both PM and VOCs) from train braking systems, to understand the phenomena involved in these emissions and to identify their drivers. The present work will thus focus on investigating the effect of braking conditions on PM and VOC emissions with respect to the tribological system, with the ultimate goal of reducing PM and VOC emissions.

This first chapter aims to present a state-of-the-art review of emissions during train friction braking, to display the scientific questions underlying the present work, and to define the motivations and scientific objectives of my thesis work. In the second chapter, the experimental framework is detailed, outlining the test scales, materials, instrumentation, and analysis techniques employed. Then, chapter 3 explores the impact of braking power, testing normal and heavy pathways, with a particular focus on VOC emission dynamics during the heavy pathway. Chapter 4 examines how brake pad design, especially variations in curing processes influencing rigidity and thermal expansion, affects PM and VOC emissions under normal braking conditions. It also addresses the role of braking system scale and its representativeness in shaping the emission behavior. Finally, the main results obtained during this thesis are summarized in a general conclusion, and research perspectives are proposed. The insights into PM and VOC emissions, along with their physicochemical characteristics in urban railway friction braking, aim to support the development of effective pollution reduction strategies.

This thesis was carried out as part of the ADEME BREAQ project. This project was supported by the French State as part of the Investments for the Future Programme, now integrated into France 2030, and operated by ADEME. The project was led by Alstom SA.

This research was conducted collaboratively between two laboratories: CERI EE at IMT Nord Europe (Douai) and LaMcube at Centrale Lille (Villeneuve d'Ascq). The tests were performed using the tribometer at LaMcube, while all collected samples were analyzed in the laboratories of IMT.

Chapter 1: Review of particulate and gaseous emissions from urban railway braking

1.1 Air quality

Europe's urban outdoor air quality has improved over the past decades, but this progress remains insufficient when measured against regulatory air quality standards, particularly for PM levels. The studies (*Department for Environment, Food & Rural Affairs*, 2024; *EEA*, 2024) examine the reduction of PM concentrations in Europe's urban outdoor air, specifically focusing on $PM_{2.5}$ and PM_{10}, showing a significant decline in both pollutants. A study covering the 2000-2020 period found a global reduction of about 36% and 47% in PM_{10} and $PM_{2.5}$, respectively, in Europe (Aas et al., 2024). These improvements likely reflect the influence of stricter air quality regulations and advancements in pollution control technologies.

Yet, a significant percentage of the European population continues to be exposed to harmful levels of air pollution (Figure 1.1), well above the health-based guidelines set by the World Health Organization (WHO). In particular, 96% of the European population is exposed to $PM_{2.5}$ concentrations exceeding these guidelines, while 83% faced similar exposure to PM_{10}. Under European Union (EU) standards, the annual limit concentration of $PM_{2.5}$ is 25 $\mu g/m^3$, while PM_{10} daily concentration must not exceed 50 $\mu g/m^3$ for more than 35 days per year. On the other hand, WHO guidelines are stricter, with recommended limits of $PM_{2.5}$ annual concentrations not exceeding 5 $\mu g/m^3$ and PM_{10} annual concentrations staying below 15 $\mu g/m^3$. Despite these guidelines, many urban areas in the EU experience higher levels of air pollution, posing potential health risks (*EEA*, 2024). These statistics illustrate the pressing need for stronger European air quality measures.

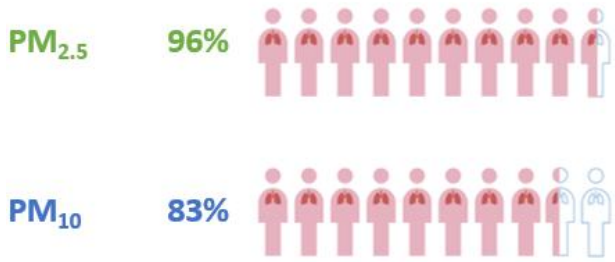

Figure 1.1 Population exposure to $PM_{2.5}$ and PM_{10} exceeding the WHO guidelines (Chang et al., 2021)

1.1.1 Overview of Main PM Sources in Europe

The main sources of PM in Europe include traffic emissions, industrial activities, residential heating, agricultural emissions, and natural sources. Traffic emissions, both exhaust and non-exhaust, are a significant contributor. Exhaust emissions primarily result from fuel combustion in vehicles, especially diesel engines, while non-exhaust emissions originate from brake wear, tire wear, road dust resuspension, and clutch wear. Industrial activities also play a crucial role, with emissions arising from combustion in power plants, steel production, and cement manufacturing, as well as process emissions from the chemical and metal industries. Residential heating contributes significantly, particularly in colder months, with wood and biomass burning being a major source, alongside coal-based heating in some regions. In agriculture, ammonia (NH_3) emissions from fertilizers and livestock contribute to secondary PM formation.

Additionally, natural sources such as Saharan dust transport, sea spray, and wildfires add to the overall PM levels. Among these sources, non-exhaust traffic emissions from road, rail, and metro transport are particularly important in urban PM pollution, especially in enclosed environments like underground railway systems (*EEA*, 2021).

1.1.2 Impact of non-exhaust emissions

This public health issue is further intensified in underground rail stations, where low air quality can be even more dangerous. Due to limited ventilation and the enclosed nature of these spaces, commuters and workers are often exposed to higher concentrations of PM, which creates potential health risks, particularly for those with pre-existing respiratory or cardiovascular diseases. Combining these elevated indoor pollution levels with already high outdoor exposure underscores the need for full measures to improve air quality both outside and in underground places.

Though rail transportation helps reduce road traffic and is widely regarded as a greener and more CO_2-efficient mobility solution, contributing less than 1% of total outdoor PM emissions in Europe (Figure 1.2), numerous studies have raised concerns about poor air quality in confined or underground railway stations with a particular focus on non-exhaust emissions (Evtyugina et al., 2021; Xu & Hao, 2017).

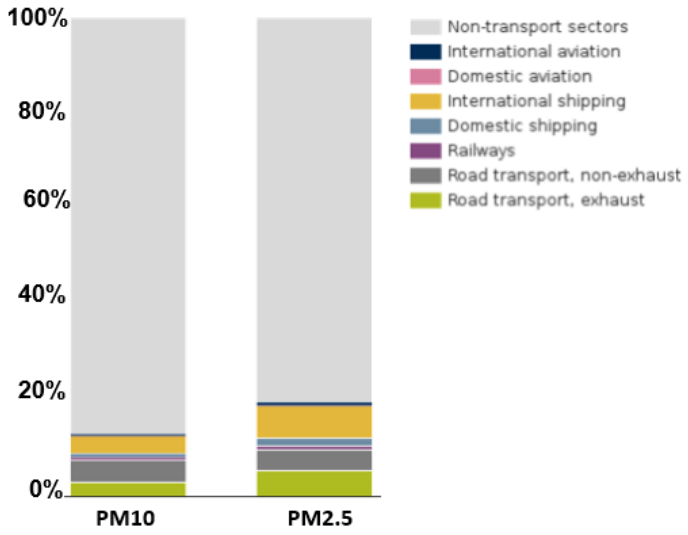

Figure 1.2 Contribution (%) of different transport sectors to total emissions of PM_{10} and $PM_{2.5}$ in Europe (*EEA*, 2019)

Non-exhaust railway particles mainly originate from mechanical wear, including wheel-rail contact (17%), pantograph-catenary contact (3%), and braking systems, which account for 80% of the sources (Figure 1.3). Other sources include infrastructure wear, erosion of building materials, and resuspension of soil PM (*UBA*, 2020).

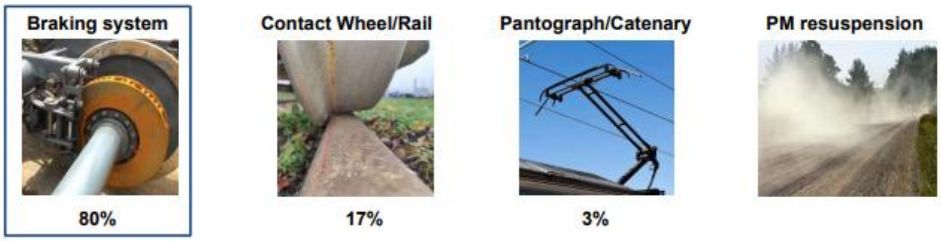

Figure 1.3 Sources of railway emissions (*UBA*, 2020)

These non-exhaust railway emissions are expected to increase in the future due to the foreseen growth of railway transportation, and as the braking source is the major contributor, it is worth focusing on braking systems (The Future of Rail, 2019).

Among underground railway AWP, brake wear particles (BWP) make up the highest proportion (Grigoratos & Martini, 2015). They are generated specifically by the friction between brake pads and rotors during braking. The phenomenon of wear itself was formally defined in 1986 as 'the progressive loss of material from the operating surface of a body occurring as a result of relative motion at its surface'; with the relevant surfaces in this context being the brake pad and disc (Lansdown & Price, 1986).

Wear particles are generated when two materials are pressed together and displaced, causing degradation that eventually results in the liberation of these particles (Fillot et al., 2007). Specifically, brake wear particles originate from various components of the vehicle's brake system and include brake abrasion dust (Hagino et al., 2016; Liati et al., 2019)

1.2 Exposure and health effects

It has been shown that PM globally increase the risks of heart disease and lung cancer (Woo et al., 2018). Understanding their health implications requires an examination of various influencing factors, with size being particularly the first significant factor affecting how they deposit in the respiratory tract and their subsequent impact on human health (Wahlström et al., 2011). Commonly used terms to describe mass concentrations of particulate matter include Total Suspended Particles (TSP) and PMx (particulate matter with an aerodynamic diameter less than x µm), such as $PM_{2.5}$ and PM_{10}, which are routinely monitored. TSP refers to the mass concentration of atmospheric dust smaller than 40–50 µm (Seinfeld et al., 2016).

PM_{10} may be classified into three categories (as shown in Figure 1.4) to distinguish them:

- **coarse particles** with an aerodynamic diameter between 10 and 2.5 µm,
- **fine particles** with a diameter less than 2.5 µm,
- and **ultra-fine particles** with a diameter of less than 0.1 µm. Indeed, the smaller the particles, the more they can penetrate deeply into the respiratory system and infiltrate blood. This highlights the importance of knowing particle size in assessing health risks associated with air pollution (C. M. Lee et al., 2011).

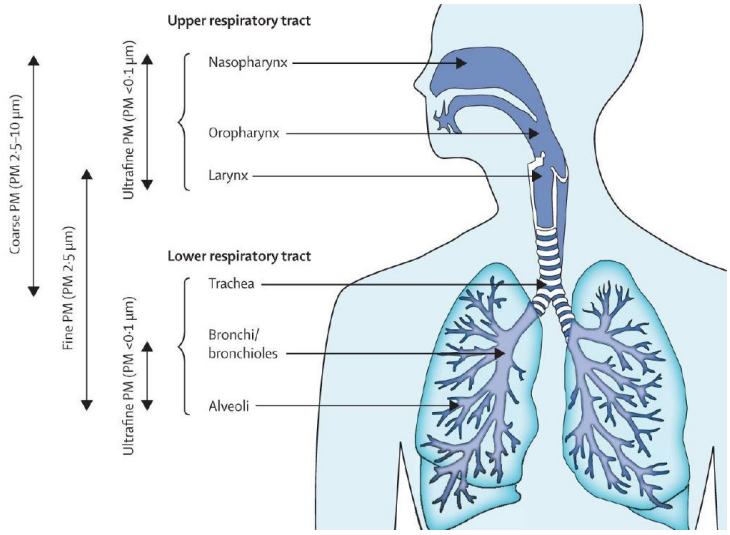

Figure 1.4 Representation of the ability of PM to penetrate the respiratory system according to their size (Guarnieri & Balmes, 2014)

$PM_{2.5}$ particles pose significant health risks due to their prolonged suspension in the air and ability to transport toxic substances deep into the lungs and bloodstream. A positive correlation between elevated $PM_{2.5}$ concentrations and the occurrence of respiratory, cardiopulmonary, and cardiovascular diseases, particularly among vulnerable populations, has been demonstrated (Chang et al., 2021). Short-term exposure, lasting from a few hours to weeks, can trigger heart disease, while long-term exposure significantly increases the risk of cardiovascular mortality (Tu et al., 2019). This relationship is particularly concerning in light of emerging evidence linking $PM_{2.5}$ exposure to worsened health outcomes during the COVID-19 pandemic. Specifically, a 1 µg/m³ increase in $PM_{2.5}$ has been associated with an 8% rise in the COVID-19 death rate (Chang et al., 2021). Moreover, exposure to ultrafine particles has been found to cause DNA damage (Vinzents et al., 2005), further highlighting the extensive implications of $PM_{2.5}$ on public health.

Exposure to ambient air in subway environments has been linked to a reduced anti-inflammatory response among individuals with asthma (Lundström et al., 2011). Moreover, PM found in metro air may pose a greater risk of inducing lung cancer and myocardial infarction compared to ambient air, largely due to its higher metal content (Xu & Hao, 2017). For instance, the concentration of iron (Fe) in subway environments accounts for 99%, 80%, and 95% of the daily exposure in Toronto, Montreal, and Vancouver, respectively. Elevated levels of other metals daily exposure have also been recorded, with barium (Ba) at 96% and manganese (Mn) at 93% in Toronto, copper (Cu) at 97% in Montreal, and molybdenum (Mo) at 91% in Vancouver (Chang et al., 2021). Frequent users of the Paris subway may experience inflammatory injuries due to inhaling metal-containing particles, particularly iron (Bachoual et al., 2007).

Subway particles have been found significantly more harmful than those from urban roads; they are reported to be eight times more genotoxic and five times more likely to induce oxidative stress in lung cells (Woo et al., 2018). One specific example includes magnetite (Fe_3O_4) particles emitted from subway systems, which have been associated with oxidative stress in human lung cells and classified as highly toxic to the body (Karlsson et al., 2005). Additionally, urinary isoprostane concentrations in metro workers, a biomarker of oxidative stress, correlate with the number of years spent working in the subway system, indicating further health risks compared to bus drivers or office workers (Grass et al., 2010).

Finally, exposure to VOCs, such as formaldehyde and benzene, has been linked to various adverse health effects. Inhalation of formaldehyde can worsen asthma symptoms and contribute to the development of allergies, while prolonged exposure to benzene is associated with an increased risk of childhood leukemia (Gong et al., 2017; International Agency for Research on Cancer; Tagiyeva & Sheikh, 2014; Tang et al., 2016).

1.3 Brake system

1.3.1 Braking phenomena

During a braking event, a pair of brake linings (the pads) is pressed into a rotating disc, transforming by friction the kinetic energy essentially into heat (Figure 1.5), which may cause important wear and increase the surface temperatures of the materials up to several hundred degrees Celsius (Frangieh et al., 2023).

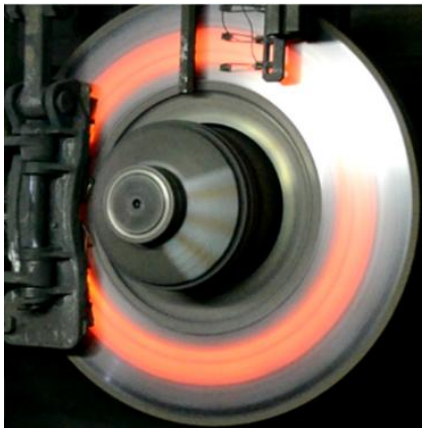

Figure 1.5 Railway disc brake - Alstom Flertex full-scale test bench

These phenomena result in the degradation of the materials, preferentially at microscopic interfaces, which are subjected to higher thermal and mechanical stresses, then potentially spreading at larger scales. The material degradation may involve many thermomechanical processes (thermomechanical fatigue, cracking, fracture, abrasion …) and chemical ones (tribocorrosion of metallic compounds, oxidation, or pyrolysis of organic polymers…), which contribute to wear of the pads and disc (Verma, 2015; CUEVA, 2003; Godet, 1984) releasing PM of various sizes and gases (including VOCs). To understand the generation of these emissions and their driving factors, we must understand the tribological circuit, which involves the interactions between sliding surfaces.

1.3.2 Wear and tribological circuit

The wear of two solids in contact and in relative motion is a highly complex phenomenon involving multiple scales. As a result of deformation, deviations in shape and roughness, the two sliding surfaces localize contact over very local, micrometric-sized areas, where the materials are subjected to extreme mechanical and thermal loading, of the order of gigapascals and hundreds of degrees Celsius. Figure 1.6 illustrates, at this very local scale, the multi-physical complexity of the possible phenomena occurring when sliding as well as the complexity of the structural evolution at the interface. Two different solids with rough surfaces and relevant material microstructures are brought into mechanical contact and exposed to various factors: mechanical, thermal, electrical, and environmental.

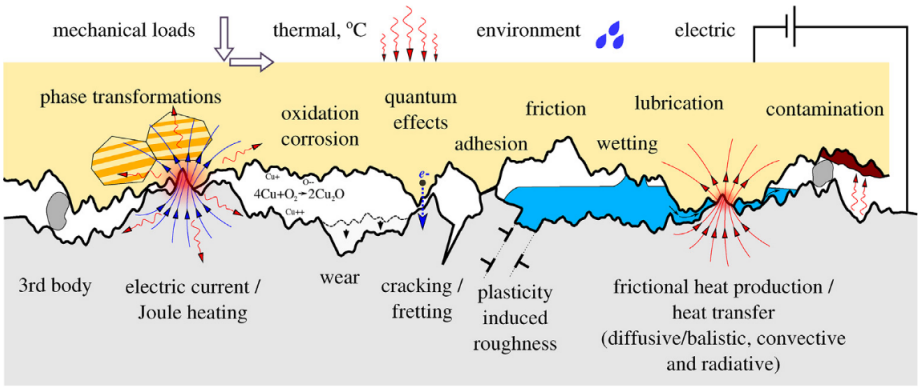

Figure 1.6 Physico-chemical phenomena involved in the contact (Vakis et al., 2018)

This situation of 'direct' contact between surfaces is only possible in the very early stages of interaction. This is because the very rapid degradation of the material leads to the detachment of debris which, during a running-in period, forms a superficial layer that interposes itself between the solids, a 'solid lubricant' that regulates the local contact areas so as to make the loading bearable. These tribofilms play an essential role in friction and sliding mechanisms and processes.

It is essential to place oneself in a model that allows one to understand the exchanges of energy, matter, and the mechanisms set up at the interface. The 'third body' concept proposed by Maurice Godet provides a framework to elucidate the role of wear debris (Godet, 1984). After a bedding-in period, friction brake systems in use form tribological triplets composed of three elements:

- the mechanical system including its environment, which determine the contact conditions (loads, sliding velocities, mechanical stiffnesses, contact areas, temperature, humidity, etc.);

- the first bodies, which are the solids in sliding contact (disc and pads);

- the third body, a wear product of the first bodies, separates the pads and the disc and provides load-bearing capacity and accommodation of sliding velocity.

From a scientific point of view, wear depends on the ability of the tribological triplet to maintain frictional performance. Wear of a sliding contact is thus defined as the quantity of material lost for the tribological system. The modeling of wear and the identification of the source factors of emissions require the formalization of the tribological circuit in terms of material flow rates (Berthier, 2001). Wear in terms of material loss corresponds to the flow rate of the third body leaving the tribological circuit. The associated mechanisms are complex, chemical, multi-physical, and multiscale, and within the case of braking, they are mostly thermomechanical phenomena (1.3.1). Also, wear depends on the contact openings and closings, thus affecting the holding capacity of the third body in the interface (Frangieh et al., 2023).

In a simplified model of the tribological circuit (Figure 1.7), the material balance involves different main flows:
- the source flows (Q_S), which supply third-body material from the couple of first bodies;
- the environment flow (Q_e), which corresponds to material introduced in the contact from the environment;
- the internal flows (Qi), when the third body is trapped and circulates between the first bodies, providing load-bearing areas and velocity accommodation;

- the external flow, which represents the third body flowing out of the contact, which is divided into 2 flows according to their fate:

- the recirculation flow (Q_R) which reintroduces the material recirculated back to the entrance of the contact;

- the wear flow (Q_W), which represents the third body particles definitively lost for the tribological system. The wear flow thus represents the wear of the contact.

In this model, the emitted airborne PM is considered part of the wear flow, Q_w. The contribution of gases to the mass balance is not considered.

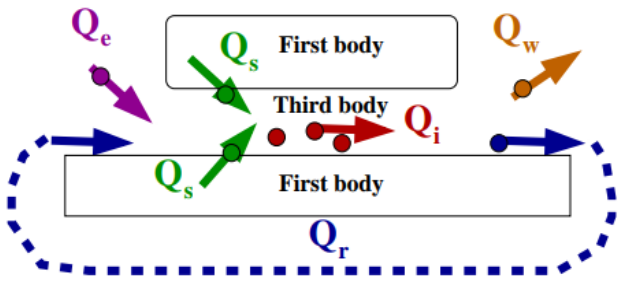

Figure 1.7 Tribological circuit (Renouf & Saulot, 2015)

This view of the tribological circuit highlights the importance of the third body in facilitating contact interactions and material transfer. The mechanisms of particle generation that contribute to the source flow during braking occur across different lengths and time scales, affecting both the disc and pad materials (Österle et al., 2009).

• The first main mechanism involves severe deformation of the disc surface due to mechanical and thermal constraints. As a result, extreme plastic flow and fracture lead to the detachment of fine and coarse iron particles. These detached particles become part of the third-body source flow and contribute to the friction performance and wear behavior.

•The second key mechanism is tribo-oxidation, which creates nano-sized iron oxide particles since brake discs are typically made of cast iron or stainless steel. This occurs at the contact surface during braking due to high temperatures and power. Oxygen, water molecules, or galvanic corrosion between different materials can accelerate this reaction. The iron oxides that are formed help in creating larger particles, known as secondary plateaus, on the worn surface, which play an important role in maintaining stable friction (Frangieh et al., 2025)

The third body (Figure 1.8) lies between the contacting solids (the two first bodies) (Denape, 2019). It is interposed between the disc and the brake lining when they have a relative movement with respect to each other. This third body is composed of nano-sized particles (“powder”) and plateaus (“third-body flat plates”) (Octau, 2019).

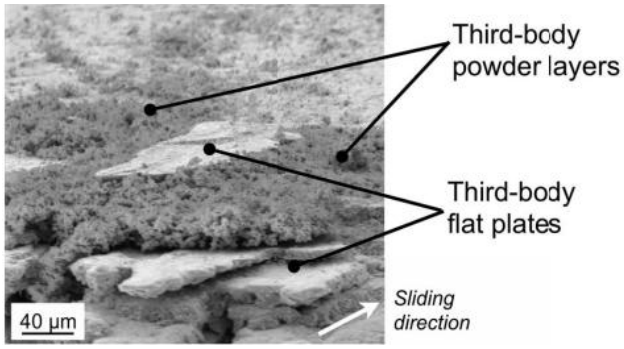

Figure 1.8 Third body (Desplanques & Degallaix, 2010)

The mass of the third body evolves with time. Its dynamics may be described as a balance between the flow of particle detachment from the first bodies (Q_S) and the flow of particle ejection during wear (Q_W), depending on the mass of the third body accumulated in the system (M_i), while any external flow not originating in the contact area (Q_e) including artificially introduced third bodies such as lubricants is considered equal to zero.

- Assuming that the environment flow is negligible ($Q_e = 0$), the mass balance under transient state is calculated according to Eq. 1-1:

$$Q_s = Q_w + \frac{dM_i}{dt} \qquad \text{Eq. 1-1}$$

with Q_S and Q_W in kg/s, M_i in kg, and t in s.

- Mass balance under equilibrium state (Eq. 1-2)

$$Q_s = Q_w \qquad \text{Eq. 1-2}$$

When the system reaches an equilibrium state, then the mass of the third body reaches a stable state mass, M_i^{stab}, which is constant (Eq. 1-3),

$$\frac{dM_i}{dt} = 0 \qquad \text{Eq. 1-3}$$

and the flow rates of detached particles (Qs) and ejected particles (Qw) become equal, resulting in a constant wear flow rate Q∞ (Figure 1.9).

Key points of this model include:

- M_i^{start} is the minimum mass at which ejection begins, and M_i^{max} is the mass beyond which no particle detachment occurs from the first bodies.
- If the mass deviates from M_i^{stab}, adjustments in the detachment and ejection processes bring it back to equilibrium.

The wear process reaches a stable equilibrium when reaching Eq. 1-4.

$$Q_s = Q_w = Q_\infty \qquad \text{Eq. 1-4}$$

This model raises the question of whether reducing particle detachment or preventing ejection could minimize wear, suggesting that conserving the third body as a lubricant within the contact could reduce degradation. This leads to a new perspective on wear management, where the goal is to maintain the third body within the system to reduce wear rates.

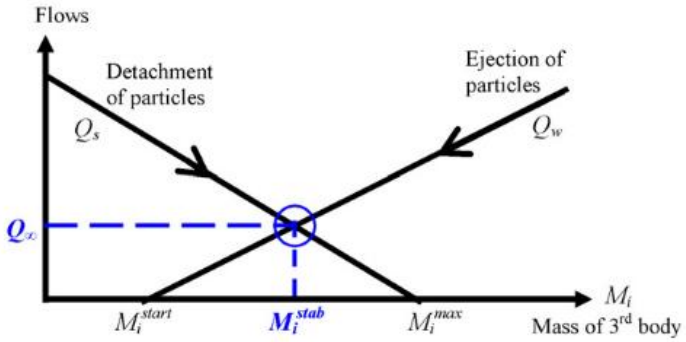

Figure 1.9 Competition of the source flow and wear flow as functions of the mass Mi of the third body (Fillot et al., 2007)

1.3.3 Factors affecting emissions

- Operating factors

Understanding the factors influencing BWP emissions is key to evaluating their environmental impact. These emissions are shaped by several interrelated parameters, including contact pressure, sliding velocity, temperature, and the composition of friction materials.

While early studies, such as Mosleh et al., (2004), linked higher contact pressure to the formation of larger particles, this was later challenged by Wahlström et al., (2010), who argued that all particle sizes should be affected when total emissions are considered. Octau et al., (2020) noted that pressure influences particle formation conditions, rather than size directly.

Temperature also plays a role in the emission dynamics, particularly in the formation of fine and ultrafine particles, but it interacts closely with other braking parameters (Namgung et al., 2016; Nogueira et al., 2020). Among these, sliding speed has shown a particularly direct and significant impact, with (Beji et al., 2020) demonstrating that increased velocity leads to a sharp rise in BWP emissions. Overall, BWP emission behavior results from a complex combination of mechanical and material-related factors, each contributing in different ways depending on the braking scenario.

- Brake system

Last but not least, understanding the composition of friction materials is crucial, in particular the pad, to understand the mechanisms behind VOC emissions and their subsequent degradation. The chemical fabrication of the pad, including its polymers, fillers, and additives, plays a significant role in determining which substances are likely to be emitted as VOCs. Heat, mechanical abrasion, or oxidation may trigger

these emissions. The mechanism of VOC release can involve the evaporation of volatile components or the breakdown of larger molecules into smaller, more volatile compounds.

Thus, understanding the pad's composition helps predicting not only the emission behavior but also how VOCs degrade during braking. Each component in the brake pad contributes to distinct properties to the overall mixture, influencing its performance and emission characteristics. These components play specific roles in friction generation, wear resistance, and thermal stability, and their primary functions can be categorized accordingly and are show in Table 1.1:

Table 1.1 Composition of pads

Category	Constituents	Composition	Function	References
Binder	Resins	• Phenol formaldehyde 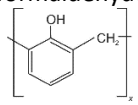 • Epoxy	• Converse mechanical strength to friction material, guaranteeing pad compactness during use. • Produce wear-resistant composites.	(Bonfanti, 2016; Buyaev et al., 2016; Menapace et al., 2019; Jayashree et al., 2024)
	Rubbers	• Nitrile rubber 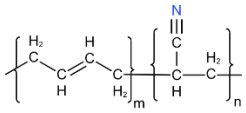	• Elevate friction and wear behavior to reduce the effect of generated vibration during braking	
Abrasives	Synthetic	Al_2O_3	Increase friction efficiency and improve compound wear resistance	(Bonfanti, 2016)
Reinforcement	Heat-resistant fiber: Twaron Aramid fibers	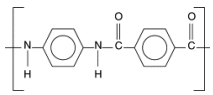	Increase mechanical strength, improving wear	(Bonfanti, 2016; Buyaev et al., 2016; Menapace et al., 2019; Plachá et al.,

	• Steel fibers • Hybrid filaments, a mixture of glass and polytetrafluoroethylene fibers • Mixture of carbon and aramid fibers • Self-lubricating materials	• Fe; • SiO_2, Al_2O_3, CaO, MgO; $(C_2F_4)_n$ • C • C & F, C, MoS_2	minimization and stabilization	2017a; Shorowordi & Celis, 2009)
Solid lubricants	Synthetic graphite Antimony trisulfide	Stacked layers of graphene Sb_2S_3	• Stabilize the friction coefficient and contrasting the build-up effect • Oil absorption: gives greater freedom when formulating the mixture	(Bonfanti, 2016; Namgung et al., 2016)
Fillers	Barium sulfate	$BaSO_4$	• Wear-resistant • High thermal stability	(Bonfanti, 2016; Menapace et al., 2019; Shorowordi & Celis, 2009)
	Fibers, sulfide, oxides..	organic fibers, graphite, tin sulfide, zinc sulfide, aluminum oxide, chromite, tin oxide, zinc oxide and magnesium oxide	Give specific performance not directly related to friction efficiency, e.g., cheap materials, pigments	
Friction modifiers	Coke (oil) brass, iron chips	C, Cu, Zn, Fe, Sr.	Ensure a high level of grain stability and a relatively high elasticity	(Shorowordi & Celis, 2009)

One of the key processes influencing VOC emissions is degradation. During braking, the brake pad experiences friction and wear, causing frictional heating and mechanical damage. In normal braking situations, the contact temperature can rise significantly depending on factors like brake material, vehicle speed, and braking intensity. The combination of heat and mechanical forces can trigger various chemical reactions at the friction surface, known as tribochemical reactions. These reactions can cause the breakdown of organic compounds in the brake pad, such as the phenol-formaldehyde binder (Shorowordi & Celis, 2009). Studies have shown that under high temperature conditions, particularly above 600°C, the destruction of the friction layer leads to the release of VOCs, including BTEX (Benzene, Toluene,

Ethylbenzene and Xylene) compounds (Plachá et al., 2017). This confirms that brake pads are a significant source of VOC emissions during braking operations.

This demonstrates the potential of brake pads as a source of VOC emissions during braking operations. Given the environmental and health concerns associated with VOCs, more in-depth studies are needed to understand these emissions qualitatively and quantitatively.

1.4 PM in railway transports

1.4.1 PM concentrations

PM levels in subway stations are significantly higher than those found above ground (Xu & Hao, 2017). For example, data from 2022 in Paris illustrate the yearly PM_{10} concentrations in the indoor air of subway stations compared to levels in the outdoor air near the Ring Road in Porte d'Auteuil (Figure 1.10). Notably, road traffic in the Porte d'Auteuil area generates PM_{10} concentrations twice the WHO threshold limits. However, PM_{10} mass concentrations in underground stations, particularly those served by the regional commuter trains (Réseau Express Régional, RER) such as the Auber station, a busy interchange connecting several lines, may exceed WHO limits by a factor of ten. In addition, trains operating within the city, including those at Châtelet metro and Franklin D. Roosevelt stations, exhibit PM_{10} concentrations three times higher than the WHO threshold.

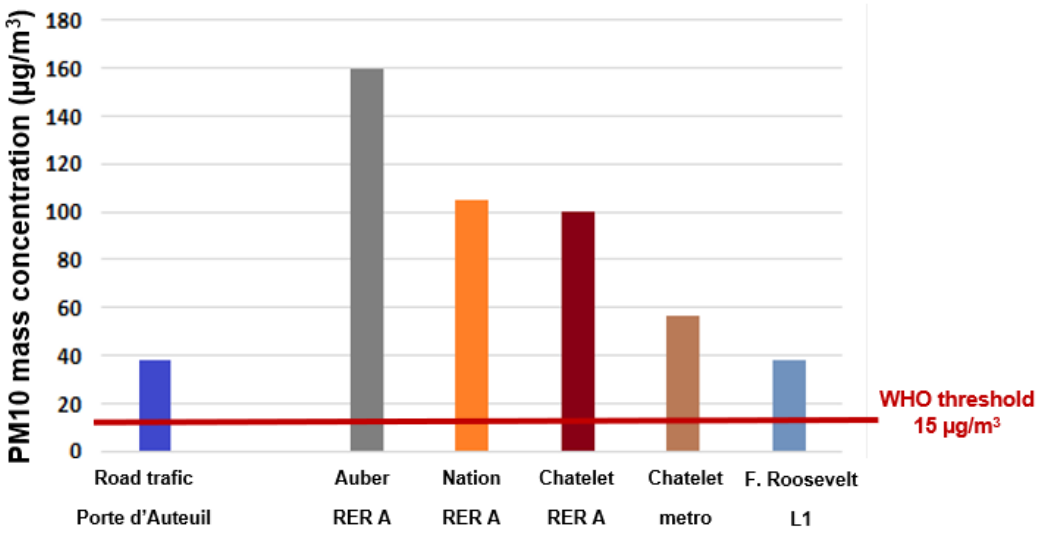

Figure 1.10 Yearly PM_{10} concentrations in 2022 in different Parisian subway stations and near the Paris ring road in Porte d'Auteuil (modified from (RATP, 2023))

Other measurements conducted in various cities, including Los Angeles, Barcelona, Milan, Prague, Rome, Stockholm, Seoul, Shanghai, and Taipei, indicate that average PM_{10} levels on subway platforms frequently surpass 50 µg/m³, with some instances showing levels as high as 300 µg/m³. In contrast, cleaner urban outdoor air PM_{10} levels typically remain below 20 µg/m³. This difference can be attributed to both additional sources of particulate pollution, such as railway AWP, and insufficient ventilation in underground environments, which limits the dilution of air pollutants and worsens air quality issues, ensuring that underground air quality is a pressing concern (Moreno et al., 2014).

$PM_{2.5}$ has also been widely measured in subway systems due to its impact on air quality and public health. Chang et al., 2021 examined their concentrations in subway stations across various cities globally, where concentrations vary from less than 60 to more than 200 μg/m^3. Moreover, measurements in staff areas (Table 1.2) revealed that the driver's cabin is the most affected, with a mean concentration of 128 μg/m³. In contrast, other areas, such as station offices, restrooms, and ticket offices, showed an average concentration of 62 μg/m³, which is approximately 50% lower. Yet, it should be remembered that air quality standards for workers are often much less requiring than national outdoor standards.

Table 1.2 $PM_{2.5}$ concentrations measurements in μg/m^3 in staff areas (Chang et al., 2021)

station offices	restrooms	ticket offices	driver's cabins
56.7 (29.2– 120.9)	65.6 (26.7–160.4)	65.0 (38.7–138.9)	127.8 (79.3–184.8)

In Italy, ground-level stations did not show significant differences in PM levels between station platforms and urban environments. However, a direct correlation between train passages and PM measurements was observed, increasing to 42% above the average value (Cartenì et al., 2015). On the contrary, Martins et al. found significantly higher PM levels on platforms in the Barcelona subway system, ranging from 1.3 to 6.7 times higher than in outdoor environments.

Globally, studies from major cities such as Naples, Paris, Stockholm, Budapest, Athens, Prague, London, and Istanbul consistently show that PM concentrations in subway stations are significantly higher than both inside the trains and outdoors, with an increase ranging from a factor of 2 to 30, detailed in Table 1.3; (Assimakopoulos et al., 2013; Barmparesos et al., 2016; Braniˇ, 2006; Cartenì et al., 2015; Dura & Szalay, 2007; Johansson & Johansson, 2003; Onat & Stakeeva, 2014; Raut et al., 2009; Xu & Hao, 2017)

For example, in Sweden, a comparison of PM_{10} and $PM_{2.5}$ concentrations between the platform and the tunnel revealed that tunnel PM concentrations were up to 16 times higher than those on the platform (Tu et al., 2019). In the Naples metro system, PM_{10} concentrations on underground platforms ranged between 172-262 μg/m³, 2 to 14 times higher than outdoor levels (Cartenì et al., 2015). In Paris, PM_{10} and $PM_{2.5}$ concentrations were 5 to 30 times higher in the metro system compared to the streets (Raut et al., 2009). Similarly, in Stockholm, PM_{10} and $PM_{2.5}$ concentrations in two underground stations were measured at 470 and 260 μg/m³, respectively, 5 to 10 times higher than on Stockholm's busiest streets (Johansson & Johansson, 2003). In Budapest, PM_{10} concentrations were 2 to 3 times higher in metro stations than outdoors (Dura & Szalay, 2007) while in Athens, PM_1, $PM_{2.5}$, and PM_{10} levels were 3 to 10 times greater than ambient air concentrations (Assimakopoulos et al., 2013; Barmparesos et al., 2016). In Prague, PM_{10} concentrations inside metro trains were twice those of outdoor environments (Braniˇ, 2006). London's metro system exhibited PM exposure levels of 247.2 μg/m³, which were 3 to 8 times higher than other transport modes (Xu & Hao, 2017). In Istanbul, Fe-containing PM was 3.5 to 8 times more abundant in metro stations than in the city's atmosphere, with $PM_{2.5}$ concentrations averaging between 49.3 and 181.7 μg/m³ (Onat & Stakeeva, 2014).

Table 1.3 Comparison of indoor/outdoor ratios of PM concentrations (PM1, $PM_{2.5}$, and PM_{10}) across various cities

City	Ratio indoor/outdoor
Naples	PM_{10}: 2-14
Paris	PM_{10} & $PM_{2.5}$: 5-30
Stockholm	PM_{10} & $PM_{2.5}$: 5-10
Budapest	PM_{10}: 2-3
Athens	PM_1, $PM_{2.5}$, and PM_{10}:3-10
Prague	PM_{10}: 2
London	PM: 3-8
Istanbul	$PM_{2.5}$ of Fe: 3.5-8

The WHO limits for PM are exceeded in some stations globally. In Frankfurt, for example, the WHO limits were exceeded at all types of stations for PM_{10} and $PM_{2.5}$. The WHO has established limits for PM_{10} and $PM_{2.5}$ concentrations, which have been legally binding in the EU since January 2005 (PM_{10}) and since 2010 ($PM_{2.5}$), respectively. The following tables (Table 1.4, Table 1.5, and Table 1.6) show other studies of PM concentrations according to their diameter.

Table 1.4 Average PM_{10} concentration levels in metro and subway environments worldwide

Average PM_{10} concentration [µg /m^3]	**City**	**Location**	**Reference**
172 - 262	Naples	Underground station platforms	(Cartenì et al., 2015)
175	Sweden	Platform	(Cha et al., 2019)
41 – 469	Worldwide	Subway platforms and trains	(Woo et al., 2018)
50	Hong Kong	Inside the metro	(Xu & Hao, 2017)
366	Shanghai	Metro system	(Qiao et al., 2015)
78	California	Station platforms	(Kam et al., 2011)
31.5	California	Inside the train	(Kam et al., 2011)
470	Stockholm	Subterranean stations	(Johansson & Johansson, 2003)
321	Athens	Coaches of the trains	(Assimakopoulos et al., 2013; Barmparesos et al., 2016)

The analysis of PM_{10} concentrations in metro and subway systems worldwide reveals notable variations across different locations and periods. Older studies, such as the one by Johansson & Johansson in 2003, report high concentrations exceeding 300 µg/m^3 attributed to less advanced ventilation systems. In contrast, more recent research indicates improved air quality control measures in modern systems, with Xu & Hao, (2017) noting a PM_{10} level of 50 µg/m^3 in Hong Kong's metro in 2017, highlighting effective air filtration.

Globally, subway platform PM_{10} concentrations vary significantly, ranging from 41 to 469 µg/m³ (Woo et al., 2018). This variation is influenced by factors such as station design, ventilation, train frequency, and local pollution levels.

Older subterranean metro systems generally exhibit higher PM_{10} levels due to outdated infrastructure and less effective ventilation. In contrast, modern systems in regions like California and Hong Kong report lower concentrations, reflecting advancements in air quality management. Additionally, the age of trains, their energy sources, and braking systems play a crucial role in PM_{10} emissions. Older diesel-powered trains and those relying on friction-based braking systems tend to generate more particulate matter. In comparison, newer electric trains equipped with regenerative braking contribute to improved air quality by minimizing particle emissions (Q. Zhang et al., 2024).

Table 1.5 Average $PM_{2.5}$ concentration levels in metro and subway environments worldwide

Average $PM_{2.5}$ concentration (µg/m³)	**City**	**Location**	**Reference**
45 and 60	Italy	Underground station platforms	(Cartenì et al., 2015)
35	Sweden	Platform	(Cha et al., 2019)
21 – 258	Worldwide	Subway platforms and trains	(Woo et al., 2018)
287	Shanghai	Metro system	(Qiao et al., 2015)
260	Stockholm	Subterranean stations	(Johansson & Johansson, 2003)
88.1	Athens	Coaches of the trains	(Assimakopoulos et al., 2013; Barmparesos et al., 2016)
49.3-181.7	Istanbul	Inside the metro	(Onat & Stakeeva, 2013, 2014)
151.43	Tianjin	Subway passenger cars	(B. Wang et al., 2016)

Table 1.6 Average PM_1 concentration levels in metro and subway environments worldwide

Average PM_1 concentration (µg/m³)	**City**	**Location**	**Reference**
231	Shanghai	Metro system	(Qiao et al., 2015)
18.7	Athens	Coaches of the trains	(Assimakopoulos et al., 2013; Barmparesos et al., 2016)

Numerous studies show that brake particles are the highest contributor to the emissions; however, the diversity in materials and methodologies employed across these studies hinders the comparability of their findings (Y. Wang et al., 2022). Estimating BWP emissions under real-world operation imposes several challenges, including, amongst others, the proper collection of particles (Dp >1µm) and interference with the brakes convective cooling. Brake dynamometers allow for an alternative approach offering tighter

control of the braking and cooling conditions, allowing for the development of a standardized test procedure (Mamakos et al., 2021).

The AWP emission rate was suggested to be used in legislation to control non-exhaust emissions from transport modes, particularly rail transport. The purpose of this index is to get closer to the real cases. Figure 1.11 shows the results for two different brake pad materials against steel brake disc with the organic pad having higher emission rates. Note that those values are calculated based on proposed test conditions, test setup, and duration selection. Any changes in those factors can affect the magnitude calculated below (Abbasi et al., 2012)

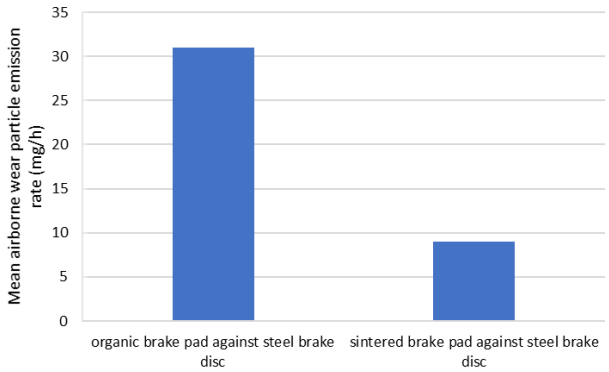

Figure 1.11 Mean particle emission rates for different braking materials adapted from (Abbasi et al., 2012)

1.4.2 PM properties

a) Elemental chemical composition

Particles collect from subway stations contain a significant number of metals and minerals, and studies conducted in major cities, particularly across Asia (e.g., Shanghai, Seoul, and Tianjin), have consistently shown that the elemental composition of PM in subway stations is dominated by iron (Aarnio et al., 2005; Chang et al., 2021; Furuya et al., 2001; Namgung et al., 2016; Qiao et al., 2015; Tu et al., 2019)

However, the concentration of Fe often varies even within the same city (Table 1.7). For instance, in a Shanghai subway station, the concentration of Fe ranges from 0.3 to 48 µg/m³ (Chang et al., 2021).

Table 1.7 Iron in $PM_{2.5}$

Subway station	Fe in $PM_{2.5}$ [µg/m^3]	Reference
Helsinki	29	(Aarnio et al., 2005)
Tianjin	18	(Wang et al., 2016)
Budapest	16	(Salma & Maenhaut, 2007)
Daejeon	12	(Lim et al., 2011)
Mexico	3	(Mugica-Alvarez et al., 2012)
Tehran	19	(Kamani et al., 2014)

Particles generated by braking friction also contain oxides. These particles can include magnetite (Fe_3O_4) (Namgung et al., 2016), or laminar hematite (Fe_2O_3), the predominant form of iron in subway particulate

matter subway tunnels (Querol et al., 2012). In Seoul, for example, Fe_2O_3 was found to constitute 48% of the $PM_{2.5}$ mass (Chang et al., 2021).

Many studies have identified high concentrations of Fe, along with elements such as aluminum (Al), calcium (Ca), and magnesium (Mg), in subway particulate matter, as well as other trace metals (Table 1.8). Approximately 84% of these metals are attributed to mechanical friction processes (Namgung et al., 2016).

Table 1.8 Summary of metals identified in subway particulate matter by various studies

Metals identified	Study
Fe, Al, Ca, Mg, Cu, Zn, Sb, Na, Ni, Mn, Ba, Cr	(Abbasi, Olander, et al., 2012)
Fe, Al, Ca, Mg, Mn, Cu, Cr, Ni, Pb, Hg	(Qiao et al., 2015)
Fe, Al, Ca, Mg, Ba, Cu, Ca	(Furuya et al., 2001)
Fe, Al, Ca, Mg, Zn, Mn, Cr, Ni, Pb	(Namgung et al., 2016)
Fe, Al, Ca, Mg, Mn, Ni, Cr, Cu	(Woo et al., 2018)

A comparison between above-ground stations vs underground stations (Table 1.9) in Shanghai shows that the underground stations are twice as polluted with inorganic particles (Chang et al., 2021):

Table 1.9 Comparison of $PM_{2.5}$ metallic content between above-ground and underground stations

Elements in $PM_{2.5}$	**Above-ground station**	**Underground station**
Fe	4.5%	9.3%
Cu	330 mg/kg	680 mg/kg
Mn	900 mg/kg	1000 mg/kg

Antimony (Sb) is commonly detected in railway emissions across several studies (Grigoratos & Martini, 2014; Namgung et al., 2016; Tu et al., 2019), as it is a component in the manufacturing of brake pads for railway vehicles. During braking, Sb is released in the form of **Sb_2S_3** (antimony trisulfide), which is employed as a lubricant for brake pads in order to reduce vibrations and improve friction stability, which then oxidizes to **Sb_2O_3** (antimony trioxide) under the intense heat generated by friction (Namgung et al., 2016). Additionally, the braking system releases other elements, such as **Ba** and **strontium (Sr),** in varying quantities.

The high temperatures generated by some processes during train operation can cause chemical reactions among elements in the particles (Chang et al., 2021), such as:

- Oxidation of some metallic elements from sulfides to sulfates and oxides, e.g., FeS_2 to Fe_2O_3
- Volatilization processes of semi-volatile elements, such as As, Hg, and Zn.
- Condensation of semi-volatile elements onto very fine iron oxides.

Carbon is also present but is less studied. Wang detected organic carbon (OC) as a major component of $PM_{2.5}$(B. Q. Wang et al., 2016).

The chemical composition of brake wear particles should be considered when trying to fully characterize them and assess their possible adverse effects on human health, although modern brakes are composites of many different and sometimes unknown ingredients. Table 1.10 provides an overview of the concentration of the most common elements found in brake wear dust.

Table 1.10 Element concentrations found in emitted brake wear dust adapted from (Grigoratos & Martini, 2015)

Metal	Brake dust [mg/kg]
Al	330 – 20 000
As	2 – 110
Ba	5 800 – 140 000
Ca	500 – 8 600
Cd	0.06 – 11
Co	12 – 42
Cr	140 – 12 000
Cu	70 – 210 000
Fe	1 300 – 640 000
K	190 – 39 000
Mg	1 700 – 83 000
Mn	620 – 5 600
Mo	5 – 740
Na	80 – 5 100
Ni	80 – 730
Pb	4 – 1 300
Sb	4 – 19 000
Sn	230 – 2 600
Ti	100 – 110 000
Zn	120 – 27 000

b) Physical properties (size and morphology)

Studies investigating PM in subways have highlighted distinct characteristics in terms of source, morphology, and size distribution. A major distinction must be made between general PM in subway environments and braking-generated PM, as well as between mass size distributions and number size distributions, which describe particle properties from different perspectives.

Braking events are known to generate fine particles, with most distribution mode peaks occurring below 600 nm. Several studies have examined the **number size distribution** under varying braking conditions (Table 1.11).

Table 1.11 Reported peak particle sizes and braking conditions in various studies

Peak size(s) reported [nm]	Conditions	Study
~350, 280, and 600 nm	Field measurements during train braking	(Abbasi et al., 2012)
~350 nm	Observed in subway braking scenarios	(Cha et al., 2018)
178–275 nm	Peaks dependent on speed, brake force, time, and deceleration	(Namgung et al., 2016)

These findings consistently show that **fine particles (<600 nm)** dominate the **number size distribution** during braking events.

While fine particles dominate by number, larger particles can contribute significantly to the mass size distribution, particularly in the coarse fraction. For instance: (Abbasi et al., (2012) identified a mass mode peak between 3–6 µm using Field Emission Scanning Electron Microscopy (FESEM), with particle sizes ranging from 50 nm up to several microns.

Scanning electron microscopy (SEM) images show that braking-generated PM consists of a variety of shapes and structures: small spherical particles (often submicron), flake-like particles (several microns, large and flat with sharp edges), and agglomerates of smaller particles (Kukutschová et al., 2011; Nosko et al., 2017; Octau et al., 2020).

It's important to note that not all PM in subways originates from braking. Subway PM includes: Wear from wheels, rails, and electrical components Resuspension of settled dust, ventilation system particles. However, braking remains a major contributor to fine and ultrafine particles found in subway environments.

1.4.3 PM sources in railway transport

While the tribological circuit is the primary source of PM emissions, other contributors exist. In subway environments, elements like cooling systems (air conditioning) can affect the results, and seasonal variations such as meteorological conditions, instrument characteristics, and measurement techniques can influence particle emission readings (Chang et al., 2021; Matti Maricq, 2007; Salma et al., 2009; Wahlström et al., 2020). For example, infiltration from polluted outdoor air and different metro system designs contribute to PM levels inside subways (Xu & Hao, 2017). Researchers have focused on factors such as outdoor $PM_{2.5}$ levels and station depth, but less attention has been given to factors like station age, passenger density, and outdoor traffic, which also influence $PM_{2.5}$ concentrations in subways (Chang et al., 2021). During peak traffic hours in Paris, $PM_{2.5}$ levels increase by about 35%, with concentrations rising from 61 µg/m³ during off-peak hours to 93 µg/m³ during rush hours (Chang et al., 2021; Raut et al., 2009).

Studies have shown that non-exhaust PM emissions in subways are influenced by factors such as braking systems, axle load, brake materials (pad and disc), pantographs, catenaries, infrastructure design, and operational parameters such as rail gauge, vehicle speed, mechanical abrasion of rails and wheels, and electric-powered components (Abbasi et al., 2013; Cha, et al., 2018; Plachá et al., 2017; Querol et al., 2012; Woo et al., 2018; Xu & Hao, 2017). Mechanical wear and friction of electric conducting rails are identified

as primary sources of subway particulate matter, with wheel, brake, and track wear contributing to 40-73% of total PM_{10} mass (Colombi et al., 2013; Perrino et al., 2015). Research led by Abbasi et al., (2018) found that PM mass in subway tunnels increased by a factor of 12 during braking events. Some studies suggest that 35% to 55% of total brake system wear becomes airborne, and these particles can enter train carriages when doors open, increasing PM concentrations inside by 5-25%.

1.5 Gases in railway transports

Commuters are exposed to gas emissions across various transportation modes, including walking, trams, subways, and buses. These emissions include VOCs, polycyclic aromatic hydrocarbons (PAHs), a group of organic compounds formed during incomplete combustion (Do et al., 2014; Yan et al., 2015). and inorganic species like CO, CO_2, and NO_x.

In Shanghai metro carriages (Gong et al., 2017), for instance, the air contains VOCs such as benzene, toluene, ethylbenzene, xylene, styrene, formaldehyde, acetaldehyde, acetone, and acrolein. Moreover, lower concentrations of aromatic compounds and higher levels of carbonyl compounds have been observed in metro carriages in suburban areas compared to urban ones. Given the exposure to VOCs and PAHs in various transportation environments, including metro carriages, further investigation should focus on identifying these emissions.

1.5.1 Gas concentrations

According to studies conducted in Asia, the levels of VOC concentrations in subway stations have been found to vary widely from one subway to another by a factor of 7.4 to 8.5 (Li et al., 2006). In Shanghai, acetone and acrolein increased from 7.71 to 26.28 $\mu g/m^3$, with commuters increasing from 40 to 200 in the carriages (Gong et al., 2017). The total carbonyl concentrations in-train were about 1.4-2.5 times lower than in the stations, and most carbonyl concentrations were much higher in the morning rush hour than at other times. Carbonyl compounds presented in the indoor air are thought to result from indoor emissions, indoor chemical formation, and outdoor infiltration and even human beings; for example, acetaldehyde is a product of human metabolism and is present in human expired air (Feng et al., 2010). Below is a detailed table (Table 1.12) showing the different average concentrations of gases in subways worldwide.

Table 1.12 VOC concentrations in railway stations worldwide

Pollutant species	Average concentrations [μg/m³]	City	Location	Reference
CO	≤1	Barcelona	Platform	(Moreno et al., 2015)
CO_2	728 to 1114	Barcelona	Platform	(Moreno et al., 2015)
	2257 to 6613	Beijing	Subway	(Park & Ha, 2008)
Benzene	14	Beijing	In passenger cars	(Li et al., 2006)
	13	Mexico City	Breathing zone of trained technicians	(Perales et al., 2004)
Toluene	12	Beijing	In passenger cars	(Li et al., 2006)
Xylene	4	Beijing	In passenger cars	(Li et al., 2006)
Total BTEX	61	Guangzhou	Close to the routes of roadway transport	(Houston et al., 2013)
	147	Seoul	Ventilation system	(Y. S. Son et al., 2011)
Carbonyl compounds	99	Beijing	Subway	(Pang & Mu, 2007)
	24	Shanghai	Platforms	(Feng et al., 2010a; Y. Zhang et al., 2012)
PAHs	93	Los Angeles	Traveling in public transportation	(Houston et al., 2013)

VOCs have also become a significant concern in subway environments, with sources ranging from materials and surface coatings to outdoor air infiltration and human activities. The rapid development of subway transportation systems has led to a continuous increase in the number of commuters in metropolitan cities. For example, Shanghai, one of the world's largest metro systems, recorded a daily ridership of approximately 10.3 million in 2015. This increasing ridership has raised concerns about commuter exposure to VOCs in metro carriages, as highlighted by various environmental health studies. Further investigation into this issue should involve air quality monitoring and identification of pollutants and their sources (Gong et al., 2017; Shiohara et al., 2005; Xu & Hao, 2017) indicate significant concentrations of VOC and gases in subway environments worldwide. Limited research has focused on the specific impact of train braking systems on VOC emissions. Further investigation should focus on understanding how train braking processes release VOCs and gases within subway stations. However, due to this limitation, there is a lack of standard methods for sampling VOCs (Plachá et al., 2017).

1.5.2 Gas sources in railway transport

VOC concentrations in subway environments are influenced by several factors, including whether the train is underground or above-ground, its location in urban or suburban areas, and ambient pollutant levels. Additionally, factors such as train model and service time also play a role, while CO_2 concentrations inside the train are primarily affected by the number of passengers (Gong et al., 2017; Xu & Hao, 2017).

Aromatic VOC concentrations were 1–2 times higher in older metro carriages than in newer ones, as newer trains use less emissive paint formulations and surface coatings. Poor air circulation and ventilation in underground tracks contribute to approximately 10% higher VOC levels compared to above-ground tracks. However, this increase is relatively limited because VOC levels in the metro carriage are less affected by

street vehicle emissions, reducing the overall impact of external pollution sources (Gong et al., 2017). The in-train exposure to VOCs, including benzene, toluene, ethylbenzene, xylene, styrene, formaldehyde, acetaldehyde, acetone, and acrolein, depends heavily on factors such as service time, passenger density, and driving conditions (Gong et al., 2017). In addition, aliphatic hydrocarbons may originate from oils used during brake tests, contributing to additional VOCs (Plachá et al., 2017).

1.6 Mitigation strategies

Strategies for controlling PM emissions in railway systems primarily focus on material formulation. For example, using non-metallic materials like rubber or those with low metal content can reduce exposure to heavy metals in stations (Chang et al., 2021). Additionally, advanced and optimized ventilation systems, along with air conditioning, can significantly improve air quality inside carriages. In China, air purifiers installed on carriage ceilings improved air quality by 15-26%. In contrast, in Barcelona, tunnel ventilation systems were more effective, reducing PM levels by half when activated (Cha et al., 2018; Moreno et al., 2014; Xu & Hao, 2017).

Three methods were investigated to reduce PM concentrations indoors: platform screen doors (PSD), magnetic filters, and electrostatic purifiers. PSD were recognized as an efficient measure to improve the metro air quality, they reduced 16-30% of PM_{10} concentrations (Xu & Hao, 2017). However, seeing that there are many Fe-containing particles in subway stations, applying magnetic filters can remove the magnetic particles, but this depends on the particle size and concentrations (Chang et al., 2021). The effectiveness of magnetic filters on removing PM from subway tunnels was evaluated, and the maximum removal efficiency of PM_{10} (52%), $PM_{2.5}$ (46%), and PM_1 (38%) was observed at 60 Hz fan frequency to extract the air (Son et al., 2014). In Paris, an electrostatic precipitator prototype was installed to remove PM in the metro air; this process was efficient. With 20 filters installed, the PM concentrations decreased from 230 to 135 µg/m^3, with a decrease of about 40 %, which is more than that of magnetic filters and PSD (Tokarek & Bernis, 2006).

In summary, mitigation strategies for controlling PM and improving air quality in subway environments include using non-metallic materials (although emissions of organic particles or VOCs may increase instead), electrodynamic braking, advanced ventilation systems, air-conditioning, air purifiers, platform screen doors, filters, magnetic filters, and electrostatic precipitators. Extra studies should focus on optimizing and combining these strategies to develop comprehensive and effective solutions.

1.7 Conclusions of the bibliographic study

Subway air pollution poses a significant health risk due to the presence of fine and ultrafine particles, as well as toxic components, which are airborne and can penetrate the respiratory system. Nevertheless, measuring VOCs is also important as they play a key role in atmospheric chemistry and the formation of secondary aerosols. Brake wear, for instance, not only releases particulates directly but also emits gaseous pollutants, including VOCs, which can undergo photooxidation and contribute to the formation of secondary particulate matter (Patel et al., 2024). They should be studied to evaluate their risk since millions of daily commuters and metro employees are exposed to them. Therefore, understanding the sources and characteristics of particulate and gaseous pollutants is essential for implementing effective measures to improve air quality.

Thus, the information obtained on PM and VOCs from field measurements serves multiple purposes, ranging from local to global scales. Initially, they shed light on the variability of PM and VOC depending on the type of pad and disc, scale system, type of braking, and other factors. Moreover, in field measurement campaigns, the mixture of sources and pollutants is complex. Thus, it is preferable to perform on a lab scale in a more controlled environment.

The first lab test of a typical daily trip of a commuting train was carried out in the thesis of Octau, (2019). This work aims to further her findings by characterizing the airborne wear particles and VOC emissions, clarifying their dynamics. Moreover, Octau found that the composition of the emitted particles matched that of the original materials in the brake linings, based on their chemical elements. However, the elemental composition of the disc is also close to that of the lining for the main elements, which makes it difficult to clearly identify the exact source of the particles analyzed. A deeper analysis was conducted in this thesis to address this, as well as other perspectives that arose from it, particularly regarding certain particle characteristics, such as composition and its variation according to size. Are the largest particles composed of certain elements different from the finest? Does this composition vary according to the conditions? Moreover, what are the physico-chemical transformations within materials due to the increase in temperature or the severity of braking conditions?

As mentioned in previous sections, the lack of a sampling method of VOC for braking experiments was highlighted, full or lab scale, (Plachá et al., 2017). Contamination, long experimentation time, cost, and installation complexity are the challenges in sampling. Therefore, one of the objectives of this thesis is to develop a new method to sample VOC from braking. Thus, a group of analytical measurement methods has been developed to identify and qualify VOCs emitted from braking. It is believed that inlet and blank measurements can give a better view of VOCs that don't originate from the braking, and this is discussed in more detail in Chapter 2 of this document.

Additionally, Chapter 3: of this document investigates the effect of the braking power (normal vs heavy pathways) with a detailed look at the VOC dynamics during the heavy pathway. Chapter 4: investigates the effect of the design of the pad (focusing on curing process variations affecting rigidity and thermal expansion) on PM and VOC emissions under the normal pathway. It also explores the influence of the braking system scale.

1.8 Framework

1.8.1 BREAQ project

This PhD thesis is developed in the frame of the BREAQ project (**BR**aking **E**missions characterization and mitigation for **A**ir **Q**uality improvement), which is a multidisciplinary project carried out by four different partners: Alstom (coordinator), Alstom Flertex, CERI EE (IMT Nord Europe), LaMcube (Centrale Lille) and LAMIH (University of Valenciennes). The funding comes from ADEME, the French Environment and Energy Management Agency. This collaboration aims to understand and characterize the phenomena of wear as one of the main sources of PM emissions and VOCs from train braking systems, and on the other hand, to develop solutions to limit these emissions or to capture them, in order to ensure a healthier air, especially in underground networks and railway stations.

1.8.2 Thesis Objectives

All the above-mentioned needs in this bibliographic review and future perspectives raising scientific questions regarding railway emissions during braking processes, as well as the choice of organic pad for

VOC measurements, set the framework of the current PhD thesis, based on the deep experimental characterization of the particle and VOC emissions (including the dynamics) produced by a mechanical brake system during a typical subway journey. A reduced-scale braking bench (LaMcube) and a full scale bench (Alstom-Flertex) have been used, varying certain braking conditions and pad characteristics. The reduced-scale braking bench was designed to reproduce the same thermo-mechanical conditions as at full scale in the thesis of Joseph Frangieh (2025) where some experiments have been pooled with his results on material wear during braking to investigate the relationship between wear and emissions.

The following specific objectives will be addressed in the upcoming chapters:

1. Address PM and VOCs measurement uncertainty with duplicates to ensure the reliability and consistency of the results.
2. Study the effect of power, pad design, and pad's softness/rigidity on the emissions generated during braking.
3. Investigate the relationship between average PM emissions and wear, checking consistency between mass loss and mass emissions.
4. Link between VOC emissions and wear mechanisms, by focusing on their dynamics during braking.
5. Compare different scales of testing (full and reduced), estimate emission factors, and address the representativeness of the emissions.

The expected outcomes of the thesis are to enhance our understanding of the emissions, particularly suspended PM and VOCs, from train friction braking and to improve our knowledge of the processes and parameters influencing these emissions. This research could contribute to developing innovative mitigation strategies to reduce the exposure of railway users and workers to air pollutants.

Chapter 2: Experimental setups and methods

2.1 Materials

In this study, braking system configurations with a cast iron disc and various organic pads were used, in both a full-scale test bench and a reduced-scale one. For the reduced-scale tests, pads were extracted from real metro braking pads, and the discs were manufactured from the same lamellar graphite cast iron batch used to manufacture the full-scale disc. A brief description of these materials is provided in this section. A more detailed physico-chemical characterization will be presented in Chapter 3:

2.1.1 Braking disc

The braking tests were conducted using two braking discs made of the same lamellar-graphite (GL) cast-iron material, provided by ALSTOM IBRE, but differing in size and design according to the scale of the test bench used: full-scale or reduced-scale.

2.1.2 Pad

Braking organic pads provided by ALSTOM FLERTEX and equipped with a spindle were also used for both scales, with adjustments in design and size. The exact composition of the pads is confidential but the relative mass fractions of the main components is given in Table 2.1.

Table 2.1 Main components of the braking pad formulation.

Components	**Weight [%]**
Rubber	20
Phenolic resin	5
Non-metallic fibers	5
Metallic fibers	30
Friction modifiers and fillers	40

2.2 Full-scale brake system

The braking tests were conducted on an ALSTOM FLERTEX brake bench, a test bench generally used to test brake lining wear (Figure 2.1). The test facility consists of two rooms. The inertia dynamometer cabin and all the instrumentation for sampling and analysis of gases, particles, and thermomechanical properties are in the first room. In the second room is the air filtration system. Concerning the air circulation through the cabin, outdoor air is drawn from the roof of the building towards the inlet air filtration unit equipped with HEPA filters, then pushed in a duct with an inner diameter of 0.56 m (the inlet duct) connected to the top of the dynamometer cabin. The speed of the air entering the cabin (the inlet air) varies between 3 to 8 m/s depending on the rotation speed of the brake disc from 0 to 110 km/h. At the bottom of the cabin, the air exiting the cabin (the outlet air) is aspired from the dynamometer cabin through a duct (the outlet duct) with an inner diameter of 0.56 m, and is discharged at the roof after filtration. The speed of this outlet air in the outlet duct is constant at around 7 m/s. The door of the cabin is closed during the braking tests but the cabin has leaks. Accordingly, some “indoor air” from the surrounding first room enters the

cabin when the outlet air flow rate exceeds the inlet air flow rate, depending on the brake disc rotation speed.

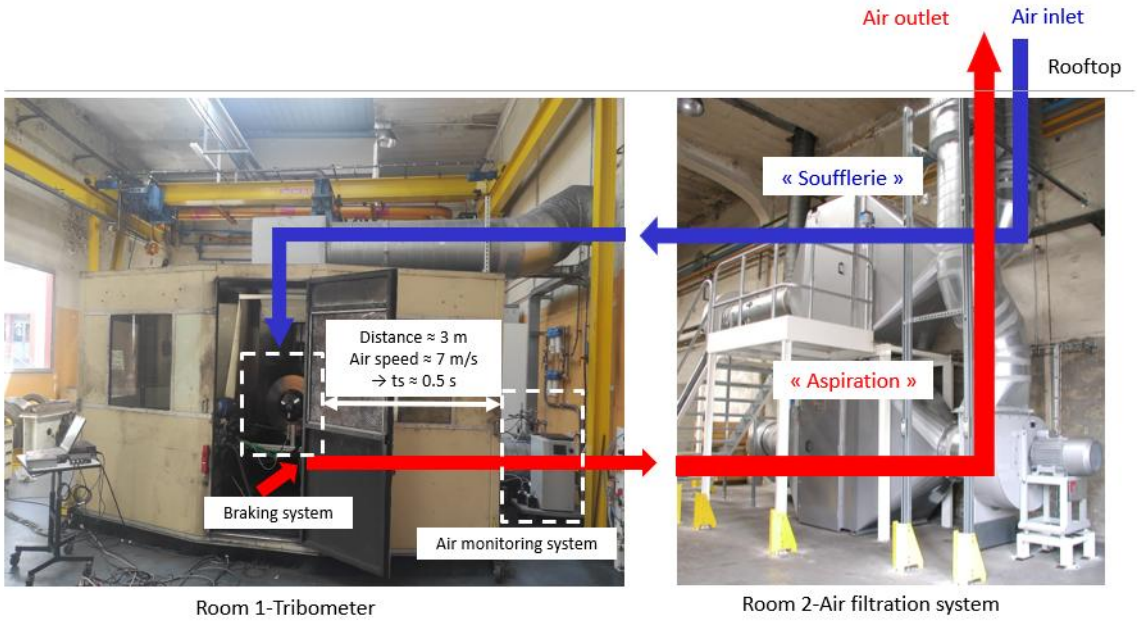

Figure 2.1 Full scale test bench at Alstom Flertex. The blue arrows indicate the trajectory of the inlet air; the red arrows refer to the trajectory of the outlet air. In the photography of room 1, the door of the cabin is open to show the dynamometer inside. This door is closed for safety when tests are performed.

During full-scale testing, a lamellar graphite cast-iron auto-ventilated disc (ALSTOM IBRE reference: ES0009) with a diameter of 610 mm and a thickness of 110 mm was used, along with two pairs of organic pads. A ventilated disc promotes air circulation when rotating to cool down the disc after braking events. The organic pads are commercial ones for metro trains provided by ALSTOM FLERTEX and complying with the requirements of the UIC (International Union of Railways). Two pads are used, one at each side of the brake disc. Each pad is grooved to give mechanical flexibility, and also to prevent the formation of a film of water between the disc and the lining when used in wet weather. The surface of one pad is 346 cm^2 excluding grooves, so the total pad area is 692 cm^2. The thickness of the fitting is around 3.5 cm (Figure 2.2).

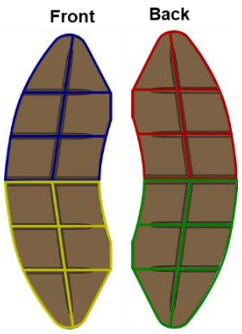

Figure 2.2 Pads in full scale

The design of the disc-pad assembly is shown in Figure 2.3.

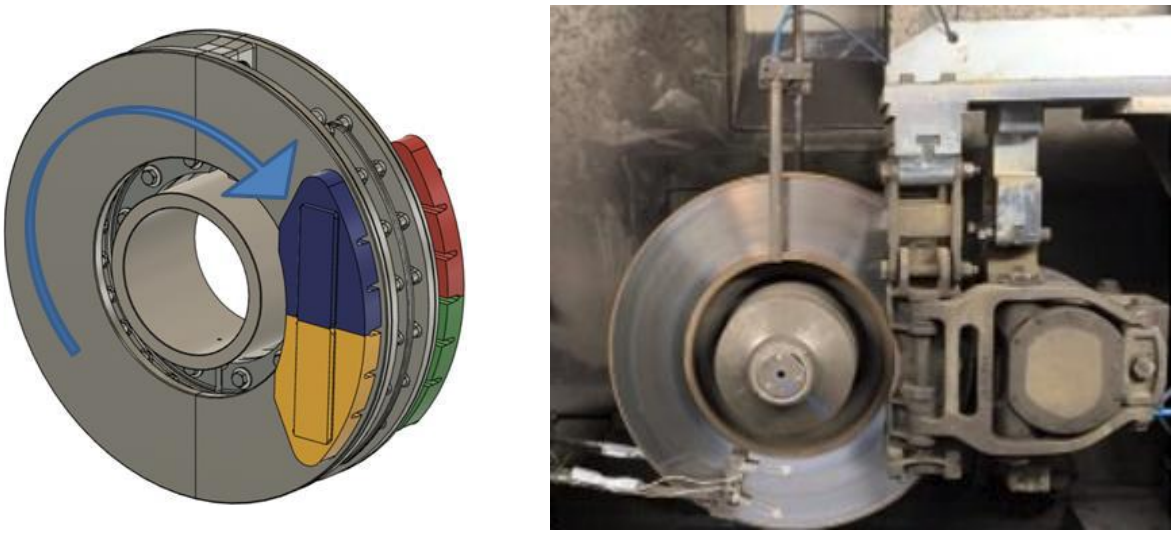

Figure 2.3 Disc-pad assembly at full scale.

The campaigns took place in June 2022 and June 2024. The choice to conduct these tests at the ALSTOM Flertex site was based on their unique capacity to host a full-scale testing bench, duplicating the pad and disc configuration. This setup enables us to replicate braking emissions as they would behave in real-world braking systems.

2.3 Reduced-scale brake system

A reduced-scale braking bench was integrated in the LaMcube test room (Figure 2.4) following a downscaling strategy to best reproduce the thermal, mechanical and wear phenomena observed at full scale, with a better control of experimental conditions. The downscaling strategy was based on thermal and thermomechanical similarity, and was developed by Joseph Frangieh as part of his PhD (Frangieh et al., 2023). It ensures similar surface temperature trends at both scales, and similar thermomechanical localizations (hot bands, local deformation), resulting in an energy scale factor of 15.4.

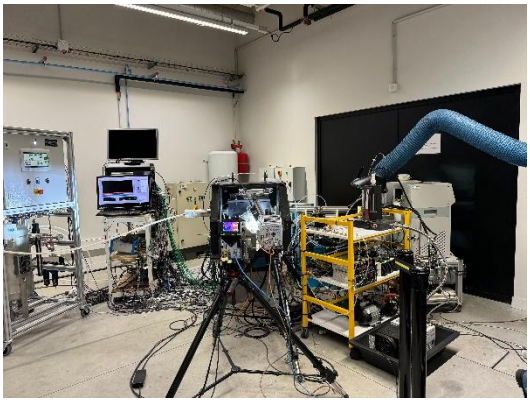

Figure 2.4 LaMcube test room

For the reduced scale, an unvented solid disc is used, with a diameter of 210 mm and a thickness of 22 mm. The pads were specifically manufactured by ALSTOM FLERTEX in the same composite material as for the full scale. A single pad is used to rub on the disc, composed of two independent pieces fixed on the same plate. Each piece is oblong and slightly curved, 16 mm wide and 20.5 mm high. The total surface area is 15.8 cm^2 (Figure 2.6).

Four different pad configurations were studied: one **reference** configuration and three variants. Although the brake pads have a similar formulation, variations in the manufacturing process resulted in distinct properties for each. We will refer to the pad with the lower stiffness as "**soft**" and the pad with the higher stiffness as "**rigid**." The difference in stiffness of materials was achieved by altering the manufacturing process of the industrial reference pad. For the soft pad, the molding pressure was reduced to 110 daN/cm^2, while the temperature and curing time remained unchanged at 200°C for 4 hours. For the rigid pad, the curing time was increased to 8 hours, while the molding pressure (200 daN/cm^2) and temperature (200°C) remained the same as the industrial reference pad. In these conditions, the degree of cross-linking of the phenolic resin is expected to rise as both temperature and time will favor it.

Joseph Frangieh's thesis examined the mechanical and thermal properties. The results are presented in Frangieh, (2025). Table 2.2 and Figure 2.5 summarize the main results and compare them with the properties of the industrial reference material. The compressive stiffness values of the soft and rigid materials differ by a factor of eight, while their thermal expansion is fairly similar. From a mechanical point of view, the tests also showed a significant reduction in structural integrity for the soft and rigid materials compared to the reference one, particularly for the soft material, which was most sensitive to mechanical damage. Regarding thermal properties, the materials exhibited anisotropy, favoring greater heat diffusion in the tangential direction of the pad surface; this difference was particularly pronounced for the soft material.

Table 2.2 Physical parameters: Compression modulus, thermal expansion and density

Pad materials	**Soft**	**Rigid**	**Reference**
Compression modulus [MPa]	240	1880	1425
Thermal expansion coefficient [10^{-4} K^{-1}]	1.41	1.31	1.49
Density [g/cm^3]	1.99	1.97	1.91

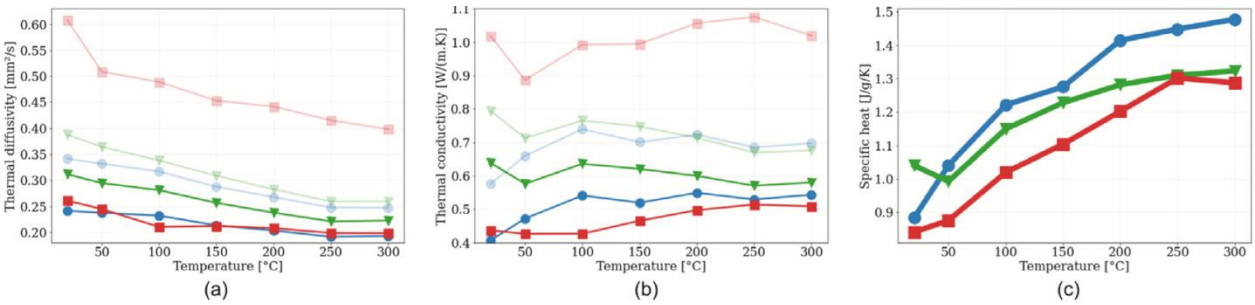

Figure 2.5 Thermal properties of soft (in red), rigid (in green) and reference (in blue) pad materials:(a) thermal diffusivity, (b) thermal conductivity in both normal (in dark) and tangential (in light) directions, and (c) specific heat capacity (Frangieh, et al., 2025).

As part of the chemical characterization of the pad materials, carbon weight content (pad total carbon analyzed by the commercial laboratory SOCOR) is presented in Table 2.3.

Table 2.3 Carbon weight content in pad materials

Pad materials	**Soft**	**Rigid**	**Reference**
Carbon [wt%]	29.7	31.2	27.1

The final pad has a different design, featuring eight grooves, as shown in Figure 2.6. This grooved design affects the rigidity and thermal expansion behavior of the pad due to the thermomechanical independence of the 'plots' separated by the radial grooves.

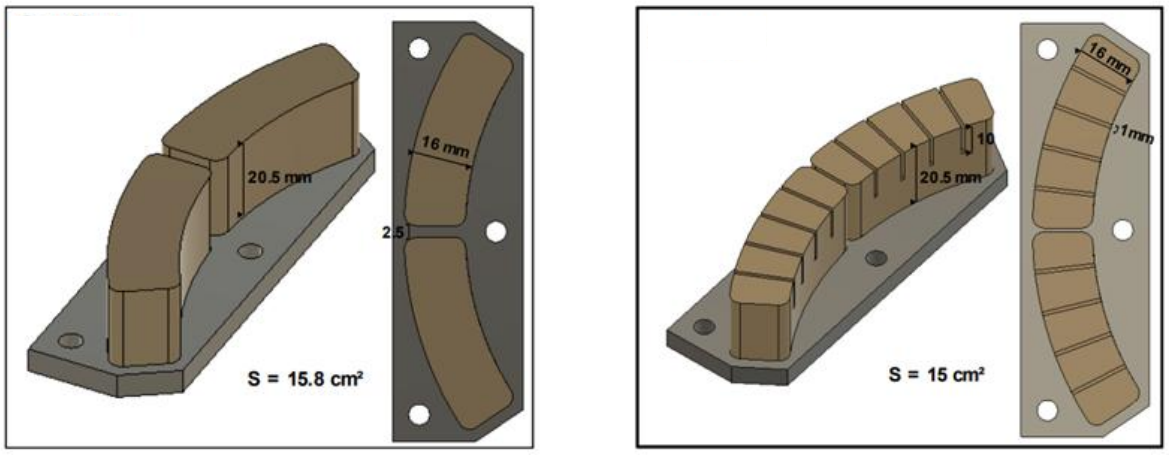

Figure 2.6 Designs of the reduced-scale pads “reference”, “rigid” and “soft” (left) and of the reduced-scale pad “grooved” (right).

The disc-pad braking system takes place inside a transparent polycarbonate (Makrolon trademark) chamber measuring approximately 380 x 340 x 100 mm^3, which allows control of the gaseous environment of the contact and confinement of the particulate and gaseous emissions. The downscaled disc and pad were placed in the enclosure, with air flowing in the upper part in the same direction as the disc rotation

direction (Figure 2.7). The air is injected and then evacuated through ducts that are aligned with the friction face of the disc, with an offset 120 mm above the disc's axis of rotation. The temperature of the gas flow is measured by a thermocouple in the enclosure and in the outlet duct (exit enclosure). The distance between the exit thermocouples and the enclosure was around 47 cm.

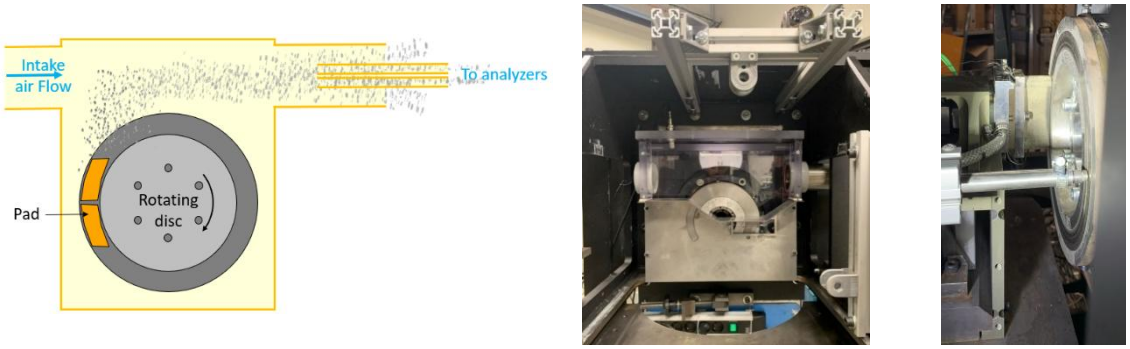

Figure 2.7 Reduced-scale enclosure of the disc-pad system.

The total volume of the chamber minus the volume of the disc, which is the real volume of the air inside the chamber, is approximately 13 L (Appendix 1).

In order to prevent any external contamination, pure air from cylinders (Alphagaz 1, Air Liquide) was introduced in a humidity center, generating an airflow with controlled initial temperature of 30-35°C, and humidity of 30-40%. The choice of these values was made to present the same conditions as in full scale, so that the humidity center provides unsaturated air. The airflow exits the humidity center through a plastic (polyamide) pipe to the entrance of the enclosure and was set at 18 m^3/h (300 L/min) in this study. As it passes through the enclosure, the flow pulls away the emitted particles and VOCs from the braking system. The inlet and outlet pipes are made of stainless-steel tubing. The inner diameter of the pipe is 73.8 mm. The conditioned air travels a distance of one meter in the inlet pipe before entering the enclosure. At the outlet of the enclosure, the outlet pipe guides the air flow to an isokinetic sampling point towards the sampling systems and then to the measuring and/or analysis instruments. Not all of the airflow circulating in the system is sampled by the sampling system. The excess flow is captured by an extractor hood and then filtered. We have chosen to work with a flow rate of approximately 300 L/min, which corresponds to a speed of around 1.2 m/s in the inlet or outlet duct (Figure 2.8).

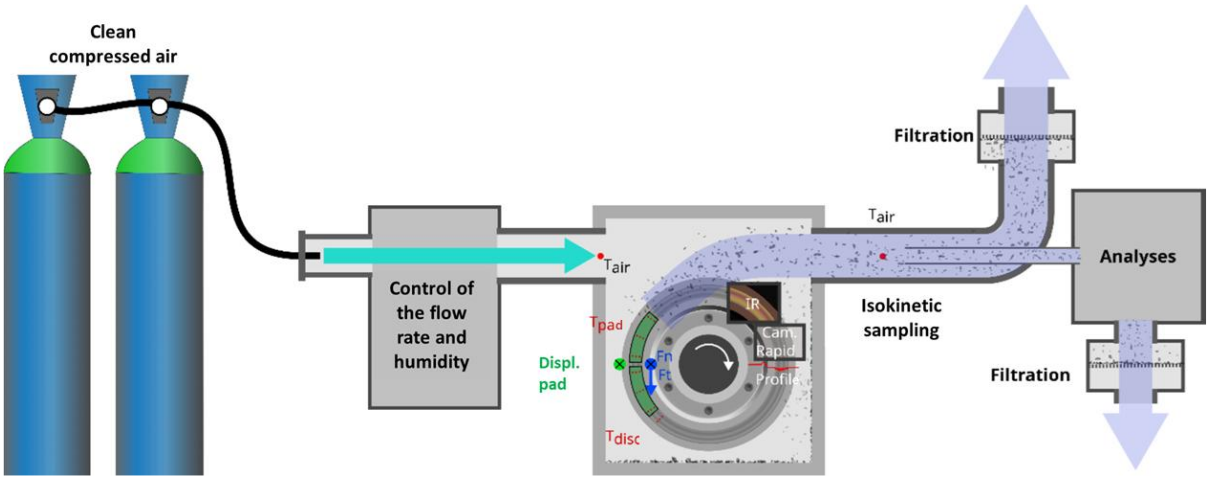

Figure 2.8 Overall scheme of the experimental set-up at reduced scale.

2.4 Test protocols

In order to study emissions as close as possible to real ones, we chose to simulate typical metro journeys, focusing on 2 pathways: normal and heavy. These pathways were applied at both scales.

2.4.1 Pathways

2.4.1.1 Normal pathway (NP)

The normal pathway represents a normal load for operating a 6-cabin lightweight train on a realistic commuter train. It simulates a typical subway braking scenario through mechanical and electrodynamic braking. Each round trip of this route consists of 72 station stops and lasts approximately 2.5 h. A whole operating day includes three round trips (216 stops) covering 458.5 km and lasting about 8 h (including a 3-min dwell time at the end of each round trip). During a stop, the train speed decreases from its initial speed (maximum speed of 110 km/h) to 60 km/h using a single or multiple mechanical braking applications, and then using electrodynamic braking from 60 km/h to zero (stop at the metro station). This real pathway involves many different mechanical braking events, depending on the initial and final speeds to be reached, the gradients and curves of the route or the proportion of electrodynamic braking, among others (Figure 2.9).

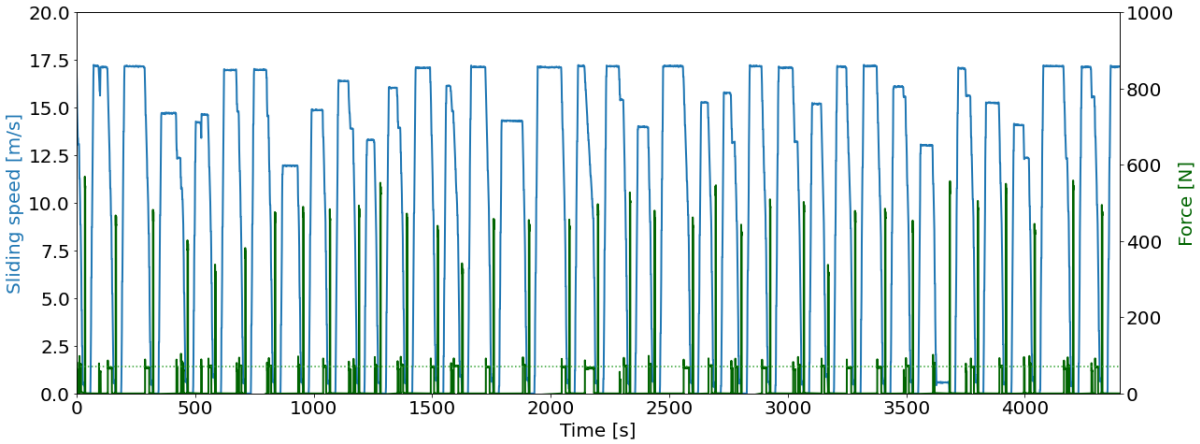

Figure 2.9 Braking conditions during one way of a round trip of the normal pathway (Frangieh 2025)

As shown in Figure 2.10 on the left, this includes a single mechanical braking event that decreases the speed or, as shown in Figure 2.10 on the right, multiple brake applications that may consist of two or three braking events. The last short braking is to stop at the right place on the platform. The time between two successive braking applications varies depending on the type of braking and on the distance between the train stations. Under this route, the maximum mean surface temperature reached by the disc is expected to be 73°C (simulation by ALSTOM).

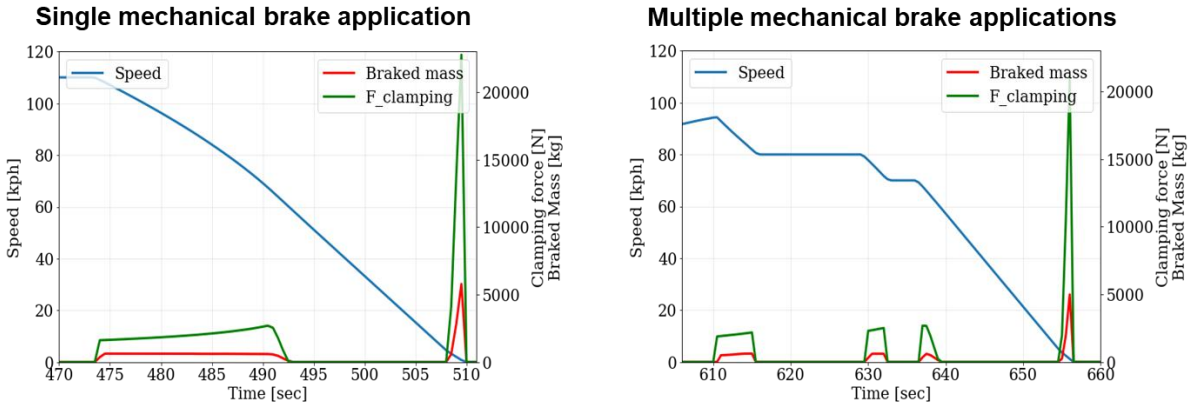

Figure 2.10 Mechanical brake applications in the normal pathway

2.4.1.2 Heavy pathway (HP)

The pathway studied in normal operation was tested in a heavy mechanical braking mode, that is with the mechanical braking system remaining engaged continuously in parallel with the electrodynamic braking system, involving 9 times the dissipated power of NP. Under this pathway, the maximum temperature reached by the disc is expected to be 258°C (simulation by ALSTOM). Comparison with the previous route allows to study the effect of braking severity on emissions, and also to generate more emissions in order to overcome the limits of detection of the instruments, particularly for VOCs.

2.4.2 Background measurements

The aim of the background measurements is to get a reference without braking events in order to be able to detect and quantify emissions during braking routes.

2.4.2.1 Particle background characterization in reduced scale setup

For the reduced scale, we conducted a pre-test procedure that involved collecting a background sample of particles or VOCs over 60 min. The initial 15 min featured a flow rate of 18 m^3/h without disc rotation, followed by 45 min with disc rotation at 1700 rpm. Air (ALPHAGAZ™ 1 pure gases) was circulated in the system at 30-40% humidity. VOC sampling at both the inlet and outlet of the tribometer chamber was simultaneously performed.

The average TSP mass concentration of 7 blanks was 32 ± 19 µg/m^3, which is approximately three times higher than the limit of quantification. Compared with 1 blank at higher humidity, there is no trend indicating potential condensation of water droplets on the filters over time.

Figure 2.11 shows the total number concentration of fine and ultrafine particles using FMPS over time during the blank measurement, since online mass concentration data were not available. After a period of approximately two minutes of strong decrease due to the flushing of contaminants from the previous test, the TSP concentration decreases steadily, with a negative slope of -0.0475 #/cm^3/s indicating a decrease in PM with time.

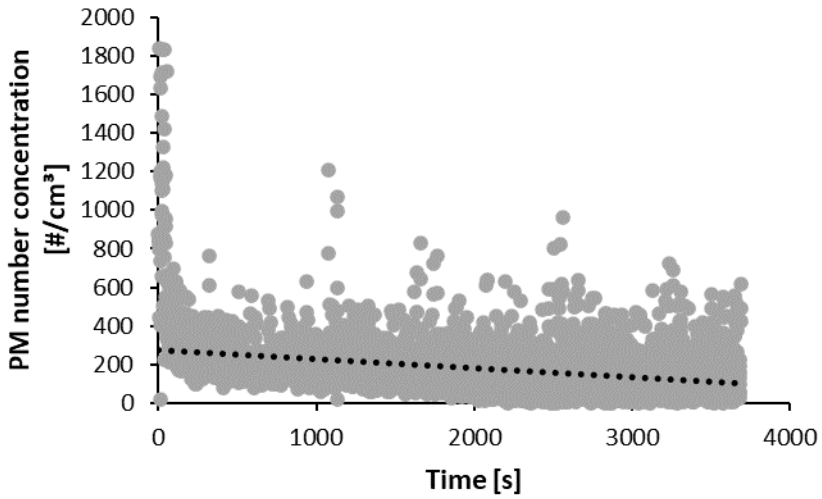

Figure 2.11 PM temporal profile of total particle number concentration measured by FMPS in a blank sample

2.4.2.2 Assessment of airflow dynamics and indoor air infiltration in the full-scale setup

In order to assess the indoor air infiltration in the cabin, blank tests (corresponding to air circulation in the setup without any braking) were conducted for 1 hour at various disc speeds ranging from 0 to 110 km/h. The inlet air flow rate is driven by the disc speed to simulate the air around a real moving train while the

outlet air flow rate is kept constant. During each test, air speeds were simultaneously measured at both the inlet and outlet ducts, which have same inner diameters.

From the measured air speeds, the volumetric flow rates of both the inlet air and the outlet air were calculated. The indoor air volumetric flow rate entering the dynamometer cabin was estimated as the difference between the outlet and inlet air volumetric flow rates (Figure 2.12).

A positive indoor air volumetric flow rate indicates that air from the indoor environment enters the cabin to compensate for the lower inlet flow for the air exiting through the outlet. In fact, the inlet and indoor air contributions together should balance the outlet flow; therefore, when the inlet flow is insufficient, a positive indoor air flow arises to match the outlet flow leaving the cabin. This situation occurs when the disc speed is below ≈ 95 km/h.

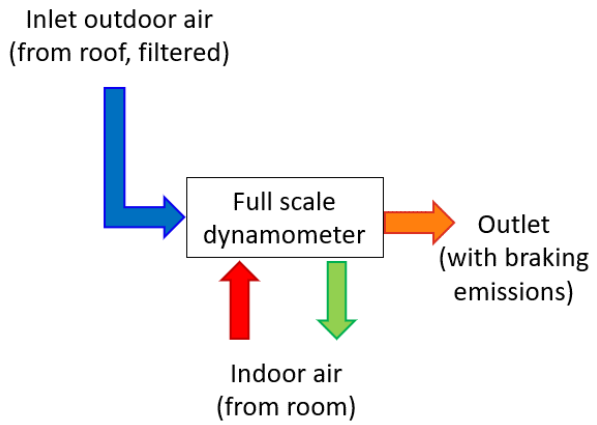

Figure 2.12 Schematic of airflow and emission sampling in the full-scale dynamometer setup, with the red arrow indicating a positive indoor air flow rate and the green arrow indicating a negative indoor air flow rate.

The ratio of indoor air penetrating the cabin is the highest when the disc stops, reaching 40% of the outlet air flow (Figure 2.13).

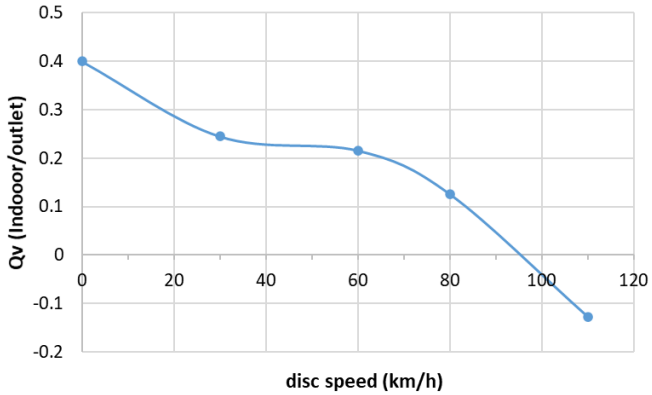

Figure 2.13 Ratio of the volumetric flow rate of indoor air to outlet air in function of the disc speed. A positive ratio means that indoor air penetrates into the cabin. A negative one means that no indoor air enters the cabin but that some cabin air escapes to the workshop.

Thus, in the full-scale setup, the disc-and-pad braking system was installed in a cabin that was kept at negative pressure most of the time, unlike the smaller-scale system, which was at positive pressure. As a result, indoor air from the workshop could enter the cabin. This indoor air was influenced by outdoor air (when the workshop windows were open), by the nearby pad factory, and by the activities taking place in the workshop itself.

2.4.3 Bedding

Before each test, a bedding of the disc and the pad was done in order to make a tribological preparation of the contact and get representative operating conditions (Table 2.4). The bedding must allow, in particular, geometric accommodation of the surfaces, modification of the surface layer of the materials (through mechanical and thermal stress), and the creation of an adequate amount of third body at the interface.

Table 2.4 Conditions for the bedding of disc and pads.

Component to bed	Bedding procedure	Number of brake events	Speed [km/h]	Force [kN]	Initial disc temperature [C]	Braked mass [tons]
Disc (day 1)	Alstom Flertex (using a worthless pad)	100	100 → 0	20	100	6
Pad (day 2)	Alstom Flertex	50	100 → 0	20	100	6
	1 round-trip of a simplified pathway	72	110 → 0	2	45	0.6
Pad (day 3)	2 round-trips of a simplified pathway	144	110 → 0	2	30-35	0.6

For a given scale, a single disc was used for all tests, while new or old pads were used depending on the experiments.

2.4.4 Summary of the tests performed at both scales

The summary of the tests done at both scales is presented in Table 2.5.

Table 2.5 Summary of the tests performed at both scales

Scale	Nr.	Pathway	Year	Pad	Comment
Reduced	1	NP1	2024	Reference	Replicate1
Reduced	2	NP2	2024	Reference	Replicate2
Reduced	3	HP1	2024	Reference	Replicate1
Reduced	4	HP2	2024	Reference	Replicate2 (with PTR-MS)
Reduced	5	NP1	2024	Rigid	Replicate1
Reduced	6	NP2	2024	Rigid	Replicate2
Reduced	7	NP1	2024	Soft	Replicate1
Reduced	8	NP2	2024	Soft	Replicate2
Reduced	9	NP1	2024	Grooved	Replicate1
Reduced	10	NP2	2024	Grooved	Replicate2
Full	11	NP	2022	Reference	-
Full	12	HP	2022	Reference	Replicate1
Full	13	HP	2024	Reference	Replicate2

2.5 Physical measurements during the tests

For the experimental simulation of the two scales, several physical parameters were set (such as the force exerted on the pads, the rotation speeds of the disc, and the braked mass) and numerous variables were measured, in particular the temperature 2 mm below the surfaces of the disc and pad and the variations in the thickness of the disc and pad. These measurements were managed by the LaMcube team.

2.5.1 Temperature measurement

The reduced and full scales used a similar temperature measurement approach. For the disc, three embedded 1 mm K-type thermocouples (TC Direct) were positioned at the same radial location (visible near the entrance pad on Figure 2.14. While for pad temperature measurements, 18 thermocouples were positioned 2 mm from the pad surface across the entrance and exit pads. In each pad, three thermocouples were positioned at the front, three in the middle, and three at the outlet. At full scale, three rubbing thermocouples were used for the surface disc temperature, instead of embedded thermocouples. The distance between the thermocouples, located in the sampling pipe (referred to as the ‘exit'), and the enclosure is around 47 cm. All temperature data were recorded at low frequency (20 Hz).

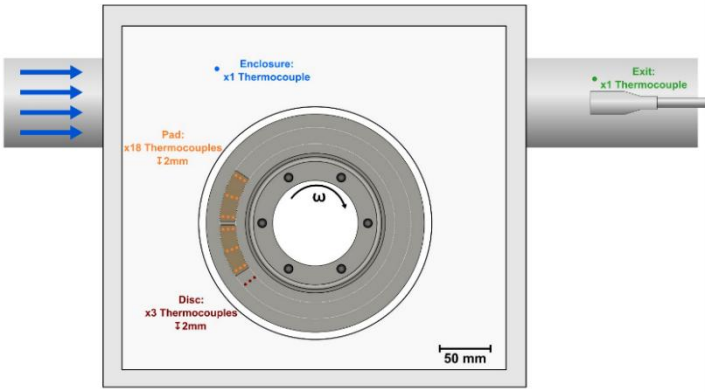

Figure 2.14 Thermocouples: red dots in the disc, orange dots in the pads, blue dot in the enclosure, and green dot at the exit, shown at reduced scale (detail of Figure 2.8)

2.5.2 Pad and disc wear measurements

The wear of the pad (respectively of the disc) was assessed by measuring the thickness loss of the pad (respectively of the disc) using positioning laser sensors (respectively using 2D laser profiler on the surface of the disc). Thermal expansion of the materials was taken into account to evaluate the volumetric wear of both pad and disc (Frangieh, 2025).

2.6 Experimental set-up for PM and VOC measurement at reduced scale

Similar sampling and measurement setups were employed for both scales, but more controlled conditions were achieved at reduced scale. The studied emissions are categorized into two groups: PM and VOCs, further classified depending on the measurement technique as online or offline (i.e., requiring a previous sampling). The VOCs were sampled both at the inlet and outlet ducts, while PM were only sampled at the outlet duct using an isokinetic sampling probe. A general view of the set-up is shown in Figure 2.15. Details are provided in the following subsections.

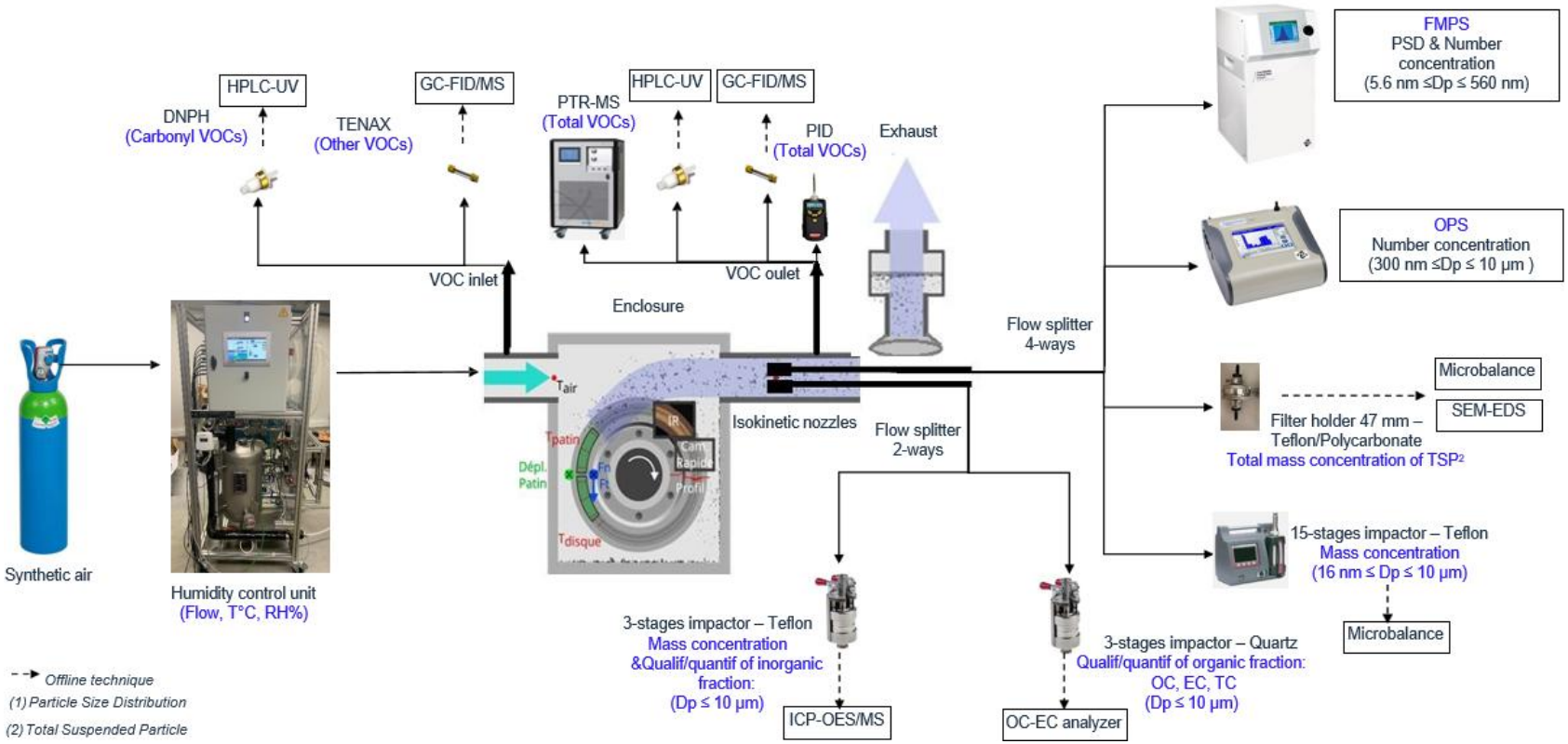

Figure 2.15 Reduced-scale emission measurement instrumentation

2.6.1 Experimental set-up for PM measurement at reduced scale

At reduced scale, two sampling isokinetic nozzles were installed in the outlet duct, facing the flow for PM isokinetic sampling, at about 23 cm away from the enclosure (Table 2.6). Nozzle 1 was connected to 2-way splitter supplying two offline PM samplers (3-stage impactors), while nozzle 2 was linked to a 4-way splitter connected to two online particle size analyzers: Fast Mobility Particle Sizer (FMPS) and Optical Particle Sizer (OPS), and two offline PM samplers (14-stage impactor and filter-holder). The front surface areas of the nozzles were designed in order to get the same air speed as in the outlet duct (1.17 m/s). This was achieved for nozzle 1 but a little less good for nozzle 2 where air speed was +16% higher than the desired speed (super-isokinetic). Super-isokinetic sampling may lead to overestimating particles with high inertia (big particles).

Similarly, one may notice that the air flow is turbulent with a Reynolds of 5490 (> 2000) calculated at an ambient temperature of 25°C. Therefore, the PM sampling is not strictly "isokinetic" (the flow regime should be laminar) but it can be considered to be close to it, and may at least be named "iso-mean-velocity". Note also that particles below a few µm in diameter are not concerned by isokinetic deviations because of their low inertia.

Table 2.6 Isokinetic PM sampling in the reduced-scale experimental set-up.

Reduced scale set-up	Diameter [mm]	Surface [mm^2]	Flow rate [L/min]	Speed [m/s]	Connected instruments
Outlet duct	73.8	4278	300	1.17	Temperature, humidity, air speed, PID, VOC sampling port
Nozzle 1	33	855	60	1.17	2-way splitter: Two 3-stage impactors
Nozzle 2	22	380	31	1.36	4-way splitter: FMPS, OPS, 14-stage impactor, filter-holder (TSP)

2.6.1.1 Sampling of PM for off-line analysis at reduced scale

Samples of PM were collected on filters: polytetrafluoroethylene (PTFE), quartz, or polycarbonate using different samplers: generally, two stainless-steel Pall filter holders (with a diameter of 47 mm or 25 mm), two 3-stage impactors (Dekati PM10 impactor in a modified version, Table 2.7 and Appendix 2), and one 14-stage impactor (Dekati DLPI+) (Figure 2.16). Prior to the sampling, the filters were pre-weighed and stored in labelled boxes (Millipore PetriSlides). After sampling, each filter was put back in its box and kept in a freezer before analysis to determine PM mass concentration and chemical composition, including metals and carbon content.

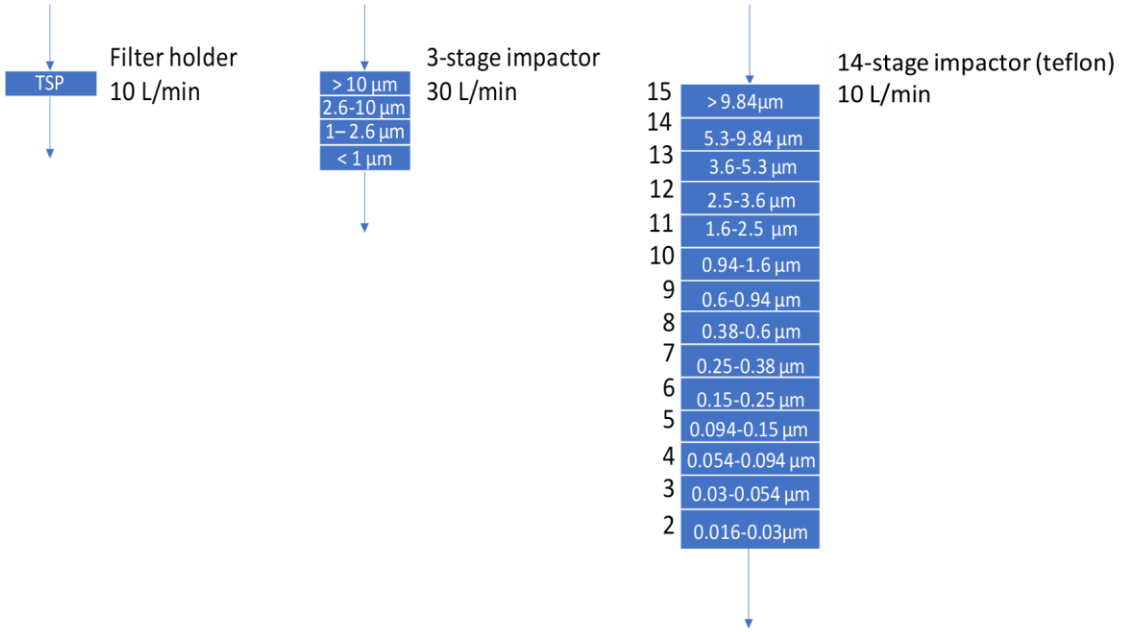

Figure 2.16 Scheme of the filter holder and the 3-stage and 14-stage impactors with their respective sampling air flow rates

To determine TSP mass concentration, a pre-weighed 47-mm diameter PTFE filter (Sartorius) was placed in a filter holder. A black antistatic tubing (ADDAIR) of about 50 cm long and 4.5 mm inner diameter connected the flow splitter to the filter holder. The filter holder was connected to a vacuum pump, and the volumetric air flow was set with a mass flow controller. A single filter was employed over the whole route (8-h sampling). The gravimetric assessment of sampling filters was performed in a climate-controlled (temperature: 22 ± 0.2 °C, relative humidity: 45 ± 5 %), manual weighing system using a precision balance Sartorius MCA.

The two modified 3-stage impactors were used, one with 25-mm PTFE filters for metal analysis and one with 25-mm quartz filters (PALL), which were pre-baked in the oven at 500°C to remove any residual organic compounds from manufacturing, handling, or storage before sampling for carbon analysis (NIOSH, 2003). Both impactors were equipped with a 47-mm backup filter. These impactors worked at a volumetric flow of 30 L/min.

Table 2.7 Effective particle size classes (aerodynamic diameters) of the modified 3-stage impactors (Appendix 2)

Stages	Effective size ranges [µm] of the modified 3-stage impactor
Stage 1	>10
Stage 2	2.6 – 10
Stage 3	1.0 – 2.6
Backup filter	< 1.0

The 14-stage impactor DLPI+ (Dekati® Low Pressure Impactor) was used to determine airborne particle mass size distributions. The DLPI+ classifies and collects particles into 14 size fractions based on the

equivalent aerodynamic diameter (whose definition assumes spherical particles with reference to a density of 1 g/cm^3) in the range of 16 nm—10 µm (Table 2.8). In each size fraction, the particles are collected on 25 mm PTFE filters (Sartorius) that are weighed before and after the measurement to obtain the particle gravimetric size distribution. The analyzed particles, which may be very different in size and composition and, therefore, densities, challenge the particle sampling procedure concerning particle losses and rebounds.

Table 2.8 Particle size classes (aerodynamic diameters) of the 14-stage impactor

size class	1	2	3	4	5	6	7	8	9	10	11	12	13	14
D50% [µm]	0.0157	0.0303	0.0541	0.0943	0.154	0.254	0.38	0.600	0.943	1.62	2.46	3.64	5.34	9.84
Dg [µm]	0.022	0.040	0.071	0.121	0.198	0.311	0.477	0.752	1.236	1.996	2.992	4.409	7.249	22.181

D50% median cut-off diameter of an impaction stage;
Dg: geometric mean of the lower and upper diameters of a stage (for the 14th size class, the upper diameter is considered to be 50 µm).

2.6.1.2 Particle mass concentration and uncertainties

The results will be presented as mass concentrations Eq. 2-1 under reference temperature (25°C) to ensure consistency and comparability.

$$C = \frac{m}{V} \qquad \text{Eq. 2-1}$$

Where:

C: particle mass concentration [µg/m^3]

m: mass of particles collected on the filter [µg]

V: volume of sampled air [m^3]

Relative uncertainties were calculated for each measurement according to Eq. 2-2:

$$(\frac{U_C}{C})^2 = (\frac{U_m}{m})^2 + (\frac{U_V}{V})^2 \qquad \text{Eq. 2-2}$$

Where:

U_C: uncertainty of the mass concentration C [µg/m^3]

U_m: expanded uncertainty of the mass m [µg]

U_V: uncertainty of the volume of sampled air V [m^3].

- Mass uncertainty:

The collected mass on the filter is calculated according to Eq. 2-3:

$$m = m_{after} - m_{before} \qquad \text{Eq. 2-3}$$

Where:

m_{before}: mass of the particle-unloaded filter before the PM sampling [µg].

m_{after}: mass of the particle-loaded filter after the PM sampling [µg].

To estimate the uncertainty from weighing, each filter is weighed three times before and three times after sampling (n=3).

The uncertainty of the PM mass of a sample is calculated following Eq. 2-4:

$$u_m = \sqrt{(u_{m,before})^2 + (u_{m,after})^2} \quad \text{Eq. 2-4}$$

Where:

u_m is the uncertainty of the weighed mass of particles on a filter [µg].

$u_{m,before}$ is the uncertainty of the mass of the unloaded filter, equal to the standard deviation of 3 repeated weighings [µg].

$u_{m,after}$ is the uncertainty of the mass of the particle-loaded filter, equal to the standard deviation of 3 repeated weighings [µg].

Usually, it was found that $u_{m,before} = u_{m,after} = 1$ µg, so that $u_m = \sqrt{2} \times 1 = 1.4$ µg.

To account for additional sources of uncertainty beyond repeatability, the expanded uncertainty was calculated using a coverage factor of k=3. This choice allows for the inclusion of various unquantified errors, such as those arising from manual handling (Eq. 2-5):

$$\mathrm{U_m} = \mathrm{k} \times \mathrm{u_m} \quad \text{Eq. 2-5}$$

Therefore, the expanded uncertainty of the PM mass of a sample is estimated as:

$$\mathrm{U_m} = 3 \times 1.4 = 4.2 \text{ µg}.$$

In the case of particle sampling done with a cascade impactor, the total mass of the sampled particles corresponds to the sum of the PM masses of all the stages of the impactor, including the backup filter, if there is one. If N is the number of stages (including the backup filter) of a cascade impactor, the expanded uncertainty of the particle mass is calculated as Eq. 2-6:

$$U_{m,impactor} = \sqrt{N} \times U_m \quad \text{Eq. 2-6}$$

For the 3-stage impactor + its backup filter, the expanded uncertainty of the total mass is calculated with N=4 and equals 8.4 µg. For the 14-stage impactor, the expanded uncertainty of the total mass is calculated with N=14 and equals 15.7 µg.

- Air volume uncertainty:

The sampled air volume (V) is calculated according to Eq. 2-7:

$$V = Q_v \times \Delta t \qquad \text{Eq. 2-7}$$

Where:

V: volume of air sampled [m^3].

Q_v: sampling air flow rate [m^3/s] at the ambient temperature and pressure of the experiment.

Δt: sampling duration [s].

Therefore, the volume relative uncertainty is calculated following Eq. 2-8:

$$\left(\frac{U_V}{V}\right)^2 = \left(\frac{U_{Q_v}}{Q_v}\right)^2 + \left(\frac{U_{\Delta t}}{\Delta t}\right)^2 \qquad \text{Eq. 2-8}$$

The volume relative uncertainty is mainly affected by the relative uncertainty of the sampling flow rate, as the relative uncertainty of the sampling duration is negligible (because the uncertainty associated with a time measurement - a few seconds - is very small compared to the sampling duration for a normal or heavy pathway, approximately 8 h). The uncertainty of the sampled volume is thus mainly affected by the sampling flow rate, which is measured both just before the beginning ($Q_{v,\ before}$) and just after ($Q_{v,\ after}$) the end of a pathway. The average of these two values is taken as the representative flow rate, and the uncertainty considered is the standard deviation, given the limited availability of only two data points.

The volume is then regulated by the temperature of 25°C, considering that the pressure during the experiments was always close to 1 atm (Eq. 2-9). Note that other standard temperatures, such as 0°C or 20°C, may also be used when dealing with air quality to be closer to ambient air conditions (Hernández-Castillo et al., 2014). As this work shall represent underground railway stations, it is chosen to express the gas volumes in the following conditions: 25°C, 1 atm, assuming air behaves as an ideal gas.

$$V[m^3] = \frac{V_{measured}[m^3] \times 298[K]}{T_{measured}[K]} \qquad \text{Eq. 2-9}$$

T: average temperature of the sampled air during the experiment [K].

2.6.1.3 Online PM measurement at reduced scale

Real-time size distribution measurements were performed using a TSI 3091 FMPS, which was used to count the number of particles depending on their electrical mobility diameters, between 5.6 nm and 560

nm, at a time resolution of 1 s and with a 32-channel size resolution. This instrument is equipped with a cyclone head (50% cut-off aerodynamic diameter = 1 µm) and operates at a sampled air flow rate of 10 L/min and a sheath air flow rate of 40 L/min. It relies on an electrical mobility measurement technique associated with a low-noise electrometer for particle detection (Beji et al., 2020). The FMPS is primarily used to measure fine and ultrafine airborne particles. In addition, the TSI® OPS model 3330 is designed to analyze fine and coarse particles, providing valuable data on larger aerosol particles. The OPS was used to measure the particle number concentration in the size range of 0.3 µm to 10 µm with up to 16 separate channels, at a sampling frequency of 1 Hz, using optical detection.

2.6.1.4 Summary of PM measurements at reduced scale

Table 2.9 presents a comprehensive overview of particle measurement methodologies employed at reduced scale. The table categorizes sampling techniques according to their sampling type, the measurement objective, and the analysis method used. High-frequency online instruments (1 Hz resolution) capture rapid changes in particle number distributions over defined diameter ranges (5.6–560 nm via FMPS and 0.3–10 µm via OPS). Filter holders are used to quantify and qualify the TSP, and perform microscopic observations via scanning electron microscopy (SEM). Impactors with multiple stages (PTFE and Quartz) enable detailed size-resolved mass and composition analysis, including metals inductively coupled plasma mass spectrometry (ICP-MS) and atomic emission spectroscopy (AES) and carbon fractions Organic Carbon (OC)-Elemental Carbon (EC). This structured approach ensures a full-spectrum characterization of both the physical (size, number, mass) and chemical (metals, carbon) properties of PM.

Table 2.9 Summary of particle measurements at reduced scale

Type of sampling	**Aim**	**Analysis technique**
Online (1 Hz)	Number size distribution of particles with an electric mobility diameter between 5.6 to 560 nm	FMPS
Online (1 Hz)	Number size distribution of particles with an optical diameter between 0.3 to 10 µm	OPS
Filter holder 47 mm-**PTFE**	Mass concentration of TSP	gravimetry
	Quantification of metals in TSP	ICP-MS, ICP-AES
Filter holder 25 mm-**Polycarbonate**	Microscopic observation of particles	SEM-EDS
3 stage impactor - **PTFE**	Mass size distribution per aerodynamic size (4 classes)	gravimetry
	Metal mass size distribution per aerodynamic size (4 classes)	ICP-MS, ICP-AES
3 stage impactor - **Quartz**	Quantification of particulate carbon in the backup filter	OC-EC thermo-optical analysis
14 stage impactor - **PTFE**	Mass size distribution per aerodynamic size (14 classes)	gravimetry
	Metal mass size distribution per aerodynamic size (14 classes)	ICP-MS, ICP-AES

2.6.2 Experimental set-up for VOC measurements at reduced scale

2.6.2.1 Off-line VOC measurement at reduced scale

VOC sampling was carried out in order to conduct detailed laboratory analyses of the various chemical species. To this end, two active sampling techniques were used: DNPH-Silica cartridges (Waters Sep-Pak) and Tenax tubes TA (MARKERS international). The DNPH-Silica cartridge is aimed to collect aldehydes and ketones which react with 2,4-dinitrophenylhydrazine (DNPH) to form hydrazone derivatives. In the laboratory, the hydrazones are eluted from the cartridge with acetonitrile, then separated and quantified by high-pressure liquid chromatography with ultraviolet detection (HPLC-UV). The Tenax TA tubes contain an adsorbent, with a specific surface area of about 35 m^2/g, to trap VOCs. In the laboratory, the adsorbed VOCs are removed from the tube by thermal desorption followed by gas chromatography with tandem flame ionization detection and mass spectrometry (TD-GC-FID-MS) analysis. Offline VOC sampling flows have been set at 1 L/min for both techniques. A mass flow controller or a critical orifice controls the flow. The sampling duration typically varies according to the length of the pathway, which is usually around 8 h.

2.6.2.2 Online VOC measurement at reduced scale

- Photoionization Detector (PID)

A portable PID was used to detect total VOCs in air samples. It works by using ultraviolet light to ionize the gas molecules, producing ions that can be measured to determine the concentration of the target compounds. Only compounds with ionization energies (IE) equal to or below that of the lamp energy can be detected. I**sobutylene** is most commonly used for the calibration of a PID. This compound is selected because it has a well-known ionization potential, making it a reliable standard to calibrate the detector. The PID's response to other VOCs is then expressed relative to its response to isobutylene. In this set-up, a ppbRAE 3000+ (Honeywell) PID was used with a 10.3 eV lamp, and a sampling flow rate of 0.5 L/min, able to detect VOC from 1 ppb with a time resolution of 3 s. As several compounds from different families of VOC (such as aromatics, alkenes, ketones, alcohols…) can be detected, the PID is said to measured “total VOC”.

- Proton Transfer Reaction-Quadruple interface-Time of Flight-Mass Spectrometer (PTR-Qi-ToF-MS)

PTR-Qi-ToF-MS (IONICON) is an analytical technique based on chemical ionization through proton transfer. It is composed of three main parts: the ion source, the drift tube, and the ion detection system (Figure 2.17). The ion source consists of a hollow-cathode discharge source, where water vapor produces H_2^+, H^+, and O^+ ions, which further react with water molecules to form H_3O^+. A proton transfer reaction occurs between H_3O^+ ions and the emitted VOC. This ionization occurs only if the proton affinity of the compound is higher than that of water (166.5 kcal/mol). The ion detection system accelerates ions through an electric field and then separated according to their masses (the heaviest ion reaches the lowest speed).

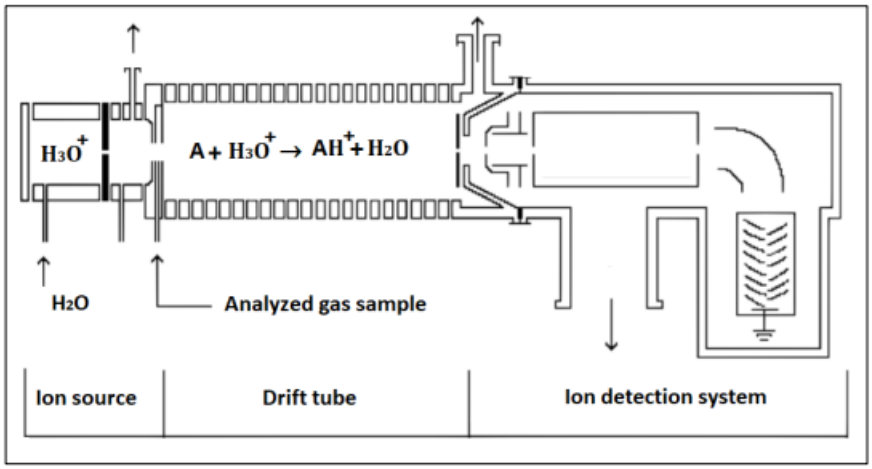

Figure 2.17 Simplified diagram of PTR-MS (adapted from Amann et al., 2010)

To prevent the potential entry of particles during the long sampling duration, four filters were implemented prior to the PTR-MS, as shown in Figure 2.18. In addition, a non-continuous measurement was employed to protect the instrument from further accumulation. The selected measurement periods were based on temperature conditions, specifically targeting times when the temperature is at its highest with notable variation. Identical stops were maintained across all three round trips for comparability. Additionally, data collection focused on the final approximately 20 braking events of each outbound and return trip. During periods when sampling from the enclosure was not performed, the PTR-MS was instead sampling from the gas calibration unit (GCU), which provided clean air for baseline measurements.

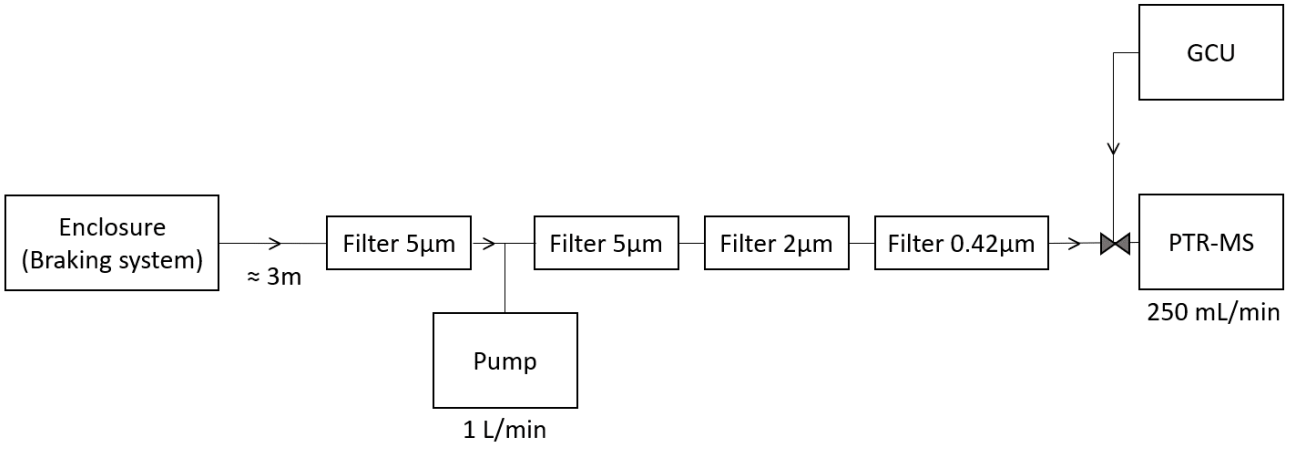

Figure 2.18 PTR-MS set up during sampling

Since a direct cable connection was not available to synchronize the force and speed signals with the PTR-MS—as is typically done for PM measurements using FMPS and OPS—a manual synchronization approach was adopted. This involved aligning the onset of braking events with the initial rise in VOC signals. This method assumes that VOC emissions begin concurrently with braking; however, it is important to consider that the PTR-MS may experience a slight delay of 1-2 s (Appendix 1) due to the dead volume between the emission zone and the instrument (response time of PTR-MS <100 ms according to the manufacturer). We estimate the accuracy of this manual synchronization to be within approximately one second.

2.6.2.3 Summary of VOC measurements at reduced scale

The following table (Table 2.10) summarizes the various VOC measurements carried out at reduced scale.

Table 2.10 Summary of VOC measurements at reduced scale

Type of sampling	**Aim**	**Analysis technique**
DNPH cartridges	Carbonyl compounds (C=O)	HPLC-UV
Tenax tubes	Hydrocarbons (CmHn) and other VOCs	TD-GC-FID/MS
Online (1 Hz)	VOCs	PTR-MS
Online (1 Hz)	Total VOCs	PID

2.7 Experimental set-up for PM and VOC measurement at full scale

At full scale, the sampling and measurement systems were installed in the horizontal outlet duct, where air exits from the dynamometer cabin, using the location of an existing inspection hatch at 1.55 m from the cabin wall (Figure 2.19).

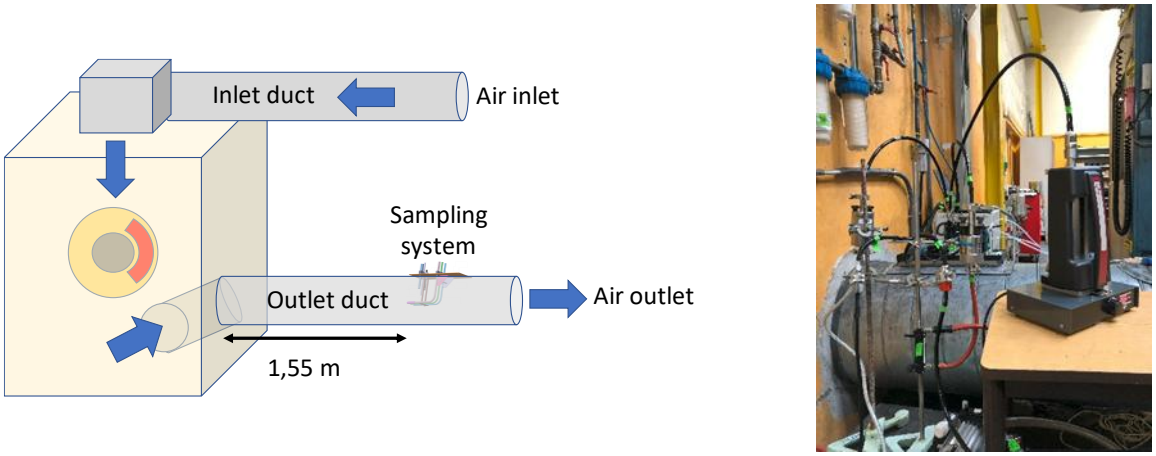

Figure 2.19 Position of the sampling system in the dynamometer facility at full scale.

A tailored hatch was designed for the measurement campaign in 2022, including three stainless steel isokinetic nozzles for PM sampling (Table 2.11), a port for VOC sampling, and locations for different sensors measuring temperature, humidity and air speed.

Table 2.11 Isokinetic PM sampling in the full-scale experimental set-up.

Full-scale set-up in 2022	Diameter [mm]	Flow rate [L/min]	Speed [m/s]	Connected instruments
Outlet duct	560	103446	7	Temperature, humidity, air speed, PID, VOC sampling port
Nozzle 1	5.5	10	7.02	FMPS
Nozzle 2	9.5	30	7.05	One 14-stage impactor, two 47-mm filter-holders
Nozzle 3	13.4	60	7.09	Two 3-stage impactors

An exploded view of the assembly is presented in Figure 2.20, showing the isokinetic nozzles facing the air flow and the instrumentation which was the same as for the experiments at reduced scale.

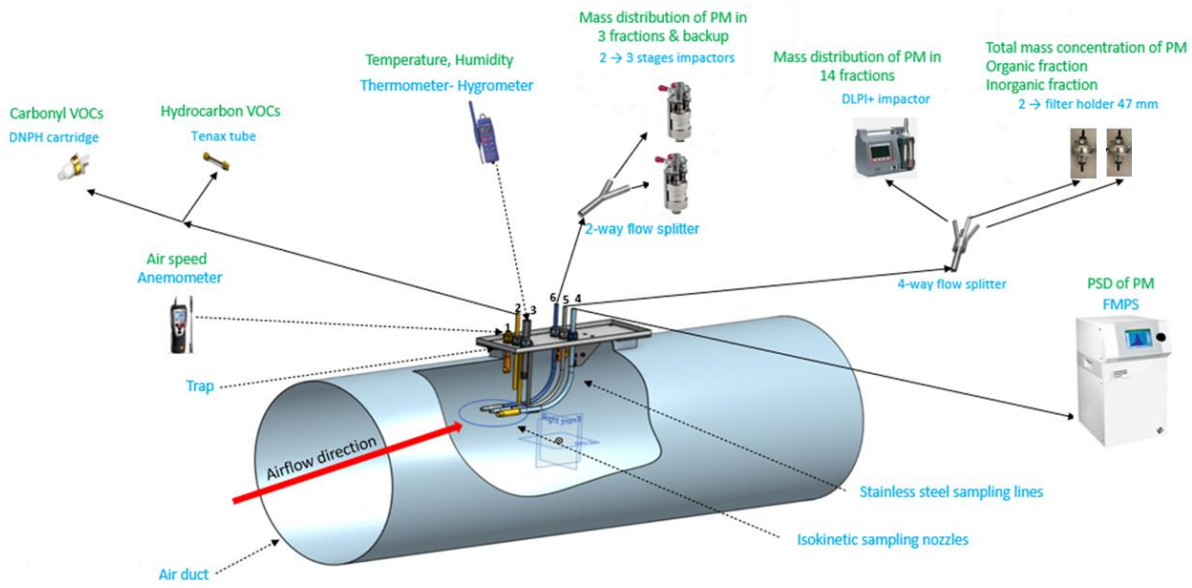

Figure 2.20 Full scale emission measurement instrumentation

2.8 Offline analytical techniques and procedures

2.8.1 Elemental analysis of particles by ICP-MS and ICP-AES

2.8.1.1 Experimental methods

Brake particles collected on filters were digested by an acid mix in a microwave oven (Ethos TC, Milestone) in acid-cleaned Teflon reactors using a two-stage temperature increment over a 30-min-long procedure reaching a 220°C plateau. The acid digestion mixture (2 mL HNO_3 (67%), 100 µL HF (47%)) was optimized to quantitatively mineralize a large set of major and minor elements (35) without significant contamination or loss. In addition, 1 mL of H_2O_2 is used to dissolve any organic matter. Two powder standard reference materials provided by the National Institute of Standards and Technology (NIST): NIST SRM 1648a and SRM 2584, with certified metal contents, were used to verify that the acid digestion procedure was quantitatively effective, except for Ba, which was reported as an element of "potential interest to users" in the NIST SRM 2584. The digests were then transferred to clean polypropylene tubes (all appliances were

cleaned by 4% HNO_3 acid during 24 h, followed by ultra-pure water 3 times) and diluted to 50 mL with high-purity de-ionized water (resistivity > 18×10^6 Ωm). The solubilized elements were analyzed by ICP-AES (Thermo iCAP 7000) and ICP-MS (PERKIN NexION 300). The concentrations were measured for the following elements: Al, Ba, Ca, Fe, K, Mg, Na, P, S, Si, Sr and Ti (ICP-MS/AES), Ag, As, B, Be, Bi, Cd, Ce, Co, Cr, Cs, Cu, Ge, Hf, La, Li, Mn, Mo, Ni, Pb, Pd, Pt, Rb, Ru, Sb, Se, Sn, Sr, Te, Th, Tl, U, V, W, Zn and Zr (ICP-MS following an optimized procedure (Alleman et al., 2010)). An internal standard (Ga/Rh/In isotope chosen not to be disturbed with another metal) has been added in all standards, blanks, and samples at a known concentration to monitor the drift in the ICP-MS signal due to plasma instability and sample cone clogging.

The terms "major" and "minor" elements refer to internal procedural categorizations rather than the absolute concentrations found in the NIST-certified reference materials. These designations correspond to different analytical programs: ICP-AES and ICP-MS, each optimized for different calibration ranges. Elements present in concentrations sufficient to be quantified by both techniques were measured using both methods to cross-validate results and identify any analytical inconsistencies. Eventually, for each element, the values reported were selected from the method that demonstrated the most reliable performance, based on a set of quality control criteria including blank levels, detection limits, and recovery rates from the NIST reference materials.

2.8.1.2 Validation of the analytical method

- Validation of the mineralization protocol using certified reference materials:

In order to verify the efficiency and homogeneity of microwave acid digestion for low particle quantities, acid attacks were also performed on certified reference materials (CRM) of urban particles (NIST SRM 1648a) and indoor dust (NIST SRM 2584). The recovery rate calculated using Eq. 2-10 corresponds to the ratio between the concentration determined by the method implemented and that certified in the CRM.

$$Recovery\ [\%] = \frac{Method\ concentration}{Certified\ concentration} \times 100 \qquad \text{Eq. 2-10}$$

The recovery rates of the elements analyzed and validated on different CRM (n=9) are, in general, close to 100% except for Si: (73.0±4.2)% and S: (275.1±5.5)% (Appendix 3). For some elements, the standard deviations were higher than expected, partly because the reported NIST reference values originate from different analytical sessions, which increases the variability of the measurements. It should also be noted that the mass of NIST powder used in these assays was lower than the mass recommended in the certificate, which may have contributed to the increased uncertainty in the results.

- Evaluation of blanks and limits of detection & quantification

The limit of detection (LD) is defined as the minimum detectable concentration considering the background level and the noise, while the limit of quantification (LQ) is the lowest analyte concentration that can be quantitatively detected with a stated accuracy and precision. The calculations are according to Eq. 2-11 and Eq. 2-12:

$$LD_i = 3 \times SD_{i,blank}$$ Eq. 2-11

$$LQ_i = 10 \times SD_{i,blank}$$ Eq. 2-12

in which:

LD_i: Limit of detection of species i in the braking system [ng/filter].

LQ_i: Limit of quantification of species i in the braking system [ng/filter].

$SD_{i,blk}$: Standard deviation of the repeated measurements of the concentration of species i in the blank filter [ng/filter].

The detection limits of 47 mm filters varied between 0.03 ng/filter for Be and U and 9 µg/filter for Fe. While for 25 mm filters, the detection limits vary between 0.1 ng/filter for Th and U and 1.2 µg/filter for Ca (Appendix 4).

The quantification limits of 47 mm filters varied between 0.1 ng/filter for Be and U and 30 µg/filter for Fe. While for 25 mm filters, the quantification limits vary between 0.02 ng/filter for Th and U and 4 µg/filter for Ca (Appendix 4).

- Evaluation of the method: accuracy and intermediate precision

Accuracy was assessed using the recovery rate (% of the amount of analyte measured compared to the amount of analyte actually present) of the **quality control (QC) solutions**. The standard deviations of repeatability (Srept, n=9) and internal reproducibility (Srepr, n=35) were calculated to estimate the precision (Feinberg, 2012). To express the performance of the method, the coefficients of variation for the repeatability ranged from 2.6% (Al) to 22.5% (Ca), and those of intermediate precision (internal reproducibility) from 2.0% (Na) to 26.1% (Ca) (Appendix 5).

- Estimation of elemental concentration uncertainty

Measurement uncertainty can arise from several sources, including sampling, matrix effects and interferences, environmental conditions, inaccuracies in measurement, sampling, or weighing devices, the solution preparation step, and operator variability (EURACHEM/CITAC 2000). To estimate the overall uncertainty, it may be necessary to evaluate each source of uncertainty individually to determine its contribution. Each separate contribution to the overall uncertainty is referred to as an uncertainty component. Figure 2.21 presents a simplified Ishikawa (5M) cause-and-effect diagram, commonly known as a 'fishbone' diagram, which lists and illustrates the sources of uncertainty. This diagram highlights not only the uncertainties associated with specific elements but also the overall performance of the method, such as precision and accuracy, as well as uncertainties related to sampling volume and potential contamination.

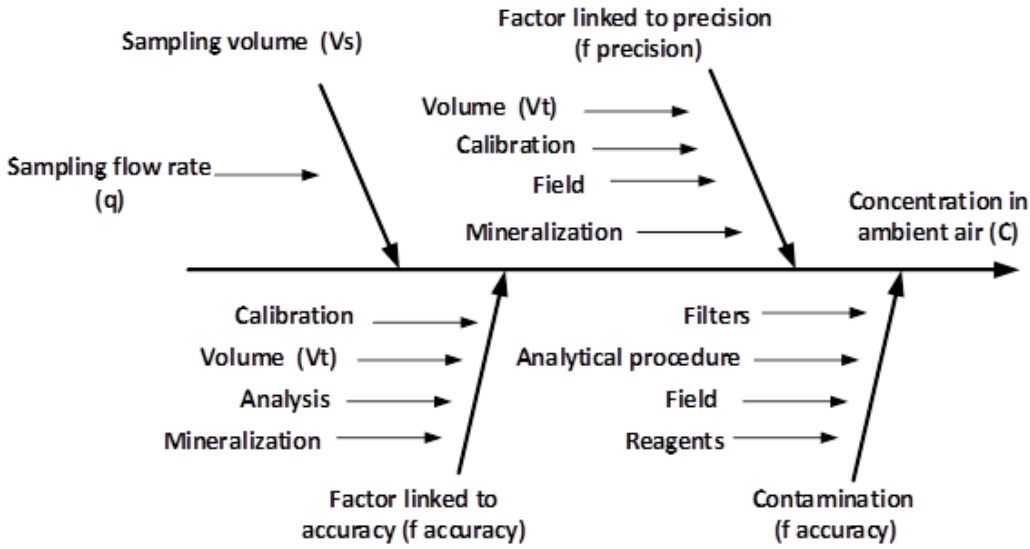

Figure 2.21 Simple cause and effect diagram to identify factors related to accuracy and precision (Lamaison 2006)

The estimate of the standard uncertainty of accuracy ($u_{accuracy}$) was calculated from the repeated measurements (n=9) of **certified reference materials (CRM)** according to Eq. 2-13:

$$u_{accuracy} = \sqrt{u_{CRM}^2 + u_{bias}^2} = \sqrt{u_{CRM}^2 + \frac{SD_{bias}^2}{n_{bias}}} \qquad \text{Eq. 2-13}$$

where u_{CRM} is the uncertainty associated with the mean of the results for the measured quantity, as provided by the supplier of the Standard Reference Material (SRM 1648a), whereas n_{bias} is the number of measurements (n=9), and SD_{bias} is the standard deviation of the mean of these n measurements on SRM obtained during our laboratory analysis.

The overall precision of the method accounts for all random effects that influence the measurement. Precision should be estimated, whenever possible, over an extended period. In this study, we choose to evaluate precision based on analytical reproducibility. The standard uncertainty associated with precision is calculated from the recovery rates of the QC samples by dividing the standard deviation of the measurements $SD_{reproducibility}$ by the square root of the number of measurements $n_{reproducibility}$ as shown in Eq. 2-14:

$$u_{precision} = \frac{SD_{reproducibilty}}{\sqrt{n_{reproducibilty}}} \qquad \text{Eq. 2-14}$$

The sampling volume v_s is expressed as a function of the airflow rate (q) and the sampling time. The uncertainty associated with the sampling time is negligible. A maximum drift of 5% is tolerated for the flow rate. Considering that the flow rate has a rectangular distribution (Lamaison, 2006), the uncertainty on the sampling volume is given by Eq. 2-15:

$$u_q = u(v_s) = \frac{1}{\sqrt{3}} \times \frac{q \times 5}{100} \quad \text{Eq. 2-15}$$

For sampling flow rates of 30 L/min (3-stage impactor), u_q is estimated at 0.87 L/min, and for 10 L/min (14-stage impactor and filter holder), u_q is estimated at 0.29 L/min, giving the relative uncertainty on the volume of 2.9% regardless of the element.

The uncertainty related to filter contamination ($u_{contamination}$) is determined from the median of the results obtained on the field blanks (FB), denoted as u_{FB}. These field blanks are measured in the same enclosure setup where the experiments are conducted, but without performing any actual tests, using Eq. 2-16. The uncertainty u_{FB} accounts for background contamination introduced by the sampling environment or materials. It is divided by 2 assuming a uniform distribution of contamination, which is a standard approach when no specific bias is expected.

$$\mathrm{u_{contamination}} = (\frac{\mathrm{u_{FB}}}{2}) \quad \text{Eq. 2-16}$$

The contamination uncertainty is divided by the square of the concentration to account for the comparison between blank measurements and test sample concentrations. This approach reduces the relative impact of blank uncertainty, particularly at higher concentrations, improving the reliability of the reported values.

In this step, the relative combined standard uncertainty is introduced. The use of relative standard uncertainties (denoted by the subscript r) allows normalization of the uncertainty contributions with respect to the measured concentration C. Thus, the combined standard uncertainty u(C) is estimated by applying the uncertainty propagation law calculated using Eq. 2-17:

$$u(C) = C \times \sqrt{u_{r\,CRM}^2 + \frac{SD_{r\,bias}^2}{n_{bias}} + \frac{SD_{r\,reproducibility}^2}{n_{reproducibility}} + u(v_s)^2 + \frac{u_{contamination}^2}{C^2}} \quad \text{Eq. 2-17}$$

All uncertainties are initially evaluated as percentages. However, since they are multiplied by the concentration, the resulting unit becomes ng/m³**,** scaled by a factor of 1/100 due to the percentage conversion. This ensures that the final uncertainty values remain consistent with the concentration units while accounting for relative variability.

The expanded uncertainty U defines an interval in which the measured value is estimated to lie with a higher level of confidence. It is obtained by multiplying the combined uncertainty by a coverage factor k

(Eq. 2-18). The choice of factor k depends on the desired level of confidence. For an approximate confidence level of 95%, k is taken as 2 (EURACHEM/CITAC 2000).

$$U = k \times u(C) \text{ with } \mathrm{k} = 2 \qquad \text{Eq. 2-18}$$

2.8.1.3 Estimation of the chemical speciation of the elements

Table 2.12 shows a simplified list of possible metal oxides and metal sulfate species likely to be present in the pad, in an attempt to perform the mass closure. These species were selected based on the literature related to the composition of organic pads used in railway braking and XRD analyses of particulate emissions (Grigoratos & Martini, 2015).

Table 2.12 Oxide forms, molar masses, and conversions used for metal-to-oxide calculations

Metal	Metal molar mass [g/mol]	Probable species used for calculation	Metal species molar mass [g/mol]	Other forms (not used)
Al	53.96	Al_2O_3	101.96	
Ba	137.33	$BaSO_4$	233.38	BaO
Ca	40.09	CaO	56.08	
Cr	103.98	Cr_2O_3	151.99	$Cr(OH)_3$
Cu	63.55	CuO	79.55	Cu_2O, $CuCO_3$
Fe	111.70	Fe_2O_3	159.69	FeO, Fe_3O_4
Mg	24.31	MgO	40.30	
Mn	54.94	MnO	70.94	
Sr	87.62	SrO	103.62	
Ti	47.87	TiO_2	79.87	

The weight content of the metal oxide is estimated by multiplying the metal content by a conversion factor as shown in Eq. 2-19:

$$\text{Metal oxide } [\mu g/g] = \text{Metal } [\mu g/g] \times \frac{\text{Metal species molar mass } [g/mol]}{\text{Metal molar mass } [g/mol]} \qquad \text{Eq. 2-19}$$

Based on the simplified speciation of Table 2.12 and on a carbon content of 271 µg/mg (Table 2.3), the sum of the oxide or sulfate metallic species (542 µg/g) and of the carbon accounts for approximately 81% of the pad total mass. The remaining mass is likely attributable to silicon-containing compounds. While wollastonite ($CaSiO_3$) was identified through its X-ray diffraction pattern (Appendix 6), the full calcium and silicon content cannot be solely attributed to this phase. Other detected phases, such as clays (aluminosilicates), may also contribute, possibly containing additional elements like aluminum. Therefore,

calcium and silicon were not systematically combined as $CaSiO_3$ in the metal-to-oxide conversion for mass closure, to avoid oversimplifying the speciation.

It is assumed that all the elements in the emitted particles are in an oxidized form as done for the pad previously. For emitted particles, based on Transmission electron microscopy (TEM), Kukutschová et al., (2011) detailed that Fe is present in different oxide forms depending on size fractions. Fe dominated the metallic content in both the fine and coarse fractions. TEM analysis revealed the presence of maghemite (γ-Fe_2O_3) and magnetite ($FeO,\cdot Fe_2O_3$) in the nanoparticle fraction, while maghemite, magnetite, and hematite (α-Fe_2O_3) were identified in the fine fraction. Since Fe is a dominant metallic component in both supermicronic and submicronic fractions (>60%) in our samples as well, its oxide form will affect the mass the most. Based on the comparison of oxygen content in different iron oxides (see Table 2.13), choosing either Fe_3O_4 or Fe_2O_3 would result in only minor differences in oxygen estimation, while FeO would yield a significantly lower value. Therefore, Fe_2O_3 was selected as a conservative and representative oxide form for Fe in the mass balance.

Table 2.13 Total oxygen percentage varying with iron oxide

Oxygen percentage	TSP filter			
	NP1	NP2	HP1	HP2
Fe_2O_3	18	24	24	24
Fe_3O_4	17	22	22	23
FeO	13	17	19	19

In the following results, the estimated contributions of oxygen and sulfur are separated from those of the metal oxides by subtracting the calculated oxide mass from the metal mass.

Since additional oxides listed in Table 2.13 may also form during the estimation process, they could contribute to the unknown fraction. This unknown fraction is calculated according to Eq. 2-20. It can mostly be attributed to the particulate carbon fraction not analyzed in the TSP. Particulate carbon may be present as black carbon (elemental carbon), particulate organic carbon, or semi-volatile organic compounds (SVOCs) condensed on particles. Other contributions are less probable. For example, water is not expected to be part of the unknown fraction, as the medium is relatively dry. And even though water can adsorb onto some components, the weighing is performed at the same humidity both before and after sampling. Therefore, the adsorption is assumed to be stable, and the influence of water on the mass is minimized. As for ions, the dominant species in this case is sulfate, which has already been accounted for in the mass closure by estimation.

$$\text{Unknown fraction} = \text{Total mass concentration} - (\text{metals} + \text{estimated oxygen \& sulfur}) \quad \text{Eq. 2-20}$$

2.8.1.4 Methodology of source apportionment based on the metal analysis of particles

One interesting question is to understand how much the different pathways (NP, HP) and the different pad designs influence the specific wear rates of the pad and the disc, and consequently, the emissions. To answer it, Frangieh (2025) made measurements of the respective volumetric loss of the pad and the disc, to assess their respective wear rates. For the same purpose, in this work, a method of source apportionment based on the mass conservation of metals, tracing either the pad or the disc, is proposed.

As many metals are conservative species under braking conditions (i.e. they remain in a solid phase), some metals may be considered, in an overall approach, as tracers of one of the first bodies, either pad or disc. These metal tracers may be defined as metals which are present only in one of the first bodies. In practical terms, the definition may be extended to metals which are present in very contrasting concentrations between the two first bodies. Knowing the metal composition of both first bodies (expressed by instance in µg of metal per mg of pad or disc), one may identify these possible metal tracers.

However, in the case of the pad which is a composite material made of several heterogeneous components (such as fibers, fillers, polymeric matrix), the metal tracers are not strictly representative of the overall pad wear, but rather on the wear of specific components of the pads. Similarly, the grey cast iron disc may also be considered as a heterogeneous material because the carbon it contains is in a different solid phase from the melt metals. Nevertheless, for long-lasting experiments with hundreds of braking events such as the Normal and Heavy Pathways, one may consider that the different rates of wear of the different components of the pad (or disc) are not distinguishable and tend towards an average rate of pad (or disc) wear.

Then, when considering the average chemical composition of particles emitted by mechanical friction of the first bodies and, accumulated for many braking events over a long period of time, each time a pad (or disc) metal tracer is found in the emitted braking particles (expressed by instance as µg of metal tracer per mg of emitted particles), it is possible to estimate, on average, the relative mass contribution of the pad (or disc) to the emitted particles. If no other source of the metal tracer is involved (such as metal tracer present in the background air), then the sum of the relative contributions of the pad and disc, estimated independently thanks to their respective metal tracers, should be equal to 1.

The following equations present the calculations which may be carried out.

- Eq. 2-21 of mass conservation of <u>any conservative metal</u> (not necessarily a tracer) in a 2-source (pad and disc) system:

[Mass (µg) of metal in 1 mg of emitted particles] = [Mass (µg) of metal from pad in 1 mg of emitted particles] + [Mass (µg) of metal from disc in 1 mg of emitted particles] Eq. 2-21

This equation can be applied to an element, which is present in both first bodies.

- Eq. 2-22 of mass conservation of <u>a metal tracer of the pad</u>, in a 2-source (pad and disc) system:

[Mass (µg) of metal tracer of pad in 1 mg of emitted particles] ≈ [Mass (µg) of metal tracer from pad in 1 mg of emitted particles] Eq. 2-22

Then, knowing the weight content of the metal tracer in the pad [Mass (µg) of pad metal tracer in 1 mg of pad], it can be written as Eq. 2-23:

[Mass (µg) of metal tracer from pad in 1 mg of emitted particles] = [Mass (µg) of pad metal tracer in 1 mg of pad]x[Mass of pad (mg) in 1 mg of emitted particles] Eq. 2-23

Therefore, the mass relative contribution of the pad to the emitted particles may be calculated by Eq. 2-24:

$$[\text{Mass of pad (mg) in 1 mg of emitted particles}] = \frac{[\text{Mass (µg) of pad metal tracer in 1 mg of emitted particles}]}{[\text{Mass (µg) of pad metal tracer in 1 mg of pad}]} \quad \text{Eq. 2-24}$$

This set of equations may be applied to pad metal tracers. However, the same calculations can be done for the disc metal tracers.

Finally, if the assumptions are fulfilled (the chosen metals are good tracers of one of the first bodies; there is no other source than the pad and the disc for the metals in the emitted particles; the differences between the averaged wear rates of the different components of the pad and disc are not significant) and, if the overall uncertainty of the sampling and the chemical analyses are not too large, then the sum of the relative contributions of the pad and disc should be close to 1.

$$[\text{Mass of pad (mg) in 1 mg of emitted particles}] + [\text{Mass of disc (mg) in 1 mg of emitted particles}] \approx [\text{1 mg of emitted particles}]$$

The closest the sum is to 1, the better is the validity of the metal tracers' method.

2.8.2 Thermo-optical analysis of particulate carbon

The organic carbon (OC), elemental carbon (EC), or the total carbon (TC = EC + OC) in particles were analyzed using an OC-EC Analyzer (Sunset Laboratory Inc., USA). The particles were collected on a quartz filter and a punch of 1.5 cm^2 was used for the particulate carbon analysis (Figure 2.22). The thermal and optical analysis is performed using the analytical protocol from the European Supersites for Atmospheric Aerosol Research (EUSAAR2), based on thermal optical transmittance.



Figure 2.22 Quartz filter (blank) showing the punch ready for carbon analysis

The results provided by the carbon analyser are expressed in mass of carbon per unit of filter surface area (e.g. µg C/cm^2). Then by multiplying this latter value by the total surface area of the filter, one can calculate the mass of carbon on the filter (Eq. 2-25).

$$C_C = \frac{m_C \text{ x Ar}}{\text{V}} \qquad \text{Eq. 2-25}$$

Where:
C_C: Concentration of carbon [µg C/m^3]
m_C: mass of carbon per area [µg C/m^2]
Ar: filter sampling area [m^2]
V: volume of sampled air [m^3]

One necessary condition to determine both OC and EC is to use a filter with an homogeneous deposition of particles on the quartz filter. The reason is that the carbon analyzer uses an IR laser to measure the unwanted formation of EC during the thermal degradation of the sample, in order to make a correction. But if the sample is not homogeneously covered by particles, then the laser may point on a non-representative location. When sampling particles by filtration, this homogeneity is achieved. On the contrary, when sampling particles by impaction, it is not the case. Figure 2.23 presents examples of filters sampled by the 3-stage impactor. It shows that the mass on stage 1 was very low (a), and stages 2 (b) and 3 (c) were sampled by impaction, getting spots of particles instead of a homogeneous deposit. Finally, unlike the other stages that rely on impaction, the backup filter (d) works as a filtration system by allowing air to pass through the filter, capturing particles homogeneously on the filter medium. The impacted particles on the stages 1 to 3 (a, b, and c) are not suitable to separate OC from EC. Since the OC-EC instrument uses a laser that detects a random spot on the filter, the result can vary depending on where the laser hits effectively a spot or not. Thus, the best filter to be analyzed by OC-EC is the backup filter with a homogeneous distribution of the particles.

(a) Stage 1 (b) Stage 2 (c) Stage 3 (d) Backup filter



Figure 2.23 Particles captured on filters using the 3-stage impactor with aerodynamic diameters of (a) >10 µm, (b) 2.6-10 µm, (c) 1-2.6 µm and backup filter <1 µm.

2.8.3 Microscopic observation of particles

The size and shape of individual particles were observed using a Hitachi S-4300SE/N scanning electron microscope (SEM) (Hitachi High-Technologies Corporation, Tokyo, Japan) operating in high vacuum mode.

Sample Preparation and Collection:

- Particulate samples were collected on 47 mm polycarbonate filters using a filter holder.
- A flow rate of 10 L/min was maintained during a single braking event for sample collection.
- Prior to SEM observation, samples were coated with a thin gold-palladium layer via sputtering.

The SEM was operated at accelerating voltages ranging from 5 kV to 15 kV, depending on the desired magnification and the selected observation mode (backscattered or secondary electrons).

2.8.4 Determination of volatile carbonyl compounds by HPLC-UV

This method provides procedures to determine carbonyl compounds in various matrices by derivatization with DNPH. The method utilizes HPLC with UV/vis detection to identify and quantify the target analytes (HPLC Ultimate 3000-UV). The column is an Acclaim™ RSLC Carbonyl has dimensions of 2.1×150 mm with Dionex Bonded Silica Products. Acetonitrile (53%) and ammonium acetate (47%) were employed as eluents for chromatographic separation (Detournay et al., 2011). This method includes two procedures for all aspects of the analysis (from the extraction to the determination of concentration). The carbonyls were extracted from DNPH cartridges using 3 mL of acetonitrile; the resulting eluate was separated on the chromatographic column and then detected by ultraviolet absorption. The results are obtained in the form of peak areas. They are interpreted into mass concentrations by internal standard calibration. The schematic diagram is presented in Figure 2.24.

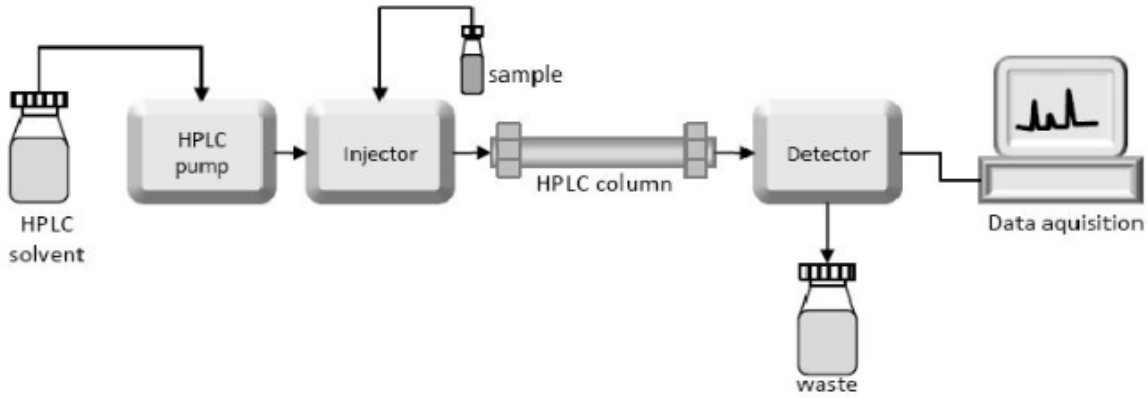

Figure 2.24 Schematic diagram of the High-Performance Liquid Chromatography (HPLC) system (Czaplicki, 2013)

2.8.4.1 Uncertainties

Uncertainties in VOC quantification using HPLC-UV were estimated according to an analytical study done in CERI EE lab (Y. Pachy, 2023) where the following factors were evaluated:

- Accuracy, through standard solution samples with a precisely known concentration of each analyte,
- Linearity, which is the direct proportionality between peak area and analyte concentration, demonstrated using a calibration curve for each analyte,
- Precision, through repeatability tests aiming at determining the difference in mass calculated between a group of samples of the same mass and injected on the same day,
- Reproducibility, aimed to measure the differences in area measurement of the same sample between days or weeks.
- Selectivity, which is the parameter that measures the good separation of peaks on the chromatograms,
- Blank, used to determine the mass of VOCs present in the blank analysis; it must not contain any traces of the VOCs being analyzed,
- Stability, which consists of measuring the possible degradation of solutions over time or the escape of VOCs due to their volatility from the trapping medium during storage.

Linearity of the response using standard solutions was the main source of uncertainty. Overall uncertainty varies from one VOC to another, depending on the optimization of the method in relation to the physicochemical properties of each compound.

2.8.4.2 Blank assessment

To assess the consistency of our blanks over different days (we selected 7 days before each test), we will compare these values. Additionally, to determine whether a 1-hour blank measurement is representative of our 8-hour tests, we will compare these results with a single 8-hour blank measurement.

Table 2.14 presents the limit of detection of HPLC/UV in addition to the detailed blank measurements.

The detection limit in terms of mass is determined by multiplying the volume of the eluted solution by the minimum detectable concentration specified by the HPLC manufacturer. This product gives the lowest measurable mass of analyte in the elution. To express this as an atmospheric concentration, the resulting mass is then divided by the total volume of air sampled, yielding the detection limit in $\mu g/m^3$.

From the 1-hour blank test, we detected the presence of several compounds (formaldehyde, acetaldehyde, propanone, propanal, MVK, MEK, pentanal, o-tolualdehyde, and hexanal) in both the inlet and outlet, where inlet represents the sampling point before the enclosure, while the outlet is the sampling point after the enclosure. The highest concentrations were observed for propanone and MEK. The high standard deviation suggests significant variability in the blank measurements. This could be attributed to the absence of system flushing between tests, leading to the accumulation of carbonyls within the system.

In comparison, the 8-hour blank test revealed a lower number of detected compounds. Only formaldehyde, acetaldehyde, and propanone were found in both the inlet and outlet, with only trace amounts of butanal, benzaldehyde, and hexanal in the outlet. This reduction in detected compounds over longer sampling durations could be due to the dilution effect. We measure all these VOCs at the beginning of a blank test, and as the blank duration increases, the sample volume increases while the amount of VOCs remains the same. This results in a significant decrease in both the number and concentration of detected carbonyls.

Table 2.14 LD of HPLC/UV for carbonyl compounds in air and detection in blank samples

Compound	Av ± SD [µg/m^3]				
	LD	1 h blank inlet	1 h blank outlet	8 h blank inlet	8 h blank outlet
Formaldehyde	0.01	0.18 ± 0.10	0.72 ± 0.27	0.06	0.63
Acetaldehyde	0.015	0.51 ± 0.35	0.99 ± 0.59	0.06	0.25
Propanone	0.015	29.92 ± 48.34	28.98 ± 39.02	0.31	2.36
Acrolein	0.01	<LD	<LD	<LD	<LD
Propanal	0.015	0.09 ± 0.05	0.14 ± 0.08	<LD	0.05
Methyl vinyl ketone (MVK)	0.02	4.77 ± 6.27	3.30 ± 4.51	<LD	<LD
Crotonaldehyde	0.015	<LD	<LD	<LD	<LD
Methyl ethyl ketone (MEK)/2-butanone	0.02	19.37 ± 34.57	14.29 ± 21.82	<LD	<LD
Methylpropenal (methacrolein)	0.02	<LD	<LD	<LD	<LD
Butanal	0.02	<LD	<LD	<LD	0.03
Benzaldehyde	0.025	<LD	<LD	<LD	0.04
Isopentanal	0.014	<LD	<LD	<LD	<LD
Pentanal	0.015	0.34 ± 0.13	0.26 ± 0.13	<LD	<LD
Glyoxal	0.02	<LD	<LD	<LD	<LD
o-Tolualdehyde	0.02	<LD	0.28± 0.14	<LD	<LD
m-Tolualdehyde	0.015	<LD	<LD	<LD	<LD
p-Tolualdehyde	0.015	<LD	<LD	<LD	<LD
Methylglyoxal	0.02	<LD	<LD	<LD	<LD
Hexanal	0.015	0.63 ± 0.24	1.15 ± 0.15	<LD	0.03
2,5-Methylbenzaldehyde	0.015	<LD	<LD	<LD	<LD

2.8.5 Determination of VOC by TD-GC-MS-FID

VOC emissions were collected on Tenax tubes under a constant flow rate of 1 L/min and analyzed in the lab using TD-GC-MS-FID (AGILENT 5975B inert MSD) (Figure 2.25), equipped with Rtx-5MS (5% diphenyl / 95% dimethyl polysiloxane) column. The analysis output is a chromatogram showing peaks with different areas at different retention times. The area of a peak is proportional to the quantity of the corresponding VOC. Gas chromatography was used to separate compounds. Coupled MS and FID allows the identification and quantification of different families of VOCs.

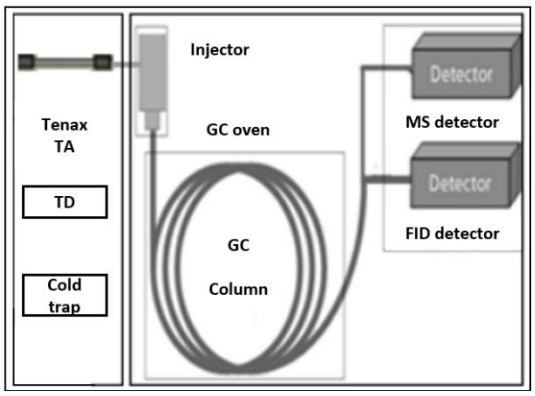

Figure 2.25 Schematic diagram of the TD-GC-MS-FID

In the thermal Desorption (TD) oven, the Tenax tube is heated to 290°C. This ensures that all the trapped VOCs are desorbed and transmitted by an inert carrier gas (Helium) into a cold trap. The cold trap cools at 5°C to recollect all the compounds. These first 2 steps take 10 min. Afterwards, the temperature increases to 300°C in a few seconds (flash desorption), and they are then ejected at the same time to the GC column through a transfer line at 300°C for separation by the carrier gas.
The retention time of compounds depends on their affinity with the stationary phase and the column temperature (boiling point). The column operates in an oven where the temperature gradient is optimized for separation based on the column's stability and the properties of the analyzed compounds (Table 2.15).

Table 2.15 GC oven temperature program

	Ramp rate [°C/min]	Temperature [°C]	Duration [min]
Initial state		60	3
Ramp 1	20	180	2
Ramp 2	5	300	5

At the exit of the column, the compounds are sent to the detectors: a capillary pipe to the MS for qualitative analysis (electron impact ionization and quadrupole mass spectrometer) and a second capillary pipe to the FID for quantitative analysis. The resulting MS spectra are used to identify compounds through a provided database (NIST).

2.8.5.1 Quantitative analysis

The ambient concentration C_i of a VOC i is related to the peak area A (FID chromatogram) by the following relationship (Eq. 2-26):

$$C_i = \frac{A_i}{k_i} \qquad \text{Eq. 2-26}$$

Where k_i is the response factor for compound i.
Therefore, calibration involves determining the response factor k for each compound to be quantified.

This paragraph proposes a reliable calibration method linked to a standard compound, allowing semi-quantitative to quantitative analysis through a single compound calibration.

2.8.5.2 Laboratory calibration

Since toluene was a common compound detected in the samples and commercially available in the lab, it was chosen as a reference. A standard solution was prepared, and several solutions were diluted with methanol as solvent. The toluene concentration of the diluted standard is noted as C_r. The response of an FID is proportional to the number of effective carbon atoms in the molecule (Tranchant, 1982). Thanks to this theory, it is possible to estimate the response factor k for all other compounds from that of toluene. The response factor k_i for a compound i detected on the FID is calculated according to Eq. 2-27:

$$k_i = \frac{A_r}{C_r \times n_r} \times \mathrm{n} \qquad \text{Eq. 2-27}$$

Where n_r and n_i are, respectively, the effective numbers of carbon atoms for the reference compound (toluene, $n_r = 7$) and compound i.

2.8.5.3 Blanks assessment

The blanks were done for 1 hour in the morning before starting the test; the following compounds were commonly detected in the blanks (inlet and outlet), and their average concentration along with the standard deviation (Av ± SD) is presented in Table 2.15.

Table 2.16 Compounds found in the 1-hour blanks

Compounds	Av ± SD [µg/m^3]
Hexamethylcyclotrisiloxane	0.83 ± 0.57
2,6-bis(1,1-dimethylethyl)-2,5-Cyclohexadiene-1,4-dione	2.95 ± 2.39
2,4-bis(1,1-dimethylethyl) Phenol	0.39 ± 0.20
N-butyl Benzenesulfonamide	22.26 ± 15.67

To evaluate the sufficiency of the 1-hour blank, a comparison was performed with an 8-hour blank, which matches the duration of both the normal and heavy pathways. This comparison will be conducted for both the inlet and outlet to evaluate any significant differences.

Figure 2.26 shows the comparison of the blanks. This figure shows two types of contamination: residuals from previous experiments and materials within the system itself. Contamination from previous experiments gradually decreases over time due to the continuous flushing of the system, which helps remove sticky compounds. Notable contaminants from prior experiments include 2,4-bis(1,1-dimethylethyl) phenol and 2,6-bis(1,1-dimethylethyl)-2,5-cyclohexadiene-1,4-dione, which are progressively eliminated as clean air runs through the setup. Conversely, contamination from the system itself tends to increase over time. The plastic tubing that connects the humidity center can release compounds such as N-butyl benzenesulfonamide, accumulating as experiments proceed.

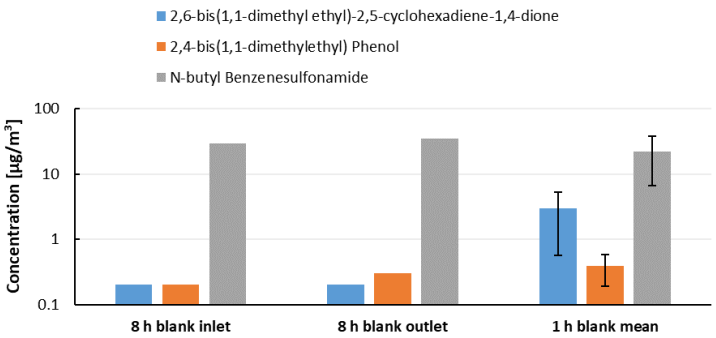

Figure 2.26 Concentrations of selected compounds in 8 h and 1 h blank samples

An appropriate VOC sampling methodology is essential for accurately distinguishing emissions from background contamination. The comparison between 1-hour and 8-hour blanks revealed time-dependent changes in compound levels due to residuals from prior tests and emissions from system components. To ensure reliable results, inlet measurements were always accounted for, allowing correction for baseline VOC levels measured by HPLC-UV and TD-GC-MS-FID.

2.8.6 Pad thermogravimetric analysis by TGA-FTIR

In this study, thermogravimetric analysis (TGA) was employed to characterize the materials by directly measuring their mass as a function of temperature and/or time. The TGA measurements were performed using a TGA/DSC1 instrument (Mettler Toledo, Switzerland), which was coupled with a V spectrometer (Nicolet iS20, Thermo Scientific) to enable simultaneous analysis of evolved gases. Experiments were conducted under controlled gas atmospheres, specifically using either 100% oxygen (O_2) or 100% nitrogen (N_2), with a constant gas flow rate of 60 mL/min and a heating rate of 10 K/min, ranging from ambient temperature to 1000°C. This setup ensured precise monitoring of thermal events and the identification of volatile products released during the thermal decomposition process.

Chapter 3: Effect of braking severity on emissions at the reduced scale bench

This chapter investigates the effect of braking severity on the emissions of particles and VOCs, based on tests conducted using a reference pad and a cast iron disc under normal and heavy braking conditions. It deals with:

- The consistency of PM and VOC emissions measured across different devices and test replicates.
- The average concentrations of PM and VOC emissions, including a detailed chemical characterization.
- The temporal dynamics of VOCs and their relationship with operating parameters.

3.1 Average emissions for the normal and heavy pathways

3.1.1 Average and maximum temperatures recorded during the normal and heavy pathways

The particle and VOC emissions are extremely impacted by multiple parameters, including thermal behavior at the contact interface (Frangieh et al., 2025). For that, temperatures during the experiments were continuously measured.

Table 3.1 presents the average and maximal temperatures of the airflow, measured inside the enclosure and in the outlet pipe (enclosure exit), as well as average and maximal pad and disc bulk temperatures, calculated from thermocouple measurements taken 2 mm beneath the friction surfaces. Airflow temperatures are higher at the exit than inside the enclosure because of the location of the enclosure thermocouple set relatively close to the inlet pipe and in the air flow passing through this enclosure. The rise is more noticeable when experiencing heavy pathways (HP 1 & HP 2, rise of about 15°C on average) compared to normal pathways (NP 1 & NP 2, rise of about 1 to 2°C on average). This is mainly due to higher heat dissipation during powerful braking operations. This result shows the influence of operational intensity on temperature dynamics, consistent with pad and disc temperature rises, which will be further interpreted based on TGA results.

Table 3.1 Average and maximal temperatures for normal (NP) and heavy pathways (HP)

Location	Temperature [°C]	NP 1	NP 2	HP 1	HP 2
Enclosure	Average	32	33	40	39
	Max	41	36	77	47
Enclosure exit	Average	34	34	54	54
	Max	37	38	63	63
Pad	Average	41	41	103	107
	Max	53	53	148	148
Disc	Average	51	51	136	137
	Max	65	66	218	215

3.1.2 Average mass concentrations of Total suspended particles (TSP), sampled using filtration and impaction, during the normal and heavy pathways

3.1.2.1 TSP average mass concentrations of replicates across different sampling supports

Table 3.2 shows the TSP mass concentrations found for replicates of NP and HP using different particle sampling devices. For the normal pathway (NP), the filter holder measurements showed that NP2 had about 17% lower particle concentration than NP1. This trend was confirmed by the 3-stage impactor with backup filter, which indicated a 15% decrease in NP2 compared to NP1. However, data from the 14-stage impactor for NP2 were unreliable due to sampling issues.

Table 3.2 Mass concentration in [µg/m3] by the three sampling methods (Filter Holder, 3-stage, and 14-stage impactors) across four test scenarios (NP1 and NP2 in blue, HP1 and HP2 in orange)

Test	FH	3-stage	14-stage	Av ± SD	CV %
NP 1	185 ± 7	168 ± 3	172 ± 3	175 ± 9	5
NP 2	154 ± 1	142 ± 3	NA	148 ± 9	6
HP 1	2030 ± 51	1716 ± 157	1233 ± 177	1660 ± 402	24
HP 2	2038 ± 47	1524 ± 75	1029 ± 233	1530 ± 505	33

For the heavy pathway (HP), the filter holder results showed similar concentrations for HP1 and HP2. The 3-stage impactor revealed that HP2 concentrations were 11% lower than HP1, while the 14-stage impactor showed a 17% decrease in HP2, though with increased uncertainty due to necessary mass corrections on certain stages. Overall, the heavy pathway emitted 6–11 times more mass than the normal pathway, depending on the sampling method.

Among the measurement methods shown in Table 3.2, the filter holder recorded the highest values, especially during HP, due to its reliance on filtration as a sampling technique and the collection onto one simple filter. In contrast, the 3-stage and 14-stage impactors utilize impaction for sampling with many filters in series. The TSP mass concentrations measured by the FH are consistently higher than those obtained using the 3-stage and 14-stage impactors. This discrepancy can be explained by two assumptions.

First, both the 3-stage and the 14-stage impactors have an inlet designed to prevent large particles from entering the sampling line. However, this design can also promote particle deposition on the inlet surface and on the internal walls of the systems, increasing the risk of particle loss compared with the FH, which does not have any inlet (Von Der Weiden et al., 2009).

Second, the pressure drop across the sampling devices significantly affects the retention of semi-volatile compounds. Pressure drop measurments are shown in Table 3.3; the 3-stage impactor, with a backup filter, has a much higher pressure drop (538 mbar) compared to the FH (81 mbar). This higher pressure drop promotes the volatilization of semi-volatile compounds, reducing the likelihood of their condensation or adsorption on the filter medium. As a result, more semi-volatile material is likely to be captured in the FH, contributing to higher observed TSP concentrations.

Table 3.3 Pressure drop across all sampling supports

Sampling support	FH	3-stage		14-stage
		without backup	with backup	
Pressure measured in the inlet (bar)	1.004	1.016	1.016	1.016
Pressure measured in the outlet (bar)	0.923	0.812	0.478	0.025
Pressure drop (bar)	0.081	0.204	0.538	0.991
Pressure drop (%)	8%	20%	53%	97.5%

The 14-stage impactor presents an additional limitation due to the absence of a backup filter. Without this filtration stage, semi-volatile compounds condensing on fine particles are more likely to be lost, especially under high-pressure drop conditions. Consequently, this configuration further underestimates the actual TSP mass.

Moving forward, this mass difference is primarily attributed to the volatilization of semi-volatile compounds. This interpretation is supported by findings from Eckenberger et al., (2025) , who compared various sampling methods. Given that some filters in the 14-stage impactor were overloaded, reliance was placed on the results from the 3-stage impactor. The observed difference between the filter holder and the 3-stage impactor corresponds to 314 µg/m³ for HP1 and 514 µg/m³ for HP2, suggesting that semi-volatile compounds contribute approximately 15–25% of the total particle mass emissions.

Additionally, during the HP, which emits more particle mass, there is an increased risk of errors in the mass size distribution due to overloading of some stages of the cascade impactors. First, particle bouncing may occur during sampling, giving wrongly more mass to a subsequent stage, that is to say to a smaller size fraction. This can occur up to the backup filter, leading to an overestimation of the mass of the smallest particle size fraction. In the case of the 14-stage impactor, the absence of a backup filter fails to capture particles that bounce off overloaded filters, leading to additional losses that weaken the reliability of the measurements. Secondly, an overloaded filter is difficult to handle for weighing because particle detachment may occur during the manipulation of the filter, decreasing the weighed mass.

Conversely, if the mass is too low (close to the detection limits), especially during the NP for the 14-stage impactor (Appendix 7), the confidence in the cumulative mass measurement is very low. The handling and manipulation of these many filters increase the possibility of contamination (contamination may be of the same order of magnitude as the particle mass), thereby introducing greater uncertainty into the results due to the involvement of multiple filters (14 in total).

In summary, the experiments were repeatable, even with the possible sources of error mentioned earlier. Additionally, there was a clear and important difference between NP and HP.

3.1.2.2 Mass size distributions for NP and HP

In the last paragraph, the discussion on the various sources of error allowed us to confirm that our sampling methods gave significant results. Nonetheless, these sources of error have to be kept in mind when interpreting the following results given by the 14-stage impactor.

Figure 3.1 presents the mass size distributions of the particles for NP and HP based on the mass concentrations determined for each stage of the 14-stage impactor. The size distributions are almost

unimodal with a mode in the range of 0.94-1.62 µm for the normal pathway and similar results for HP with a wider range between 0.6 and 3.64 µm (due to the overloading of some filters).

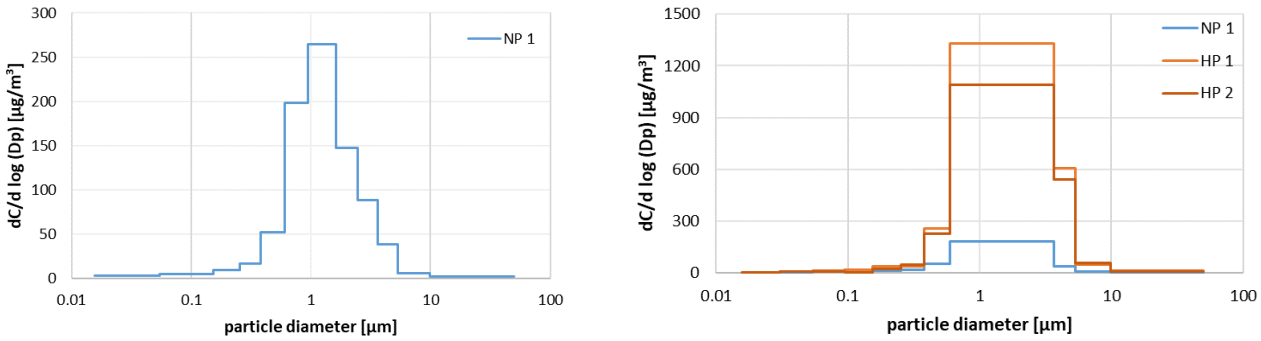

(a) (b)

Figure 3.1 Mass size distribution of the emitted particles for the normal pathway (a), and (b) superimposition of the normal and heavy pathway using a reference pad and the cast iron disc

It is important to note that the Gaussian curves characterizing these distributions are defined by their peak position and width. Ideally, the width is assessed at half the maximum height; however, due to limitations in our data, particularly the inability to capture the full peak height, we are likely underestimating the height and consequently overestimating the width. Therefore, while the apparent size range extends from 0.6 up to 3.64 µm, the true distribution is likely narrower than this, though precise quantification is constrained by the data available.

The results are similar to other findings from a cast iron disc against an organic pad on a pin-on-disc tribometer with a peak around 2-3 µm (Lyu et al., 2024). Moreover, an estimated wear debris average density of 5000 kg/m^3 (consistent with the fact that most particles are probably iron oxides) was used to calculate the aerodynamic diameter by Sanders et al. and Wahlström et al., who noted a maximum peak in particle size distribution at a particle diameter of approximately 1 µm for both low metallic and non-asbestos organic brake pads against a grey cast iron disc, conducted on a dynamometer test stand . (Sanders et al., 2003; Wahlström et al., 2010)

Following the analysis of the average PM and VOC emissions under both braking pathways, the following section focuses on the physico-chemical characterization of the pad and disc materials. This characterization provides essential context for interpreting the emission profiles, as the material composition directly influences both particle generation and the types of organic compounds released during braking.

3.1.3 Physico-chemical characterization of the pad and disc materials

3.1.3.1 Chemical analysis of pad and disc by ICP-MS/AES

A piece of the organic composite pad and a cast iron disc, both of which had not undergone any braking tests, were drilled and ball-milled into a powder to facilitate acid digestion prior to ICP analysis.

The elemental analyses for both pad and disc were first tested for 43 metals; however, 28 of them were below detection limits: Ag, As, B, Be, Bi, Cd, Ce, Co, Cs, Ge, Hf, La, Li, Mo, Ni, Pb, Pd, Ru, Sb, Sn, Te, Th, Tl, U, V, W, Zn, Zr. Also, 5 light elements that were affected by interferences and high measurement uncertainties in ICP-MS/AES could not be considered: K, Na, P, S, Si. Therefore, we selected a list of 10 elements well analyzed in this technique: Al, Ba, Ca, Cr, Cu, Fe, Mg, Mn, Sr, Ti.

Table 3.4 shows the pad and disc composition of the main elements analyzed by ICP-MS/AES. Some elements (Fe and Ca) were measured after a 500x dilution, and the others after 50x or 10x dilutions, depending on the concentrations in the samples.

Table 3.4 Pad and disc weight content of elements analyzed by ICP-MS/AES

	Organic pad [µg/mg]	Cast iron disc [µg/mg]
Al	13.91 ± 0.31	0.01 ± 0.004
Ba	68.76 ± 4.82	0.004 ± 0.001
Ca	82.90 ± 1.36	0.07 ± 0.03
Cr	0.06 ± 0.02	4.06 ± 0.21
Cu	0.40 ± 0.03	6.38 ± 0.15
Fe	199.05 ± 10.07	894.79 ± 17.87
Mg	2.08 ± 0.05	0.02 ± 0.01
Mn	2.02 ± 0.04	7.74 ± 0.37
Sr	0.45 ± 0.02	0.0002 ± 0.0001
Ti	0.56 ± 0.03	0.09 ± 0.01
total	370.19 ± 11.25	913.16 ± 17.88

The total weight percentage of the metals analyzed in the pad is roughly 37±1 % while it is 91±1 % in the disc.

For the disc, grey cast iron often contains 2.5% to 4% carbon and 1% to 3% silicon (Singh, 2016), that should be added to the analyzed metals in order to get the total mass. An XRD powder analysis of the milled disc chips confirmed the presence of ferrite (α-Fe) as the main phase with graphite (C) as a minor phase (Appendix 6).

For the organic pad, the mass content of carbon, silicon, oxygen and sulfur should be added to the analyzed metals in order to get the total mass. An attempt of mass closure is described thereafter, based on complementary analyses of total carbon and sulfur, and on the hypothesis that most of the metals are in their most stable oxidation state, except barium (assumed as barium sulfate).

3.1.3.2 Identification of pad and disc metal tracers

The elemental composition of the pad and disc shows that some metals can be considered as tracers of either the pad or the disc, because they are present only in one of the two materials. Table 3.5 shows the different metal ratios, pad/disc or disc/pad, obtained for different potential tracers. Considering both a good analysis and a large ratio, and based on the results, we decided to choose Al, Ba, and Ca as pad tracers (highlighted in yellow in the table) and Cr, Cu, and Fe (highlighted in blue) as disc tracers that were robust. It is also important to note that Sr and Ti are characteristic of the pads, while Mn is distinctive of the disc; however, the results were more consistent with the chosen tracers.

Table 3.5 Ratios of metallic elements between brake pad and disc: pad-to-disc and disc-to-pad fractions (yellow cells: pad tracers, blue cells: disc tracers)

Metals	$\frac{\text{Pad metal}}{\text{Disc metal}}$	$\frac{\text{Disc metal}}{\text{Pad metal}}$
Al	1293.18	0.001
Ba	15309.70	0.0001
Ca	1174.09	0.001
Cr	0.02	63.01
Cu	0.06	15.94
Fe	0.22	4.50
Mg	131.87	0.01
Mn	0.26	3.84
Sr	2591.51	0.0004
Ti	6.27	0.16

3.1.4 Average elemental composition of the emitted TSP

Having recognized the physico-chemical characteristics of the pad and disc materials, section 3.1.3 will focus on the average elemental composition of the emitted TSP and establish links between material wear and particle emissions, offering insight into the potential sources and composition of brake-related particles. Elements were analyzed by ICP-MS/AES in emitted TSP collected on Teflon filters after acid digestion.

3.1.4.1 Repetition consistency of elemental composition of TSP from NP & HP

Figure 3.2 presents the scatter plot with the 1:1 line for the concentrations (ng/m^3) of metals in particles collected with filter holders with the reference pad for both the normal and heavy pathway repetitions. The slopes show consistency, with a regression coefficient of 1.11 for the normal pathway and 1.02 for the

heavy pathway, showing minimal variation. This indicates a strong correlation between the two repetitions, with a regression coefficient very close to 1.

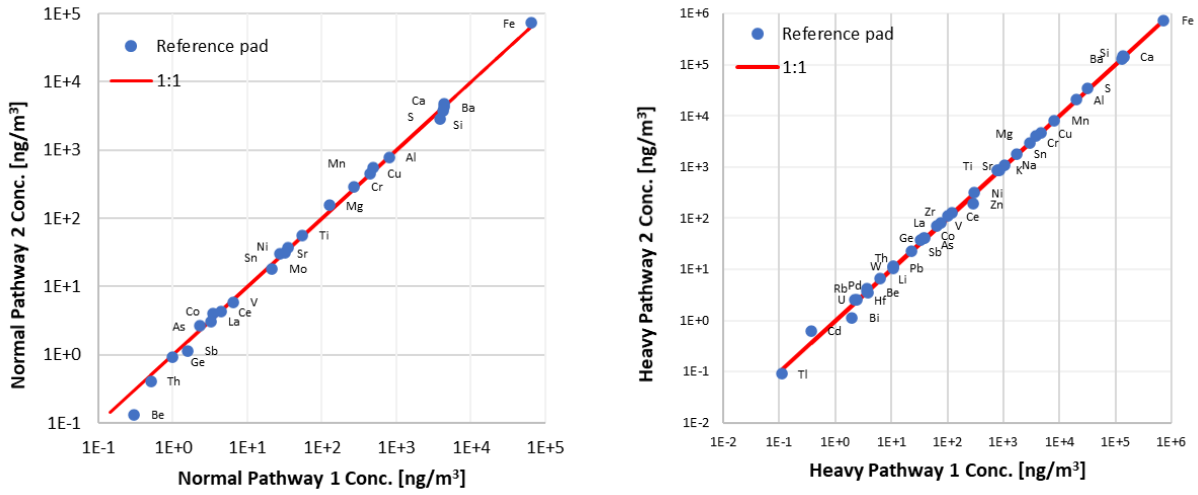

(a) (b)

Figure 3.2 Comparison of the metal concentrations in the emitted TSP between the 2 repetitions of the normal pathway (a) and heavy pathway (b) using the reference pad

3.1.4.2 Mass closure & elemental composition of TSP from NP & HP

- Normal pathway

Figure 3.3 shows the mass concentration and chemical composition of TSP collected under two normal pathway braking conditions, NP1 and NP2. The left chart illustrates the relative proportions of metals, oxygen & sulfur, and unknown components, along with total mass concentration values, and the right-hand chart presents the absolute mass concentrations with uncertainties. For NP1, the metal content measured was 76.6 ± 4.1 µg/m^3, and the unknown fraction was 74.2 ± 7.8 µg/m^3. For NP2, a slightly higher metal concentration of 84.6 ± 4.5 µg/m^3 was recorded, but the unknown fraction dropped to 32.5 ± 4.8 µg/m^3. Notably, in NP1, metal oxides and barium sulfate accounted for 59% of the mass, while in NP2, metal oxides and barium sulfate increased to 79%. Thus, during NP2, more metals are observed, yet less total mass.

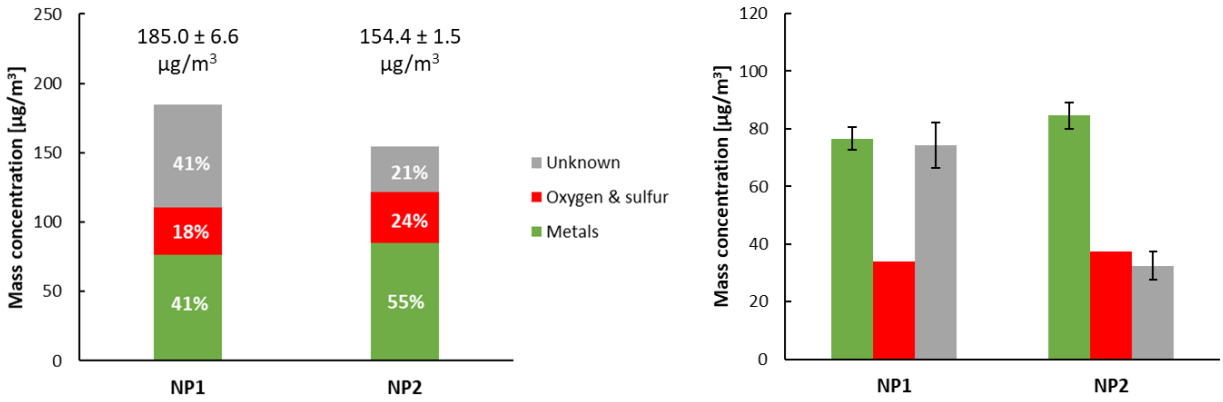

Figure 3.3 Mass closure and chemical composition of particulate emissions (NP1 and NP2)

Concerning the higher emissions of NP1 compared with NP2: the NP1 tests were conducted first after the bedding, while the NP2 tests were later. It is likely that the bedding period was insufficient for the tribological system to reach a mature state in terms of emissions. Therefore, the NP2 results are probably more representative of emissions under normal service conditions.

Tribological maturity in a sliding contact is achieved when a nominal operation is established, i.e., the quantities characteristic of sliding have reached equilibrium and no longer vary, or vary slightly. To assess maturity, parameters such as the stabilized contact area, steady friction levels, constant wear rates, and stable emission levels can be considered. In our case, the variability of emissions indicates a lack of maturity, meaning that the contact requires more time to reach a steady state.

This observation aligns with findings from Briatte's thesis (2024), which showed that the maturity of the tribological system requires significantly more time to establish for emissions than for friction or surface wear.

The chosen list of 10 metals is presented here on a logarithmic scale (Figure 3.4). Fe dominates, followed by other metals present in much smaller amounts, including Ca, Ba, and Al, and the minor contributions of Mn, Cu, Cr, Mg, Ti, and Sr.

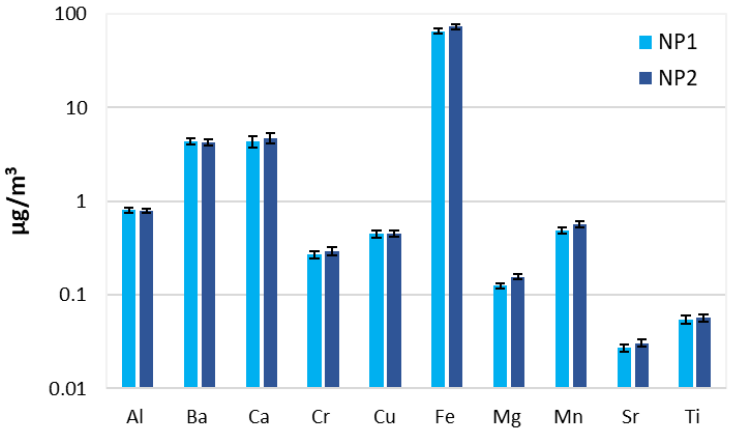

Figure 3.4 Metal content in TSP for NP1 & NP2 using the reference pad

In addition, the mass concentration ratio of NP2 to NP1 for pad tracers is approximately 1 (Table 3.6) indicating that the pad is wearing at a similar rate in both NP1 and NP2. This consistency in pad wear suggests that variations in the unknown fraction cannot be solely attributed to carbon content.

Table 3.6 Tracer ratio in TSP of NP2 to NP1 (yellow cells: pad tracers, blue cells: disc tracers)

Tracers	$\frac{NP2}{NP1}$
Al	0.99 ± 0.09
Ba	0.97 ± 0.10
Ca	1.09 ± 0.20
Cr	1.09 ± 0.15
Cu	1.01 ± 0.12
Fe	1.12 ± 0.10

- Heavy pathway

Figure 3.5 shows the chemical distribution of HP1 and HP2, where metal oxides and barium sulfate presented 75-76% of the total mass. Generally, when the mass is higher, there is less uncertainty during weighing and analysis. This helps to give better and more reliable results. For HP1, the metal content measured was 1034.8 ± 49.0 µg/m^3, and the unknown fraction was 512.3 ± 70.9 µg/m^3. For HP2, a similar metal and unknown concentration of 1062.7 ± 50.3 µg/m^3 and 479.3 ± 68.7 µg/m^3 was recorded, respectively.

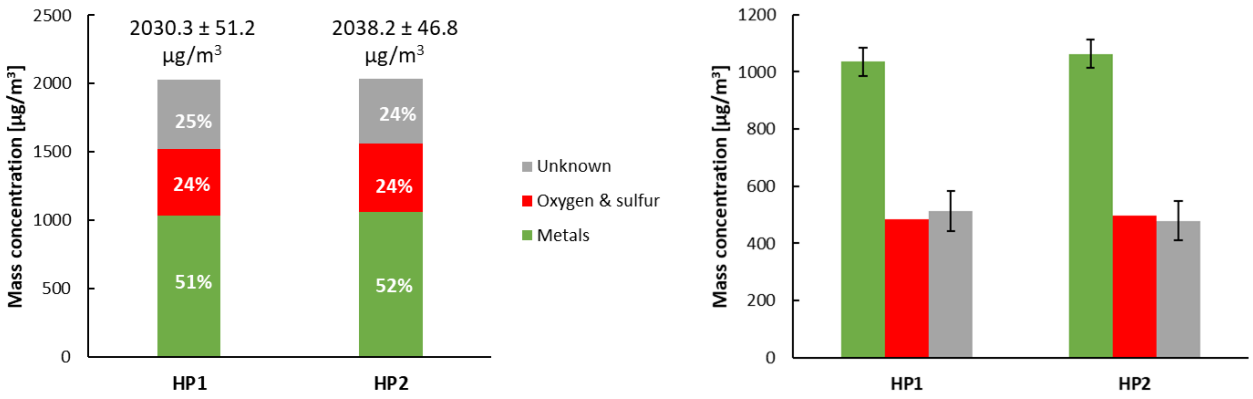

Figure 3.5 Mass closure and chemical composition of particulate emissions (HP1 and HP2)

Unlike the normal pathways, the wear rate is very rapid, leading to high emissions in both repetitions. The order of metal concentrations remains consistent with that observed in NP1 and NP2, as seen in Figure 3.6. The complete list of metals, along with their uncertainties, of NP & HP is presented in Appendix 8.

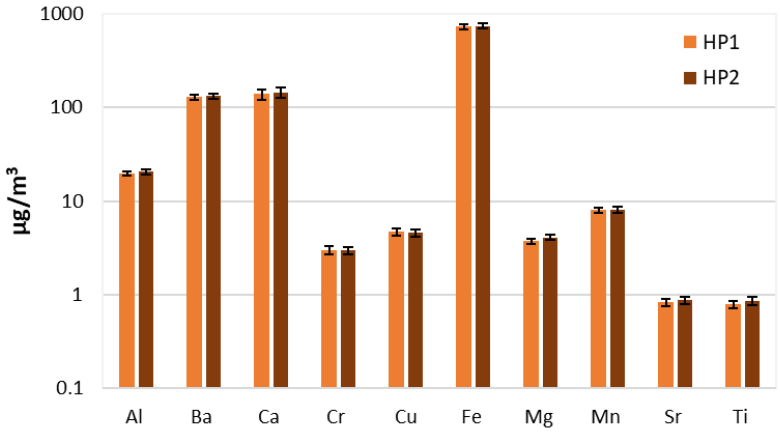

Figure 3.6 Metal concentration in TSP for HP1 & HP2 using the reference pad

Table 3.7 presents the ratio of tracer concentrations in HP2 relative to HP1 along with associated uncertainties. All values are close to 1, ensuring minimal variation between the two heavy pathway tests.

Table 3.7 Tracer ratio in TSP [µg/m3] of HP2 to HP1 (yellow cells: pad tracers, blue cells: disc tracers)

Tracers	$\frac{\text{HP2}}{\text{HP1}}$
Al	1.04 ± 0.09
Ba	1.02 ± 0.11
Ca	1.05 ± 0.19
Cr	0.99 ± 0.14
Cu	0.97 ± 0.11
Fe	1.02 ± 0.09

3.1.5 Submicron particle composition from the 3-stage impactor

Following the elemental analysis of TSP, this section will focus on the chemical composition of submicron particles collected using the 3-stage impactor. The chemical composition is particularly interesting as it can be linked to potential health risks.

3.1.5.1 Consistency of metallic composition using different sampling supports

To validate the metallic composition consistency of measurements across sampling methods, the total mass concentration of all detected metals was compared between the 3-stage impactor (sum of all stages) and the filter holder. A statistical analysis was performed using a t-test, which revealed no statistically significant difference between the two methods.

3.1.5.2 Mass closure & elemental composition of submicronic particles from NP & HP

- Normal pathway

Using the 3-stage impactor, the collected particles were classified based on their aerodynamic diameters: >10 µm, 2.6–10 µm, 1.0–2.6 µm, and <1.0 µm. Generally, no particles with a diameter larger than 10 µm were detected.

The submicronic particles (PM1) represent one-third of the TSP on a mass basis. Their chemical distribution for NP1 and NP2 is presented in Figure 3.7. The stacked bar chart on the left displays the relative percentage of each chemical group within the total mass concentration. The bar chart on the right illustrates the absolute mass concentrations (in µg/m³) of the individual components with their uncertainties. In NP1, oxides were the dominant fraction, making 74% of the total mass. This was followed by organic carbon 12% (6.10 ± 0.36 µg/m³) and unknown materials at 14%. In contrast, NP2 exhibited a shift in chemical composition: oxides noticeably decreased to 46%, the unknown fraction increased to 40%, while OC was consistent 13% (5.90 ± 0.04 µg/m³). EC remained consistently low in both NP and NP2, around 1% (0.32 ± 0.06 and 0.79 ± 0.02 µg/m³, respectively). These findings align with those reported by Garg et al., (2000), where over 96% of carbon was found in the organic form, and EC was nearly absent, similar to what is observed in the normal pathway.

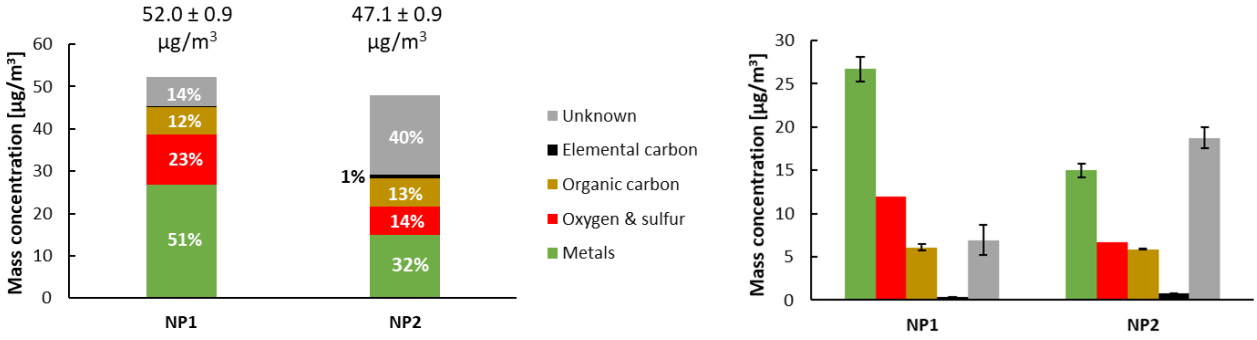

Figure 3.7 Mass closure and chemical composition of submicronic (PM1) particulate emissions (NP1 and NP2)

The ionic concentrations of sulfate (SO_4^{2-}), nitrate (NO_3^-), and phosphate (PO_4^{3-}) measured from the backup filters in the normal braking pathway presented in Table 3.8 were all found to be very low, with values ranging between 0.039 and 0.633 µg/m³. These concentrations represent less than 1% of the total measured particulate matter by this method. However, these low concentrations may be influenced by the analytical technique used—ion chromatography with water as the extraction solvent. Since some sulfate compounds, such as barium sulfate, are poorly water-soluble, their detection by this method may be limited, potentially underestimating the true ionic content.

Table 3.8 Ionic concentrations measured in backup filter samples from the normal pathways

	Concentration [µg/m³]		
	SO_4^{2-}	NO_3^-	PO_4^{3-}
NP1	0.633	<LD	0.128
NP2	0.417	0.039	<LD

The list of metals in submicronic particles emitted using the reference pad is presented here (Figure 3.8) on a logarithmic scale with detection and quantification limits. In the case of NP1 and NP2, the masses on the backup filters appeared to be too low to yield repeatable results. The complete list of metals, along with their uncertainties, is presented in Appendix 9. The order of the metals is the same as in TSP.

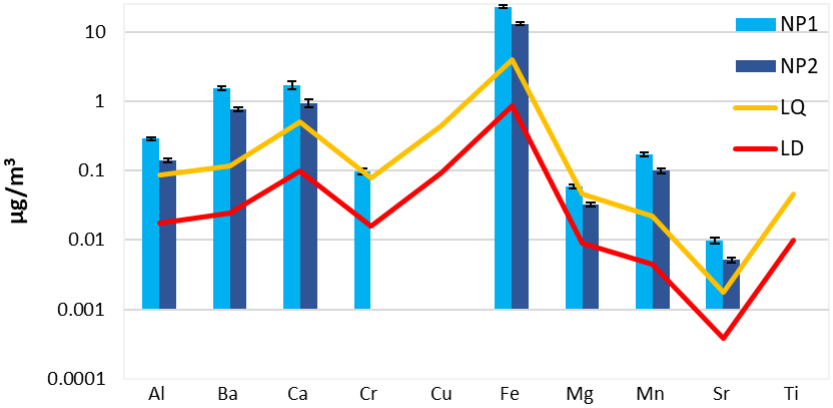

Figure 3.8 Metal content in submicronic particles for NP1 & NP2 using the reference pad

- Heavy pathway

The chemical composition of submicronic particles collected during the two heavy pathway tests (HP1 and HP2) is illustrated in Figure 3.9. The complete list of metals, along with their uncertainties, is presented in Appendix 10. The stacked bar chart on the left shows the relative percentage contributions of different chemical components to the total mass concentration, while the bar chart on the right displays their absolute mass concentrations (in µg/m³).

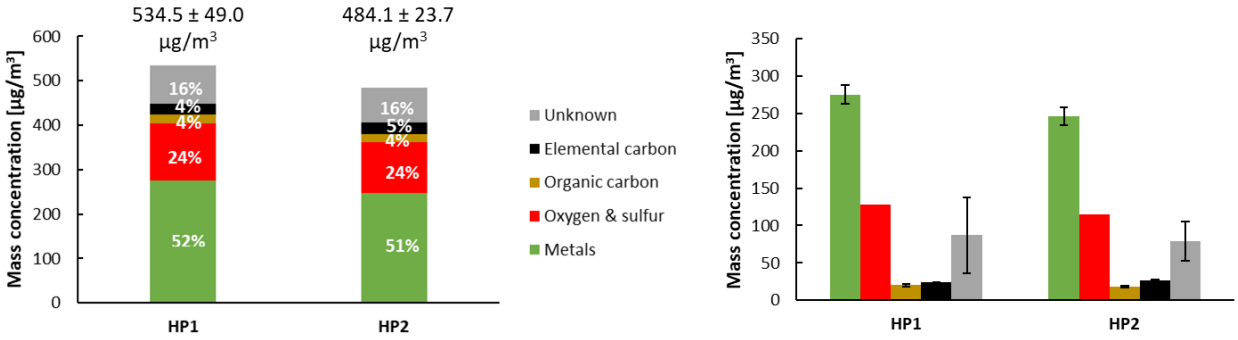

Figure 3.9 Mass closure and chemical composition of submicronic particulate emissions (HP1 and HP2)

In both HP1 and HP2, metal oxides and barium sulfate were the dominant components, accounting for approximately 76% and 75% of the total mass, respectively. Organic carbon, elemental carbon, and unidentified components made up smaller fractions of the total mass. The unidentified fraction accounted for about 16% in both tests, while organic carbon contributed 4% of the total mass with concentrations of 20.40 ± 1.79 μg/m^3 in HP1 and 17.98 ± 1.03 μg/m^3 in HP2. Elemental carbon contributed, with concentrations of 23.62 ± 0.73 μg/m^3 in HP1 and 26.03 ± 2.02 μg/m^3 in HP2. The consistent patterns observed across both tests indicate a stable chemical profile for emissions under the heavy pathway conditions.

In the heavy pathway, the ionic concentrations of SO_4^{2-}, NO_3^-, and PO_4^{3-} measured from the backup filters are presented in Table 3.9, and were also found to be very low, with values ranging from 0.273 to 4.281 μg/m³. Similar to the results observed in the normal braking pathway, these concentrations account for less than 1% of the total particulate matter measured by this technique. As previously explained, this underrepresentation may be attributed to limitations of the analytical method, ion chromatography using water as the extraction solvent. Poor water solubility of certain sulfate compounds, such as barium sulfate, likely leads to their incomplete extraction and underdetection, thereby affecting the reported concentrations.

Table 3.9 Ionic concentrations measured in backup filter samples from the heavy pathways

	Concentration [μg/m^3]		
	SO_4^{2-}	NO_3^-	PO_4^{3-}
HP1	3.705	0.273	0.436
HP2	4.281	0.311	0.400

The order of the metals is the same as in TSP (Figure 3.10).

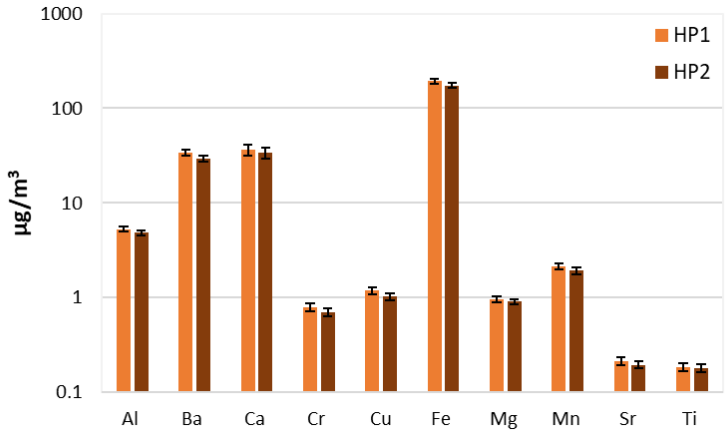

Figure 3.10 Metal concentrations in submicronic particles for HP1 & HP2 using the reference pad

The pad and disc tracers behave similarly at HP1 and HP2 with ratios of around 1, as shown in Table 3.10.

Table 3.10 Tracer ratio in submicronic particles of HP2 to HP1 (yellow cells: pad tracers, blue cells: disc tracers)

Tracers	$\frac{HP2}{HP1}$
Al	0.92 ± 0.08
Ba	0.87 ± 0.09
Ca	0.93 ± 0.17
Cr	0.87 ± 0.12
Cu	0.87 ± 0.10
Fe	0.89 ± 0.08

3.1.5.3 Effect of severity of braking on total carbon emissions

Figure 3.11 shows the total carbon (TC) percentage during normal and heavy pathways for both repetitions. In the normal pathway, TC ranged between 12% and 14% across the two repetitions, with a small variation in standard deviation, which was more than 30% higher than that of the heavy pathway, where TC ranged between 8% and 9%, indicating good repeatability.

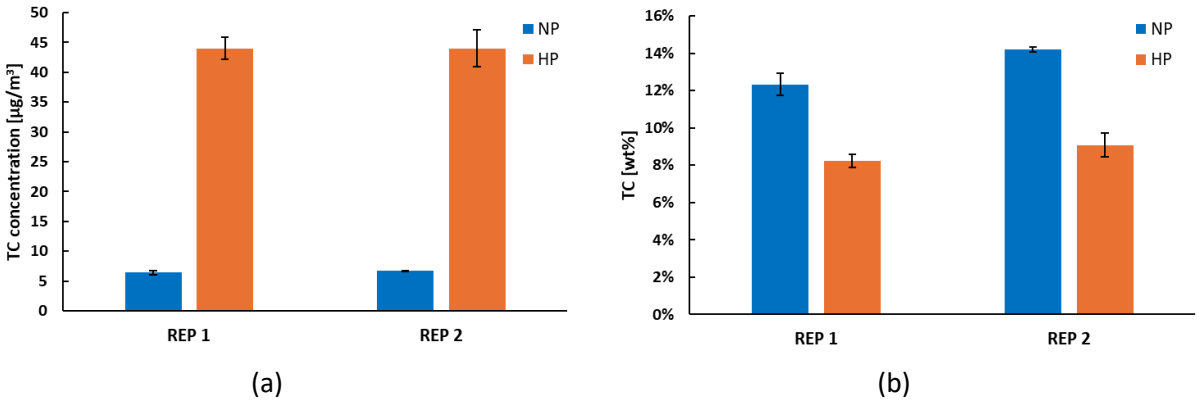

Figure 3.11 Total carbon emissions with the reference brake pad: (a) carbon concentration in submicronic particulate matter collected during NP and HP braking pathways; (b) weight percentage of total carbon content in submicronic particulate emissions collected on the backup filter for NP and HP

As the disc temperature at 2 mm from the surface increases to 218°C (Table 3.1), VOCs may be released in greater quantities, leading to carbon loss as gaseous emissions. This process represents the transformation of particulate carbon into gas. Thus, in addition to mechanical emissions due to wear and tear, it is likely that some of the brake pad materials volatilize during braking and may condense in the airstream, as well as contributing to ultrafine particle formation after some time (Alves et al., 2021). Similarly, Hagino et al., (2016) suggested that parts of the carbon components are volatilized and/or oxidized. As for the study done by Garg et al., (2000), the carbon content of the airborne PM mass decreased from 21.3 to 16.8% when the temperature of the tests increased from 100 to 300°C. The lower percentage obtained at 300°C suggests that it has been volatilized or oxidized.

VOC analysis (3.1.7) shows a higher abundance under heavy braking, indicating that a greater share part of carbon is volatilized rather than retained in the particulate phase.

The collected PM1 samples from the NP contained 12–14 wt% total carbon. Relative to the brake pad's carbon content (27.1 wt%), this indicates that a maximum of 44–52% of the carbon emitted from the pad is released in particulate form, while the remaining 48–56% are likely released as volatilized compounds, assuming all emitted carbon originates from the pad. In contrast, the samples collected from HP contained 8–9 wt% of the total carbon, suggesting that 30–33% of the emitted carbon appears in particulate carbon, while 67–70% may be emitted as volatilized species.

Alves et al., (2021) tested two non-asbestos organic (NAO) brake pads (NAO 1 and NAO 2) with varying organic content using a bench dynamometer under three braking protocols to evaluate the carbon content in airborne brake wear particle emissions. The specific braking conditions are detailed in Table 3.11.

Table 3.11 Braking protocols and corresponding TC wt% in PM10 samples for NAO1 and NAO2 under varying conditions (Alves et al., 2021)

Protocol	Braking cycle (deceleration)	Braking events	Temperature	Samples	TC wt%	
					NAO 1	NAO 2
Smooth	120-80 kph	8	100 °C	PM10	75.4	54.3
Mild	200-170 kph	8	100 °C	PM10	38.8	12.3
Severe	100-5 kph	15	550 °C	PM10	6.74	8.10

As braking severity increased, the total carbon-to-PM10 ratio (TC/PM10%) decreased for both pads NAO1 and NAO2, during friction tests (Figure 3.12).

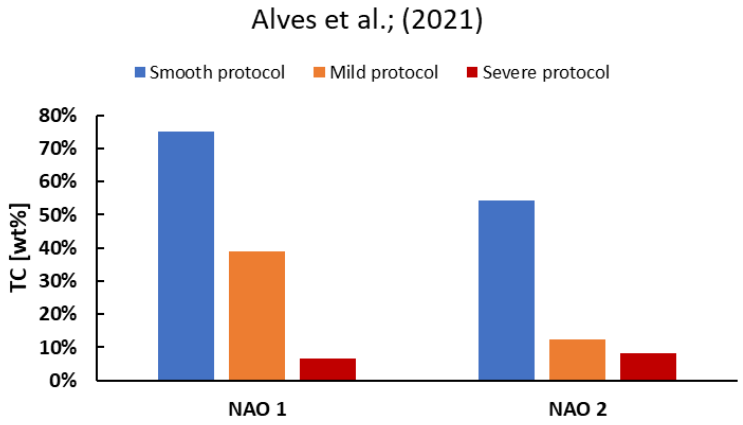

Figure 3.12 TC content in PM10 samples under different braking protocols for NAO 1 and NAO 2 (Alves et al., 2021)

Although the mechanism is complex, a plausible explanation for our results can be drawn by comparing them with those of Alves et al., (2021). When organic materials are abraded against metallic surfaces, the initial wear process tends to generate large, non-airborne particles that quickly settle due to their size. This likely explains why Alves et al., (2021), despite measuring PM10, did not detect significant amounts of these coarse particles, similar to our findings for PM1.

Based on our interpretation, we propose that the abrasion process initially produces relatively large organic particles, often several micrometers in diameter. As these particles remain within the tribological contact zone, they undergo further fragmentation due to continuous mechanical wear, eventually decreasing in size to submicron levels.

3.1.5.4 Mass size distribution of major elements under NP & HP from the 14-stage impactor

This section presents the mass size distribution of major elements based on samples collected with the 14-stage impactor. The analysis is conducted separately for the normal and heavy pathways to examine how specific elements are distributed across particle sizes.

- Normal pathway

Most of the studied elements exhibit a unimodal particle size distribution in the fine particle range, with aerodynamic diameters between 0.94 and 1.62 µm. Figure 3.13 below presents selected metals and their respective size distributions using the same metal selection as before. Among them, Ba and Fe (as well as Ce, La, and Sn) are the best characterized and most reliably quantified. Strong correlations are observed among these elements. Notably, the high correlation coefficient between the distributions of Ba and Fe (r = 0.997) suggests that these elements were incorporated into the same third-body layer during the braking process, despite originating from different first bodies. This highlights the role of the third body in homogenizing material from both pad and disc before particle release. For each metal, the concentration in µg/mg in TSP (FH) is reported to reflect the total mass of the element in the sample.

The shapes of the distributions of these metallic elements were very similar to the total mass distribution of the brake emissions shown in (Figure 3.1). This type of distribution is illustrated here by the examples of Ba and Fe (Figure 3.13). These elements are primary emitted during the process of mechanical abrasion of particles by the pad and disc. The abrasion process initially produces particles that are several micrometers in size. Larger particles form first, but they remain in the contact and gradually reduce in size through mechanical wear, eventually reaching sizes as small as 1 µm.

This suggests that the mechanical properties of the third body, which acts as a mediator within the contact, may effectively retain particles above a certain size threshold. This dynamic implies that modifying material properties or the design of the tribological system could influence not only the quantity of PM emitted but also its size distribution, offering a pathway for emission mitigation.

This type of distribution was also reported by Hagino et al., (2016) and Iijima et al., (2007) where they included elements such as Ba and Fe, showing size distributions similar to those of the PM emissions, consistent with a unimodal mode between 1.25-3.2 µm and 3-6 µm, respectively.

One element that is possibly affected by a bimodal distribution is Al, illustrated in Figure 3.13. The graph presented here clearly shows 2 maxima between 0.94 and 1.62 µm and a second mode between 0.09 and 0.15 µm. A bimodal distribution can indicate that particles are emitted from two distinct sources: a mechanical abrasion process and a high-temperature chemical process. This type of distribution has also been reported by Hagino et al., (2016), the presence of Al in ultrafine particles (<0.1µm), although their concentrations were relatively low, was still **notable and consistent across multiple vehicles**. In another study, Iijima et al., (2007) indicated the presence of another element, potassium (K), in the sub-micro size, suggesting that this size of particles is generated by the aggregation of volatile compounds.

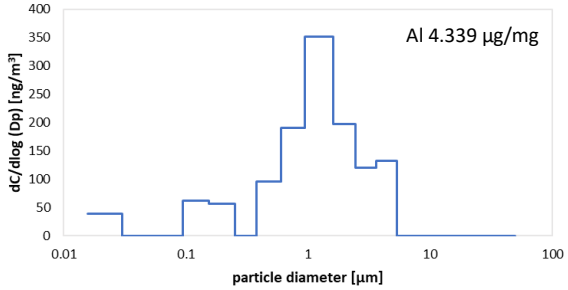

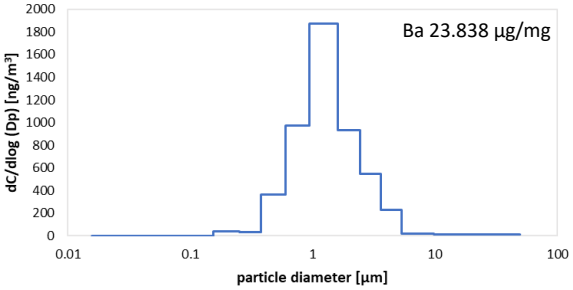

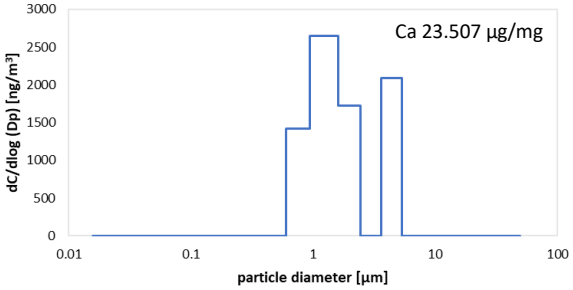

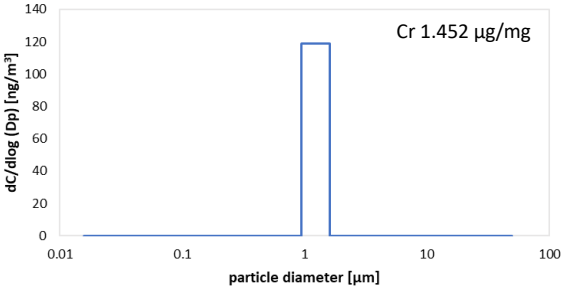

Insufficient mass to get a good PSD

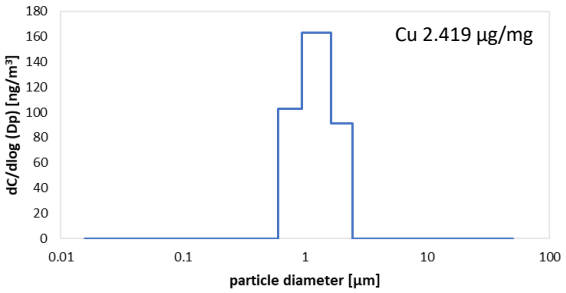

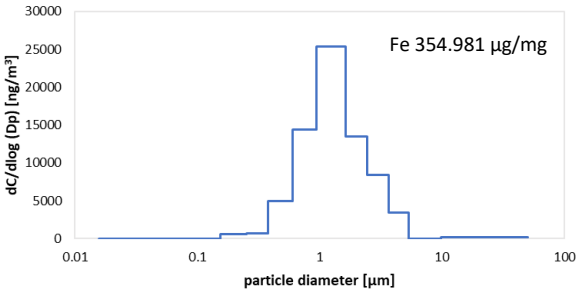

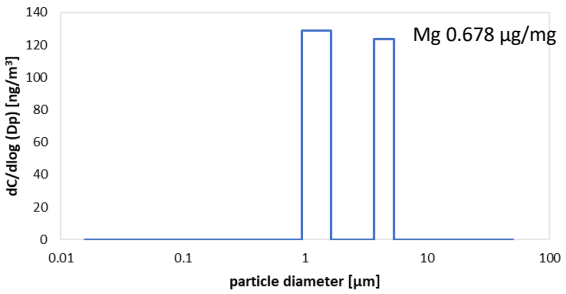

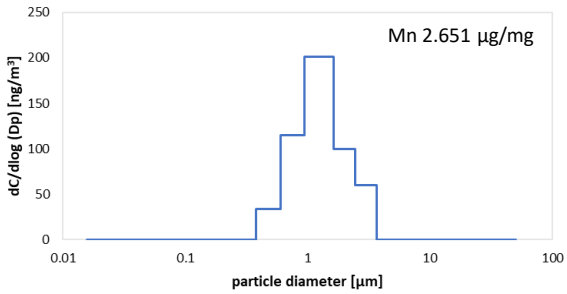

Insufficient mass to get a good PSD

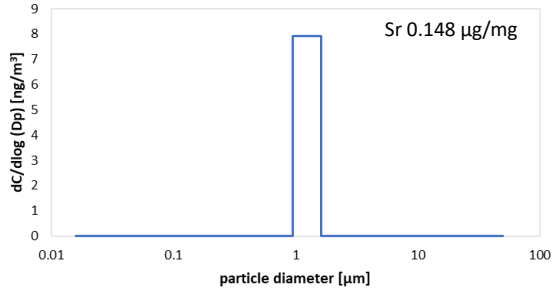

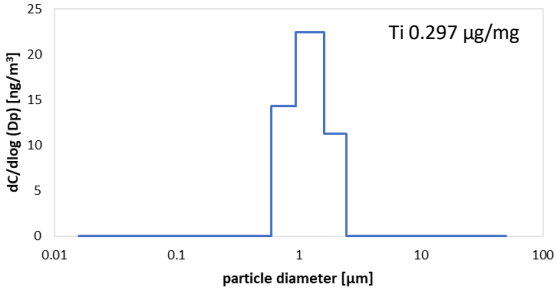

Insufficient mass to get a good PSD

Insufficient mass to get a good PSD

Figure 3.13 Particle mass concentration size distribution of selected metals during NP1

3.1.6 Wear and emissions characteristics in normal vs heavy pathways

The analysis of metals in particulate emissions serves several key purposes. Firstly, using the identified tracer metals specific to brake pad and disc materials allow us to estimate their wear contributions to emissions. Secondly, the metal composition is characterized by particle size, particularly within the submicron range. This approach will help us to better understand the emission mechanisms. Moreover, this size-resolved analysis is especially important, as finer particles are more likely to penetrate deep into the respiratory system, thereby posing greater health risks, especially in the presence of toxic metals.

3.1.6.1 Effect of braking severity on the metal enrichment of TSP

Table 3.12 displays the ratios of weight content between the heavy and normal pathways with uncertainties that are based on Chapter 2:. If the ratio is higher than 1, then there are more metals in the heavy pathway emissions than in the normal pathways.

Table 3.12 Effect of braking severity on the metal enrichment of TSP, through the HP-to-NP ratios of the metal weight contents (µg metal per mg TSP) (yellow cells: pad tracers, blue cells: disc tracers)

	$\frac{\text{HP1}}{\text{NP1}}$	$\frac{\text{HP2}}{\text{NP2}}$	$\frac{\text{HP average}}{\text{NP average}}$
Al	2.24 ± 0.19	1.96 ± 0.17	2.09 ± 0.26
Ba	2.66 ± 0.27	2.34 ± 0.24	2.49 ± 0.36
Ca	2.90 ± 0.54	2.31 ± 0.43	2.57 ± 0.67
Cr	1.02 ± 0.14	0.77 ± 0.11	0.87 ± 0.17
Cu	0.95 ± 0.11	0.77 ± 0.09	0.85 ± 0.14
Fe	1.01 ± 0.09	0.77 ± 0.07	0.87 ± 0.11

For pad tracers, the ratios of Al, Ba, and Ca are similar, with a ratio above 2. This indicates that the contribution of the pad to the metallic fraction of the emitted particles in the heavy pathway is twice that of the normal pathway, suggesting a higher degradation of the pad during the heavy pathway.

On the other hand, assuming that the difference between first and second repetition is not significant, the average ratios for the disc tracers Cr, Cu, and Fe are also similar, with ratios ≈ 1. The tracer ratios suggest a lower degradation of the disc in the heavy pathway than in the normal pathway.

- Estimation of the relative and absolute contributions of pad and disc to the TSP concentrations for NP and HP

Under the simplifying hypothesis of a homogeneous wear of the pad and the disc, therefore knowing both the weight content of a metal in TSP (µg of metal per mg of TSP) and its weight content in either the pad or disc (µg of metal per mg of pad or disc), it is possible to estimate the relative mass contribution to the TSP of the pad (mg of pad per mg of TSP) and the disc (mg of pad per mg of TSP), through the following equations (Eq. 2-26 & Eq. 2-27) specifically to TSP:

$$\text{Pad \% w/w (mg pad / mg TSP)} = 100 \times \frac{\text{Metal weight content in TSP (µg metal / mg TSP)}}{\text{Metal weight content in pad (µg metal / mg pad)}} \quad \text{Eq. 3-1}$$

$$\text{Disc \% w/w (mg pad / mg TSP)} = 100 \times \frac{\text{Metal weight content in TSP (µg metal / mg TSP)}}{\text{Metal weight content in disc (µg metal / mg disc)}} \quad \text{Eq. 3-2}$$

The simplifying hypothesis may be considered as valid for a whole pathway lasting 8 hours. In fact, although the pad is heterogeneous and each pad component may be emitted differently from the other components, one may assume that these differences may be smoothed when considering average values over long periods of time.

The main results are given in Table 3.13 (relative mass contributions of the pad and disc to TSP) and Table 3.14 (mass concentrations of pad and disc contributing to TSP). The detailed calculations are given in Appendix 11.

Table 3.13 Relative mass contributions to TSP of the pad and disc, estimation based on metal tracers.

Relative mass contributions of pad and disc to TSP	Pad contribution to TSP [% w/w]	Disc contribution to TSP [% w/w]	Sum	Pad/disc
NP1	31%	38%	69%	0.8
NP2	38%	49%	87%	0.8
HP1	81%	38%	119%	2.2
HP2	84%	37%	121%	2.3
average NP	35%	43%	78%	0.8
average HP	83%	37%	120%	2.2
average HP / average NP	2.38	0.87		

NP results are consistent with the findings of Garg et al., (2000), who reported that, on average under different conditions, 35% of the brake pad mass loss was emitted as airborne PM.

Table 3.14 Pad and disc mass concentrations to TSP, estimation based on metal tracers.

Pad and disc mass concentrations to TSP	TSP [µg/m^3]	TSP from pad [µg/m^3]	TSP from disc [µg/m^3]
NP1	185	58	70
NP2	154	59	75
HP1	2030	1654	762
HP2	2038	1717	760
average NP	170	58	72
average HP	2034	1685	761
average HP / average NP	12,0	28,8	10,5

In Table 3.13, one may notice that the sum of the relative contributions of the pad and disc does not exactly add up to 100% but with an uncertainty of ± 20%. However, it is noteworthy to remark that the pad and disc contributions were calculated independently, using different metals, therefore, it is satisfactory to get consistent results even though with uncertainty. This uncertainty may come from the combination of the analytical uncertainties of the metals in the different materials (pad, disc, TSP), but also from overly simplistic modelling. In fact, the main hypothesis behind these calculations is that there are only two main sources of TSP (the pad or the disc), while in reality, the third-body particles built at the interface and stored on the surfaces of both pad and disc are a possible third source of TSP. The average elemental composition of the third body is unknown but should lie between the two first bodies' elemental compositions. Moreover, Fe exhibits a non-negligible contribution from the pad, and since this is not accounted for in the current calculations, the results could be slightly affected. Therefore, despite this limited lack of accuracy of the 2-source model, the results in Table 3.13 tend to show that:

- for NP, the pad contribution is slightly inferior to the disc's one, with an average pad-to-disc ratio of 0.8;
- for HP, the pad contribution is more than twice the disc's one, with an average pad-to-disc ratio of 2.2.

In terms of the concentrations of emitted TSP, the estimations based on the metal tracers indicate that the pad and the disc contribute around 29 and 10 times more, respectively, to the TSP for HP than for NP.

The same methodology has been applied to PM1 particles collected with the backup filter of the 3-stage impactor, giving similar results as for TSP (Appendix 12).

3.1.6.2 Consistency of overall wear (mg/km) and emissions (mg/km)

Before calculating the consistency between wear and emissions, we must remember the definition of wear of a tribosystem: it is the quantity of matter built up by two bodies in sliding contact that definitively leaves the tribological circuit, i.e., the wear flow. It should be noted that wear debris is not simply composed of iron provided by pad and disc rubbing; it undergoes oxidation and/or other reactions that can modify the matter within the contact, resulting in the formation of iron oxides.

Given this complexity, we can't measure the wear flow directly. Hence, we can use certain indicators to discuss wear, such as pad or disc thickness and mass loss. For example, in the thesis of Frangieh, (2025), the volume loss of the two first bodies, the pad and the disc, was used, deduced from operando measurement of thickness losses during testing. Then, by linking the volume to the density (pad or disc), we can estimate roughly the wear mass loss.

Within these conditions, a main hypothesis must be introduced in an attempt of simplification to see if emissions are consistent with wear:

Simplifying hypothesis: When the first bodies are worn, they keep the same densities.

This hypothesis assumes that the worn materials from the first bodies (i.e., the brake pad and disc) retain their original densities. While both components lose material over time, the exact evolution of their densities during wear is not measured in this study; we only have data on the initial material properties. For instance, in the case of the pad, significant loss of carbon, a light element, is likely. As a result, the residual material may become enriched in heavier elements, potentially increasing its bulk density.

Nevertheless, for the purpose of estimating the contribution of each first body to the emitted particles, we assume that the detached matter from the pad and disc retains the densities of the original materials. Furthermore, we treat the emitted wear particles as an external mixture, meaning that pad- and disc-derived particles maintain their distinct identities and respective densities within the emitted aerosol.

Therefore, this hypothesis is a simplification.

Limitation: The accumulated particle samples reflect time-average emissions. They give no information on the likely different emission rates along the duration of the pathway linked to different temperature profiles.

We can't clearly identify the different phases of emissions during the pathway because the temperature, which is an indicator of the process, varies with time. This means the emissions fluctuate during the test. However, our samples do not catch these changes over time since they only provide an average value over the entire 8-h test. Therefore, while the actual emissions likely vary throughout the braking sequence, our analysis reflects only the overall accumulated mass and its corresponding averaged emission rate.

In the thesis of Frangieh, (2025), the volumetric wear loss rates of NP and HP for both pad and disc are calculated and shown in Figure 3.14. NP had the same loss rate for the pad and disc. However, HP showed major contribution of pad over the disc (9 times).

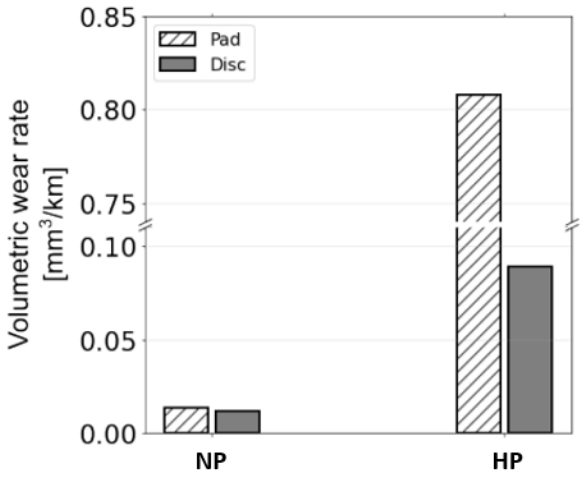

Figure 3.14 Volumetric wear loss (Thesis of Frangieh, 2025)

- Compare values (TSP)

Considering the above hypotheses, we can convert the volumetric wear loss and the particles mass emitted into emission factors according to Figure 3.15.

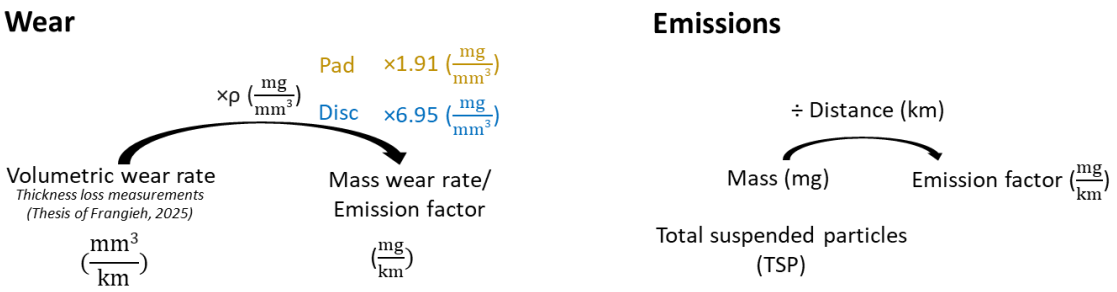

Figure 3.15 Calculation method of emissions factors based on wear volume and emission mass

However, we are not capturing all the emitted particles. Instead, we have a large duct (the outlet of the tribometer enclosure), within which an isokinetic sampling line is positioned. This setup collects a representative fraction of the particles from the main duct. The isokinetic sampling ensures that the concentration of particles (mass of particles per volume of air) in the sample is the same as in the main duct. Since the volumetric flow rate (Qv) in the main duct is known, we assume that the flow rate at the inlet of the enclosure is equal to that at the outlet (stationary flow without any leak). Thus, we can calculate the total mass of airborne particles in the main duct according to Eq. 3-3:

$$\mathrm{M(TSP)} = \mathrm{C(TSP)} \times \mathrm{Qv} \times t \qquad \text{Eq. 3-3}$$

Where:

- M(TSP): The overall mass of airborne particles (TSP) exiting the enclosure during time t [mg]
- C(TSP): The concentration [mg/m^3] of TSP measured with isokinetic sampling
- Qv: The airflow [m^3/h] in the main duct at the outlet of the enclosure
- t: The duration of a pathway [h]

The wear and emissions rates are presented in Table 3.15. The wear rates should be superior to the emission factor because of the losses. In fact, we are not collecting all the wear particles due to surface deposition and possible leaks. As a result, the wear emission factor is 44%–53% higher for NP and 29% higher for HP compared to the emission factor of emissions.

Table 3.15 The overall mass wear rate (mg/km) and the emission factors (mg/km) of TSP for NP and HP for the reduced scale.

	Wear [mg/km]	TSP [mg/km]
NP1	0.11	0.06
NP2		0.05
HP1	2.17	0.64
HP2		0.64

Two possible reasons may explain why the airborne fraction is lower in HP than in NP. First, under higher mechanical solicitation and temperature, the pad tends to release larger wear fragments that remain

trapped within the contact interface, as their size makes it difficult for them to exit the contact zone. In fact, since the solicitation is much higher in HP, the wear process or mechanisms are different. For the pad, for instance, the organic matrix is not comfortable, and the pad loses large particles (millimeters). This kind of process cannot occur with NP because the temperature is very low. So, if we have large particles, we know that they won't become airborne particles, so the quantity of wear will increase compared to the proportion of airborne particles.

Second, a portion of the pad wear may be transformed into VOCs, which are not captured in the particulate measurements, or into SVOCs, which may deposit on the inner surfaces of the setup (walls of the enclosure or the duct, or the sampling line) because the airflow is turbulent.

Other factors may influence these ratios, such as the degree of oxidation of the metals (like iron) in HP compared to NP, or in the emitted particles compared to the total wear.

- Ratios with metal tracers
    - Disc results

The disc mass wear observed by Frangieh (2025) is 7.5 greater for HP than NP. A consistent average ratio of 10.0 ± 2.7 is observed for the emitted disc tracers across the two repetitions, showing a stable emission pattern whichever disc tracer element is considered. The ratios obtained with the disc tracers are in the same order of magnitude as the disc mass wear estimated from the disc volumetric loss indicating consistency across different measurement methods, despite their limitations (Table 3.16).

Table 3.16 Disc wear and tracer element emission ratios (HP to NP)

		$\frac{\mathrm{HP1(g/km)}}{\mathrm{NP1(g/km)}}$	$\frac{\mathrm{HP2(g/km)}}{\mathrm{NP2(g/km)}}$
Disc mass wear (Calculated from the thesis of Frangieh (2025))		7.5	
Emission of disc tracers (in TSP)	Cr	10.4 ± 1.4	9.8 ± 1.3
	Cu	9.8 ± 1.1	9.8 ± 1.1
	Fe	10.4 ± 0.9	9.8 ± 0.8

    - Pad results

The pad mass wear observed by (Frangieh, 2025) is 57.9 greater for HP than NP. For the emitted pad tracers, an average ratio of 27.4 ± 9.3 is observed across the two repetitions whichever the metal tracer chosen (Table 3.17). The ratios obtained with the tracers are of the same order of magnitude but lower than the pad mass wear ratio, within a factor of 2. This difference is possibly not significant considering the unknown uncertainty of the wear loss estimation and the use of different measurement methods (particle mass collected and volume thickness loss). First it could be due to the fact that the collection efficiency of the emitted wear matter may be lower for HP, due an increased formation of organic semi volatile compounds which may easily condensed on surfaces instead of being collected. Second, the pad carbon is degraded into gases (VOCs, CO, and CO_2), more for the heavy pathway, as seen in the previous

section 3.1.7, which also may affect the particle mass. Finally, the pad's thickness evolution is affected by its porosity (air content) that can cause overestimation of thickness measurements, which has been confirmed by Frangieh (2025) but not quantified.

Table 3.17 Pad wear and tracer element emission ratios (HP to NP)

		$\frac{HP1(g/km)}{NP1(g/km)}$	$\frac{HP2(g/km)}{NP2(g/km)}$
Pad mass wear (Calculated from the thesis of Frangieh 2025)		57.9	
Emission of pad tracers (in TSP)	Al	23.0 ± 2.0	25.1 ± 2.2
	Ba	27.4 ± 2.8	29.8 ± 3.1
	Ca	29.8 ± 5.5	29.5 ± 5.4

3.1.6.3 Particle formation in the heavy pathway

The TSP mass is driven by the mass of metals (HP1=HP2), which represents the highest fraction (51-52%). The total metal mass is split between particle sizes, with around 25% in submicron particles and 75% in supermicron particles. A similar split is seen in the total particle mass (regardless of chemical composition), suggesting that particles of different sizes have a similar overall composition.

Moreover, looking at the SEM images of Figure 3.16, which show the pad surface after NP2 and HP2, we observe that after NP2, Figure 3.16 (a and b), particles with sizes ranging from 200 nm to 400 nm were present, while after HP2, Figure 3.16 (c and d) primary plateaus displayed a noticeably thicker layer of iron oxide film of around 30 µm.

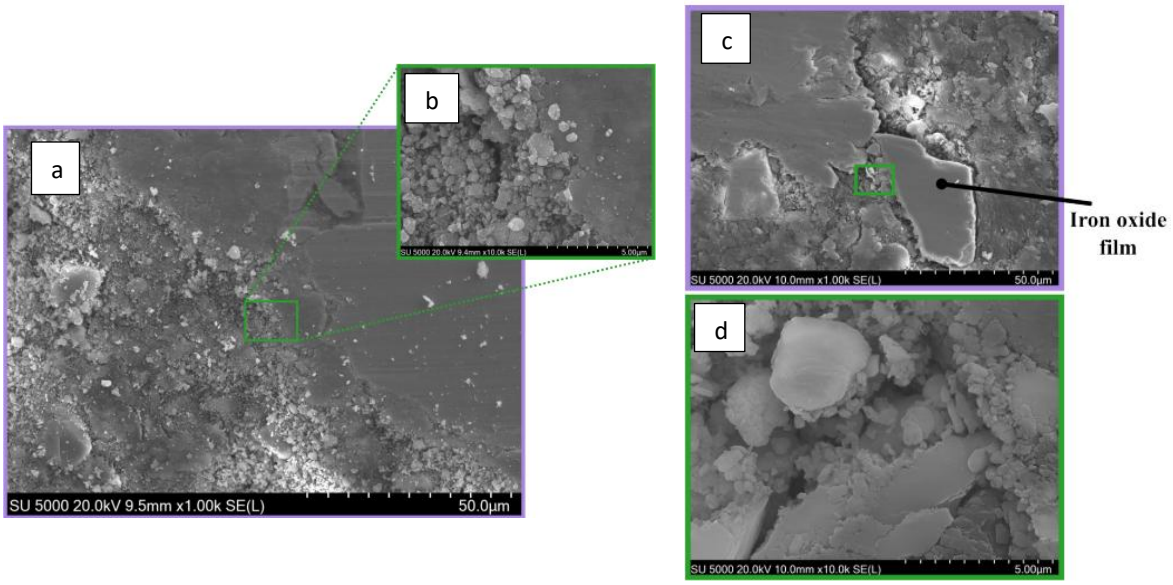

Figure 3.16 Surface observations using SEM on worn surfaces of the pads: (a) pad surface after NP2, (b) close up of the stored particles on the pad, (c) pad surface after HP2, (d) close up of stored particles on the pad (Frangieh, 2025)

These supermicronic particles observed in the HP could result either from the agglomeration of fine particles or from detachment/erosion processes. However, since their chemical composition is very similar to that of the submicronic fraction (Figure 3.6 & Figure 3.10), this tends to indicate that they are primarily composed of the same material, which supports the agglomeration hypothesis.

Agglomeration should occur mostly inside the contact, rather than outside the contact, because the third body plateaus are built inside the contact. Looking at the shape of the coarse debris, we know that part of this plateau is removed and is found in the form of coarse particles. According the thesis of Frangieh, (2025), he observed very big fragments (around 30 µm), but we couldn't see them with our sampling devices (filter holder and impactors). These big fragments stay inside the contact, since it is challenging to exit the contact within this size, they need to be reduced before escaping.

Since submicronic and supermicronic particles exhibit similar chemical compositions, it suggests a shared origin. Given that submicronic particles dominate numerically and tend to accumulate and compact within the contact zone, it's reasonable to propose that some of these may agglomerate and eventually detach as larger particles. Thus, the supermicronic particles found in emissions could result from the fragmentation or ejection of such compacted agglomerates.

3.1.6.4 Comparison of submicronic particle emissions between normal and heavy pathways

Observation 1:

For NP, we observed higher concentrations of metals in NP1 compared to NP2, in contrast to TSP mass concentrations which were similar. For HP however, HP1 and HP2 displayed the same TSP masses and composition (Figure 3.5 & Figure 3.9).

Table 3.18 presents the weight content ratio of the heavy to normal pathways for both first and second repetitions to show the effect of the braking severity on the metal enrichment of the submicronic particles (<PM1 sampled by the backup filter of the 3-stage impactor). When the ratio is higher than 1, then metals are enriched in the heavy pathway. NP2 has a less metallic contribution to the submicronic particles, leading to a higher ratio in the second repetition, specifically pad tracers. For pad tracers, HP was more enriched as for the TSP. This indicates that the pad's contribution to submicronic particles reflects its contribution to TSP. However, disc tracers were more difficult to interpret due to the detection limits, except for Fe which was well analyzed with a value of 1, as before for the TSP, showing no enrichment of the disc in either pathway.

Unlike the TSP, carbon content was measured in the backup filter. EC, on average, has a ratio of ~2, which is consistent with the pad tracers and the fact that most of the EC could come from the pad. For OC, the ratio is significantly lower than 1 since the organic carbon is more prone to be transferred into the gaseous phase under HP conditions.

Table 3.18 Effect of energy braking severity on the metal enrichment of submicronic particles (yellow cells: pad tracers, blue cells: disc tracers)

	$\frac{\text{HP1}}{\text{NP1}}$	$\frac{\text{HP2}}{\text{NP2}}$	$\frac{\text{HP average}}{\text{NP average}}$
Al	1.79 ± 0.15	3.37 ± 0.29	2.34 ± 0.29
Ba	2.12 ± 0.22	3.70 ± 0.38	2.68 ± 0.39
Ca	2.08 ± 0.39	3.57 ± 0.66	2.64 ± 0.69
Cr	0.80 ± 0.11	*0.34 ± 0.05*	0.48 ± 0.09
Cu	*0.10 ± 0.05*	*0.28 ± 0.03*	0.14 ± 0.02
Fe	0.83 ± 0.07	1.30 ± 0.11	1.01 ± 0.12
OC	0.18 ± 0.02	0.14 ± 0.01	0.16 ± 0.02
EC	4.02 ± 0.74	1.53 ± 0.13	2.17 ± 0.44

Italics font is used when the detection limit is replaced by LD/2 in the normal pathway

Observation 2: Organic carbon (%) decreased from 12–13% (Normal Pathway) to 4% (Heavy Pathway).

Based on thermocouple readings placed 2 mm from the surface (for both pad and disc), higher temperatures are expected to be observed during HP. For the disc, higher maximum temperatures were recorded during the HP (up to 218°C) compared to the NP (up to 148°C). In the same time, the pad reached 65°C during the HP vs 53°C during the NP (see Table 3.1).

Even though we believe that the source of OC is the organic pad that contains 20% rubber and 5% resin, it has a low thermal conductivity, so it does not accurately reflect the actual pad surface temperature as our measurements were made 2 mm underneath the surface. In contrast, the disc, which conducts heat better, provides a more realistic indication of the surface conditions. Nonetheless, the real surface temperature of the disc is likely even higher than the measured value. The thermogradients in the subsurface of the disc and the pad are relatively high.

These measurements clearly show that temperatures are higher during the heavy pathways, although they do not reveal the exact surface temperatures, which could explain why we have higher quantities of VOCs. There was increased volatilization of organics during HP (10 times) compared to NP (3.1.7).

In the NP, a larger part of the carbon stays in the particle phase. In contrast, during HP, the higher temperatures likely cause more carbon to shift into the gas phase, leading to a different partitioning of carbon between gas and particle phases. As demonstrated by TGA, the combustion of carbon into CO_2 occurs at temperatures exceeding 200 °C under an oxygen-rich atmosphere, conditions that are reached in HP.

The reduction in OC from 13% in the NP to 4% in the HP suggests that a large portion of the original OC is being transformed into gaseous compounds. Overall, there is a higher amount of OC present as submicron particles (in µg/m³) in HP compared to NP, although a significant part of it is lost as VOCs in HP. However, we cannot directly add the amount of carbon in the gas phase to the amount in the particle phase because the gas-phase data only include VOCs (and only those measured). Important carbon compounds like CO and CO_2 are not measured, even though they could make up a large portion of the carbon in the gas phase.

Our results agree with Kukutschová et al. (2011) where during braking at high temperatures, metallic particles in the nano- to micrometer range are produced, jointly with carbon-based particulates resulting from the condensation of evaporated organic compounds.

Moreover, HP1 and HP2 are not very repeatable (3.1.7.1); all the measured carbonyls are less detected in HP2 than in HP1, even though the temperature profiles are very similar between the two repetitions. Thus, the decrease in VOC in HP2 could be linked to the increase of EC in HP2, where less carbon is in the gas phase and more is in the particulate phase.

Observation 3: EC detected in HP

Lamellar graphite is found in the cast iron disc, with a typical carbon content (EC) between 2.5 and 4 wt%. For example, Briatte et al., (2025) reported 3.4 wt%, Nosko et al., (2017) reported 3.5 wt%, and Lyu et al., (2024) reported 3.8 wt%.

During NP, the wear of the disc is very low. This is supported by surface observations (Figure 3.17), where laminar graphite structures are still clearly recognizable. These structures are characteristic of the original cast iron microstructure and tend to be disrupted or removed under significant mechanical or thermal stress. Their preservation indicates that the disc surface has undergone minimal alteration, confirming limited wear. In contrast, after HP, only faint traces of laminar graphite were observed on the disc, suggesting more severe degradation of the surface.

In another study on cast iron discs (Briatte et al., 2025), cross-sectional analysis showed that under high solicitation, graphite is consumed deeper within the disc. This suggests that EC can be emitted not just from the surface, but also from within the disc material in depth. This may help explain the higher levels of EC observed under HP conditions.

However, the disc is not the only possible source of EC, since lamellar graphite makes up only a small fraction of the disc volume. It is also important to consider surface area: the disc surface is about six times larger than that of the pad. So, even though the disc loses a small amount of material (including graphite), the pad actually loses a larger quantity of material overall.

This is further supported by the average EC ratio in HP compared to NP for submicron particles, which is 2.17 ± 0.44 (Table 3.18), consistent with the trend observed for pad tracers. Moreover, the high temperatures reached inside the contact zone, possibly exceeding 600°C during HP, could allow the pyrolysis of organic compounds in the pad, contributing to the observed relative increase in EC.

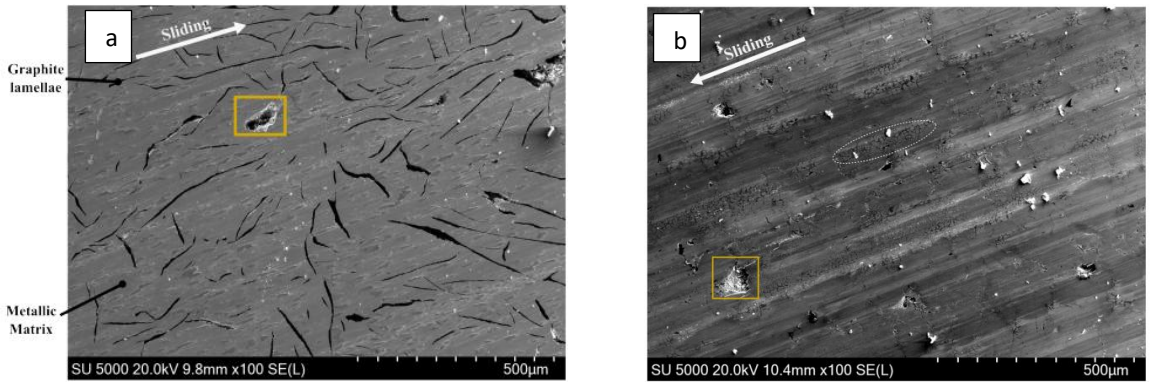

Figure 3.17 Surface observations using SEM on disc worn surfaces after (a) NP, and (b) HP2 (Frangieh, 2025)

3.1.7 Average emissions of Volatile Organic Compounds

Having established the behavior and distribution of PM under the tested conditions, the focus now shifts to evaluating the presence of VOCs, which represent a different class of pollutants.

3.1.7.1 Carbonyl compounds sampled on DNPH cartridges

Figure 3.18 presents the mass concentrations of the emissions from NP and HP. For the normal pathway, eight compounds were detected on the first day, more than on the second, where only four compounds were detected. However, as for their concentration, there is no clear trend in which repetition was higher, probably due to low concentrations detected in the normal pathways generally. Note that for propanone, there were very high concentrations of 18.51 and 4.39 µg/m^3 for NP 1 and NP 2, respectively. Before this test, the blanks were also contaminated (high concentrations of propanone). Additionally, in the last 10 minutes, there was a possibility of contamination from the room in NP1 (particularly from propanone since it had an unexpectedly high concentration). Therefore, for clarity, the graph scale is cropped.

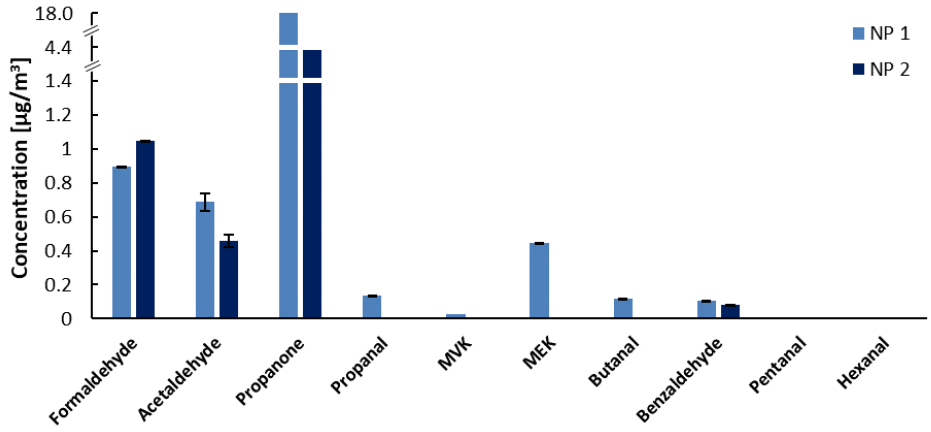

(a)

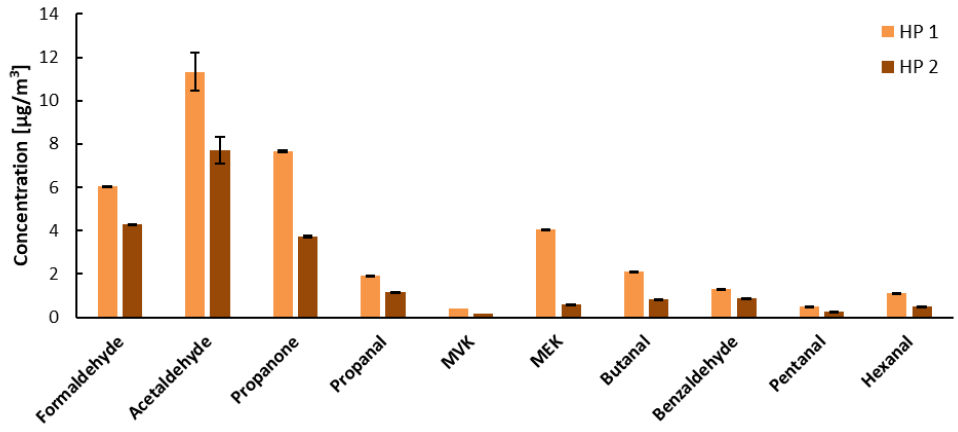

(b)

Figure 3.18 Mass concentrations of carbonyls using DNPH-HPLC/UV with the reference pad for (a) NP and (b) HP

More compounds, such as pentanal and hexanal, were detected in the heavy pathways than in the normal pathways. As we know that higher temperatures are measured in both pad and disc when the severity of the contact is increased (HP vs NP), the detection of VOCs can be explained by several phenomena. First, a higher temperature allows the evaporation of larger molecules. Second, the temperature gradient allows this release from a deeper volume in the pad, favoring the release of more of the lighter compounds. The same compounds were detected in both repetitions; however, in the heavy pathway, the trend was clearer due to higher concentrations (generally 10 times higher than NP). The elevated levels of heavy VOCs observed under HP conditions may be attributed either to the actual release of higher molecular weight compounds or to the increased overall emission quantity, which enables their detection above the analytical threshold.

These results align with the literature, where a two-day study of carbonyl compounds in Chinese subway stations detected mainly three compounds: formaldehyde 31.7±2.76 µg/m^3, acetaldehyde 20.6±2.63 µg/m^3, and propanone 17.4±2.29 µg/m^3 among other carbonyls (Feng et al., 2010). However, most studies on carbonyls are based on field measurements (ambient air), making a direct comparison difficult.

Nevertheless, examining these compounds is crucial, as they can pose health risks, particularly formaldehyde, which is regulated in France. According to guidelines from the Haut Conseil Pour La Santé Publique (2019), formaldehyde concentrations should not exceed 10 µg/m^3 for long-term exposure and 100 µg/m^3 for a single short-term exposure (1 to 4 hours). Although our measurements cannot be directly compared to these regulatory limits, their presence highlights the importance of monitoring due to the associated health risks and the existence of established guidelines.

3.1.7.2 Other VOCs sampled on Tenax cartridges

In order to identify and quantify the following compounds, we will rely on MS and FID detectors and will present here the Total Ion Chromatogram (TIC) which is a plot that represents the sum of all detected ion intensities across a range of mass-to-charge ratios (m/z) over time in GC-MS. It provides an overall view of the sample's composition, showing peaks that correspond to different compounds. The Retention Time (Rt) is the time a specific compound takes to travel through the chromatographic column and reach the detector. In a TIC, Rt is used to identify compounds, as each peak appears at a characteristic retention time based on the compound's interaction with the column. By analyzing the TIC and corresponding Rt values, we can determine the presence and relative abundance of different substances in a sample.

- Test (normal and heavy pathways)

After superimposing the chromatograms of the normal pathways (1 and 2) and the heavy pathways (1 and 2), the repetitions of NP are presented in Figure 3.19, where NP1 is in red and NP2 is in black. Slight differences are observed at the beginning, particularly for the lighter compounds.

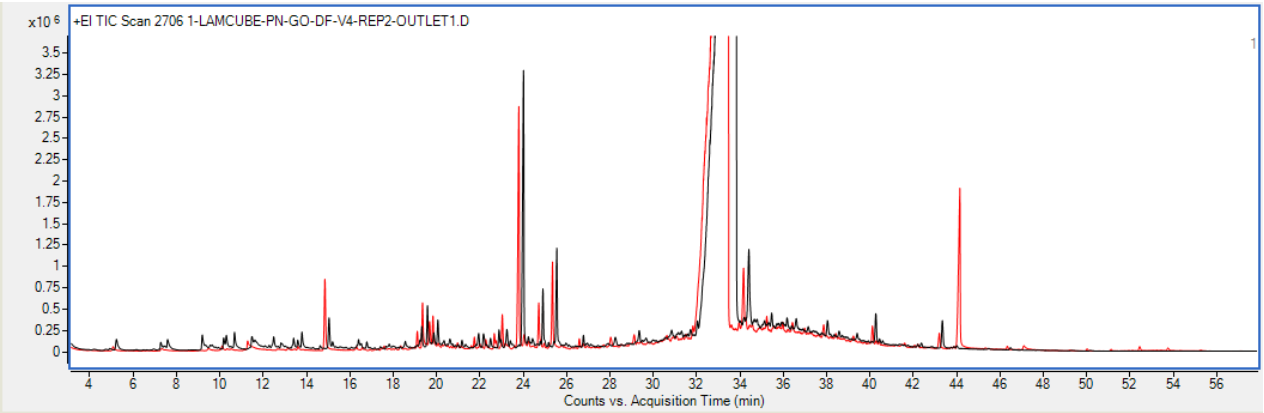

Figure 3.19 Zoomed TIC from GC/MS analysis of NP1 test outlet in red and NP2 test outlet in black

On the other side, greater similarity was observed between HP repetitions (Figure 3.20). Consequently, we will proceed with the analysis of only one normal pathway and one heavy pathway.

All the chromatograms have been zoomed in due to a very large peak at 32 min; the original chromatograms, in addition to the zoomed chromatogram for tests NP1, NP2, HP1, and HP2, are provided in Appendix 13.

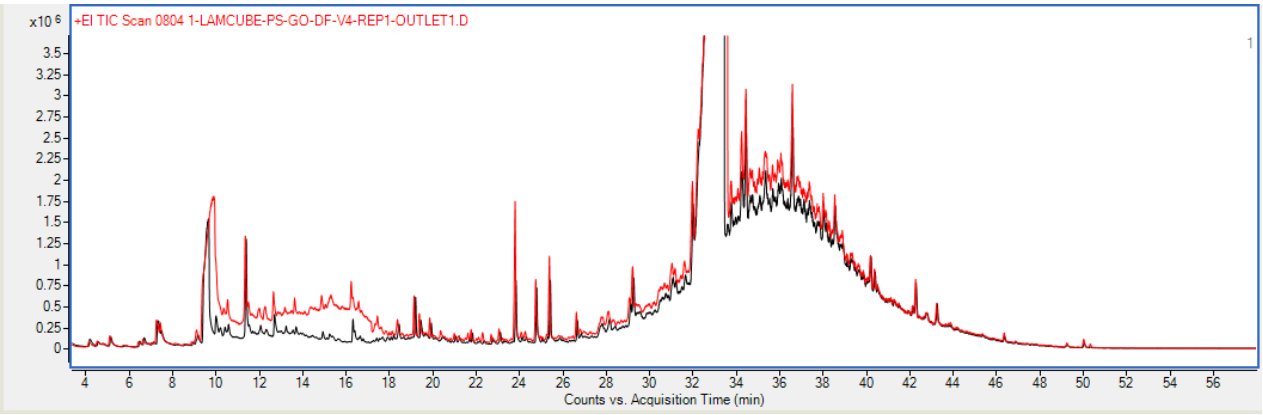

Figure 3.20 Zoomed TIC from GC/MS analysis of HP1 test outlet in red and HP2 test outlet in black

To assess the contribution of the VOC emissions under the normal pathway, we compared the outlet and inlet profiles of VOCs. Samples were collected over the same durations, resulting in comparable air volumes. Only compounds that were either absent at the inlet or present at significantly higher concentrations in the outlet, while being very low at the inlet, were retained for interpretation.

The outlet profile showed notable increases in specific compounds, as illustrated in Figure 3.21. Among these, methyl naphthalene was observed at a concentration of 0.23 µg/m³, and is probably attributed to the incomplete combustion of resin or rubber. A quinone derivative, 2,5-bis(1,1-dimethylethyl)-1,4-benzoquinone, was detected at 0.67 µg/m³, likely originating from background laboratory contamination (since it was also present in blanks). Additionally, esters such as 1,4-butylene glycol di(2-ethylhexanoate) (0.22 µg/m³) and sulfonamides like N-butyl benzenesulfonamide (24.60 µg/m³) were identified, with the latter being linked to plasticizers.

Other compounds were detected in the outlet but could not be reliably quantified due to their low peak intensities. These included silane, siloxane, and 2,4-bis(1,1-dimethyl ethyl) phenol. Their presence, although not quantified, suggests that braking events may release a broad range of volatile organics.

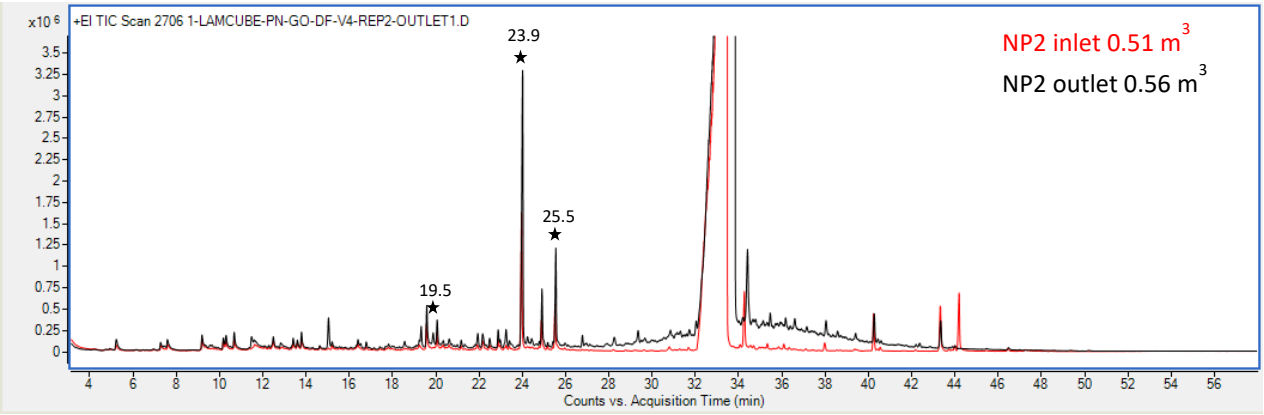

Figure 3.21 Zoomed TIC from GC/MS analysis of NP2, test outlet in black and test inlet in red

Figure 3.22 represents the superimposition of the inlet and outlet of HP 2. In comparison with NP 2, more peaks are observed. For example, compounds such as benzaldehyde and 6-methyl-1-heptanol at lower retention times of 9.2 and 11.3 min, respectively, are due to the thermal degradation of heavier compounds into smaller, more volatile fragments since the surfaces are experiencing higher temperatures (Table 3.1).

At the end of the chromatogram (>28 min), a gradual rise and broad elution were observed, which may indicate the presence of high molecular weight compounds. In this case, saturated hydrocarbons are detected, likely originating from the degradation of polymers such as rubber.

This pattern can also result from column overload. Since GC columns contain only a minimal amount of stationary phase, injecting an excessive amount of analyte can saturate the stationary phase. This leads to a concentration gradient that forces analyte molecules to migrate faster than the carrier gas, resulting in distorted peak shapes and reduced resolution.

In addition to the compounds detected under the normal pathway (**2,6-bis(1,1-dimethylethyl)-2,5-cyclohexadiene-1,4-dione**, **1,4-butylene glycol dimethacrylate**, and **N-butyl benzenesulfonamide**, at concentrations of 0.65, 0.37, and 31.5 µg/m³, respectively), additional compounds were also present under HP and are presented in Table 3.19 with their concentrations in comparison with NP. As expected, the higher pad and disc temperatures reached and measured at 2 mm from the surface during heavy brakings (Table 3.1), favor the decomposition of the organic materials in the pad. Heavy molecules such as saturated hydrocarbons present at the end of the chromatogram (<34 min) (Figure 3.22) probably originate from rubber degradation. While oxygenated compounds such as benzaldehyde and 6-Methyl-1-heptanol probably originate from resin degradation. Other compounds were also detected but could not be quantified due to their small peak intensities and are presented and summarized later in Table 3.20.

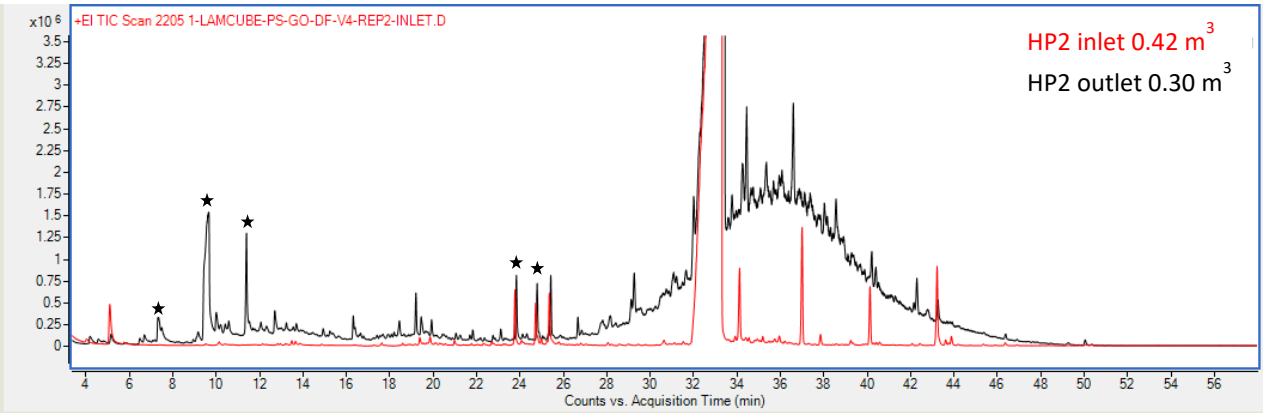

Figure 3.22 Zoomed TIC from GC/MS analysis of HP2 test outlet in black and HP2 test inlet in red

In the table below, compounds detected under both NP and HP conditions are listed along with their concentrations. The" probability" column refers to the similarity score provided by the NIST library in GC-MS analysis, indicating how closely the measured spectrum matches a known reference. Higher percentages reflect greater confidence in the compound identification.

Table 3.19 Quantified VOCs with retention times, probabilities, and concentrations under normal and heavy braking conditions

Retention time [min]	Compound	Probability [%]	Mass concentration [µg/m^3]		Structure
			NP	HP	
7.3	1,3,5,7-Cyclooctatetraene	60	-	0.51	
9.5	Benzaldehyde	100	-	1.79	
11.4	6-Methyl-1-heptanol	60	-	0.90	
19.5	Methylnaphthalene	30	0.23	-	
23.8	2,6-Bis(1,1-Dimethylethyl)-2,5-cyclohexadiene-1,4-dione	70	0.67	0.65	
25.5	1,4-Butylene glycol dimethacrylate	90	0.22	0.37	
33.8	N-butyl benzenesulfonamide	90	24.60	31.50	
34.4	Heptadecane	<10	-	0.33	

Our results align with findings from other studies conducted under similar conditions, including full-scale brake dynamometer tests using low-metallic brake pads and cast-iron discs, which are typically used in automotive applications. The released VOCs observed in these studies include phenolic compounds, aromatic aldehydes, organic substances containing oxygen (O), sulfur (S), and nitrogen (N), as well as BTEX (benzene, toluene, ethylbenzene, xylene) and polycyclic aromatic hydrocarbons (PAHs). These compounds highlight the complex chemical composition of emissions from braking systems and underline the consistency of our findings with the broader body of research (Plachá et al., 2017).

The brake wear products also have PAHs, which correspond to changes in the carbonaceous components of the brake material. Siloxane was highly detected in the emissions of braking likely due to the presence of SiO_2 and other abrasive materials commonly used in brake pad friction materials. Abrasives such as alumina, silica, zirconia, and SiC are added to improve braking performance but often exhibit low adhesion with the resin matrix. During braking, these particles are easily detached, contributing to wear and generating emissions. The wear process can release silicon-containing compounds, including siloxanes, as byproducts, which are emitted into the environment during braking events (Chauhan et al., 2022).

3.1.7.3 VOC emissions from the pad using TGA-FTIR

The analysis of HP compared to NP of the collected VOCs shows (i) an increase in VOC quantity, and (ii) a slight shift toward lower molecular masses in HP. These two simultaneous phenomena can be explained by the temperature increase in the contact area. Indeed, the higher the temperature, the faster the degradation kinetics of the organic material. Furthermore, certain temperature thresholds may be reached, thermodynamically enabling new reactions. These variations in VOC emissions can be explained in two ways: either by degradation of the organic materials in the pad (phenolic resin and rubber) during braking via a progressive combustion process that breaks down chemical functions (Y. Chen et al., 2008), or by the volatilization of semi-volatile VOCs already present in the matrix but trapped in the porosity during resin curing.

TGA combined with FTIR, conducted under nitrogen on one hand and under oxygen on the other, clarified degradation mechanisms of the brake pad's organic materials. Working with pure oxygen maximizes the oxidation of pad materials (e.g., binders and resins) and ensures complete combustion of organics, while using 100% nitrogen allows for the study of thermal decomposition and identification of pyrolysis products.

In the presence of oxygen, combustion is clearly indicated by the presence of CO_2 (FTIR double peak at 2350 cm^{-1}) and water (FTIR peaks in the 3600 cm^{-1} region). However, many other peaks are also visible (<1000 cm^{-1}), corresponding to expected bands for aromatics (present in both phenolic resin and rubber), as well as alkenes and alkanes. On the other hand, there is no clear FTIR evidence of hydroxyl or carbonyl functional groups (Figure 3.23).

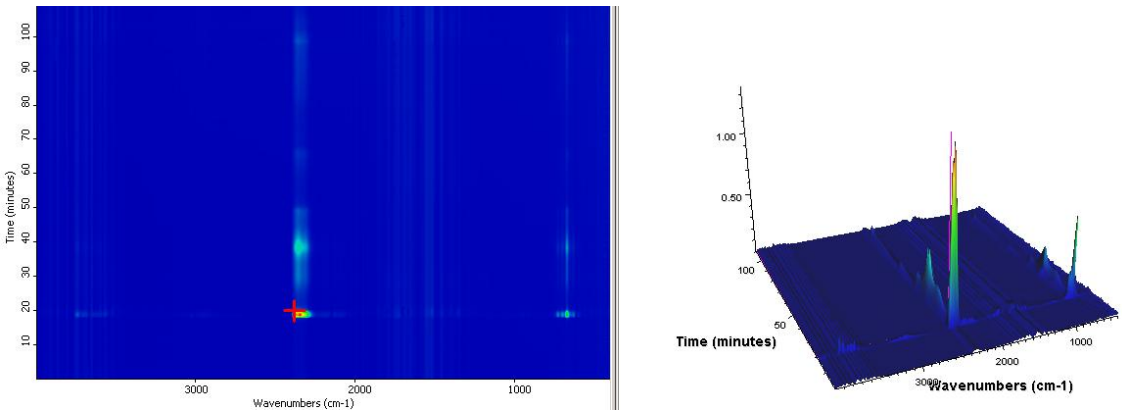

Figure 3.23 2D and 3D FTIR mapping of evolved gases during thermal degradation of the pad in oxygen atmosphere

Finally, combustion in air occurs extremely rapidly at 200°C, within one minute, just after a mass uptake begins, whereas organic material degradation under nitrogen is much more gradual, occurring between 350 and 500°C. This degradation is characterized by absorptions corresponding to C–H, C–C, and C=C bonds present in alkanes, alkenes, and aromatics. It is therefore likely that combustion in the presence of oxygen is accelerated by a catalytic effect due to the numerous metallic particles in the brake pad (Křístková et al., 2004).

This degradation of organic polymers, catalyzed by the metals present, may be even faster under actual braking conditions due to locally high surface temperatures and the presence of iron oxide nanoparticles from the third body on the pad surface. These particles may efficiently catalyze the decomposition of phenolic resin because of their high specific surface area.

An independent TGA analysis of the same pad material under an oxidizing atmosphere (20% O_2, 80% N_2) revealed a multi-stage thermal degradation process. An initial minor mass loss below 100°C was attributed to moisture evaporation absorbed during ambient storage despite prior curing. The material remained stable between 100°C and 220°C, with a slight mass increase around 200–230°C, suggesting early oxidation. Between 220°C and 430°C, two degradation phases were observed: the first likely associated with rubber decomposition (starting ~230°C), and the second with the breakdown of phenolic resin (initiating ~370°C). Above 430°C, the mass loss rate significantly slowed, indicating the presence of thermally resistant residues (Frangieh, 2025).

3.1.7.4 Synthesis of the VOCs identified in integrated samples

Table 3.20 summarizes the compounds detected in both normal and heavy pathways, in comparison with the literature, and presents a preliminary attempt to identify their source.

Phenolic compounds are among the abundant species in organic extracts. Many phenolic resins are used as binders in friction materials, such as brake linings, disc brake pads, and clutch plates, due to their heat resistance and adhesive performance. During braking, localized friction spots on the pad surface can reach temperatures of several hundred degrees Celsius, potentially leading to binder degradation. This degradation can reduce the braking system's stopping capability and significantly increase the wear rate of the system. This phenomenon, known as fading, results in a mass loss due to the breakdown of methylene and phenol groups (Alves et al., 2021; Kukutschová et al., 2011).

Table 3.20 Compounds detected in braking tests in comparison with the literature

Family	Compounds	NP	HP	Source	References	Compounds identified in the reference studies
Aldehydes	Formaldehyde, acetaldehyde, propanal, butanal, benzaldehyde	X	X	Phenolic resin	Plachá et al., 2017	Aromatic aldehydes (Benzaldehyde, Hydroxybenzaldehyde)
	Pentanal, hexanal, heptanal		X			
Ketones	Propanone, MVK, MEK	X	X	Rubber	Huang et al., 2022	Acetone, 4-methyl-2-pentanone
	Acetophenone		X			
Alcohols	Phenols (2,4-bis(1,1-dimethylethyl) phenol)	X	X	Phenolic resin	Alves et al., 2021 Plachá et al., 2017	aliphatic alcohols, sterols, benzyl alcohol, 2,4-di-tert-butylphenol), and 2,5-bis(1,1-Dimethylethyl)phenol Phenolic compounds
	6-Methyl-1-heptanol		X			
Alkenes	1,3,5,7-Cyclooctatetraene		X	Rubber	Alves et al., 2021	Tetradecene, hexadecene and octadecene
PAHs	Naphthalene		X	Phenolic resin	Plachá et al., 2017	Naphthalene and its derivatives. Fluorene …
	Methylnaphthalene 9-(Trimethylsilyl)fluorene	X	X			
Saturated Hydrocarbons	Heptadecane		X	Phenolic resin Lubricants	Plachá et al., 2017; Yao et al., 2023; Alves et al., 2021	Saturated Hydrocarbons (C12 to C29) Saturated Hydrocarbons (> C23) Saturated Hydrocarbons (C11 to C33)
Esters	1,4-Butylene glycol dimethacrylate	X	X	Stabilizer	Alves et al., 2021	Hydrocinnamic acid methyl ester
Organosilicon compounds	Hexamethylcyclotrisiloxane 1,1,3,3,5,5-hexamethyltrisiloxane Trimethyl(9H-fluoren-9-yl)silane	X	X	Lubricants	Yao et al., 2023	Methylsilxoanes and derivatives (Decamethylcyclopentasiloxane)
Sulfonamides	N-butylbenzenesulfonamide	X	X	Plasticizer	Plachá et al., 2017	N-Butylbenzenesulfonamide
Quinone	2,6-Bis(1,1-Dimethylethyl)-2,5-cyclohexadiene-1,4-dione	X	X	Phenolic resin	Plachá et al., 2017	Hydroquinone, p-Benzoquinone

3.2 Dynamics of the emissions

While average emissions provide a general understanding of overall emissions levels, they do not capture the temporal variations that occur during braking. To gain deeper insight into emission behavior, it is essential to examine the dynamics of the signal over time. For VOCs, a PID was used across all tests providing the dynamics of Total VOCs, while PTR-MS was employed only during the HP test to study the dynamics of individual VOC species, as this test was shown to produce the highest emissions and was therefore the most relevant for detailed analysis. For particles, the emission dynamics had been previously studied in (Frangieh et al., 2025) for the same experiments. Therefore, only the main findings will be cited in this chapter in order to compare both VOCs and particles dynamics.

3.2.1 TVOC emission trends under normal and heavy braking conditions using PID analysis

The PID was chosen for its simplicity in sampling and analysis, particularly as this study represents one of the first attempts to monitor VOC emissions within a braking pathway. The main purpose of PID is to monitor TVOC trends and detect peaks, rather than to precisely quantify emissions.

3.2.1.1 Peak selection

To ensure consistent identification of braking-related emissions, a systematic approach was developed to differentiate true peaks from background noise.

First, all blank measurements were analyzed, revealing only minor signal fluctuations with peak values consistently below 10 ppb. Accordingly, for the braking tests, a minimum threshold of 10 ppb was established for peak validation. Given that the baseline varies dynamically, each concentration value was assessed relative to its own local baseline, up to the peak maximum, without background subtraction. The section shown here in Figure 3.24 is an extracted part of the heavy pathway, presented solely as an example to illustrate the peak-selection procedure. Reported values will be presented as the mean concentration of all selected peaks, along with the corresponding standard deviation.

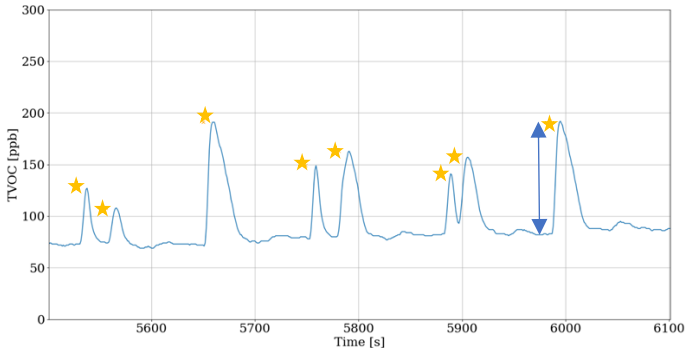

Figure 3.24 Yellow stars mark the peaks selected where the TVOC (ppb) values exceed baseline fluctuations observed in blank samples. Only peaks surpassing the background fluctuations are selected

3.2.1.2 PID dynamics during NP

The following analysis focuses on the PID signal evolution during the NP, exploring how braking events, temperature variations, and system-specific factors contribute to baseline shifts and signal interpretation challenges.

Figure 3.25 shows the evolution of the PID signal throughout the entire NP, with the exit enclosure temperature superimposed; each peak corresponds to a brake application. Thus, the PID is fully capable of detecting VOC emissions following a brake event. On the other hand, the increase in the baseline, despite using pure air at the inlet, suggests that the system is influenced by rising air temperature at the enclosure exit, which can interfere with the detection rate or the sensitivity of the detector itself to temperature fluctuations (Adamia et al., 1991). Additionally, steps in the signal correspond to the PID's automatic calibration, every hour, which alters the VOC background level. Since the PID baseline increases over extended periods, its reliability is limited, and the data should be interpreted with caution.

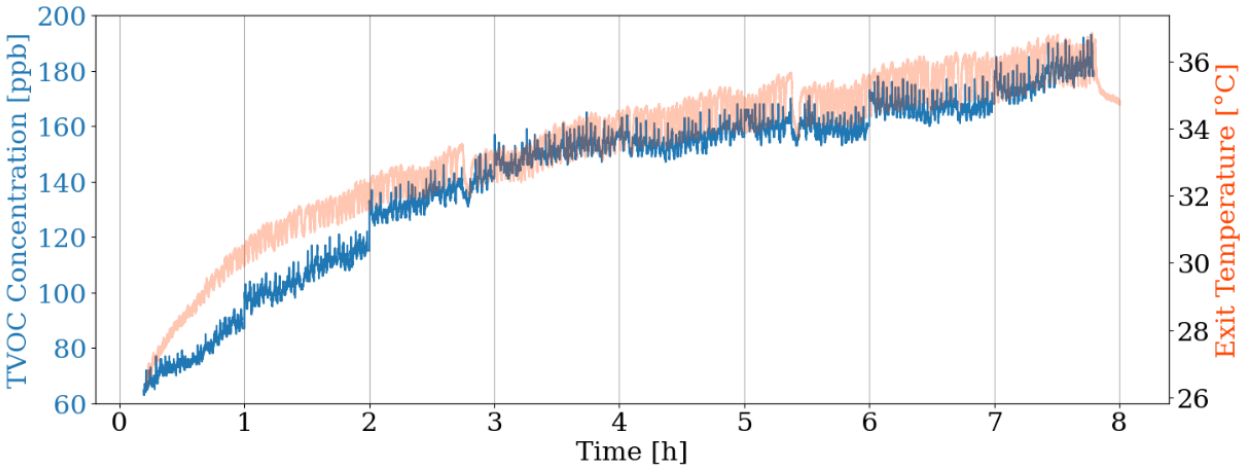

Figure 3.25 The evolution of the PID signal throughout the NP1, with the exit enclosure temperature superimposed

In addition, the increase in the PID baseline could be due to the emission of semi volatile compounds that may adhere to the inner surfaces of the set-up, mainly the tubing linking the VOC sampling point in the exit duct to the PID, requiring time to exit the system. This is supported by the fact that no similar effect on the background was observed with PTR-MS, where the sampling line was heated to prevent condensation of semi volatile species, unlike the PID setup. Additionally, the use of a 1 L/min volumetric flow rate facilitated flushing in the PTR-MS setup, and the presence of a capillary in the PTR-MS reduced residence time, further preventing baseline elevation, contrary to the smaller PID volumetric flow rate of 0.5 L/min.

Observations showed that after an experiment, the PID baseline gradually decreased from 55 ppb to 18 ppb (a drop of 36 ppb) over 87 seconds, confirming that air flushing alone, without additional intervention (brakings), is effective in clearing some of the semi-volatile compounds over time. Thus, as the average time between 2 braking events is about 93 s (min: 60.5 s), it is probable that the duration between brakings is also too short for the PID signal to fully return to its baseline.

3.2.1.3 PID dynamics during HP

The HP provides a clearer view of VOC emission dynamics under more intense braking conditions. This section examines the correlation between braking events, surface temperatures, and emission peaks, while also considering baseline behavior and system-related factors.

Figure 3.26 shows the evolution of the PID signal throughout HP1, alongside the mean temperature measured 2 mm from the surfaces of both the pad and the disc. In contrast to the NP, we can clearly

observe the trend due to higher emissions, including peaks per braking and the intensity of the peaks with respect to pad and disc temperatures.

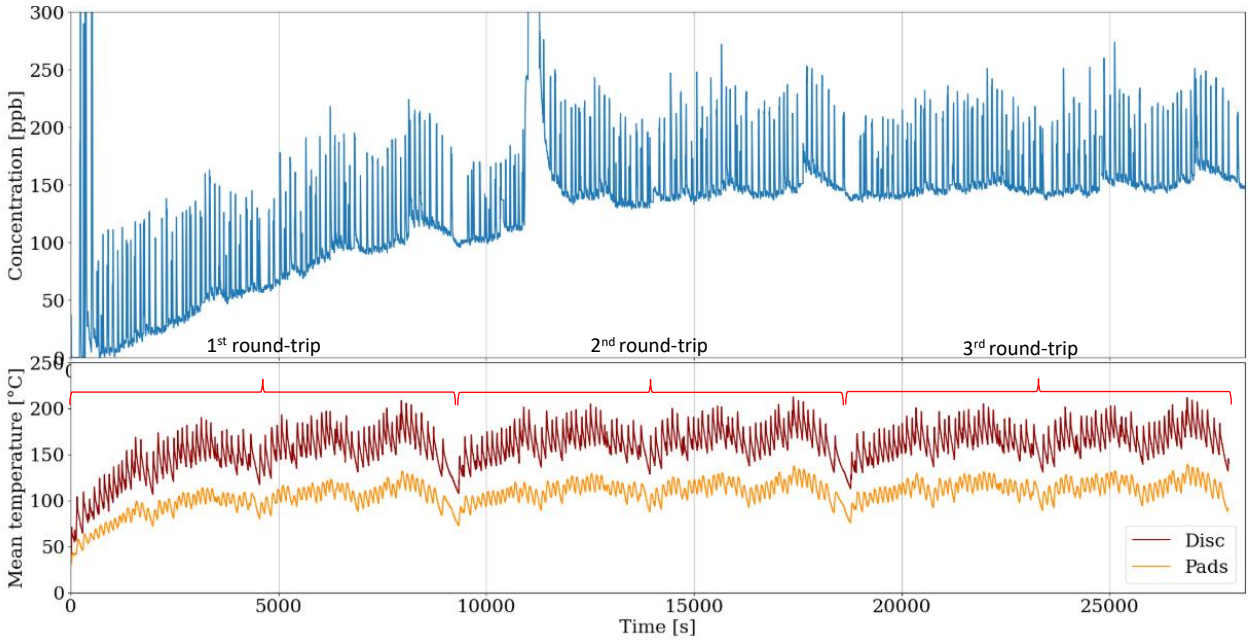

Figure 3.26 The evolution of the PID signal throughout the HP1, with the mean temperature at 2 mm from the surface of the pad and the disc

The pad and disc temperature profile and subsequently the PID baseline are related to the time/distance between stops. For example, when the time between stops increases, such as at the half and the end of each outbound and return trip, it allows the 1st bodies (pad and disc) to cool down. As a result, the temperature decreases, which is reflected by a corresponding decrease in the PID baseline.

Sharp peaks of TVOC were observed as soon as braking started, reaching the ppm level. As heat builds up in the pad and disc, the rising temperature causes the pad surface to change shape due to expansion. At the beginning, the pad takes time to recover its optimal shape and to achieve good conformity with the disc. When the conformity is not yet established, it becomes more difficult for the system to ensure proper contact between the two surfaces. With limited contact, typically occurring at only a few localized areas during the initial stage of the test, there are higher local solicitations, which lead to increased localized heating. This results in higher gas emissions, especially at the beginning, which explains the presence of these first sharp peaks. The first-round trip starts with a cold system that needs to adapt progressively. Then, with time, the system reaches thermal equilibrium and becomes more stabilized during the last two round trips.

It is also worth noting that an electrical issue occurred at around 11,000 seconds, which affected the baseline for a short period as shown in Figure 3.26.

3.2.1.4 Effect of braking power on TVOC emissions

To assess the influence of braking energy on VOC release, TVOC emissions from the NP and HP were compared using the reference pad. As shown in Figure 3.27, the HP resulted in a mean TVOC concentration increase above the local background of 69.01 ± 24.46 ppb, approximately 5.5 times higher than that observed during NP (12.64 ± 2.22 ppb). This significant increase is attributed to the

higher braking force, approximately 9 times greater in HP, which elevates the pad–disc contact temperature and consequently promotes greater VOC emission.

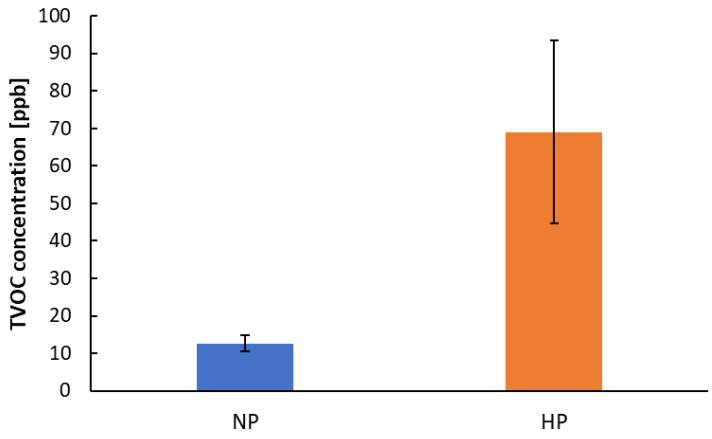

Figure 3.27 Effect of braking force using the reference pad by comparing the average TVOC concentration measured by PID of NP in blue and HP in orange

3.2.2 VOC emission dynamics during braking events: Time-resolved analysis using Proton Transfer Reaction–Mass Spectrometry (PTR-MS)

To gain a more detailed and selective understanding of VOC composition, PTR-MS was employed during the HP, targeting specific compounds beyond the total VOC signal provided by the PID. The analysis focuses on consistency with offline measurements, repeatability across the three round trips, the VOC profiles, and the behavior of VOCs between stations. Particular attention is given to the correlation with operating factors, as well as differences observed between single and multiple braking events.

3.2.2.1 Choice of compounds

The elimination of certain compounds from the analysis was based on specific criteria to ensure that only relevant VOC signals were considered. Compounds were excluded if they exhibited a consistent increase in the baseline without any noticeable variation during braking events, indicating that their presence was unrelated to the braking process. Additionally, compounds that showed zero concentrations throughout the entire measurement period were also disregarded, as they provided no meaningful information in the context of the experiment (Figure 3.28).

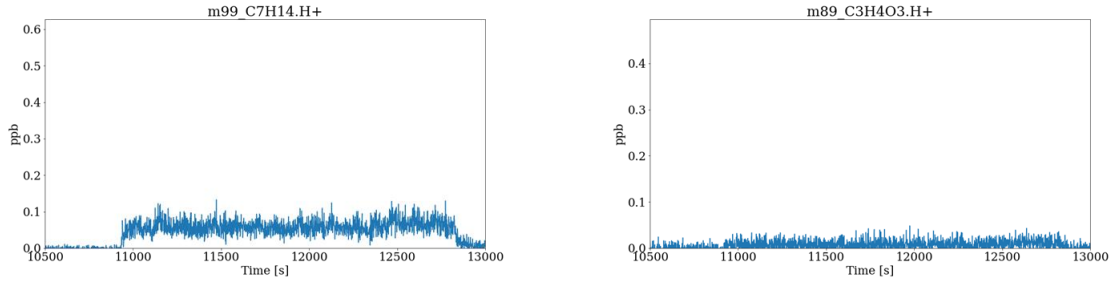

(a) (b)

Figure 3.28 Example of PTR-MS compound signals (a) exhibiting a baseline increase with no variation during braking, and (b) with zero concentration throughout the test

As a consequence, the selection focused on VOCs that exhibited changes during braking (Figure 3.29).

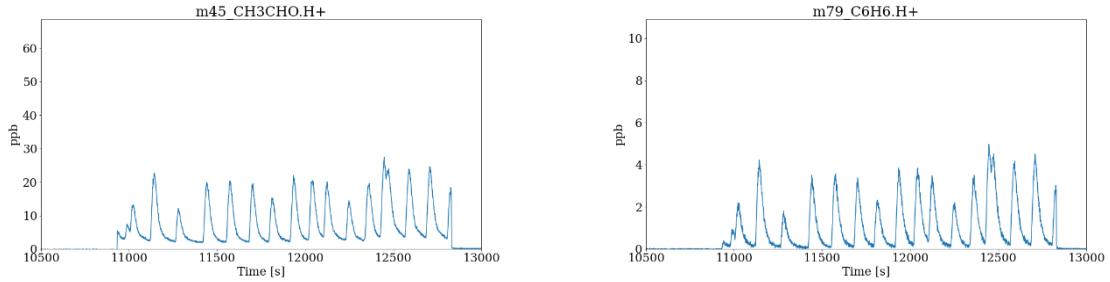

Figure 3.29 Examples of PTR-MS compound signals exhibiting strong increase from the baseline during braking throughout the test

The most intense signals were observed between 30 and 150 amu (atomic mass unit). Compounds with higher atomic masses were probably not observed due to the several filters introduced prior to the PTR-MS sampling line aiming at protecting the instrument from particles. These filters may have adsorbed semi- or non-volatile compounds, precluding them to be detected. Yet, the majority of the organic compounds corresponding to the proposed molecular formulas were typical of those commonly detected by PTR-MS from braking (Durif et al., 2025; Patel et al., 2024; Perraud et al., 2024).

They mainly included families as hydrocarbons (CxHy), ketones (R−C(=O)−R'), alcohols(R−OH), aldehydes (R-CH=O). Some of the observed peaks corresponded to amines, and to aromatic hydrocarbons including BTEX compounds (Benzene, Toluene, Ethylbenzene, and Xylenes) previously reported from simulated wear of a low-metallic pad (Plachá et al., 2017) were also detected. When the pads lose their effectiveness due to overheating, BTEX compounds could be degassed from the original brake linings (Plachá et al., 2017). However, as also observed in moderate stress conditions, they might potentially be formed, for instance, during the braking process via thermal degradation of the phenolic resin binders, as previous studies have demonstrated pyrolytic formation of benzene, toluene, and xylene from different phenolic resins (Bennett et al., 2014). Among other noticeable compounds were acetonitrile (C_2H_3N), which could come from the solvents used during the pad's manufacture.

Hydrocarbons, aliphatic and aromatics, were also confirmed by GC/MS; however, lighter and oxygenated compounds were better detected by DNPH/HPLC. For example, Table 3.21 shows a comparison between the common compounds detected by PTR-MS (averages over the limited periods of measurement) and DNPH cartridges analyzed by HPLC. Considering that the sampling periods are not the same, the agreement is rather good, except for formaldehyde where a ratio of about 17 is observed between DNPH and PTR-MS. This may be due to i) known higher uncertainty measurements

with PTR-MS because of a proton affinity close to water and ii) possible loss of formaldehyde on the filters.

Table 3.21 Comparison of PTR-MS vs DNPH measurements of some compounds during HP

Compound	DNPH [µg/m^3]	PTR-MS [µg/m^3]	Ratio DNPH/PTR-MS
Formaldehyde	3.94	0.23	17.11
Acetaldehyde	7.05	4.46	1.58
Acrolein	<LD (0.018)	0.54	-
Propanone	3.40	3.55	0.96

In comparison with literature (Dunne et al., 2018) for the C1–C3 carbonyls, the uncertainty in a set of measurements varies by a factor of between 1.5 and 2. Accordingly, our results show a ratio lower than 1.6, excluding formaldehyde that is usually not well detected with PTR-MS.

For TVOC measurements, the comparison between PID and PTR-MS was unsuccessful, as PID readings were 40 times higher than those of PTR-MS. This difference could be due to the PID being calibrated using a single compound, isobutylene, at a high concentration (10 ppm), whereas the actual emissions were in the ppb range. Additionally, PID assumes that all detected compounds respond similarly to isobutylene, which may not be accurate.

Thus, the compound name suggestions are mainly based on cross-comparison with the offline measurements (Tenax and DNPH cartridges). A selected list of compounds is presented in Table 3.22. Some compounds, such as those detected at m/z = 46, 63, 67, 85, 91, 103, 109, 111, 113, 115, 119, 121, 123, 131, 133, and 147, are included in the selection but not shown in the table, as their molecular formulas could not be identified.

A particular emphasis is placed on the major ones highlighted in orange based on their concentration intensity. Despite the underestimation of formaldehyde by PTR-MS (its concentration being approximately 17 times lower than that measured by DNPH cartridges), it was still identified as one of the major VOCs due to its well-documented presence in the thermal degradation of organic brake components (Chen et al., 2013; Shorowordi et al., 2009) in addition to the interest in studying its dynamics during braking.

The abbreviation 'frag' refers to the fragment ion's m/z ratio at which the VOC is detected, rather than its molecular ion. In contrast, the other VOCs without ‘frag' are detected at their actual (molecular) m/z ratios.

In the following sections, 'total VOCs' will refer to the total concentration of the compounds listed in Table 3.22, with the exception of m57_frag.C4H8.H$^+$, for reasons that will be discussed in the coming sections. When examining specific behaviors, the focus will primarily be on the major VOCs.

Table 3.22 List of VOC compounds detected by PTR-MS from braking during HP, compounds highlighted in orange represent the major VOCs.

List chosen ($m.H^+$)	Suggested name	Comparison with literature
m31_HCHO.H^+	Formaldehyde	(Perraud et al., 2024)
m33_CH3OH.H^+	Methanol	(Durif et al., 2025; Patel et al., 2024; Perraud et al., 2024)
m41_frag.C3H4.H^+	Isoprene	
m42_C2H3N.H^+	Acetonitrile	(Durif et al., 2025)
m43_frag.C2H2O.H^+		(Patel et al., 2024)
m43_frag. C3H6.H^+		
m45_CH3CHO.H^+	Acetaldehyde	(Patel et al., 2024; Perraud et al., 2024)
m47_C2H6O.H^+		
m57_C3H4O.H^+	Acrolein	(Patel et al., 2024)
m57_frag. C4H8.H^+		(Patel et al., 2024)
m59_C3H6O.H^+	Propanone	(Durif et al., 2025; Patel et al., 2024; Perraud et al., 2024)
m69_C4H4O.H^+		(Perraud et al., 2024)
m69_C5H8.H^+		(Patel et al., 2024)
m71_C4H6O.H^+		(Patel et al., 2024)
m71_C5H10.H^+		
m73_C4H8O.H^+		(Durif et al., 2025; Patel et al., 2024)
m77_C3H8O2.H^+		
m78_C6H5.H^+		
m79_C2H6O3.H^+		
m79_C6H6.H^+	Benzene	(Durif et al., 2025)
m81_C6H8.H^+		
m83_C5H6O.H^+		(Patel et al., 2024)
m83_C6H10.H^+		(Patel et al., 2024)
m85_C5H8O.H^+		(Patel et al., 2024)
m85_C6H12.H^+		
m87_C5H10O.H^+		
m93_C7H8.H^+	Toluene	(Durif et al., 2025)
m95_C7H10.H^+		
m97_C5H4O2.H^+		(Patel et al., 2024)
m97_C6H8O.H^+		(Patel et al., 2024)
m97_C7H12.H^+		(Patel et al., 2024)
m99_C6H10O.H^+		
m101_C6H12O.H^+		
m105_C8H8.H+		
m107_C7H6O.H^+	Benzaldehyde	(Durif et al., 2025)
m107_C8H10.H^+	Xylene/ Ethylbenzene	(Durif et al., 2025)
m137_C10H16.H^+		

3.2.2.2 Backgrounds of the major VOCs

Background measurements conducted before the test, using pure air and disc rotation, offer insight into the baseline levels of these VOCs and their behavior between stations. The levels of the major VOC are shown in Figure 3.30. For m31, m57, and m43, the concentrations were 0, while m41, m42, m45, m59, m79, and m93 showed relatively low concentrations below 7 ppb. The compound m33 exhibited the highest background concentrations, ranging between 7 and 14 ppb.

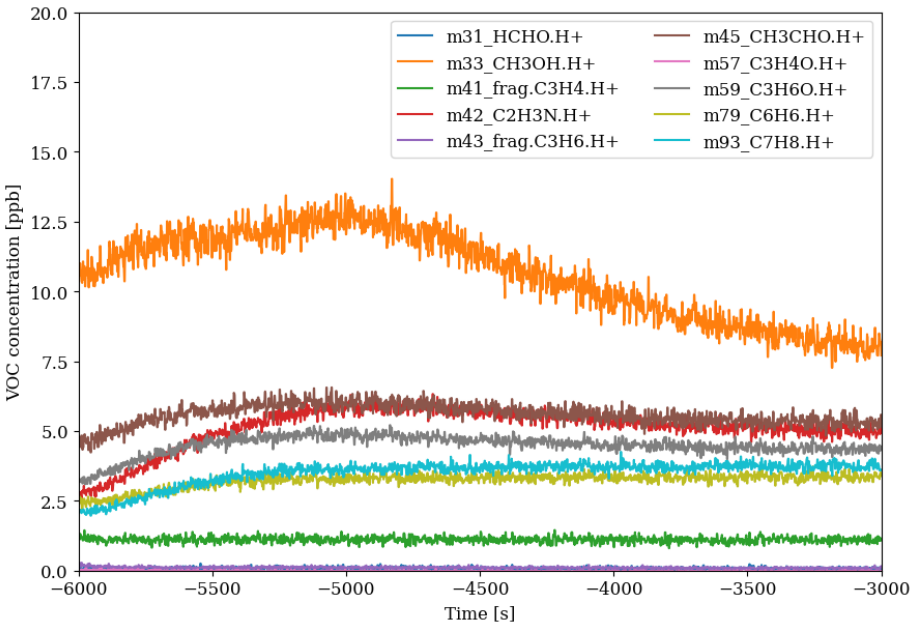

Figure 3.30 Background measurements were conducted for 50 min prior to the test, focusing on the major compounds. These measurements used pure air (Alpha Gas 1) with disc rotation inside the enclosure

The baseline check confirmed that no VOC emissions originate from the pad when the disc is rotating without braking, even if the pad remains hot; only background noise was detected.

3.2.2.3 Overview of VOC emissions and temperature evolution with time

Following the background assessment, this section provides a time-resolved overview of VOC emissions, as well as PM and temperature evolution, during the HP. The goal is to highlight overall trends across the three round trips and to establish the relationship between thermal behavior and emission dynamics before focusing on individual braking events and compounds in detail.

Figure 3.31 presents data from the three consecutive round trips of the HP using the reference pad, tracking the emissions behavior with respect to pad and disc temperatures. For comparison, the top image displays the PM emissions for both FMPS (in gray) for particles 5.6 - 560 nm and OPS (in blue) for particles 0.3 - 10 µm, while the second image represents the total VOCs of all the selected compounds in brown. The bottom image illustrates the corresponding temperature evolution recorded at 2 mm below the friction surface of the pad (in dark orange) and the disc (in dark red). The break time between the first and second round trips occurs at 2.5h, and the one between the second and third round trips at about 5h10min. They correspond to an absence of emission of particles and drops of the temperatures.

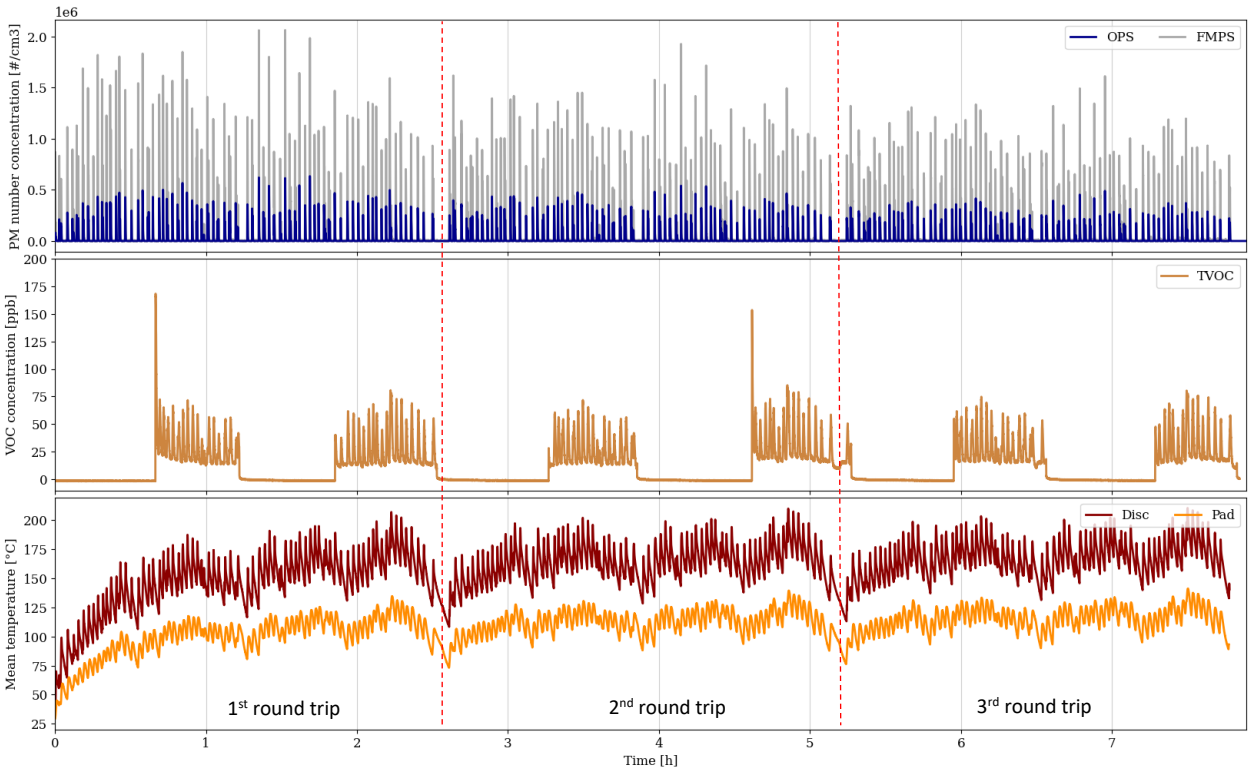

Figure 3.31 The upper panel shows particle emissions measured by OPS and FMPS; the middle panel presents the emissions of the sum of selected VOCs measured by PTR-MS (intermittent measurements); and the bottom panel shows the temperature evolution of the pad and disc, measured 2 mm from their surfaces.

Since we were measuring over 8 h in high-temperature conditions (Table 3.1), the FMPS electrometers heated, increasing the baseline throughout the test; thus, a correction has been applied to the baseline. For the OPS, there was no drift in the baseline; therefore, no correction was required.

FMPS shows higher particle emissions than OPS, indicating that fine and ultrafine particles are generally more abundant during each braking event and throughout the test compared to coarse and fine particles. Distinct peaks in PM emissions are observed, depending on the braking force. The time interval between two metro stations determines the extent of temperature drops between brake applications, which in turn affects chemical processes (such as oxidation) and thermomechanical deformations (such as expansion variations). This makes it a key factor in the thermal history of the route profile. The first round-trip is significantly different from the subsequent ones, as its temperature profile shows a stepwise increase until the system reaches thermal stability.

VOC measurements with the PTR-MS were conducted intermittently, approximately twice per round trip, to prevent any damage of the instrument due to a continuous exposure to braking emissions (see 2.6.2.2). At the start of each VOC measurement, a sharp spike in TVOC concentration is observed, likely corresponding to the accumulation of TVOC in the sampling system. Subsequent TVOC peaks are related to each braking event. Between the trips, the VOC concentration drops nearly to baseline levels. Overall, the pattern reflects a link between thermal events and VOC release. A deeper look into each braking event and for each compound will be studied in detail later.

3.2.2.4 Repeatability of VOC emissions across round trips

After establishing the overall emission trends, this section evaluates the repeatability of VOC emissions across three consecutive return (R) trips. Although consecutive braking during the HP showed a lack of repeatability, a cyclic pattern emerged between round trips. The aim is to determine whether consistent braking conditions lead to stable emission profiles, despite minor variations in temperature, wear, or friction.

Figure 3.32 presents the evolution of total VOC concentrations emitted at each station stop for eight consecutive station stops during the HP, categorized by round trip and annotated with color-coded markers. The lower section of the figure displays the corresponding speed and braking force at each station during the three round trips. The temporal alignment of station events used the first-round trip as the reference. Time shifts observed in subsequent trips are attributed to a gradual decrease in friction, resulting in slightly longer braking durations during the second and third round trips.

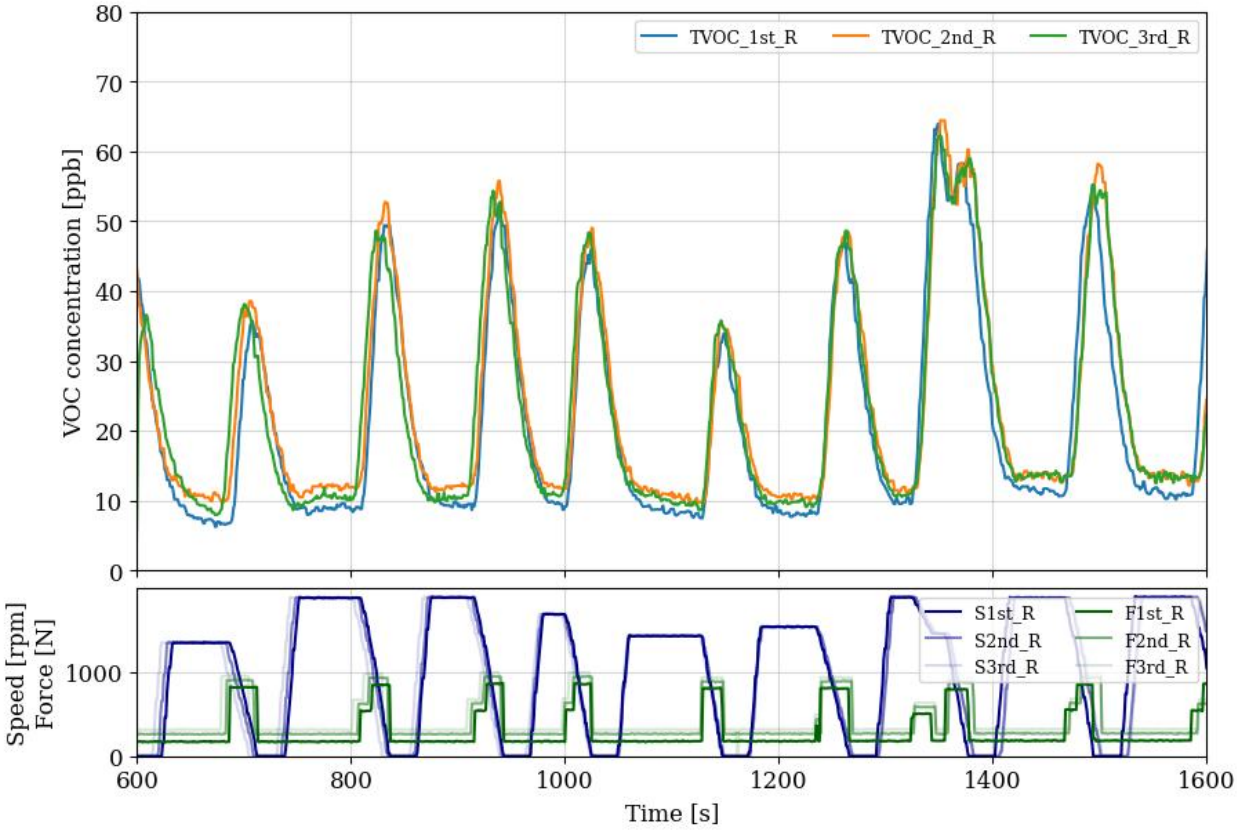

Figure 3.32 Time-resolved profiles of TVOC concentrations measured by PTR-MS (top panel) and the corresponding disc rotational speed and applied force (bottom panel) during three consecutive return rounds

Each station consistently exhibited a characteristic emission signature. Since each braking event is different from the others, and each station has a unique signature, the VOC concentrations also varied. For example, stations with lower emissions (first and fifth in the figure) during the first trip also showed lower emissions in the following two trips. This suggests that similar thermomechanical and operational conditions at each station lead to consistent tribological behavior, highlighting the role of station-specific factors in VOC generation.

Importantly, repeating the same round trip three times produced a consistent VOC emission pattern. Despite progressive wear, the total VOC concentrations remained nearly identical across TVOC and all

measured species in each return trips. This high repeatability suggests that VOC emissions are less sensitive to cumulative wear, braking history and surface bedding than PM, as discussed in Frangieh et al., (2025); particle emissions showed a clear decrease from the first to the third-round-trip, highlighting a key difference in their emission behavior compared to VOCs, which have primarily a chemical origin rather than a mechanical one.

3.2.2.5 Temporal behavior and source classification of VOC

Following the identification of major VOC compounds emitted during HP, this section explores the temporal dynamics of VOC emissions in relation to key braking parameters such as disc and pad temperatures, contact forces, and rotational speed, under different classes based on their emission patterns and response to braking.

As shown in Figure 3.33, VOC emissions begin to increase with braking but do not peak during the initial stage of braking, when surface temperatures are at their highest. Instead, maximum VOC concentrations are often observed after the peak contact temperature has been reached. Considering that the temperature is measured 2 mm below the surface, there is an even larger time delay before surface heating is reflected in the recorded VOC concentration values, particularly in the pad, which has low conductivity. Furthermore, emissions continue even after the braking event has concluded, suggesting that the thermal and chemical processes responsible for VOC generation persist beyond the deceleration phase.

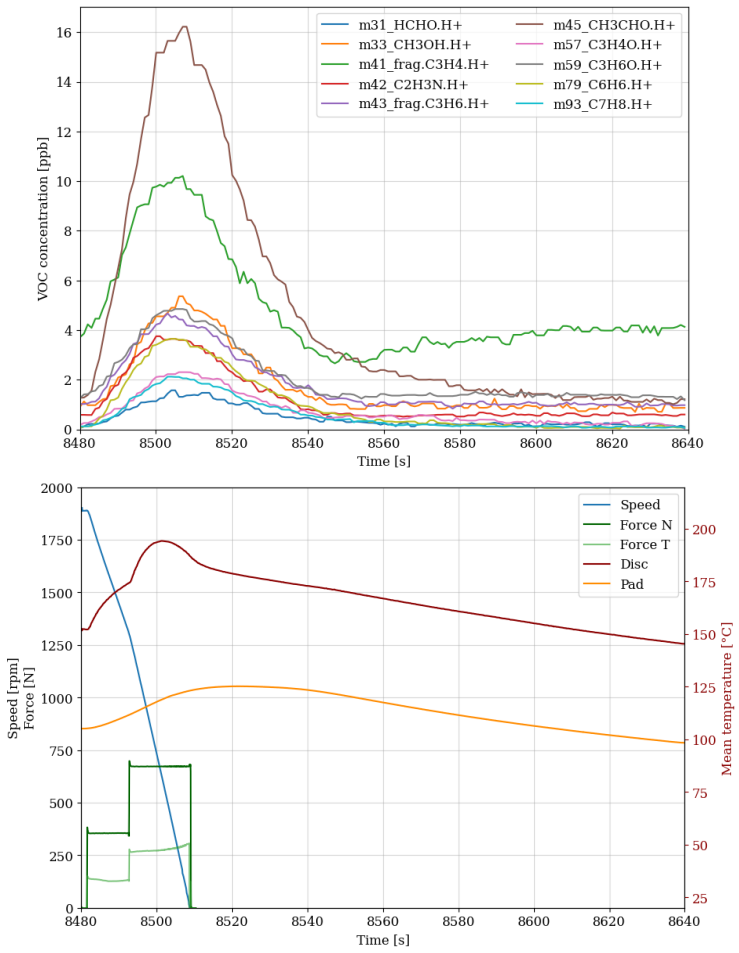

Figure 3.33 Dynamic emissions of the major VOCs measured by PTR-MS and braking parameters (pad and disc temperature, normal and tangential force, and speed) during a typical braking event

Figure 3.34 presents the major VOCs identified across the entire pathway, and highlights the proportional contribution of each compound. It is evident that the distribution of VOCs is relatively consistent throughout the three round trips, without significant shifts in dominant species from one station to another. This indicates a steady-state emission profile likely tied to continuous brake usage rather than temporary spikes.

Key contributors likely include alkanes, aromatics, and oxygenated VOCs (aldehydes, ketones and alcohols), many of which originate from thermal degradation and oxidative reactions of the brake pad's organic components under friction-induced heat. The consistent pattern across the round trip suggests a persistent emission mechanism, possibly related to pad formulation and brake application strategy.

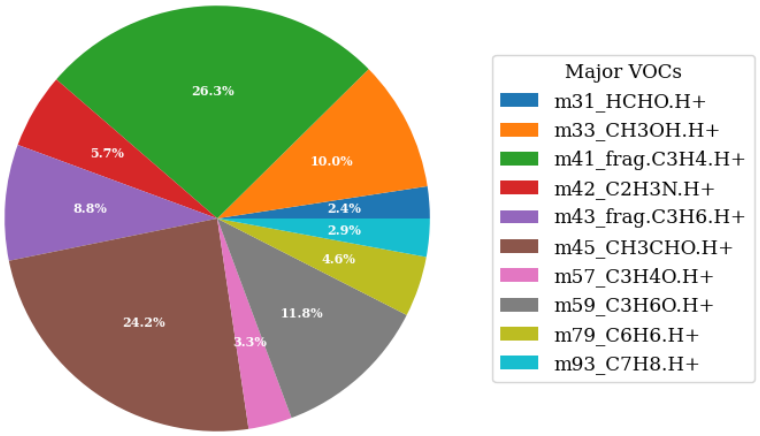

Figure 3.34 Major VOCs distribution throughout the whole heavy pathway

After analyzing the variation dynamics of each major VOC, it was observed that the majority of the compounds follow the temperature profile, with a slight delay due to the two-second system response. However, differences exist between some masses, indicating different behaviors between VOCs. The VOCs are divided into 3 categories as shown in Table 3.23.

Table 3.23 Classification of major compounds based on braking and disc rotation influence

First category	Second category	Third category
Increase with braking	**Increase with braking & disc rotation**	**Increase with disc rotation**
$m31_HCHO.H^+$ $m33_CH3OH.H^+$ $m42_C2H3N.H^+$ $m43_frag.C3H6.H^+$ $m45_CH3CHO.H^+$ $m57_C3H4O.H^+$ $m79_C6H6.H^+$ $m93_C7H8.H^+$	$m41_frag.C3H4.H^+$ $m59_C3H6O.H^+$	$m57_frag.C4H8.H^+$

First category:

These compounds are generated when the surface temperature increases during braking. Once braking is finished and the temperature starts to decrease, VOC emissions also decrease. Then, when the disc starts rotating again, compounds either stabilize at their background levels or decrease, probably because some compounds, such as formaldehyde (m31_HCHO.H^+), are sticky and get stuck inside the tube, where they are slowly removed.

Second category:

This category involves compounds which detection increases during braking and disc rotation. Figure 3.35 presents the emission profiles of these two compounds, (a) m41_frag.C_3H_4.H^+ and (b) m59_C_3H_6O.H^+, for one station (#214) with respect to speed and force. As the braking starts, the emissions begin to increase, as observed for all compounds during typical braking. After the braking ends, the VOC concentration gradually decreases. However, in all interbraking measurements, although the braking has finished and the pad and disc temperatures decrease, when the disc starts rotating again, an increase in emissions is observed, although it is less intense than during braking.

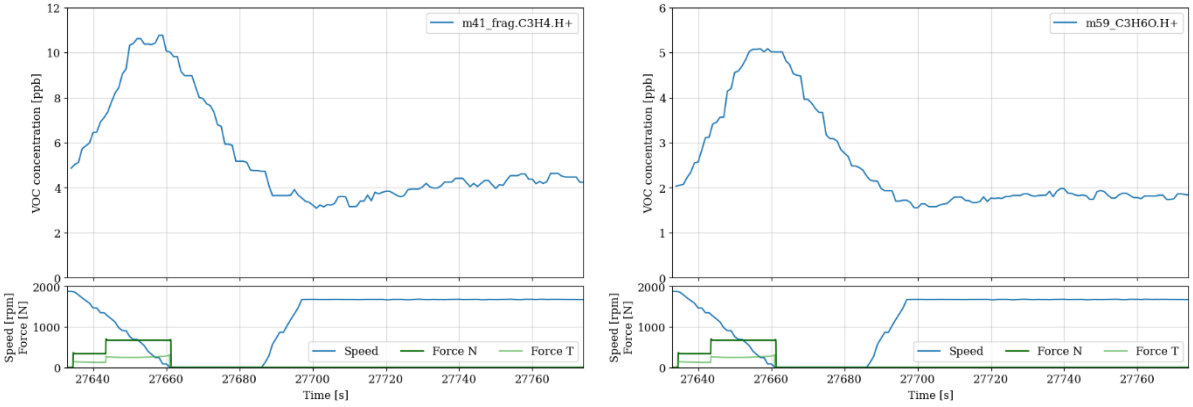

(a) (b)

Figure 3.35 Braking profiles of (a) m41_frag.C3H4.H^+ and (b) m59_C3H6O.H^+ concentrations (top panel) and their corresponding disc rotational speed and applied force (bottom panel)

Hence, we can assume that there are two sources or processes of this type of VOCs: one originating from the pad during braking (similar to the rest), and another, unlike the other compounds, during disc rotation (between two stations).

Disc rotation could be influencing the VOCs by three aspects:

1. Energy flux in the materials
2. Air circulation in the enclosure
3. System components

1. Energy flux in the materials

After the braking ends and the disc starts rotating again, the temperature in the enclosure starts rising (Figure 3.36) due to 2 sources of heat, which could promote a chemical reaction:

a) Inversion of the heat flux in the pad toward the surface
b) Cooling of the disc that is very close to the pad

a) When the pad is heated during braking, due to the energy dissipated, the heat flux flows inward; i.e., the maximum temperature is at the surface and the thermal flux is distributed throughout the pad by diffusion. producing a high peak of VOC. Then, when the contact opens, the situation is reversed; i.e., the surface layer temperature decreases rapidly, creating a temperature gradient resulting in a reverse flux, where the heat flux increases towards the surface, which could lead to the release of some VOCs.

b) When the brake is released, the pad surface remains close to the disc. Since the speed is zero, the pad faces a fixed area of the disc, which is no longer rotating. Given the close proximity of the surfaces and the elevated temperature of the disc, heat can be radiatively conducted from the disc to the pad. This contributes to the disc's cooling, but the pad's heating may lead to an increase in VOC emissions.

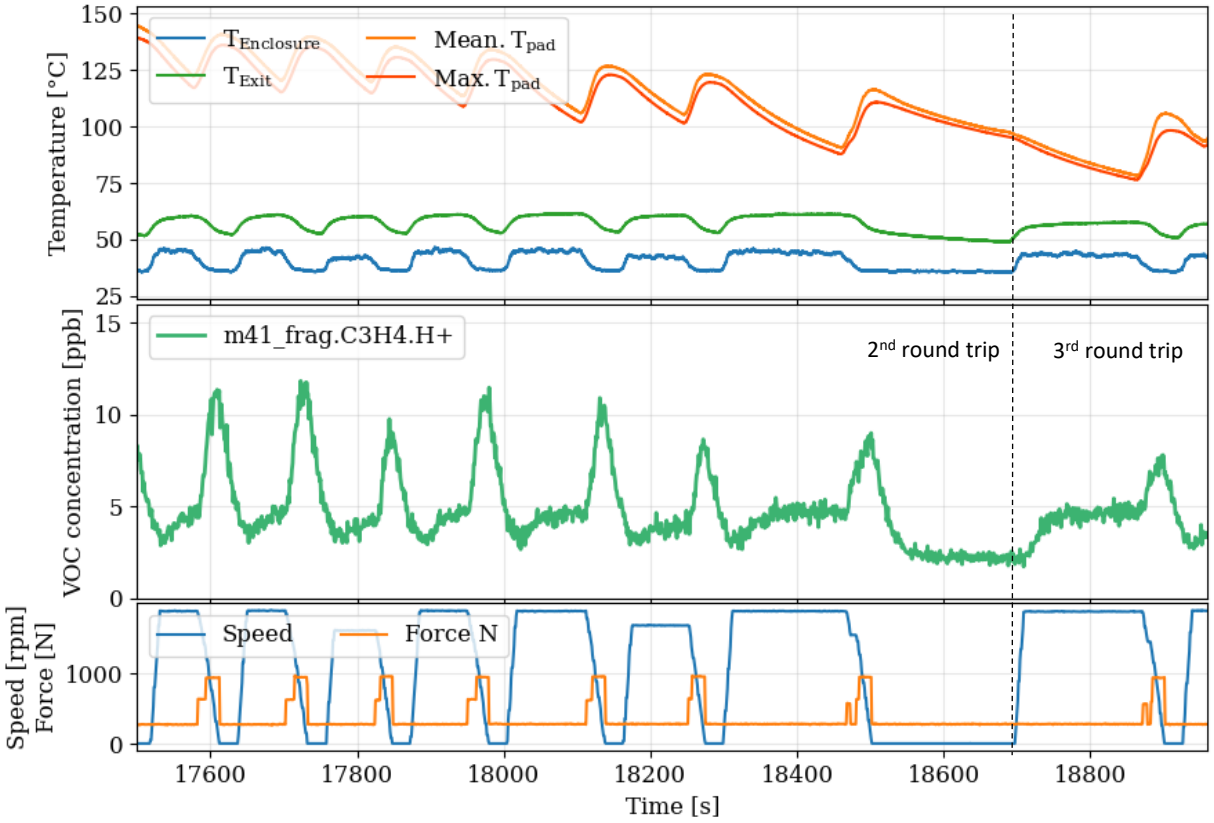

Figure 3.36 Time evolution of pad temperatures (average and maximum) and ambient temperatures (enclosure and exit) in relation to the evolution of m41_frag.C3H4.H⁺ during the transition from the second to the third round trip

In addition, as shown in Figure 3.36, after the second round trip ends and the system rests for 2–3 min, VOC concentrations (e.g., m41_frag.C3H4.H⁺) decrease and stabilize. However, once rotation resumes in the third-round trip, VOC levels rise again, even with low pad temperatures (~75 °C). This behavior suggests that VOC emissions are not just dependent on contact temperatures but are also influenced by ongoing heat exchange and air movement in the system.

This is consistent with thermal convection principles: as the disc speed increases, air circulation between the disc and pad intensifies, enhancing heat transfer into the enclosure. Since convection scales with the square of the speed, this leads to a measurable ambient temperature increase (~10 °C).

This rise is attributed to the release of heat previously stored in the disc during braking, now transferred to the enclosure as the disc cools during motion. The resulting temperature elevation and airflow may mobilize trapped VOCs or drive secondary emissions, contributing to the observed increase in background VOC concentration after each braking event.

2. Air circulation in the enclosure

Considering VOCs originate from the pad and require increased contact temperature to be produced, it is possible that these VOCs have already been produced, but have remained trapped in the enclosure until the disc begins rotating.

Another observation from the tracer experiment (Appendix 1) is that at zero rotation, when a tracer gas is introduced, it does not fully exit the system, only about half escapes, while the other half diffuses into the enclosure. When rotation resumes, it likely pushes the previously diffused emissions from the bottom of the enclosure toward the exit. Therefore, the observed increase in VOC levels when the disc starts rotating again may be attributed to the sweeping out of accumulated VOCs that had previously diffused into the system. But in this case, other species would probably also be observed.

3. System components

The enclosure (PVC) itself may be a source of emissions, as the temperature inside is increasing. However, during the 8-h offline sampling (2.8.5.3), no pronounced related peak in the measurements was observed, so it is unlikely that it was emitting VOCs.

Another source could be the grease on the bearings; however, they are located on the exterior axis. Thus, normally, they cannot enter the chamber.

Third category:

In this category, one compound is exclusively present as it only evolves with disc rotation. The background measurements are shown in Figure 3.37 (a) and the time-resolved profiles during the three consecutive return round trips of the HP of m57_frag.C4H8.H^+ in Figure 3.37 (b). Unlike the other compounds, m57_frag.C4H8.H^+ does not originate from the braking events, as it is only related to speed (same temporal profile), as shown in Figure 3.37 (b). However, during the background measurements shown in Figure 3.37 (a), conducted before the test began, when the system was cooled down with no braking but with disc rotation, no significant level of the m57_frag.C4H8.H^+ was detected. Therefore, its presence during the braking tests cannot be directly attributed to disc rotation alone. However, the same explanations can be suggested as those already discussed for the second category.

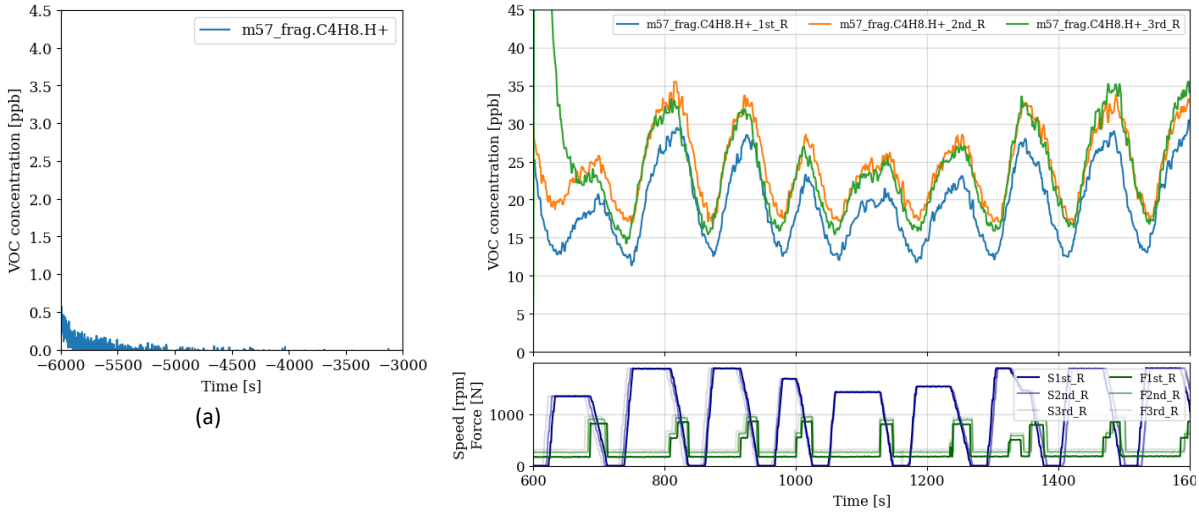

Figure 3.37 Measurement of m57_frag.C4H8.H⁺ (a) background (b) Time-resolved profiles of m57_frag.C4H8.H⁺ concentrations (top panel) and the corresponding disc rotational speed and applied force (bottom panel) during three consecutive return rounds

3.2.2.6 Correlations between VOCs and braking parameters

This section aims to examine the correlations between VOC emissions and a set of braking-related parameters exclusively under single braking application to avoid any noise that could be attributed to multiple braking applications. These parameters include dissipated energy, initial braking speed, maximum normal force, maximum disc temperature, interstation duration (duration between braking events), and braking duration. Through this focused approach, we try to better understand the contributors to VOC emissions. The results are presented in Figure 3.38.

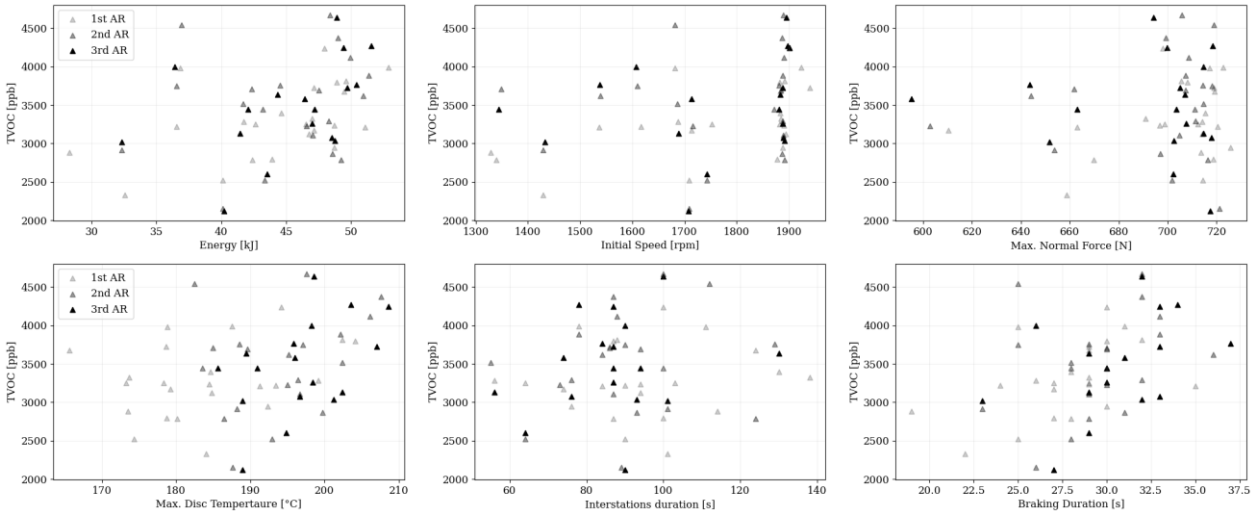

Figure 3.38 Relationship between total VOC concentrations measured by PTR-MS and braking parameters under single braking conditions

When considering total VOC emissions, identifying a clear trend is more difficult, as each individual VOC may behave differently. As a general observation, no consistent trend was found with respect to initial speed, interstation duration, or maximum normal force. However, for the force, the interval is quite short, making it difficult to draw a firm conclusion.

Regarding interstation duration specifically, unlike particles, which may accumulate in the contact interface and be released later, even if not freshly produced, Most of VOCs are expected to be emitted directly from the contact. This emission behavior makes it more reasonable that no effect of interstation duration is observed on total VOC levels.

A scan of the major VOC compounds with respect to the braking parameters showed that the compounds of the second category (m41_frag.C3H4.H^+ and m59_C3H6O.H^+), in addition to m43_frag.C3H6.H^+, have no trend with any braking parameter. For the rest of VOCs, they mostly tend to have a relation with the dissipated energy (Figure 3.39), disc temperature (Figure 3.40), and braking duration (Figure 3.38).

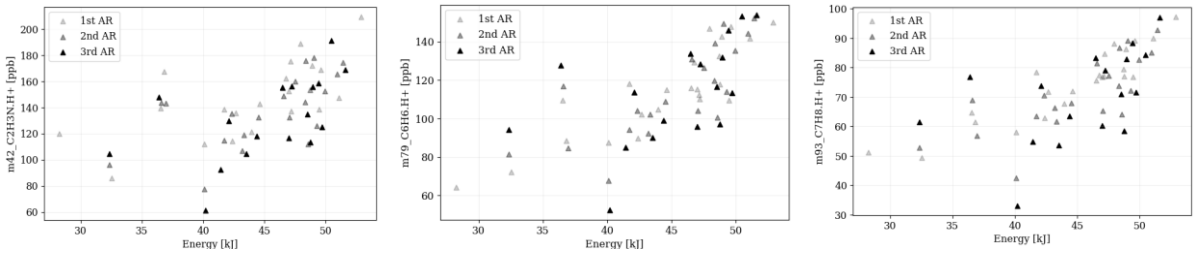

Figure 3.39 Relationship between dissipated energy and m42_C2H3N.H^+ (acetonitrile), m79_C6H6.H^+ (benzene), and m93_C7H8.H^+ (toluene) across the round trips with single braking application

The best correlation with temperature was observed for m57_C3H4O.H^+. It is also noteworthy that during the initial range of maximum temperatures, the data were predominantly from the first-round trip (indicated by lighter triangles), highlighting that the system becomes more thermally stable over time, particularly during the second and third round trips.

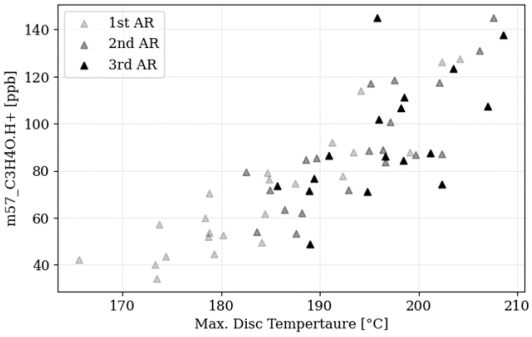

Figure 3.40 Relationship between maximum disc temperature and m57_C3H4O.H^+ (acrolein) across the round trips with single braking application

Another approach to improve the regression was to average data over defined intervals and include their standard deviations; however, the results did not change significantly (Figure 3.41).

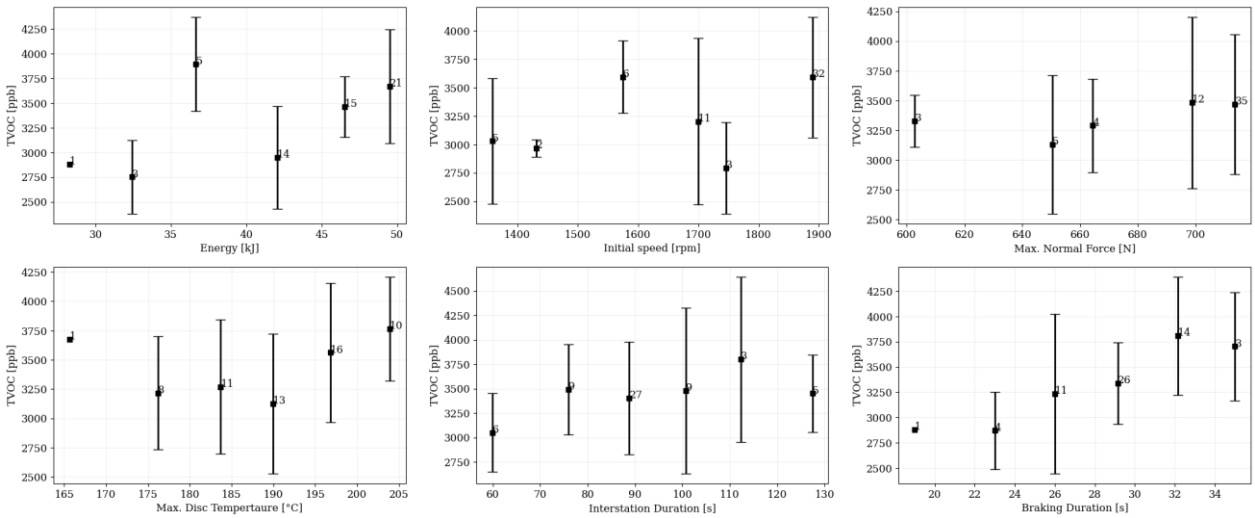

Figure 3.41 Relationship between total VOC emissions and braking parameters under single braking conditions (with averaged intervals)

Figure 3.42 presents the relationship between TVOC emissions and maximum braking power during single braking events. Each subplot incorporates a third parameter: the top plot shows normal (braking) force, the middle plot shows tangential (contact) force, and the bottom plot shows initial speed. While braking power reflects the product of force and speed, it does not appear to directly correlate with TVOC emissions across the full range of events. Generally, TVOC emissions exhibit a decreasing trend with braking power. Emissions plateau or scatter appear significantly beyond 3.6 kW.

In the top panel, even under higher normal forces (darker markers), VOC emissions span a wide range and do not follow a consistent upward trend. In the middle panel, the influence of tangential force is visualized. Here, data points with higher normal forces tend to cluster within a mid-range of VOC emissions. This supports the hypothesis that stronger contact pressure between the pad and disc results in a more tightly closed interface. Such closure can hinder the release of some volatile compounds by trapping them within the material. The bottom panel explores the role of initial speed. Higher speeds (darker points) may contribute to higher power, but again, they do not systematically result in higher VOC emissions. This suggests that although speed contributes to the thermal energy input, it does not govern VOC release without considering how it interacts with loading and contact conditions.

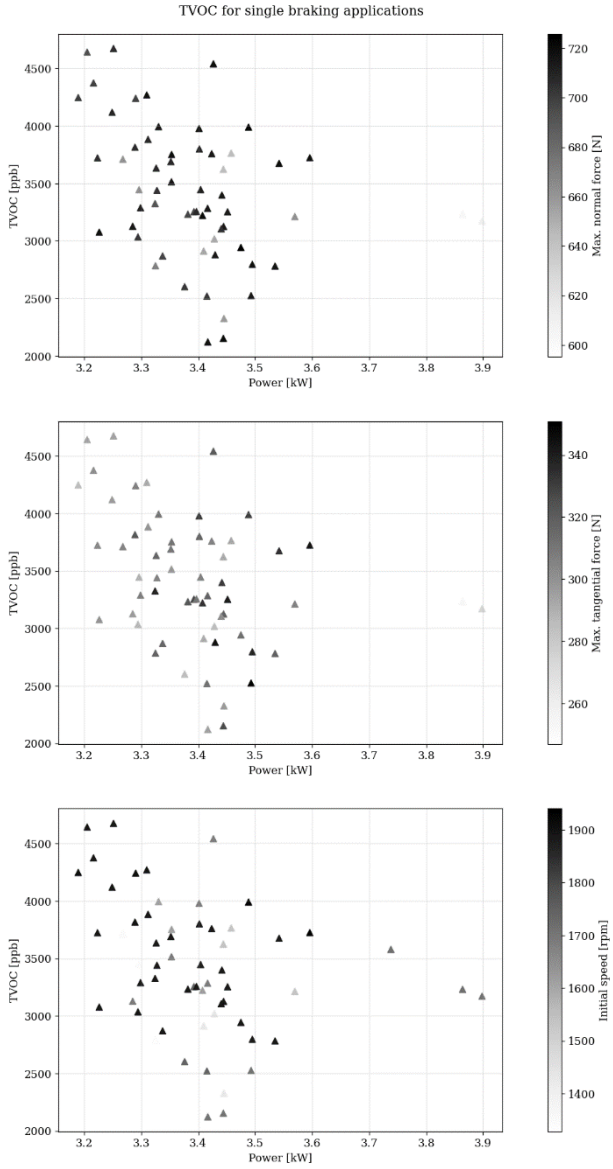

Figure 3.42 Influence of maximum braking power, force components, and initial speed on Total VOC emissions during single braking applications

Among the major compounds analyzed, m57_C3H4O.H$^+$ exhibited the strongest relationship with braking power (Figure 3.43). A clear decreasing trend is observed: as power increases, the VOC concentration steadily decreases. Additionally, the color scale (representing tangential force) shows that lower power values are associated with lower tangential forces, which coincide with higher concentrations of m57_C3H4O.H$^+$. This suggests that under lower mechanical and thermal load conditions, the emission of this compound is favored. Conversely, as both power and force increase, its emission decreases, likely due to tighter conditions at the contact interface.

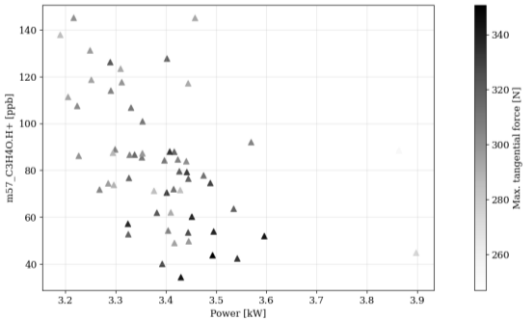

Figure 3.43 Influence of maximum braking power, tangential force on m57_C3H4O.H⁺ (acrolein) during single braking applications

3.2.2.7 Emission behavior under single braking application

- Mass-resolved and time-dependent characterization of VOC emissions

Figure 3.44 and Figure 3.45 present mass fragments on the y-axis. In the first plot, the x-axis represents time, and the grey-color scale indicates when each fragment is most concentrated on a logarithmic scale, while the blue line shows the total VOC concentration. In the second plot, the x-axis represents the total sum of VOCs over the station duration.

During braking, lower-mass VOCs tend to appear at higher concentrations than the heavier compounds. Following the emission peak, these lighter species continue to be released, while higher-mass VOCs decline rapidly. This observation must be interpreted in light of the experimental setup: four filters were positioned upstream of the PTR-MS, potentially capturing semi-volatile or larger molecules through adsorption or condensation on particles before they could be detected.

Although the filters were replaced midway through the test, their progressive loading with PM likely enhanced the retention of heavier compounds. As a result, the reduced detection of VOCs with molecular weights above ~140 amu reflects instrumental limitations rather than their true absence. In contrast, lighter VOCs are more reliably captured, although detection still varies with individual compound properties.

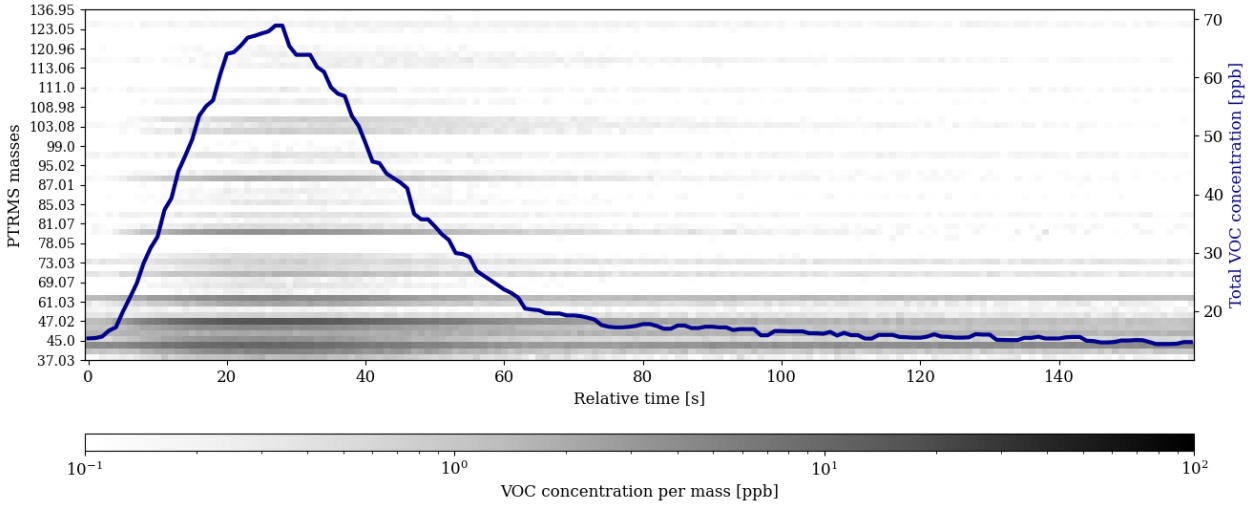

Figure 3.44 Heatmap representation of VOC concentration (ppb) per PTR-MS mass as a function of relative time of a single station. The blue line indicates the total VOC concentration (right y-axis). Each horizontal line corresponds to a specific PTR-MS mass, with darker shading indicating higher VOC concentration. The plot illustrates the dynamic release and subsequent decline of individual VOC masses and total VOCs over the course of the measurement

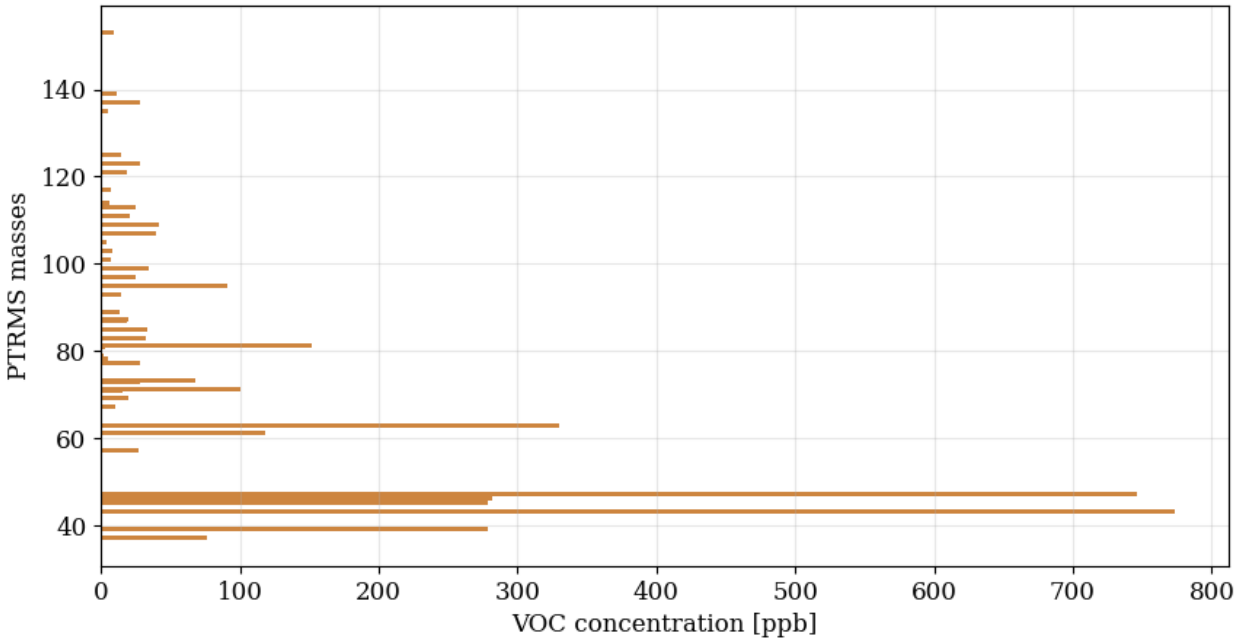

Figure 3.45 Distribution of VOC concentration (ppb) per PTR-MS mass measured at the peak of the braking event. The horizontal bars represent the molar ratio of each VOC ion at one station

- The impact of braking application strategy (1-step vs. 2-step) on VOCs

Single braking applications can consist of either one or two steps. A comparison is made between stations involving these applications that have the same dissipated energy. The selected stations are taken from the second round trip, which is considered thermally stable; however, similar trends were observed during the first and third round-trips.

Figure 3.46 presents the evolution of VOC emissions in relation to braking parameters. The concentrations of the major VOCs measured by PTR-MS are shown alongside speed, tangential force, and normal force.

Considering similar levels of dissipated energy but differing numbers of braking steps, the results indicate variable VOC emissions. During the first-round trip, the one-step braking scenario yielded a VOC concentration of 2190 ppb, compared to 2549 ppb for the two-step application. In the second round, the concentrations were 2315 ppb and 2188 ppb for the one-step and two-step scenarios, respectively (Figure 3.46). The third round exhibited concentrations of 2571 ppb for the one-step and 2269 ppb for the two-step application. These results suggest that, under the tested conditions, the number of braking steps does not exert a consistent or significant effect on VOC emissions.

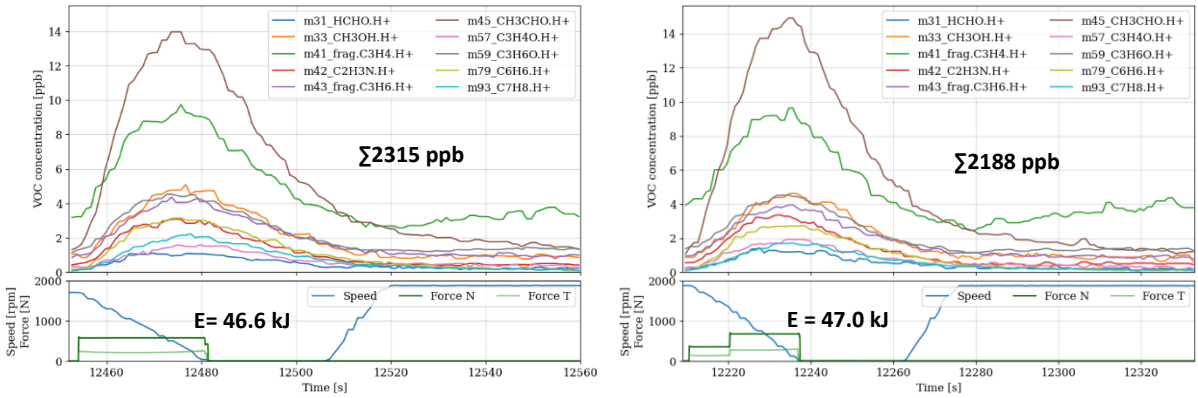

(a) (b)

Figure 3.46 VOC emissions during the second round trip under single braking scenarios for the HP: (a) one step and (b) two steps

3.2.2.8 Emission behaviors under multiple braking applications

The pathways are characterized by irregular braking applications, which cause changes in the tribological system and may lead to different VOC emission patterns. A comparison will be made between stations with one brake application and those with multiple applications. The chosen stations are from the second-round-trip (thermally stable); however, similar conclusions were observed for the first and third round-trips.

Figure 3.47 shows the evolution of VOC emissions in relation to braking parameters for three different station stop scenarios. The major VOC concentrations measured by PTR-MS are plotted along with speed, tangential force, and normal force.

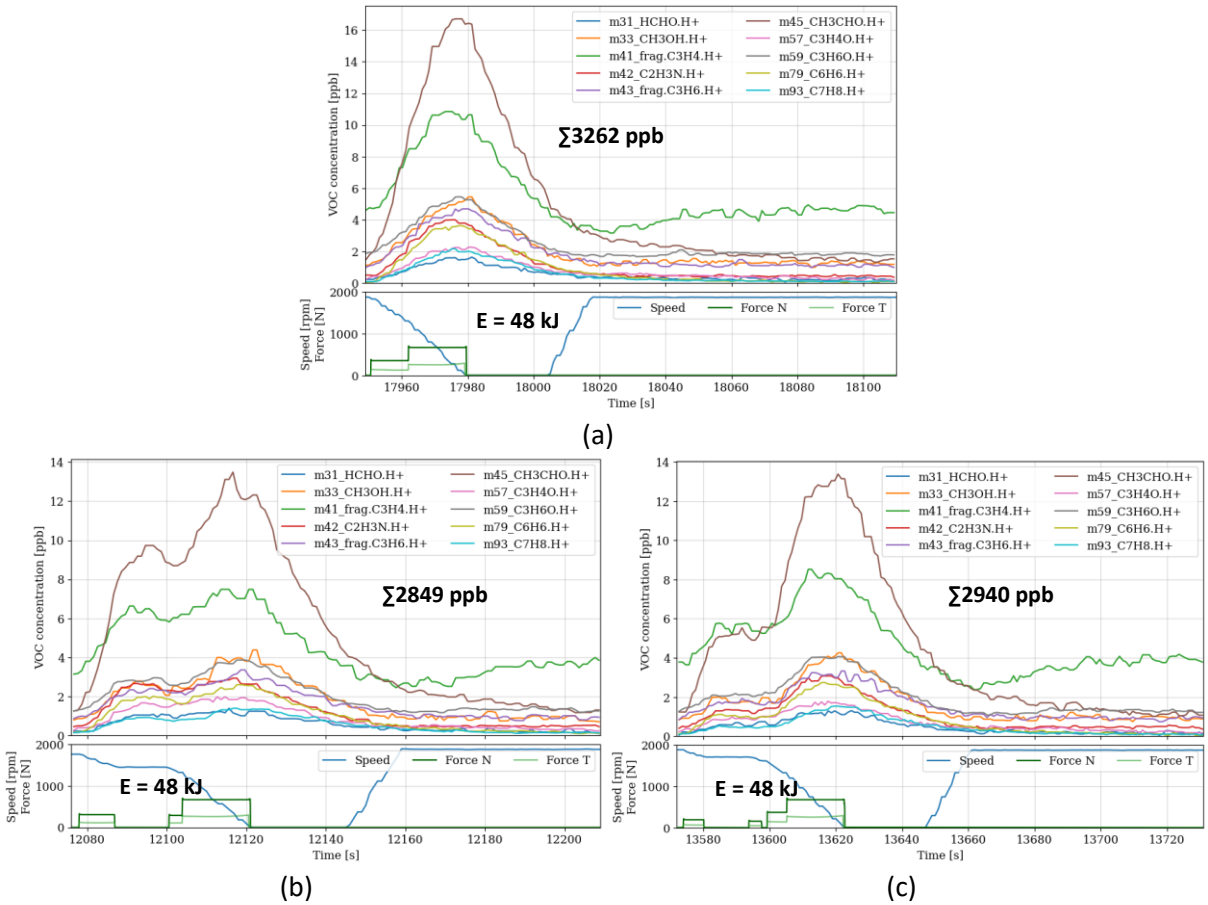

(a)

(b) (c)

Figure 3.47 VOC emissions under various braking scenarios for the HP: (a) single braking application, (b) two consecutive braking applications, and (c) three consecutive braking applications

In the first scenario (Figure 3.47 (a)), a single braking application effectively decelerated the vehicle to a stop, dissipating a total energy of 48 kJ over a duration of 100 s. As the braking process started, a gradual increase in VOC emission occurred until the end of the force application, indicating that VOCs were released throughout the entire contact phase. After the braking finishes, VOC concentrations gradually diminished to baseline levels.

In the second scenario, involving two sequential braking applications (Figure 3.47 (b)), emission peaks were observed at the onset of each application. Notably, the second braking event produced substantially higher VOC concentrations than the first. When comparing the total VOC emissions of this dual-braking station to a single-braking scenario station, both of which dissipated comparable energy, the overall emitted VOC quantities were found to be similar. This indicates that VOC emissions are not dependent on the sequence of braking events, suggesting that these compounds are not accumulated or stored within the braking system between applications.

The third scenario (Figure 3.47 (c)), which required three braking applications, revealed emission peaks at the start of the first and second applications. However, the emissions from the second and third applications appeared simultaneously due to the short interval between them. This limited the time available for VOCs to evolve and be released distinctly between the two events. Similar to the two-braking application scenario, emissions increased during the second braking. However, when comparing the total dispersed energy across the whole station, which is similar to the previous two scenarios, the total VOC emissions remain comparable.

The emission profiles of particles studied by Frangieh (2025) and VOCs under different braking scenarios reveal distinct underlying mechanisms. Particle emissions are strongly influenced by the initial braking event, with a marked peak during early contact and a consistent decline in subsequent applications (Figure 3.48), suggesting interface adjustment within the tribological circuit. In contrast, VOC emissions exhibit a more sustained release during the entire contact phase and appear less dependent on braking sequence. While particles show cumulative depletion, VOCs demonstrate consistent total emission across scenarios with equivalent dissipated energy, indicating that their generation is more thermally driven and not limited by prior releases. This contrast highlights that particle release is governed by physical wear and third-body dynamics, whereas VOC evolution is primarily a function of temperature-dependent chemical processes.

The difference between PM and VOC emissions is illustrated in Figure 3.48. PM emissions are released at the beginning of braking, as the contact surfaces close and friction initiates particle generation. In contrast, VOC emissions follow a different timeline and are governed by distinct mechanisms. Rather than being triggered solely by friction, VOC release is influenced by temperature rise, the material's heat accumulation, and the diffusion of VOC inside the material. This results in a lack of synchronicity between PM and VOC emissions. Particles, being heavier, tend to be expelled rapidly in a single burst, whereas VOCs, due to their lower mass, diffuse out gradually. During braking, VOC levels appear to rise steadily, peaking as the vehicle reaches zero speed, when energy dissipation reaches zero, after which emissions slowly decline. Unlike VOCs, particle emissions show a sharp initial peak followed by a rapid decrease. These contrasting patterns highlight the fundamentally different emission mechanisms of particles and VOCs.

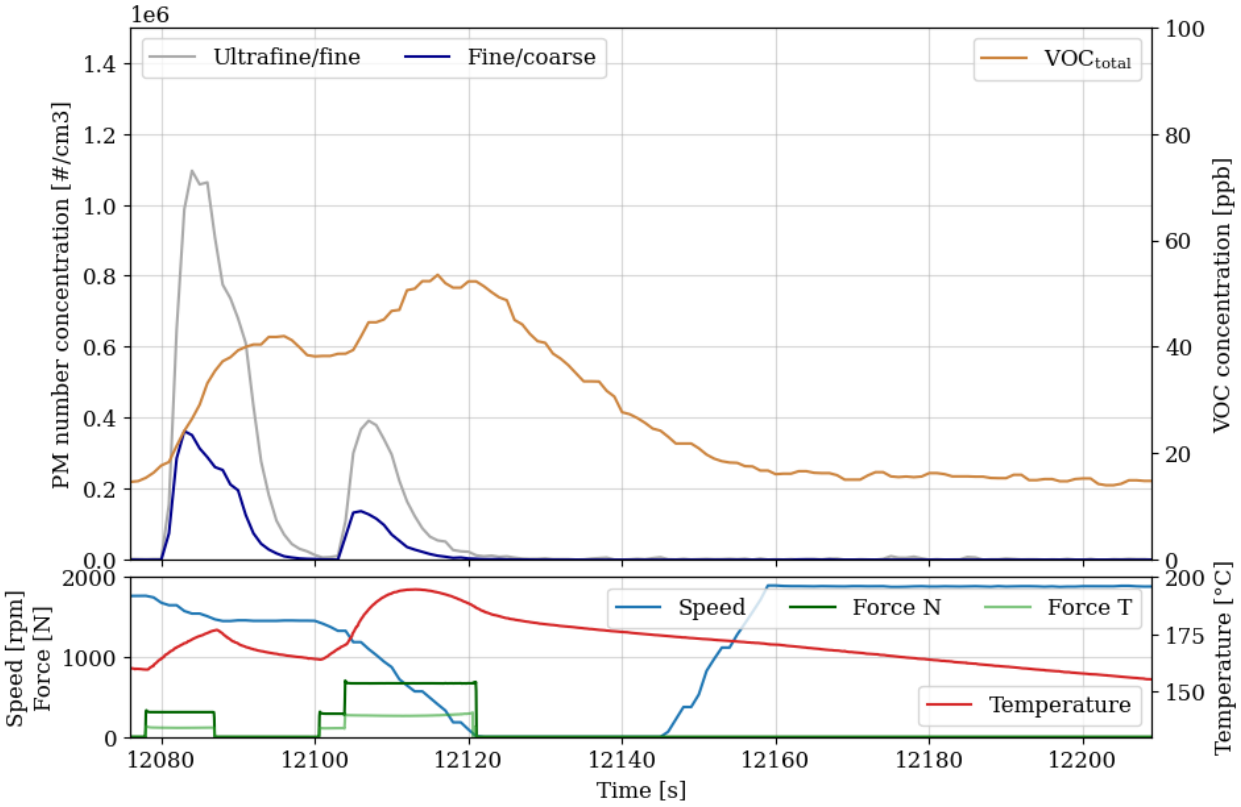

Figure 3.48 Correlation of particle number concentration and major VOC emissions with braking parameters and disc temperature during multiple braking application

Figure 3.49 presents a comparative visualization of particle number size distributions as measured by two instruments: the FMPS (bottom panel) and the OPS (top panel), for the same station. Both instruments capture the evolution of PM concentrations in terms of particle size (Dp) and time. The FMPS panel covers particle diameters from 5.6 to 560 nm, capturing the ultrafine and fine fractions, while the OPS measures from 0.3 to 10 µm, measuring fine to coarse particles. The color scale indicates the particle number concentration (dN/dLogDp) in #/cm³, with warmer colors (yellow) corresponding to higher concentrations.

Two braking applications occurred in this station, each generating spikes in particle concentration. In the FMPS data, the primary emissions are dominantly sized by particles below 14.3 nm and mainly in the range of 124.1–294.3 nm, with a mode at 191.1 nm. In the OPS data, although the concentration is lower, there is also a rise in fine particles within the range 337 nm and 522 nm. This change in mode is likely due to the reliance on different measurement principles, specifically electrical versus optical diameters. Multiple braking applications produce similar particle size modes, but total concentrations decrease with each event. This reflects the depletion of readily releasable particles and stabilization of the tribological interface after initial braking.

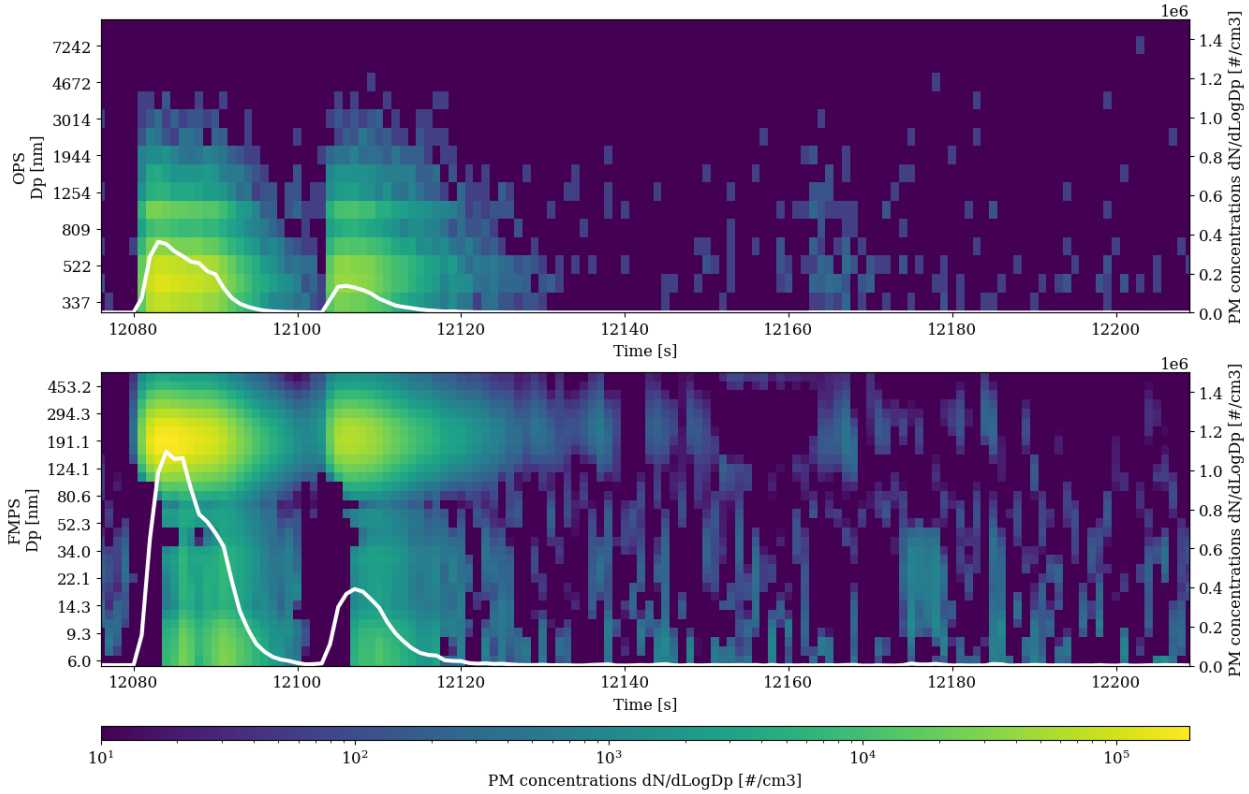

Figure 3.49 Time-resolved particle size distribution and number concentration within FMPS and OPS measurements during a multiple braking application

Chapter 4: Modification of the pad design and brake system

Beyond the importance of friction materials and operating conditions, emissions are sensitive to many factors in the braking system. The aim here is to investigate the change of brake pad design, in terms of lining rigidity or hardness. Rigidity refers to the elastic behavior that determines deformation under applied load. If we consider that wear results from the interaction between the surfaces of the two bodies in contact, the disc and the lining, rather than between two materials, the rigidity of the lining partly determines the severity of the stress experienced locally by the materials at the interface.

As the disc and lining surfaces are not perfectly flat or conforming, their imperfections imply heterogeneous contact, which exacerbates local stresses. To address this issue, the flexibility of a brake pad allows its surface to adapt to the opposing surface of the disc, softening the contact. Conversely, a rigid lining is subject to more severe local contact conditions at the interface, likely to exacerbate wear.

In addition to the local severity of energy dissipation, lining flexibility determines the interface's ability to close. For a given normal load, a soft lining efficiently closes the interface. In contrast, a rigid lining leaves a greater proportion of the apparent contact area open. This creates free spaces in the interface that are favorable to the circulation and ejection of third-body particles from the contact, which is another factor of wear and emission.

This chapter studies two brake linings specifically developed by Alstom Flertex. The main difference between these lining materials is their rigidity, without requiring any change to their composition, which remains identical to that of the reference material studied in Chapter 3. A third brake pad is studied, which differs from the reference pad in that it has radial grooves, providing flexibility.

As many factors influence braking emissions, the question of the relevance of studying the performance of friction materials on a laboratory tribometer comes up. The last part of the chapter presents a comparison of particulate emissions obtained on the LaMcube tribometer and those measured on Alstom Flertex's railway brake test bench.

This chapter investigates the effect of pad design, specifically, variations in the curing process that influence rigidity and thermal expansion, using the normal braking pathway. It also examines the comparability between the reduced-scale setup employed in this study and a full-scale bench test. It deals with:

- The consistency of PM and VOC emissions across different test replicates and samplers.
- The average concentrations and chemical characterization of emitted particles and VOCs.
- The comparison of emission factors and particle size distributions between the reduced and full-scale systems.

4.1 Effect of the brake pad design

The emissions have been studied using the normal pathway (two repetitions, NP1 and NP2, for each pad material) and using friction pairs combining soft and rigid pads with a cast iron disc. The airflow temperatures observed during the tests were very similar for each material, averaging between 32 and 33°C in the enclosure and not exceeding 40°C at the outlet pipe sampling point.

4.1.1 Average mass concentrations from NP using the modified pads

4.1.1.1 TSP average mass concentrations of replicates across different sampling supports

Table 4.1 presents the TSP mass concentrations measured for NP replicates using soft and rigid pads across different particle sampling devices. For the soft pad, NP1 and NP2 pathways yielded very similar concentrations across all devices. For the rigid pad, NP1 showed consistent results across all samplers, while NP2 exhibited a notable deviation in the 14-stage impactor, where the concentration was approximately 30% lower than NP1.

To evaluate the consistency of the sampling methods, the coefficient of variation (CV) was used to assess relative variability in this small dataset (Table 4.1). For the soft pad under both NP1 and NP2 conditions, the CV of 15% indicates limited variability and good consistency across samplers. For the rigid pad under NP1, the CV was even lower, confirming uniformity. However, for NP2 with the rigid pad, the 14-stage impactor showed greater variability, as reflected by a higher CV of 21%.

This analysis confirms that individual techniques are generally consistent, though discrepancies between methods can occur. The objective of such assessments is to verify the repeatability and reliability of results across sampling supports and test repetitions.

Table 4.1 Consistency of mass concentration in µg/m3 of the sampling supports and test repetitions

Pad	Test	Filter holder	3-stage impactor	14-stage impactor	Av ± SD	CV
Soft	NP 1	171 ± 1	135 ± 5	182 ± 9	163 ± 25	15
	NP 2	165 ± 2	136 ± 6	184 ± 2	162 ± 24	15
Rigid	NP 1	503 ± 45	447 ± 66	470 ± 4	473 ± 29	6
	NP 2	494 ± 5	450 ± 38	326 ± 2	423 ± 87	21

Table 4.1 indicate that rigid pads generate higher mass emissions, with concentrations nearly 2–3 times greater than those of soft pads and reference pads. Rigidity and hardness are closely related mechanical properties, both reflecting a material's resistance to external forces. Rigidity refers to the elastic response to deformation under load, while hardness characterizes resistance to penetration. This similarity allows us to compare our results with those of Egeonu et al., (2015), who examined brake wear emissions in relation to changes in pad hardness, confirming that harder pads contribute more to wear, consistent with our findings.

4.1.1.2. Mass size distributions of particles related to pad designs

The figure below (Figure 4.1) presents a mass particle size distribution measured in two repetitions (NP1 and NP2) using a soft pad within the normal pathway. The two repetitions exhibit close agreement in distribution shape and peak values. This indicates a consistent size distribution across measurements. The distribution follows a unimodal pattern, with a peak concentration occurring around 1.62-2.46 µm. Similar to the soft pad data, NP1 and NP2 for the rigid pad show consistent trends. Both pad types exhibit a dominant particle size range of around 1.62–2.46 µm, confirming that brake wear emissions from both materials tend to peak in the fine particle region. Like the soft pad, the rigid pad does not generate significant ultrafine (<0.1 µm) or coarse particles (>10 µm). The results also match with those of the reference pad shown in Figure 4.1 (c), with only a slight shift in the modal

range from 0.9–1.6 µm. This indicates that regardless of pad rigidity, the overall mass size distribution remains consistent.

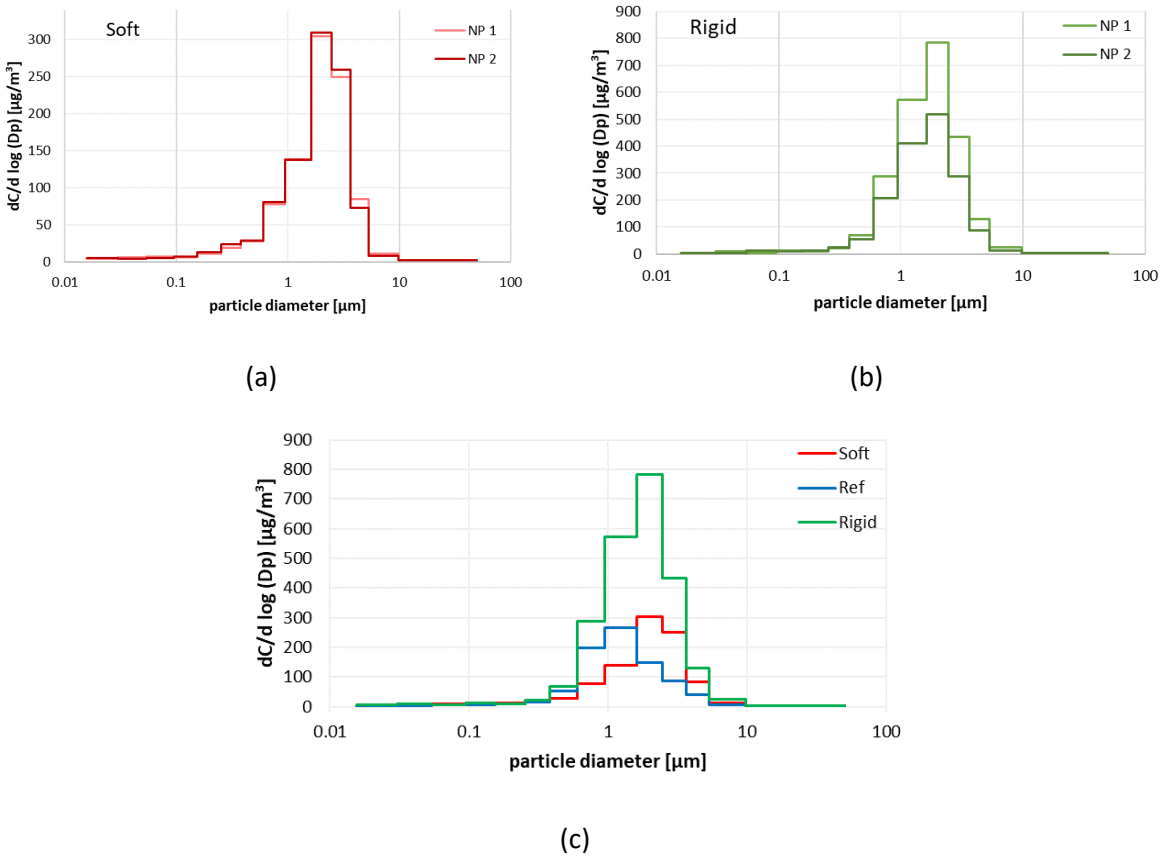

Figure 4.1 Mass size distribution of the (a) soft, (b) rigid, and (c) superimposition of the 3 pads

4.1.2 Average elemental composition of the emitted TSP from NP using the modified pads

4.1.2.1 Repetition consistency of elemental composition in TSP from NP1 and NP2 across the modified pads

Similar to what has been presented for the reference pad (section 3.1.4.1), Figure 4.2 presents a scatter plot with a 1:1 line for the concentrations (ng/m^3) of elements in particles collected using filter holders with soft, rigid, and new design pads for the NP repetitions. The slopes show a good consistency of 0.88, 0.96, and 0.98, respectively, with minimal variation. This indicates a strong correlation between the two repetitions, with a regression coefficient of 1.

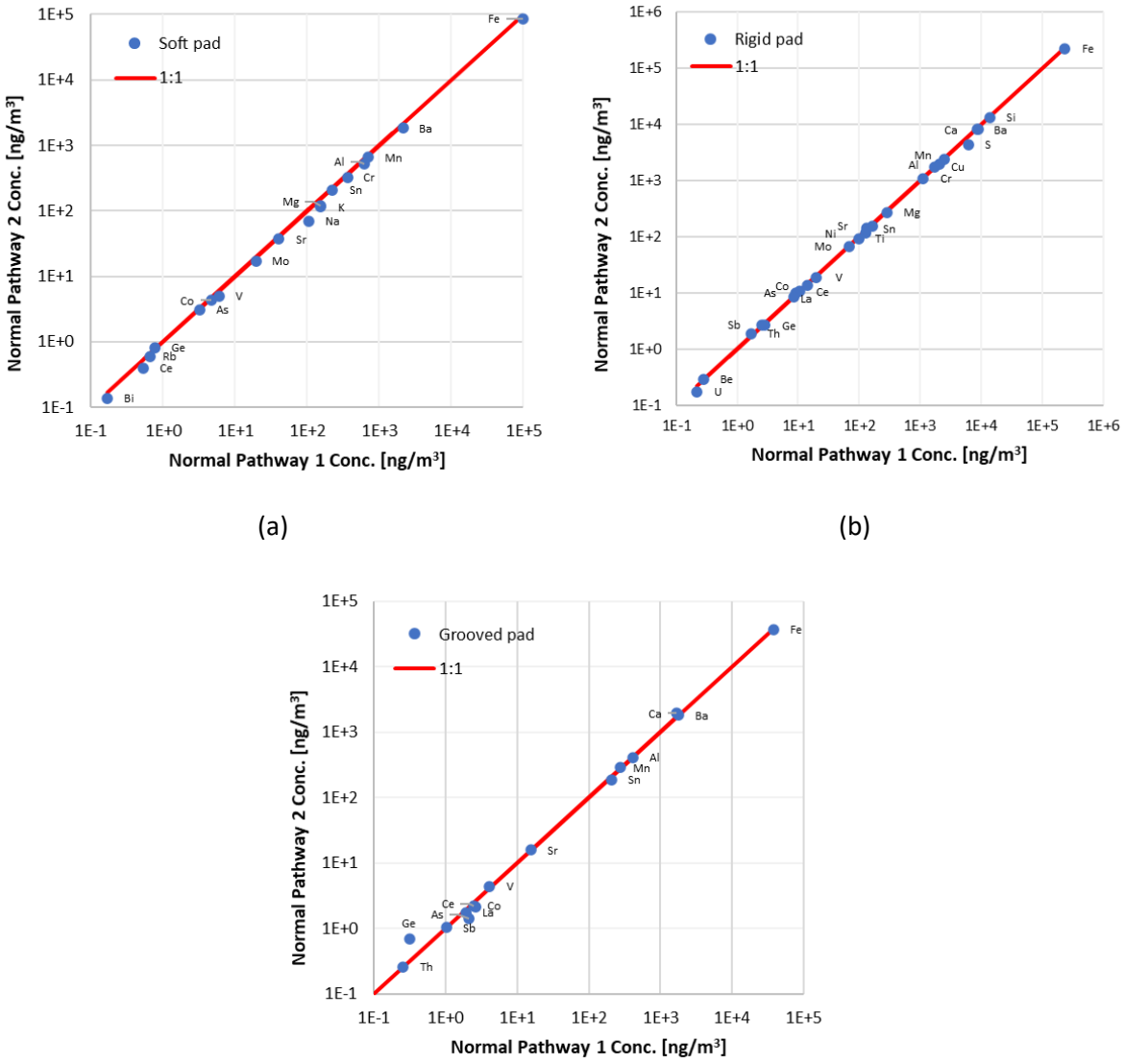

Figure 4.2 Comparison of the metal concentration between the 2 repetitions of the normal pathway using the (a) soft pad, (b) rigid pad, and (c) grooved pad

This consistency is further supported by the data presented in Appendix 14 and Appendix 15. The TSP collected using the different sampling supports across all pads is presented in Appendix 14, while the sum of metals within each sampling support is provided in Appendix 14. The results reveal similar trends across the different pad types in terms of mass and metals.

4.1.2.2 Mass closure and elemental composition of TSP from NP1 & NP2 using modified pads

Figure 4.3 presents the mass closure and global chemical composition of the TSP collected during NP1 and NP2 for soft, rigid, and grooved brake pads. The rigid pad exhibited the highest overall particle emissions resulting in the highest consistency between both pathways (because of higher masses collected). Overall, metals consistently formed the dominant fraction across all pad types, but the total

mass and composition varied significantly depending on the pad design. The complete list of metals, along with their concentrations and uncertainty measurements, is presented in Appendix 16.

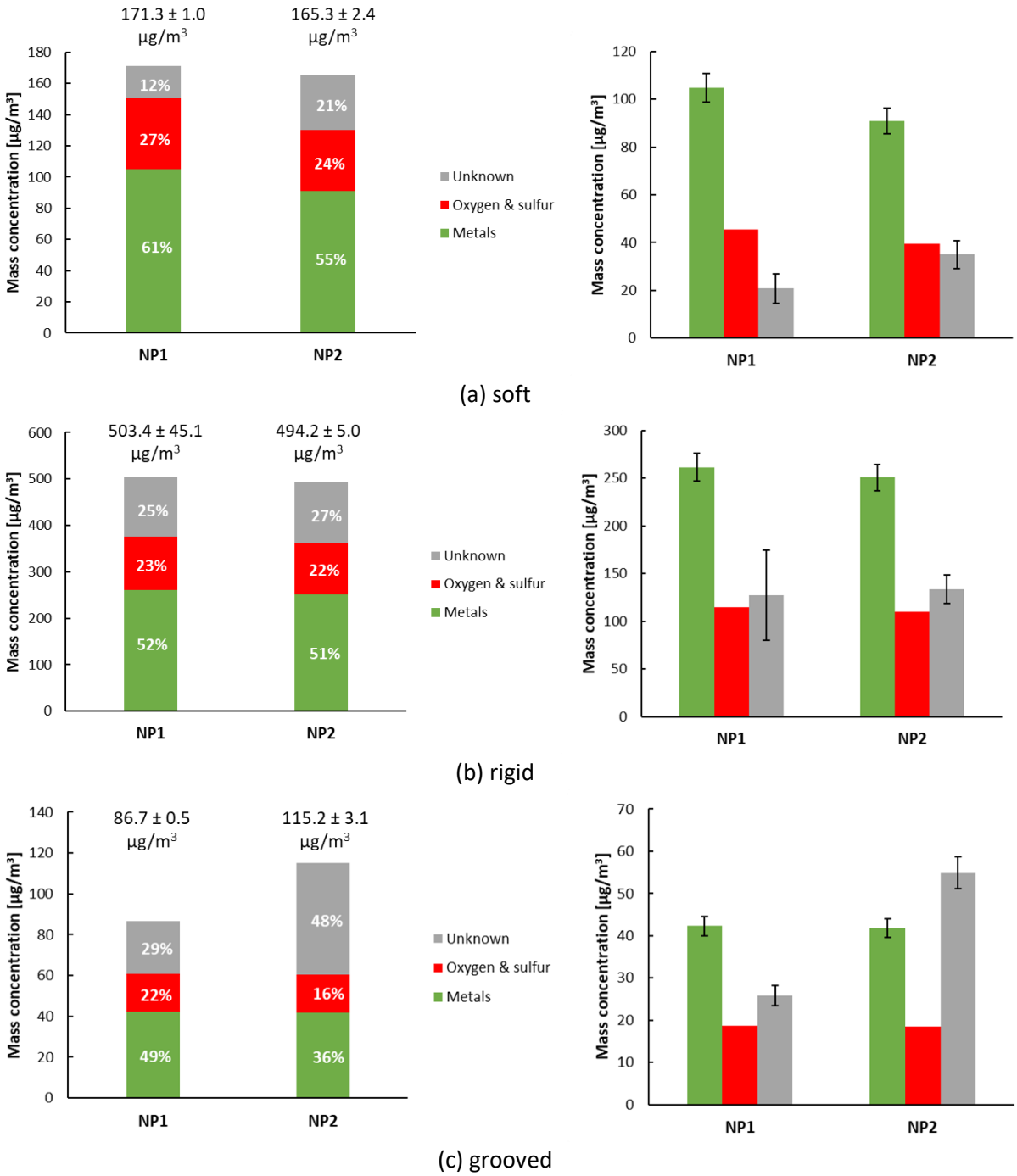

Figure 4.3 Mass closure and chemical composition of TSP of NP1 and NP2 using: (a) soft pad, (b) rigid pad, and (c) grooved pad

Figure 4.4 shows the elemental emission concentrations (in µg/m³, log scale) of selected metals collected during the two normal pathway tests (NP1 and NP2) across three brake pad types: (a) Soft, (b) Rigid, and (c) Grooved. Fe dominates across all pad types, highlighting its high concentration in the first bodies. Overall, the data are repeatable and indicate material-specific emission profiles. As for the mass of TSP collected in NP1 and NP2, the levels of elemental concentrations followed the trend Rigid > Soft > Grooved.

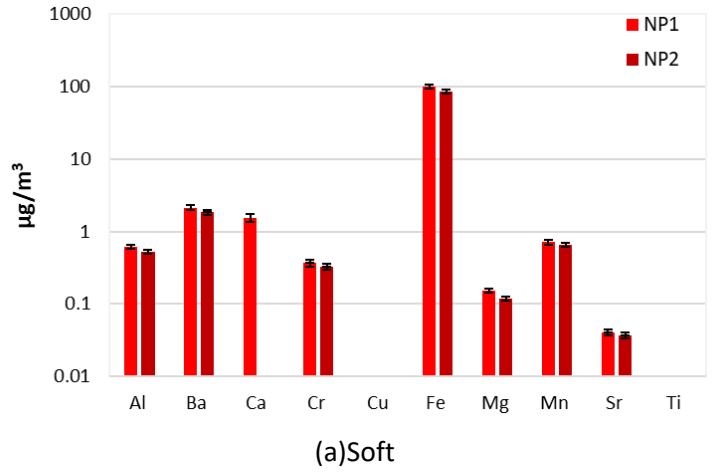

(a)Soft

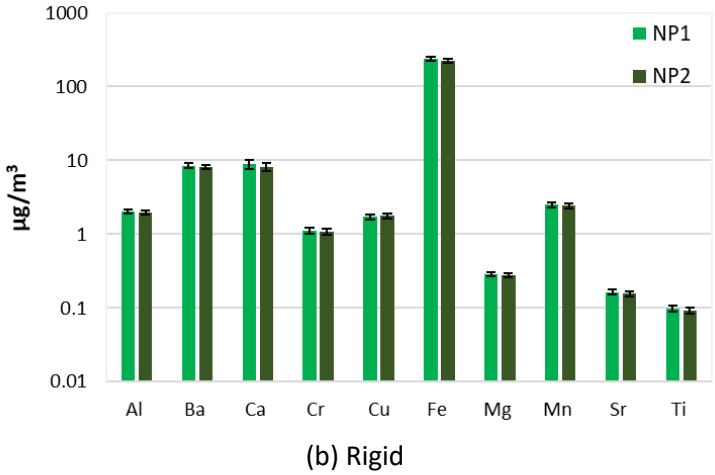

(b) Rigid

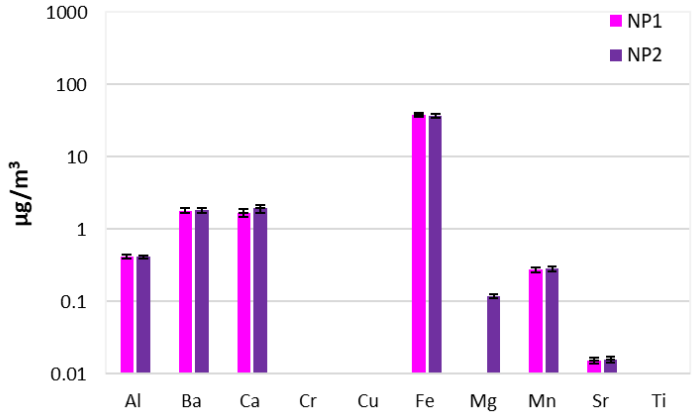

(c) Grooved

Figure 4.4 Metal content of TSP for NP1 & NP2 using: (a) soft pad, (b) rigid pad, (c) grooved pad

4.1.3 Submicron particle composition from the 3-stage impactor using the modified pads

4.1.3.1 Mass closure and elemental composition of submicronic particles from NP1 & NP2 using various brake pads

The concentrations of particles from the normal pathways 1 and 2, using soft, rigid, and grooved pads, classified by size and accompanied by their associated uncertainties, are presented accordingly.

Appendix 17 show the collected particles using the 3-stage impactor. In general, the mass of particles with a diameter larger than 10 µm was too low; therefore, these filters were not analyzed for emissions from the soft and grooved pads.

Figure 4.5 shows the mass concentrations and chemical composition of submicronic particles (<1 µm) for soft, rigid, and grooved brake pads.

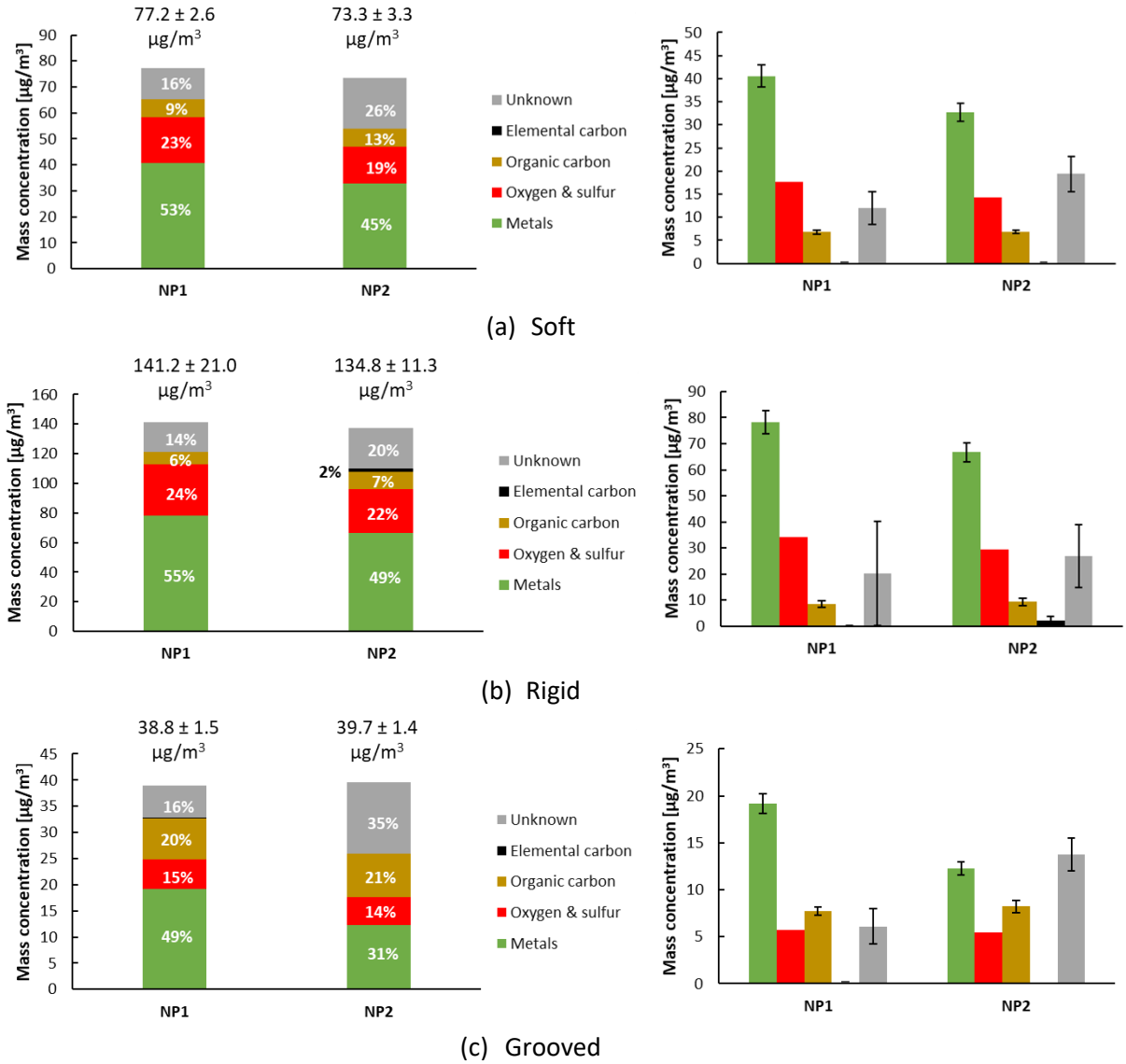

Figure 4.5 Mass closure and chemical composition of submicronic particles of NP1 and NP2 using: (a) soft pad, (b) rigid pad, (c) grooved pad

Figure 4.6 shows the elemental emission concentrations (in µg/m³, log scale) in submicronic particles of selected metals collected during two normal pathway tests (NP1 and NP2) across the three brake pad types (the complete list is presented in Appendix 17). Across all pad types, Fe remains the principal metal found in submicronic particles, followed by Al, Ba, and Ca. The repeatability between NP1 and NP2 is very good.

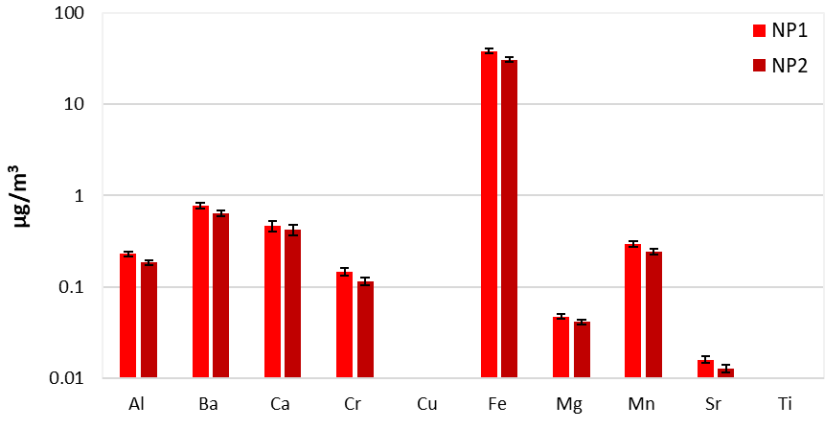

(a) Soft

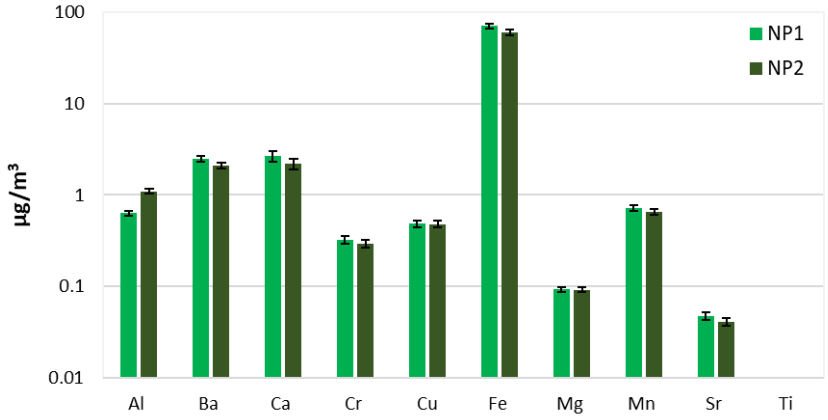

(b) Rigid

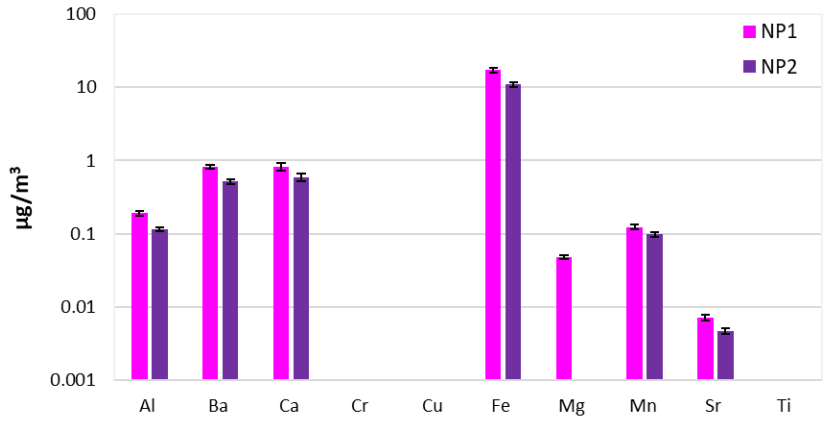

(c) Grooved

Figure 4.6 Metal content of submicronic particles for NP1 & NP2 using: (a) soft pad, (b) rigid pad, and (c) grooved pad

4.1.3.2 Effect of pad rigidity on carbon emissions and disc wear contribution in submicronic particles

When modifying the rigidity of the brake pad (either increasing or decreasing it), the %TC content in the collected submicron particles becomes lower than when using the reference pad (Figure 4.7). A comparison of surface temperatures at 2 mm depth for both the pad and disc shows similar values across all pads, with only slight variations (1–5%). Since the thermal properties of these materials are comparable, significant temperature differences on their actual surfaces are not expected, and no distinct trend was observed linking pad rigidity to particulate carbon emissions.

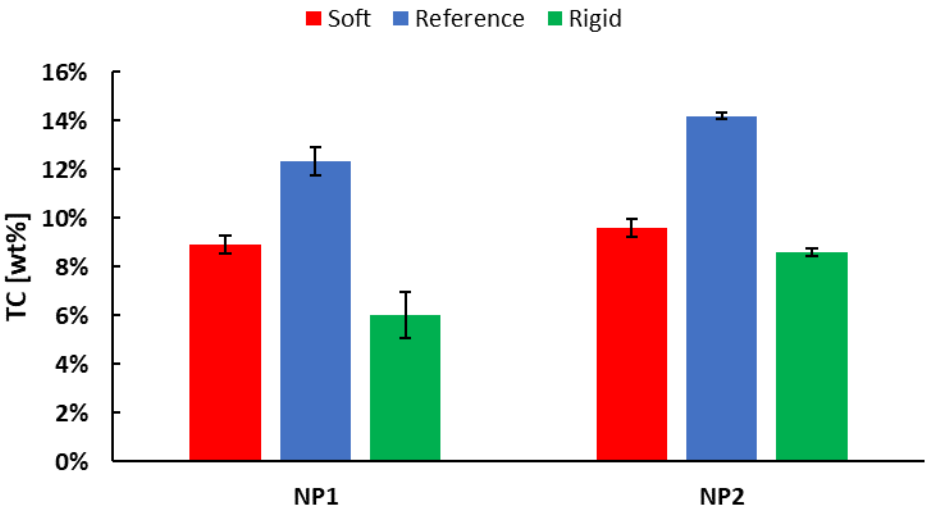

Figure 4.7 Percentage of total carbon content in normal pathways using the soft, reference, and rigid pad collected on the backup filter (submicron particles)

4.1.3.3 Effect of pad grooves on carbon emissions in submicronic particles

The expected capacity of the grooved system to store and emit particles during braking, compared to the reference pad (which has a flat surface and only one groove), will be discussed.

Two primary factors drive emissions:

1. Source flow – how materials wear.
2. Exit flow – how particles are retained within or released from the contact area.

Particles that remain trapped within the contact zone may later be expelled when the pad-disc interface reopens. This retention can enhance the production of submicronic particles: as these trapped particles are subjected to repeated mechanical interactions and elevated temperatures, they undergo further fragmentation and chemical changes. With continued accumulation and cycling through the contact, these processes intensify, leading to the formation of smaller and more chemically transformed particles.

In the reference tests, many particles originating from pad wear are lost. The third body layer contains a few organic particles as they struggle to remain in the contact. Abrasive wear particularly affects organic materials due to their lower mechanical strength, making them more likely to be released, especially as large particles.

When exposed to high temperatures, stored organic particles can further degrade into ultrafine particles (<0.2 µm). These ultrafine particles are unlikely to originate purely from mechanical wear. Generally, wear processes result in two particle size modes:

- Particles >1 µm produced by abrasive and adhesive wear (mechanical processes).
- Particles <1 µm may initially form through mechanical means but evolve chemically due to high surface reactivity at smaller sizes.

The assumption is that with more grooves in the pad, micrometric organic particles can remain in the contact. Mechanical processes initially occur, and after prolonged exposure to high temperatures, chemical reactions contribute to the formation of smaller organic particles, which are finally released.

The new pad design incorporated eight grooves, compared to the single groove in the reference pad. This design enhances the pad's ability to store more particles during braking, unlike the reference pad, which features flat surfaces with minimal capacity to retain debris. In the reference pad, a significant number of large, organic particles are lost and do not accumulate in the third-body layer. In contrast, the new design allows abrasive wear to store debris in the grooves, thereby preventing immediate loss. Figure 4.8 shows the %TC content from the particles collected on the backup filter (submicron particles) of the NP (both repetitions, both pads).

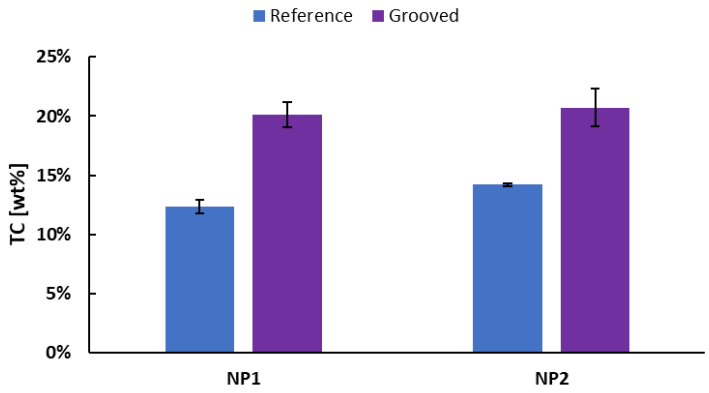

Figure 4.8 Percentage of total carbon content in submicron particles for normal pathways using the reference and the grooved pads

Table 4.2 presents a comparison of TC values with those reported in the literature, where they range between 4% and 75%, depending on several factors such as brake pad composition, sampling method, sample type, number of braking events, protocol severity, and bench scale conditions.

For non-asbestos organic (NAO) pad, there appears to be a trend where stronger testing protocols result in lower TC percentages. In the case of low-steel and low-metallic pads, the TC percentage consistently remains low, typically below 15%. Regarding the study by (Wang et al., 2016), since it involved sampling from passenger cars under real-world conditions, the collected particles likely originated from multiple sources beyond just brake wear, making direct comparison or interpretation challenging. In contrast, the findings from the study by (Garg et al., 2000) align well with those of (Alves et al., 2021), providing consistent results in terms of TC emissions from brake wear.

Table 4.2 Carbon content in brake wear particles: %TC detected from various brake pad types and sampling conditions

Pad	%TC in emissions	Relative TC content (sample/pad)	TC content in pad [%wt]	Sampling	Setting	Reference
Low metallic	4.05	28	14.47	By sweeping the bottom of the dynamometer chamber	dynamometer chamber	(Plachá et al., 2017b)
Low metallic	5.27	36		From surfaces of the wind tunnel supplying cooling air into and out of the dynamometer chamber		
Low steel 1 - Smooth protocol	14.6	-	Estimated variation 5-15	PM10 quartz filters	dynamometer chamber	(Alves et al., 2021)
Low steel 2 - Smooth protocol	5.07	-				
Low steel 1 - Moderate protocol	13.8	-				
Low steel 2 - Moderate protocol	13.7	-				
Low steel 2 - Severe protocol	6.61	-				
NAO 1-Smooth protocol	75.4	-				
NAO 2-Smooth protocol	54.3	-				
NAO 1-Moderate protocol	38.8	-				
NAO 2-Moderate protocol	12.3	-				
NAO 1-Severe protocol	6.74	-				
NAO 2-Severe protocol	8.1	-				
-	66.92	-	-	PM2.5 samples in passenger cars carried by volunteers	Tianjin Subway	(B. Q. Wang et al., 2016a)
NAO	18	-	-	TSP 47 mm diameter Quartz filters	Brake dynamometer	(Garg et al., 2000)

4.1.4 Mass size distribution of major elements using rigid pad from the 14-stage impactor

To further analyze the elemental composition of wear of using the rigid pad, size distributions for major metallic elements were examined across both repetitions, revealing consistent trends and high correlations.

Size distributions are presented for both repetitions, and there is a very high correlation between them, with coefficients of 0.966 for Al, 0.993 for Ba, and 0.989 for Fe.

The studied elements exhibit a unimodal particle size distribution within the fine particle range, corresponding to an aerodynamic diameter between 1.62 and 2.46 µm. The shapes of the distributions of these metallic elements were very similar to the total mass distribution of the brake emissions shown in (Figure 4.1). Elements well quantified displaying this distribution pattern include Al, Ba, Fe, Mn, Sn, Sr, and V. Ba and Fe presented in Appendix 18.

For NP1 (Appendix 18) and Figure 4.9 for NP2 were the best quantified in terms of the number of stages, while for the remaining elements (Ca, Cr, Cu, Mg, and Ti), although the maximum peak is observed between 1.62 and 2.46 µm, the lower stages fall below the quantification limits. Therefore, we cannot confirm the absence of a peak in the ultra-fine region.

Among these elements, Al presents a low but well-quantified concentration in submicron particles (<0.38 µm). This suggests that Al is emitted through chemical processes, though in smaller quantities compared to its emission via mechanical processes, which is consistent with the previous results.

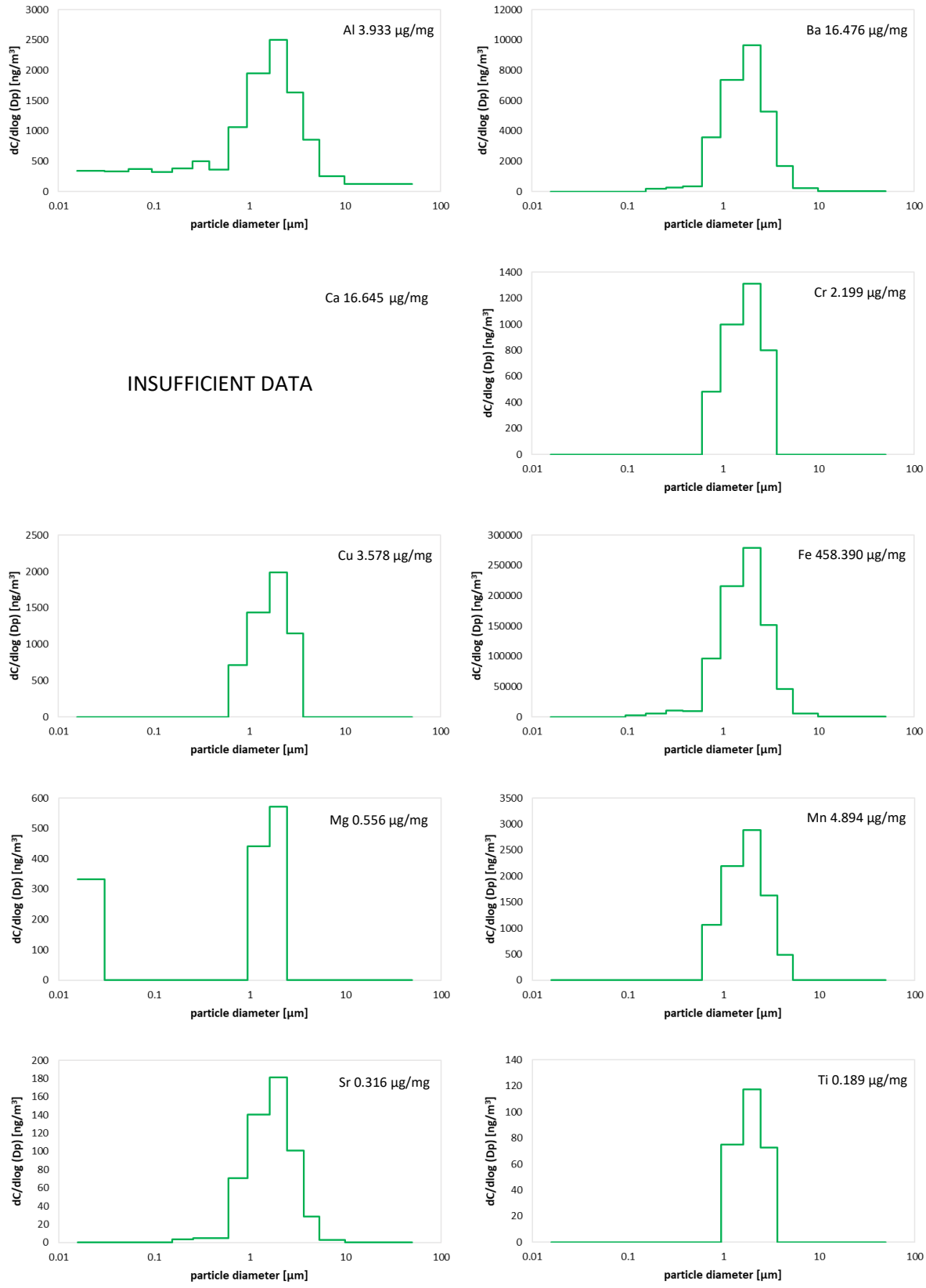

Figure 4.9 Particle mass concentration size distribution of selected metals using the rigid pad during the normal pathway 2

4.1.5 Scanning Electron Microscopy (SEM) observations of particles emitted from grooved pad under braking application

This section presents SEM analyses of airborne particles collected on filters during a single braking event using grooved pads. The SEM images reveal information on the morphology, size, and composition. The observations reveal a heterogeneous particle population, including individual particles, agglomerates, and clusters, with sizes ranging from a few hundred nanometers up to 20 µm.

Figure 4.10 shows surface observations using SEM on filter-collected particles from one braking event using the grooved pad. Clusters and agglomerates are visible in (a), while in (b), fine particles are scattered among the coarser ones. In (c), a flat, compacted layer of very fine particles is observed, which aligns with the number mode of the OPS size distribution, approximately 1 µm.

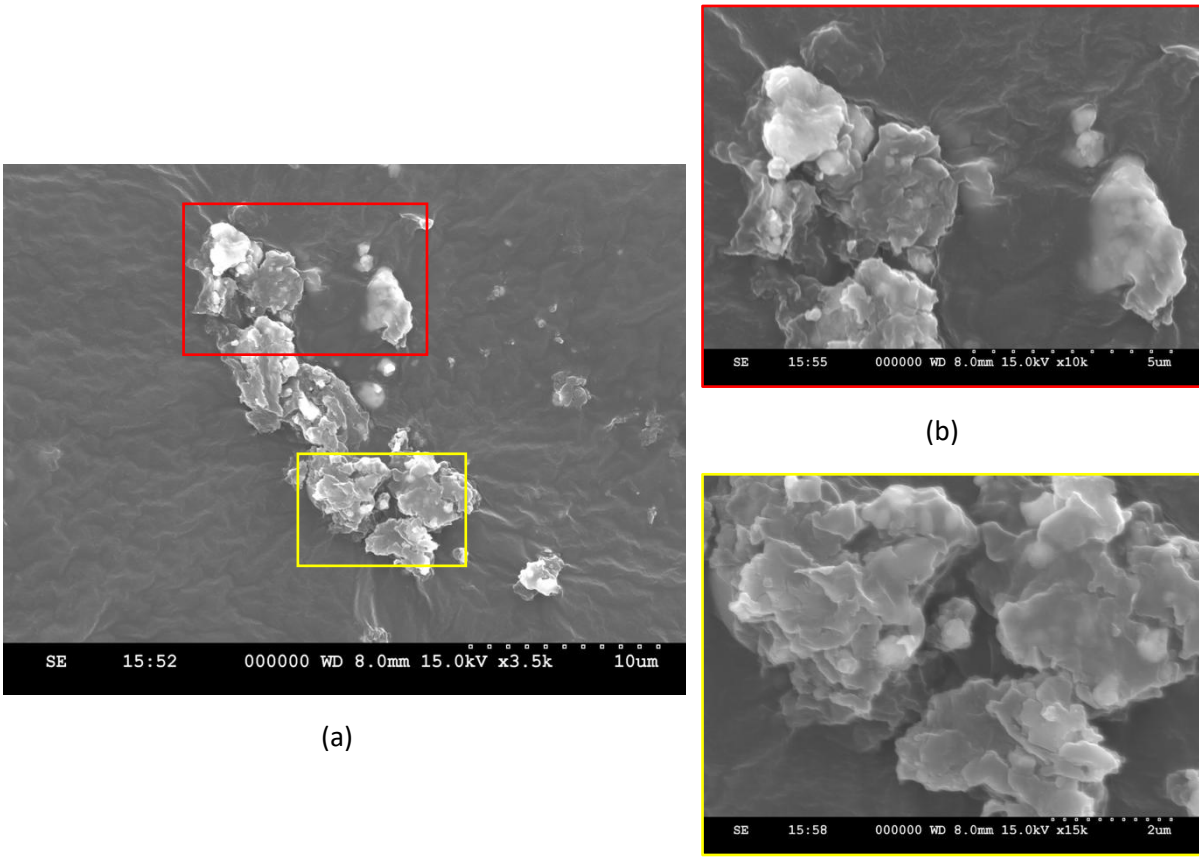

(a)

(b)

(c)

Figure 4.10 Surface observations using SEM on filter-collected particles from one braking event using grooved pad: (a) overall view, (b) magnified view of marked region 1, (c) magnified view of marked region 2

Figure 4.11 presents SEM observations highlighting key features of the wear particles. In (a), a wide and thin plateau with angular edges is observed, featuring a smooth, rubbed surface that suggests it was likely formed at the contact interface between the two friction materials, indicative of mechanical wear. In (b), agglomerated fine particles with angular shapes are observed, also suggesting mechanical wear as their primary formation mechanism. Image (c) shows clusters of particles, implying that smaller particles may undergo aggregation. Similar results were observed by (Kukutschová et al., 2011).

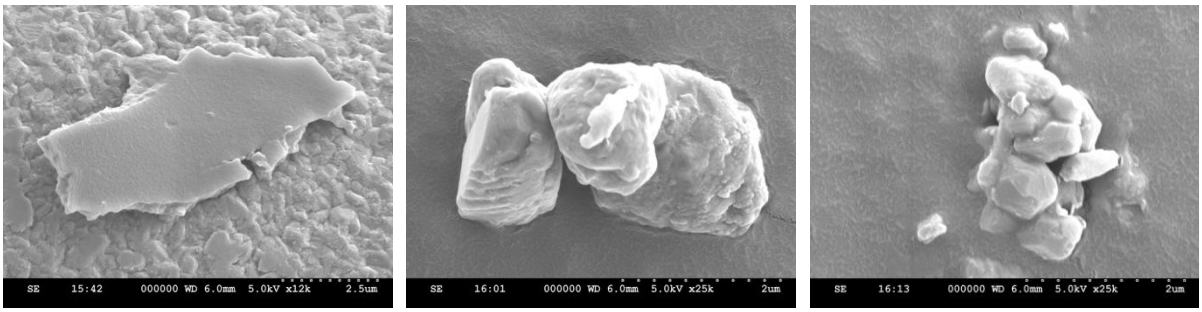

(a) (b) (c)

Figure 4.11 Surface observations using SEM on filter-collected particles from one braking event using grooved pad

Figure 4.12 presents a large fragment (20 µm) with fine particles scattered and agglomerated among the coarser particles. According to the SEM-EDS (Figure 4.12 (b)) the white particles contain Fe, Cr, and Ni, elements indicative of disc origin, while the large fragment lacks these disc-related elements, suggesting it originates from the pad. Figure 4.12 (c) provides a higher-magnification view of the region outlined in red in Figure 4.12 (a), and Figure 4.12 (d) offers a closer look at the surrounding area, revealing nanoparticles approximately 500 nm in size.

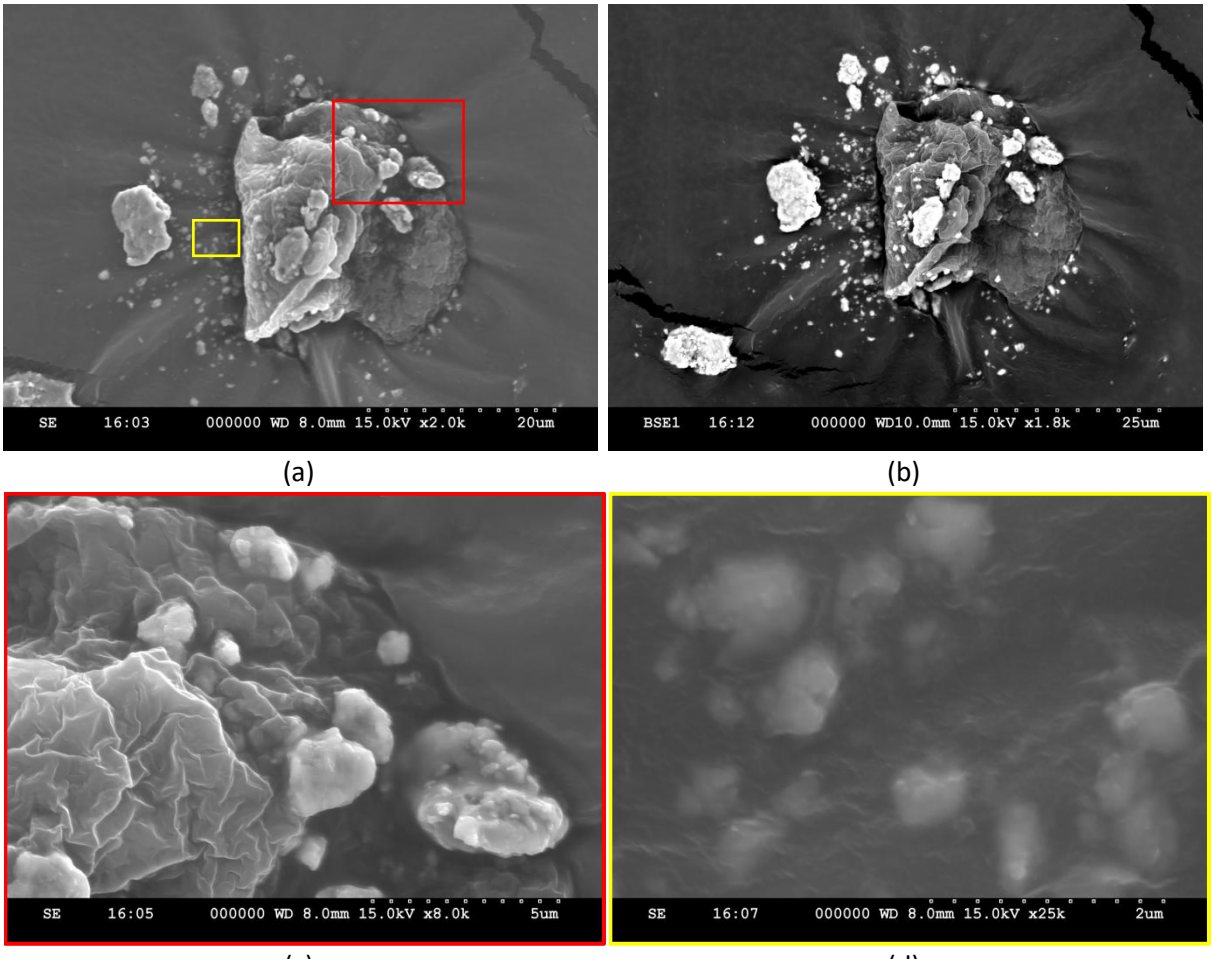

(a) (b)

(c) (d)

Figure 4.12 Surface observations using SEM on filter-collected particles from one braking event using grooved pad: (a) SEM-SE (b) SEM-BSE, (c) magnified view of marked region 1, (d) magnified view of marked region 2

In summary, the particles observed in the SEM images exhibit a wide range of sizes, from approximately 5 microns down to a few hundred nanometers. Their morphologies vary significantly and are clearly far from spherical. In addition to individual particles, clusters are present throughout the images. Agglomerates, both compacted and scattered, are consistently observed across all SEM images.

4.1.6 Average emissions of VOCs

4.1.6.1 Effect of pad rigidity and pad design on TVOC

To evaluate the influence of brake pad design parameters on VOC emissions, Figure 4.13 shows the TVOC emissions during normal pathways for the reference, soft, rigid, and grooved pads. The results show that neither pad rigidity nor the presence of grooves significantly impacts TVOC concentrations measured by PID under normal braking conditions. The average TVOC concentration per braking event in the NP is 13.16 ppb, five times lower than the emission measured during the HP.

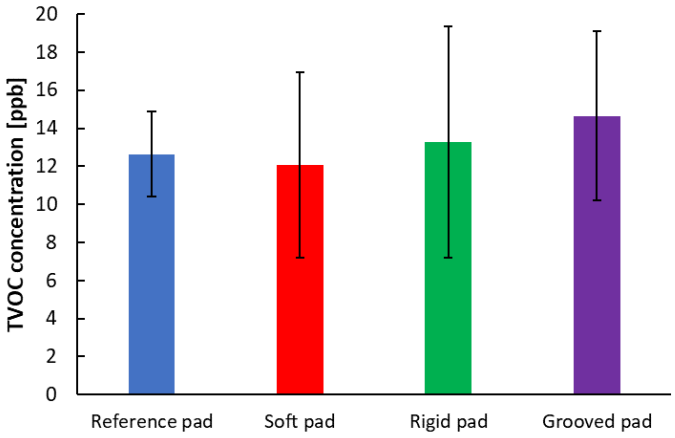

Figure 4.13 Effect of pad rigidity and design on TVOC concentration measured by PID during normal pathway

4.1.6.2 Carbonyl emissions

Figure 4.14 a & b present the concentrations of the carbonyls measured in two different materials: soft and rigid against the cast iron disc, respectively. The measurements were taken during the normal pathway tests. Note that, for the soft pad, only one repetition is presented since there was a sampling problem during the first repetition.

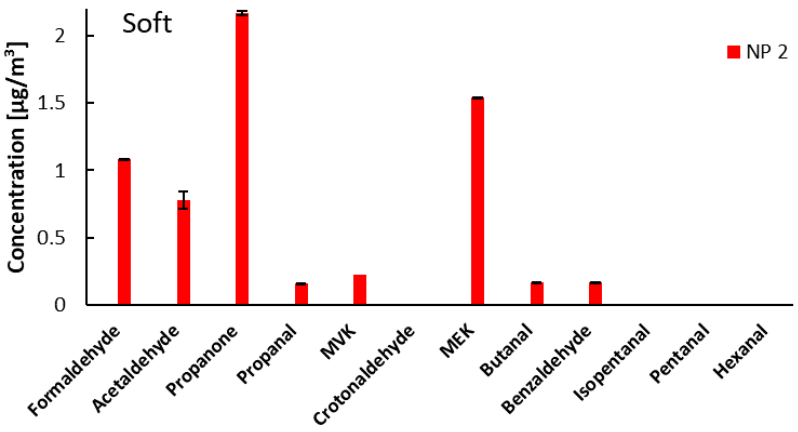

(a)

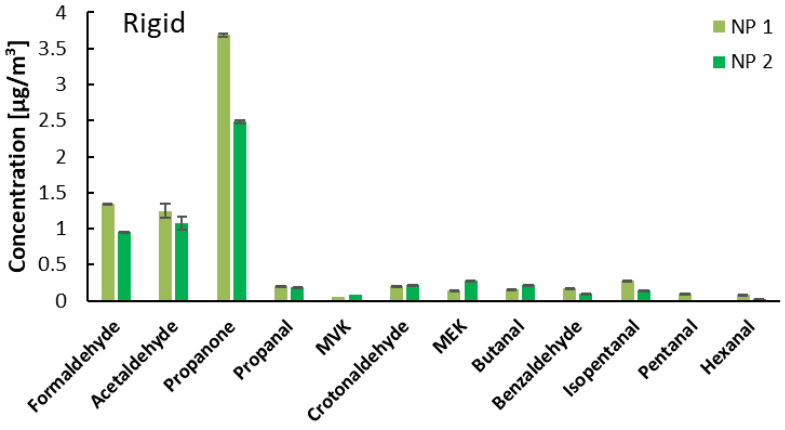

(b)

Figure 4.14 Mass Concentrations of the carbonyls for the Normal Pathway with the soft pad (a) and with the rigid pad (b) using DNPH-HPLC/UV

With the soft pad, the highest emissions are from propanone (2.17 µg/m³) and MEK (1.54 µg/m³), followed by formaldehyde and acetaldehyde. Other carbonyls appear at lower concentrations (<0.3 µg/m³). For the rigid pad, propanone dominates, especially in NP1 (3.69 µg/m³) and NP2 (2.49 µg/m³). Formaldehyde and acetaldehyde remain consistently present, while the other compounds are detected at relatively low levels (<0.3 µg/m³).

Although more species are detected, the total concentration of carbonyls using the soft pad is 6.291 µg/m³, which is comparable to the rigid pad test, with a total carbonyl concentration of 6.794 µg/m³. This result is similar to the PID, which didn't show significant variability between the two tests.

Table 4.3 indicates that emissions from the rigid brake pad material are generally higher during the initial braking test (NP1) than in the later test (NP2), particularly for compounds like formaldehyde, acetaldehyde, propanone, and others, with NP1/NP2 ratios ranging from 1.1 to 7.0. However, some compounds such as MVK, crotonaldehyde, MEK, and butanal show higher emissions in NP2, with reversed ratios between 0.5 and 0.9. Overall, the total carbonyl emissions are about 1.3 times higher in NP1, suggesting a possible decrease in emissions over time.

Table 4.3 Rigid tests emissions

Compounds	NP 1/NP 2
Formaldehyde	1.4
Acetaldehyde	1.2
Propanone	1.5
Propanal	1.1
MVK	0.7
Crotonaldehyde	0.9
MEK	0.5
Butanal	0.8
Benzaldehyde	1.8
Isopentanal	2.0
Pentanal	7.0
Hexanal	4.1

For the comparison between different pads (ref, soft, and rigid) the results are presented in Figure 4.15. The average of both repetitions was used to estimate the standard deviation, except for the soft pad, where this was not possible due to the presence of only one valid sampling repetition. For propanone in the reference pad, the graph scale was limited for better vision; however, its value is 11.45 ± 9.99 µg/m^3.

Across all pads, the highest concentrations were observed for propanone, formaldehyde, and acetaldehyde, which have relatively low boiling points. However, no trend clearly emerges from these results, especially if we take into account the uncertainties.

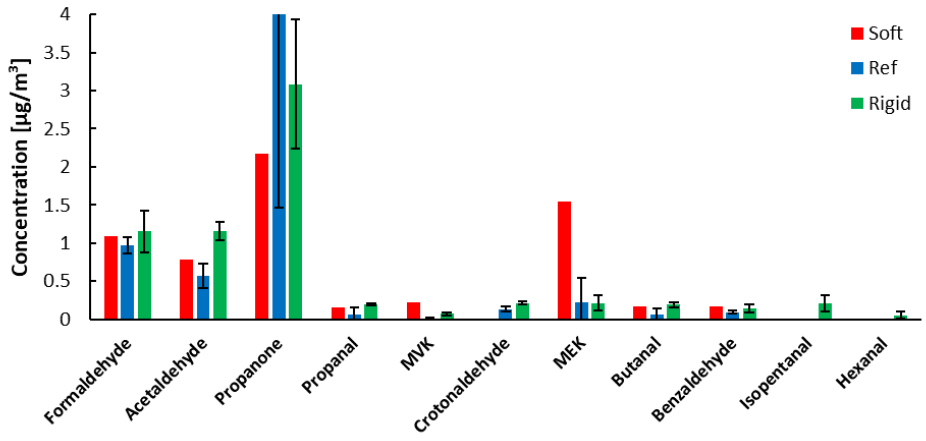

(a)

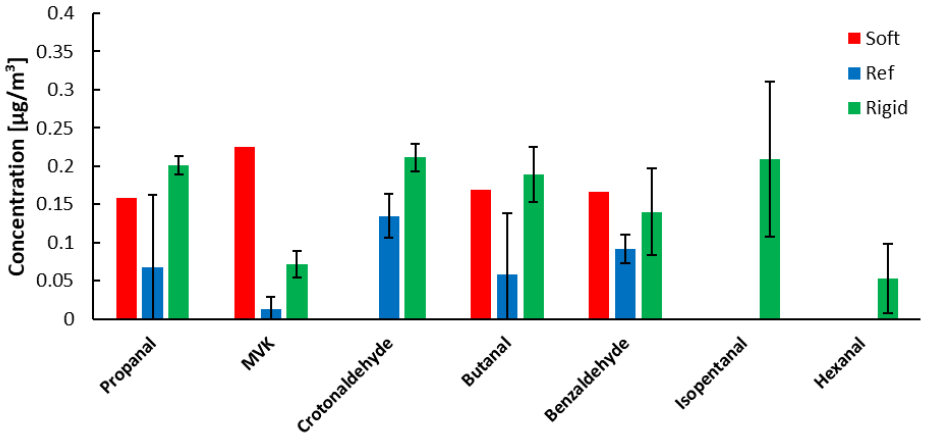

(b)

Figure 4.15 (a) Comparison of carbonyls from different pads, and (b) zoom in on the compounds with concentrations less than 0.4 µg/m³

4.2 Effect of the scale brake system

Although the following full-scale experiments were conducted prior to the reduced-scale campaign, we presented the reduced-scale results first to establish a focused understanding of the behavior of VOC and particle emissions under controlled, simplified conditions.

4.2.1 Mean to change the scales

The choice of test benches depends on several practical and technical factors. While full-scale testing offers higher representativeness of real-world conditions, its limited availability and the need for extended study durations necessitated complementary testing at a reduced scale. Reduced-scale tests offer advantages such as better control over environmental conditions and time efficiency.

The downscaling strategy is based on thermal and thermomechanical scaling factors, developed in LaMcube by Frangieh ensuring similar surface temperatures and densities of dissipated power and energy at both scales, maintaining an equal ratio between the rubbed surfaces of the disc and the pad

and similar thermomechanical localizations. The energy scale factor of 15 is achieved, allowing for effective scale-down testing (Frangieh et al., 2023).

4.2.2 Emission factors under normal and heavy pathways at both test scales

Emission factors (EF) were calculated using Eq. 4-1, taking into account the airflow differences between the two scales.

$$EF\ [\mu g/km] = \frac{TSP\ concentration\ [\mu g/m^3] \times\ air\ flow\ [m^3/h]\ \times pathway\ duration\ [h]}{pathway\ length\ [km]} \quad \text{Eq. 4-1}$$

Table 4.4 presents the EF for particle emissions generated under two pathways, NP and HP, tested on both full-scale and reduced-scale benches.

Table 4.4 TSP emission factors [µg/km] for NP and HP at full and reduced scale benches

EF [µg/km]	Full scale (2022)	Reduced scale
NP (2022)	9470 ± 1662	58 ± 2
HP (2022)	27400 ± 4809	639 ± 15
HP/NP	3	11

HP significantly increases particle emissions in both test scales. However, the disproportionately higher HP/NP ratio in the reduced-scale test (11 vs 3) may be attributed to the uncertainties (higher for full scale), as well as the depressurized state of the cabin, as discussed in the previous section 2.4.2.2. These factors likely affect the NP condition more strongly, since it is less severe and produces fewer particles, making it more sensitive to changes in measurement environment, leading to probable overestimation of the PM in full-scale experiments.

The scale ratio of the total suspended particles (TSP) mass emitted per unit distance closely aligns with the ratio of pad surface area between the two scales, indicating consistent scaling behavior. Additionally, the scale ratio of TSP mass emitted per unit of energy dissipated is approximately 1.5, which matches the expected outcome from the downscaling strategy based on energy dissipation, as proposed by Frangieh et al., (2023).
This confirms the validity of the downscaling approach in preserving the physical representativeness of wear emissions across different scales.

Table 4.5 Heavy pathway varying parameters for reduced and full scales

Bench	Full scale	Reduced scale	$\frac{Full\ scale}{Reduced\ scale}$
Pad surface area [cm^2]	7000	16	44
$\frac{TSP\ mass\ [mg]}{Distance\ [km]}$	27.4 ± 12.8	0.639 ± 0.015	43 ± 10
$\frac{Pad\ surface\ area\ [cm2]}{Distance\ [km]}$	$\frac{700\ cm^2}{280.9\ MJ} = 2.5$	$\frac{16\ cm^2}{9.7\ MJ} = 1.65$	1.5
$\frac{TSP\ mass\ [mg]}{Energy\ [MJ]}$	44.8 ± 20.8	30.2 ± 0.2	1.5

4.2.3 Particle mass size distribution

The particle mass size distributions of both NP and HP at full scale are presented in Figure 4.16. Both pathways yielded the same mode falling within the 1.6–2.5 µm range. Comparable results were obtained for both pathways. At reduced scale, the modal range shifted to 0.9–1.6 µm (Figure 3.1). Notably, despite this shift, the modes across both scales remain relatively similar.

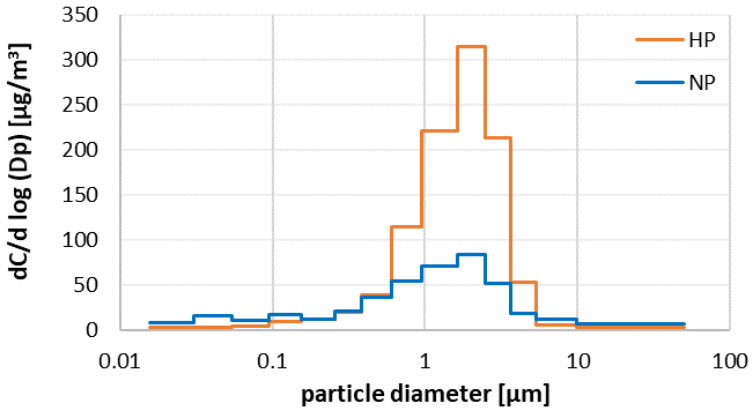

Figure 4.16 Particle mass size distribution of HP and NP at full scale

The comparison of the number size distributions between full-scale and reduced-scale is presented in Appendix 19.

4.2.4 Chemical composition and scale comparison of brake particles under HP

To better understand the detailed composition of brake particles generated under HP, chemical analyses were performed on samples collected during full-scale tests and will be compared to reduced-scale results using both TSP and PM1 fractions.

In the 2022 full scale campaign, we sampled each round trip separately using both the filter holder and the 3-stage impactor. After analyzing the samples, the third-round trip of the HP yielded the most significant results, likely due to a greater mass of particles being collected during that run for both TSP and PM1.

Figure 4.17 illustrates the chemical composition of particles collected during the third-round trip of the HP, comparing TSP collected with a filter holder and PM1 (backup of the 3-stage impactor).

For the TSP sample, the measured concentration was 284 µg/m³. The chemical distribution reveals that OC constitutes the largest fraction at 46%, followed by metals at 31%, oxygen and sulfur at 14%, and EC at 13%. Remarkably, the sum of the chemically identified components exceeds the measured TSP concentration. For instance, oxygen estimation and differences between analytical instruments can contribute to this mismatch.

In the case of PM1, the measured concentration was significantly lower at 45 µg/m³, as expected due to the exclusion of larger particles. The chemical composition shows a similar dominance of OC, which accounts for 56% of the mass, with metals at 30% and oxygen and sulfur at 14%. EC was below the detection limit, suggesting either a very low concentration or insufficient mass for accurate

quantification. This does not imply its absence but rather reflects the sensitivity limits of the analytical method.

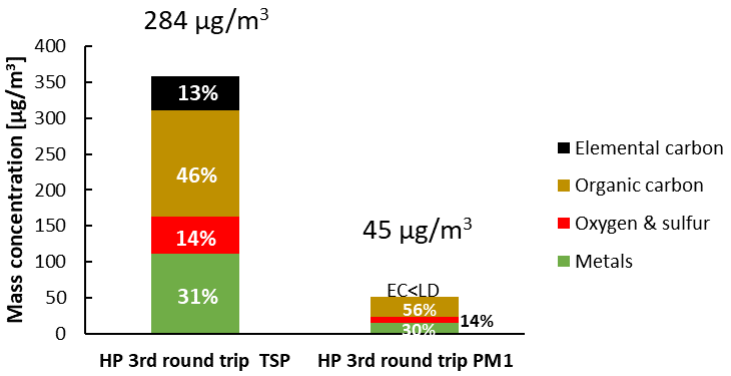

Figure 4.17 The chemical composition of particles collected during the third-round-trip of the HP at full scale, comparing TSP collected with a filter holder and PM1 collected with the 3-stage impactor

Figure 4.18 presents a comparison of the chemical composition, including Al, Ba, Ca, Cr, Cu, Fe, Mg, Mn, Sr, and Ti, of the brake particles between full-scale and reduced-scale tests for the HP, analyzed in both µg/m³ and µg/mg. A strong linear correlation is observed in both cases, with R^2 values of 0.9977, indicating the same metal relative composition between the two test scales.

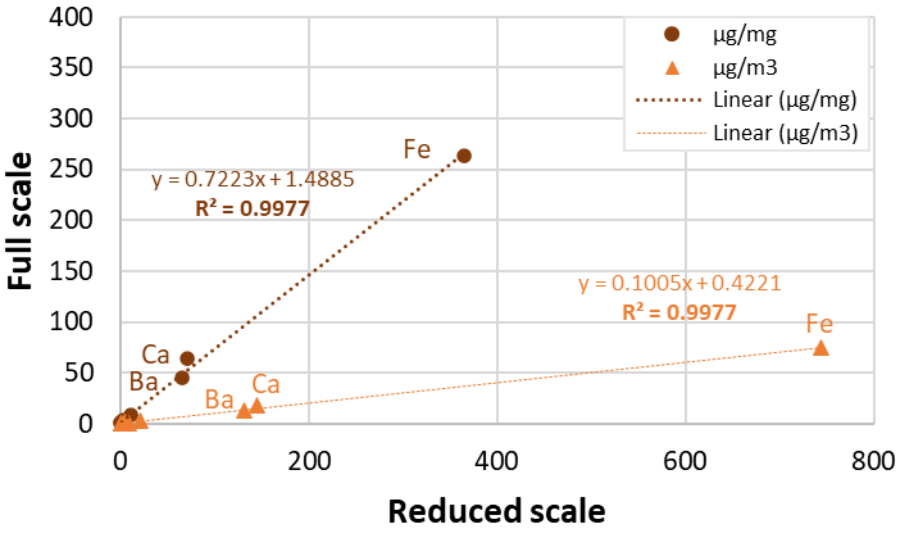

Figure 4.18 Comparison of TSP metal composition between full and reduced scales: linearity in µg/mg and µg/m³

In terms of metal mass concentration (µg/m³), the slope of the regression line is 0.1005, which aligns closely with the observed TSP mass concentration ratio of 0.14 (284 µg/m³ for the reduced scale and 2038 µg/m³ for the full scale). When looking at weight content (µg/mg), the slope is 0.7223, indicating a lower metallic content for collected TSP at full scale. This is maybe due to the fact that TSP are a mixture of braking emitted particles with indoor particles from the workshop, which are likely to contain organic material from the oil and grease used in the machinery of the dynamometer, thus lowering the metal contents compared to reduced scale under cleaner conditions.

4.2.5 Estimation and comparison of pad and disc contributions to brake particle emissions across full and reduced scales

Table 4.6 presents the results of estimating the relative mass contributions (source apportionment) of both pad and disc to the emitted TSP and PM1 for the 1st and 2nd round trips of NP and the 1st, 2nd, and 3rd round trips of HP, based on each metal tracer determined previously.

Table 4.6 Calculated relative mass contributions of the pad and disc to TSP and PM1, based on each metal tracer, for NP and HP routes at full scale.

		Mass contribution to TSP and PM1							
			pad					**disc**	**Pad + disc**
			Al	Ba	Ca	Av ± SD	CV	Cr	
			[%w in TSP]				-	[%w in TSP]	[%w in TSP]
NP	TSP	1st round trip	39%	33%	60%	**44** ± 14 %	31%	**53%**	**98%**
		2nd round trip	45%	35%	69%	**50** ± 18%	35%	**44%**	**94%**
	PM1	1st round trip	34%	11%	35%	**27** ± 13%	50%	**24%**	**54%**
		2nd round trip	27%	15%	34%	**26** ± 10%	39%	**24%**	**50%**
HP	TSP	1st round trip	63%	68%	78%	**70** ± 8%	11%	**35%**	**105%**
		2nd round trip	71%	68%	83%	**74** ± 8%	11%	**27%**	**101%**
		3rd round trip	65%	66%	77%	**69** ± 7%	10%	**25%**	**94%**
	PM1	1st round trip	49%	46%	76%	**57** ± 17%	30%	**28%**	**85%**
		2nd round trip	54%	43%	72%	**56** ± 15%	26%	**26%**	**82%**
		3rd round trip	56%	55%	78%	**63** ± 13%	21%	**24%**	**87%**

For the pad and within the HP, the calculated average mass contributions to TSP are consistent across different metal tracers and particle sizes (TSP or PM1), with a coefficient of variation (CV) of 11% for TSP and up to 30% for PM1. This indicates that higher collected mass leads to more consistent results. Nonetheless, for the NP, the CV was high, particularly for PM1, indicating greater variability in lower-emission scenarios. On the other hand, among the disc metal tracers, only Cr yielded reliable results, so it will be used to represent the disc contribution. Also, as the history increases, the CV decreases for all samples except NP (TSP), showing that the pad metallic contribution becomes more homogeneous.

Moreover, the sum of the mass contributions from the pad (average tracers) and the disc (Cr) to TSP is expected to equal 100%; however, for PM1 under NP, the error is significantly higher. In addition to the reasons previously discussed in the reduced-scale section, the low collected mass may also contribute to this discrepancy.

Figure 4.19 presents the results for HP only, as it yielded more reliable data, as discussed earlier. In Figure 4.19 (a), which shows TSP across all round trips, a consistent pattern is observed: the pad contributes significantly more to emissions, approximately 70%, in line with observations from the reduced-scale tests. Figure 4.19 (b) presents the PM1 results. Although the CV was higher for PM1, the data still suggest a dominant contribution from the pad, around 60%. This indicates that the relative contributions of the pad and disc remain similar across different particle size ranges.

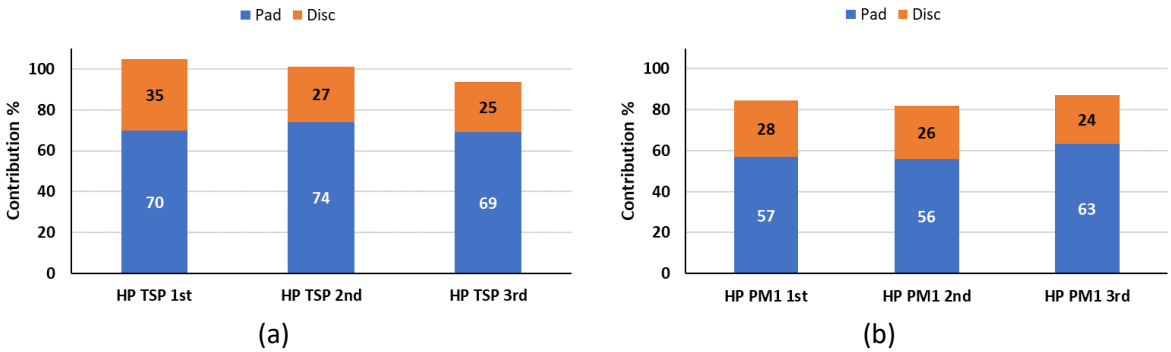

Figure 4.19 Pad and disc contributions to full-scale emissions under HP: (a) TSP, (b) PM1

To compare the reduced-scale results with the full-scale results for pad and disc contributions, the percentages were normalized to a total of 100%. These results are presented in Table 4.7. Notably for both scales, the percentage of pad contribution increased by a factor of 1.5 from NP to HP. Although NP results showed some variability, the comparison of pad and disc contributions between the two scales underlines a very good consistency.

Table 4.7 Normalized pad and disc contributions for NP and HP across both scales

	pad%	disc%
Reduced scale NP	45	55
Reduced scale HP	69	31
Full-scale NP	49	51
Full-scale HP	71	29

4.2.6 VOC analysis

Following the analysis of particle emissions under full-scale normal and heavy pathways, attention is now turned to characterizing VOCs.

Figure 4.20 compares the concentrations of various VOCs measured by GC-MS at the **inlet** (air entering the cabin), **outlet** (air sampled during braking), and **indoor** (ambient test room environment). In general, most compounds follow the trend **indoor > outlet > inlet**, with indoor concentrations being the highest across the majority of VOCs. This confirms the presence of organic compounds in the indoor air, as previously hypothesized for total carbon in particles (section 2.4.2.2).

The presence of VOCs at the inlet is attributed to the fact that standard air filtration systems used in the test setup are typically designed to remove PM and are not equipped to eliminate VOCs, and the implementation of VOC scrubbing systems or the use of purified air cylinders is not feasible in this test configuration. The higher concentrations at the outlet compared to the inlet could initially suggest that VOCs are emitted from the braking process. However, previous findings have demonstrated that at low disc rotation speeds, a possible depressurization can occur within the test cabin. This pressure gradient likely facilitates the entrance of VOC-rich indoor air into the cabin during braking.

As a result, although the elevated outlet concentrations could be partially attributed to braking-related emissions, the significant background contribution from the indoor environment complicates the interpretation. Therefore, it is difficult to attribute the VOCs observed at the outlet solely to braking activities.

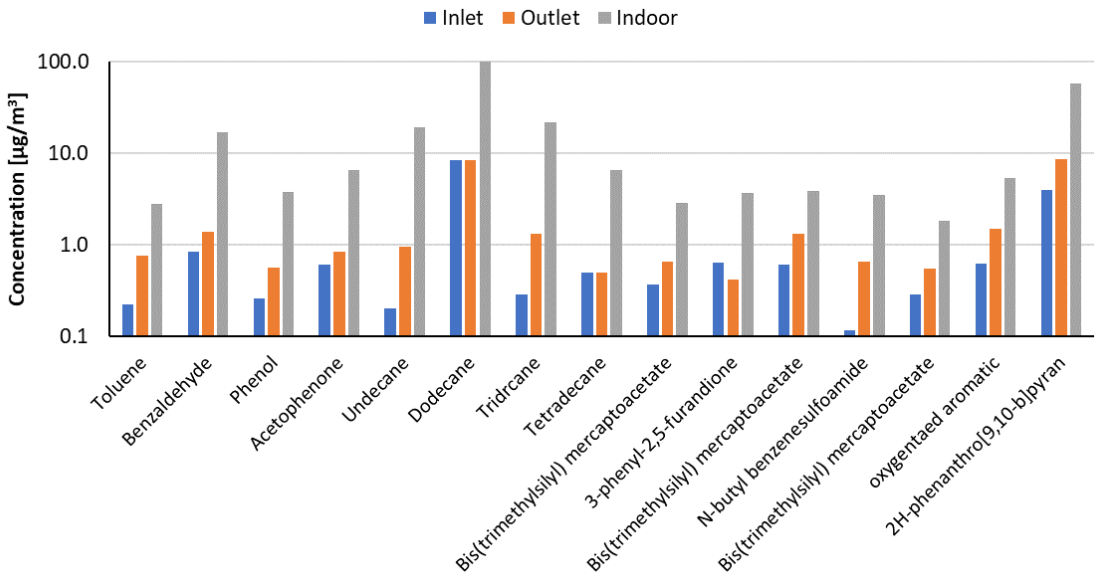

Figure 4.20 Comparison of VOC concentrations measured at the inlet, outlet, and indoor environments during HP

Due to the challenges associated with measuring VOC in industrial environments, obtaining reliable VOC data proved difficult. Even after implementing additional measures, such as monitoring both inlet and indoor measurements, the resulting data remained doubtful. Thus, for VOC analysis, the best approach is to conduct it on a reduced-scale bench in a controlled environment.

Chapter 5: Conclusions and perspectives

5.1 Conclusions

The present study investigated the influence of braking severity, pad material rigidity, and system scaling on brake wear emissions, focusing on both PM and VOCs. Experiments simulating a typical daily train journey were conducted at full and reduced scales, and focused on two primary objectives:

- Characterization of emitted particles in terms of number and mass concentration, chemical composition, number and mass size distributions, and morphology, near the emission point (partly time-resolved observations) in order to document the influence and relations of braking conditions on the particle physicochemical properties and, ultimately, on particle emission factor. To do so, relevant sampling systems and measuring instruments, based on different physical principles, have been selected and their performance (measurement uncertainty, artifacts) has been studied.
- Characterization of emitted VOCs in terms of mass concentration and speciation, in order to document the influence of braking conditions on the VOC emissions and to provide first determination of VOC emission factors. To do so, different sampling systems and measuring instruments have been selected and their performance studied.

First, regarding the effect of braking severity (normal vs heavy braking) on emissions at a reduced-scale test bench, the following main conclusions have been drawn:

Braking severity has a significant impact on both particulate and VOC emissions. HP, characterized by higher energies and higher contact temperatures, generated 6 to 11 times more TSP than NP. Sampling methods have been shown to influence the resulting collected masses of particles, with the filter holder capturing higher particle concentrations, probably due to the retention of semi-volatile organic compounds, while impactors tended to underestimate particle emissions. Both time-resolved and global measurements showed that particle size distributions were unimodal, with a main peak around 1 µm.

Similarly, VOC emissions were markedly higher and more diverse under HP. Offline analysis showed the presence of compounds such as oxygenated compounds, including phenols, acetaldehyde, propanone, and formaldehyde, as well as many hydrocarbons, including PAHs. Elevated temperatures accelerated the degradation of organic materials in the pad, primarily resins and rubbers, as confirmed by offline analyses and TGA-FTIR, which revealed a temperature-driven, multi-phase decomposition process.

The influence of braking intensity on material wear and emissions was studied by closely analyzing the physical and chemical properties of the brake components (pad and disc) and the particles they release. Under HP, pad wear dominates, leading to the enrichment of metals such as Al, Ba, and Ca in both TSP and submicron fractions. The application of the metal tracer method to particles collected by the filter holder and those from the stages of the 3-stage impactor showed good agreement, confirming that the chemical composition of TSP is consistent across different particle sizes. Mass closure demonstrates that metal oxides and carbonaceous compounds constitute most of the emissions. The submicronic fraction retained a significant portion of metallic elements but exhibited reduced organic carbon under HP, suggesting volatilization. VOC data supports this, showing tenfold higher emissions under HP.

The dynamic evolution of VOC emissions during braking, particularly under the heavy pathway, was investigated using PTR-MS in order to relate the tribology to the emissions. Several compounds previously detected by offline analysis were confirmed, along with additional ones such as methanol, isoprene, and BTEX, with acetaldehyde and isoprene dominating. The results reveal that VOC emission peaks begin with the onset of braking and increase throughout the event. However, a few compounds display a strong correlation with disc rotation. Overall, VOC emissions appear less influenced by mechanical wear or braking sequence compared to particulate matter, indicating a primarily chemical origin.

While identifying consistent trends in total VOC emissions was challenging, a general relationship with braking duration was observed. On a compound-specific level, acetonitrile, benzene, and toluene correlated well with energy, while acrolein showed a strong dependence on temperature. Greater power showed a decreasing trend with VOCs, suggesting that greater contact pressure may tighten the interface between the pad and disc, trapping VOCs and limiting their release.

In terms of braking application, no significant effect was observed when varying the single braking energy (1-step vs. 2-step) or comparing single to multiple braking applications within the same energy level.

The VOC dynamics indicate different emission mechanisms compared to PM. PM peaks immediately at the start of braking, whereas VOC emissions persist throughout the braking event and typically peak at the end of the braking event. In the case of multiple braking events, PM emissions tend to decrease as the surfaces become accommodated, while VOC emissions remain unaffected. Additionally, when comparing three round trips, PM emissions decrease at the same station from the first to the third one, whereas VOC levels stay consistent.

The **second** part of the study investigated mitigation actions that could be undertaken for the reduction of VOCs and/or particle emissions, in this case by changing pad rigidity and groove design. Despite sharing similar formulations, the soft and rigid pads exhibited significant differences in mechanical properties. Rigid pads consistently emitted 2–3 times more TSP than soft pads, although all pad types showed similar unimodal particle size distributions centered around 1–2 µm. Conversely, VOC emissions revealed similar concentrations among all pads during the normal pathway.

Across all pad types—reference, soft, rigid, and grooved—metal emissions were dominated by Fe, followed by Ba, Ca, and Al, with similar patterns observed across both braking pathways. While carbon analysis did not reveal a clear trend linked to pad rigidity, the reference pad showed the highest total carbon content.

Remarkably, the representativeness of reduced-scale tests has been confirmed for PM emissions: the emission factors measured at reduced and full scale align very well with the scaling factor proposed by (Frangieh et al., 2023), and show consistent chemical composition and particle mass size distribution, including the same dominant metals. However, for VOCs, distinguishing braking-related emissions at full scale remains challenging due to high background levels.

5.2 Perspectives

To improve both qualitatively and quantitatively the analysis of PM and VOC emitted from braking systems, several methodological and investigative improvements are proposed.

- **Sampling and characterization enhancements:**

For PM sampling, it is recommended to reduce the sampling time during heavy braking to avoid filter overload. Quartz filters should be used for TSP carbon analysis to have an overview of the results. Additionally, the original 3-stage impactor is preferred for particle size separation and collection.

For VOC characterization, reduced-scale test benches are recommended to better control environmental variables and minimize contamination risks. Pre-flushing the system before each test helps limit background interference. To detect larger VOC species, filters should be solvent-extracted or an advanced tool like the very recent Vocus PTR-TOF-MS could be used. Including CO, CO_2 and NO_x (NO and NO_2) measurements can provide insights into the combustion of organic materials during braking.

- **Understanding emissions under low severity:**

Low VOC readings, especially during normal pathway tests, may reflect instrument detection limits rather than the true absence of emissions. To address this, TGA at varied heating rates should be applied to study the kinetics of thermal degradation and explain emission differences among compounds and conditions. It is also essential to compare emissions from rigid and soft pads under heavy braking conditions, as such tests generate higher VOC levels and allow for a clearer understanding of emission behaviors and which compounds to follow at low severity. The measurement of these compounds at low concentration may require further sampling and analytical development, such as better adsorbents or program temperature.

- **Deeper characterization studies:**

Future work should include a comparison of emission rates and physico-chemical composition of wear particles, third-body particles, and airborne particles. Additionally, a detailed characterization of the microstructure of the material surfaces, as well as the generated particles across these categories, will provide deeper understandings into emission mechanisms.

- **Real-world and predictive investigations:**

Field measurements on subway platforms are essential for evaluating actual airborne particle and VOC concentrations during braking, offering context for lab findings. Additionally, advanced modeling or simulation tools should be developed to predict VOC emissions based on tribological behavior, contributing to a more comprehensive understanding of emission dynamics.

- **Health and environmental effect:**

Finally, evaluating the toxicity of both particles and VOCs will be essential to assess their environmental and health impacts and guide regulatory and material development efforts. For example, exposure boxes could be connected to the outlet of the tribological bench, in order to submit living cells (or even animals) to real emissions.

References

Aarnio, P., Yli-Tuomi, T., Kousa, A., Mäkelä, T., Hirsikko, A., Hämeri, K., Räisänen, M., Hillamo, R., Koskentalo, T., & Jantunen, M. (2005). The concentrations and composition of and exposure to fine particles (PM2.5) in the Helsinki subway system. *Atmospheric Environment*, *39*(28), 5059–5066. https://doi.org/10.1016/j.atmosenv.2005.05.012

Aas, W., Fagerli, H., Alastuey, A., Cavalli, F., Degorska, A., Feigenspan, S., Brenna, H., Gliß, J., Heinesen, D., Hueglin, C., Holubová, A., Jaffrezo, J. L., Mortier, A., Murovec, M., Putaud, J. P., Rüdiger, J., Simpson, D., Solberg, S., Tsyro, S., … Yttri, K. E. (2024). Trends in Air Pollution in Europe, 2000–2019. Aerosol and Air Quality Research, 24(4), 1–19. https://doi.org/10.4209/aaqr.230237

Abbasi, S., Jansson, A., Olander, L., Olofsson, U., & Sellgren, U. (2012). A pin-on-disc study of the rate of airborne wear particle emissions from railway braking materials. *Wear*, *284–285*, 18–29. https://doi.org/10.1016/j.wear.2012.01.016

Abbasi, S., Jansson, A., Sellgren, U., & Olofsson, U. (2013). Particle Emissions From Rail Traffic: A Literature Review. *Critical Reviews in Environmental Science and Technology*, *43*(23), 2511–2544. https://doi.org/10.1080/10643389.2012.685348

Abbasi, S., Olander, L., Larsson, C., Olofsson, U., Jansson, A., & Sellgren, U. (2012). A field test study of airborne wear particles from a running regional train. *Proceedings of the Institution of Mechanical Engineers, Part F: Journal of Rail and Rapid Transit*, *226*(1), 95–109. https://doi.org/10.1177/0954409711408774

Adamia, T. V., Budovich, V. L., Nevjagskaya, I. A., Shlyakhov, A. F., & Jakovlev, S. A. (1991). Effect of temperature on the sensitivity of the photoionization detector. *Journal of Chromatography A*, *540*(C), 441–448. https://doi.org/10.1016/S0021-9673(01)88836-1

Alleman, L. Y., Lamaison, L., Perdrix, E., Robache, A., & Galloo, J. C. (2010). PM10 metal concentrations and source identification using positive matrix factorization and wind sectoring in a French industrial zone. *Atmospheric Research*, *96*(4), 612–625. https://doi.org/10.1016/j.atmosres.2010.02.008

Alves, C., Evtyugina, M., Vicente, A., Conca, E., & Amato, F. (2021). *Organic profiles of brake wear particles*. *255*(February). https://doi.org/10.1016/j.atmosres.2021.105557

Amann, A., Schwarz, K., Wimmer, G., & Witkovský, V. (2010). Model Based Determination of Detection Limits for Proton Transfer Reaction Mass Spectrometer. *Measurement Science Review*, *10*, 180–188. https://doi.org/10.2478/v10048-010-0031-5

Assimakopoulos, M. N., Dounis, A., Spanou, A., & Santamouris, M. (2013). Indoor air quality in a metropolitan area metro using fuzzy logic assessment system. *Science of The Total Environment*, *449*, 461–469. https://doi.org/10.1016/J.SCITOTENV.2012.12.043

Bachoual, R., Boczkowski, J., Goven, D., Amara, N., Tabet, L., On, D., Leçon-Malas, V., Aubier, M., & Lanone, S. (2007). Biological Effects of Particles from the Paris Subway System. *Chemical Research in Toxicology*, *20*(10), 1426–1433. https://doi.org/10.1021/tx700093j

Barmparesos, N., Assimakopoulos, V. D., Assimakopoulos, M. N., & Tsairidi, E. (2016). Particulate matter levels and comfort conditions in the trains and platforms of the athens underground

metro. *AIMS Environmental Science*, *3*(2), 199–219. https://doi.org/10.3934/environsci.2016.2.199

Beji, A., Deboudt, K., Khardi, S., Muresan, B., Flament, P., Fourmentin, M., & Lumière, L. (2020). Non-exhaust particle emissions under various driving conditions: Implications for sustainable mobility. *Transportation Research Part D: Transport and Environment*, *81*(March), 102290. https://doi.org/10.1016/j.trd.2020.102290

Bennett, A., Payne, D. R., & Court, R. W. (2014). Pyrolytic and elemental analysis of decomposition products from a phenolic resin. *Macromolecular Symposia*, *339*(1), 38–47. https://doi.org/10.1002/masy.201300136

Berthier, Y. (2001). Background on Friction and Wear. *Handbook of Materials Behavior Models*, 676–699. https://doi.org/10.1016/b978-012443341-0/50074-0

Bonfanti, A. (2016). *Low-impact friction materials for brake pads*. *June*, 1–214.

Braniˇ, M. (2006). The contribution of ambient sources to particulate pollution in spaces and trains of the Prague underground transport system. *Atmospheric Environment*, *40*(2), 348–356. https://doi.org/10.1016/J.ATMOSENV.2005.09.060

Briatte, M. (2024). *Relation entre l'état métallurgique d'aciers inoxydables martensitiques et les émissions de particules en situation de freinage*. Centrale Lille.

Briatte, M., Mege-Revil, A., Desplanques, Y., & Santacreu, P. O. (2025). Effect of the microstructure of martensitic stainless steel discs on wear processes and particle emission in automotive braking. *Wear*, *January*, 205825. https://doi.org/10.1016/j.wear.2025.205825

Buyaev, D. I., Naumkin, A. V., Yudin, A. S., Alekseev, V. V., Maslakov, K. I., Afonicheva, O. V., Kiselev, S. S., Osipchik, V. S., Klabukova, L. F., & Krasnov, A. P. (2016). Tribochemical processes in epoxyorganic textolite–steel friction pair. *Journal of Friction and Wear*, *37*(1), 15–22. https://doi.org/10.3103/S1068366616010049

Cartenì, A., Cascetta, F., & Campana, S. (2015). Underground and ground-level particulate matter concentrations in an Italian metro system. *Atmospheric Environment*, *101*, 328–337. https://doi.org/https://doi.org/10.1016/j.atmosenv.2014.11.030

Cha, Y., Abbasi, S., & Olofsson, U. (2018). Indoor and outdoor measurement of airborne particulates on a commuter train running partly in tunnels. *Proceedings of the Institution of Mechanical Engineers, Part F: Journal of Rail and Rapid Transit*, *232*(1), 3–13. https://doi.org/10.1177/0954409716642492

Cha, Y., Tu, M., Elmgren, M., Silvergren, S., & Olofsson, U. (2019). Variation in airborne particulate levels at a newly opened underground railway station. *Aerosol and Air Quality Research*, *19*(4), 737–748. https://doi.org/10.4209/aaqr.2018.06.0225

Chang, L., Chong, W. T., Wang, X., Pei, F., Zhang, X., Wang, T., Wang, C., & Pan, S. (2021). Recent progress in research on PM2.5in subways. *Environmental Science: Processes and Impacts*, *23*(5), 642–663. https://doi.org/10.1039/d1em00002k

Chauhan, V., Darpe, A., & Bijwe, J. (2022). Susceptibility of eco-friendly brake-pads to noise-vibration emanation due to siloxane treatment on alumina particles. *Applied Acoustics*, *185*, 108377. https://doi.org/https://doi.org/10.1016/j.apacoust.2021.108377

Chen, Y., Chen, Z., Xiao, S., & Liu, H. (2008). A novel thermal degradation mechanism of phenol-formaldehyde type resins. *Thermochimica Acta*, *476*(1–2), 39–43. https://doi.org/10.1016/j.tca.2008.04.013

Chen, Z. Q., Chen, Y. F., & Liu, H. B. (2013). Study on thermal degradation of phenolic resin. *Applied Mechanics and Materials*, *422*, 24–28. https://doi.org/10.4028/www.scientific.net/AMM.422.24

Colombi, C., Angius, S., Gianelle, V., & Lazzarini, M. (2013). Particulate matter concentrations, physical characteristics and elemental composition in the Milan underground transport system. *Atmospheric Environment*, *70*, 166–178. https://doi.org/https://doi.org/10.1016/j.atmosenv.2013.01.035

Conca, E., Malandrino, M., Diana, A., Abollino, O., Giacomino, A., Bartrolí, R., Moreno, T., Querol, X., & Amato, F. (2022). Methods for Elemental Analysis of Size-Resolved PM Samples Collected on Aluminium Foils: Results of an Intercomparison Exercise. Molecules, 27(21). https://doi.org/10.3390/molecules27217442

Czaplicki, S. (2013). *Chromatography in Bioactivity Analysis of Compounds* (pp. 99–122). https://doi.org/10.5772/55620

Daellenbach, K. R., Uzu, G., Jiang, J., Cassagnes, L. E., Leni, Z., Vlachou, A., Stefenelli, G., Canonaco, F., Weber, S., Segers, A., Kuenen, J. J. P., Schaap, M., Favez, O., Albinet, A., Aksoyoglu, S., Dommen, J., Baltensperger, U., Geiser, M., El Haddad, I., … Prévôt, A. S. H. (2020). Sources of particulate-matter air pollution and its oxidative potential in Europe. *Nature*, *587*(7834), 414–419. https://doi.org/10.1038/s41586-020-2902-8

Dekati, Technical Documentation. (n.d.).

Denape, J. (2019). Introduction to tribology. *Course of National School of Engineeers of Tarbes - ENIT*, 20 slides.

Department for Environment, Food & Rural Affairs. (2024). Concentrations of Particulate Matter (PM_{10} and $PM_{2.5}$). UK Government. https://www.gov.uk/government/statistics/air-quality-statistics/concentrations-of-particulate-matter-pm10-and-pm25

Desplanques, Y., & Degallaix, G. (2010). Genesis of the Third-Body at the Pad-Disc Interface. *SAE International Journal of Materials and Manufacturing*, *2*(2), 25–32.

Detournay, A., Sauvage, S., Locoge, N., Gaudion, V., Leonardis, T., Fronval, I., Kaluzny, P., & Galloo, J. C. (2011). Development of a sampling method for the simultaneous monitoring of straight-chain alkanes, straight-chain saturated carbonyl compounds and monoterpenes in remote areas. *Journal of Environmental Monitoring*, *13*(4), 983–990. https://doi.org/10.1039/c0em00354a

Do, D. H., Van Langenhove, H., Chigbo, S. I., Amare, A. N., Demeestere, K., & Walgraeve, C. (2014). Exposure to volatile organic compounds: Comparison among different transportation modes. *Atmospheric Environment*, *94*, 53–62. https://doi.org/https://doi.org/10.1016/j.atmosenv.2014.05.019

Dunne, E., Galbally, I. E., Cheng, M., Selleck, P., Molloy, S. B., & Lawson, S. J. (2018). Comparison of VOC measurements made by PTR-MS, adsorbent tubes–GC-FID-MS and DNPH derivatization–HPLC during the Sydney Particle Study, 2012: a contribution to the

assessment of uncertainty in routine atmospheric VOC measurements. *Atmospheric Measurement Techniques*, *11*(1), 141–159. https://doi.org/10.5194/amt-11-141-2018

Dura, G., & Szalay, B. (2007). Particle exposure through the indoor air environment. *Indoor Air*, 271–276.

Durif, O., Bard, L., Elihn, K., Nozière, B., Olofsson, U., & Steimer, S. S. (2025). Emissions of Volatile Organic Compounds from Brake Wear and Their Role in Ultrafine Particle Nucleation. *ACS ES&T Air*. https://doi.org/10.1021/acsestair.5c00070

Eckenberger, E., Mittereder, A., Gawlitta, N., & Schnelle-kreis, J. (2025). *Performance evaluation of four cascade impactors for airborne ultrafine-particle (UFP) collection : the influence of particle type , concentration , mass , and chemical nature*. 45–64.

EEA. (2019). https://www.eea.europa.eu/publications/air-quality-in-europe-2019

EEA. (2021). https://www.eea.europa.eu/publications/air-quality-in-europe-2021/sources-and-emissions-of-air

EEA. (2024). https://www.eea.europa.eu//publications/europes-air-quality-status-2024

Egeonu, D., Oluah, C., & Okolo, P. N. (2015). Production of Eco-Friendly Brake Pad Using Raw Materials Sourced Locally In Nsukka. In *Article in International Journal of Energy Technology and Policy* (Vol. 23). https://www.researchgate.net/publication/286927474

EURACHEM/CITAC 2000. (n.d.). https://eurachem.org/images/stories/Guides/pdf/QUAM2000-1.pdf

Feinberg, M. (2012). Validation des méthodes d'analyse quantitatives au moyen du profil d'exactitude. Qualité et Sécurité Au Laboratoire, 33(0). https://doi.org/10.51257/a-v2-p224

Feng, Y., Mu, C., Zhai, J., Li, J., & Zou, T. (2010). Characteristics and personal exposures of carbonyl compounds in the subway stations and in-subway trains of Shanghai, China. *Journal of Hazardous Materials*, *183*(1–3), 574–582. https://doi.org/10.1016/j.jhazmat.2010.07.062

Fillot, N., Iordanoff, I., & Berthier, Y. (2007). Wear modeling and the third body concept. *Wear*, *262*(7–8), 949–957. https://doi.org/10.1016/j.wear.2006.10.011

Frangieh, J. (2025). *Wear Determinants in Railway Friction Brakes using Thermomechanical and Tribological Coupling*. Centrale Lille.

Frangieh, J., Desplanques, Y., Mann, R., & Dufrenoy, P. (2023). Downscaling for disc-brake wear testing using a thermomechanical approach. *Mechanics and Industry*, *24*. https://doi.org/10.1051/meca/2023016

Frangieh, J., Grira, A., Davin, E., Brunel, F., Al-kaderi, R., Perdrix, E., Tomas, A., Henrion, M., Mann, R., Desplanques, Y., & Dufrénoy, P. (2025). Railway braking wear dynamics and particle emissions : Relationship between tribological circuit and pad design. *Wear*, *February*, 205854. https://doi.org/10.1016/j.wear.2025.205854

Frangieh, J., Grira, A., Davin, E., Coustenoble, L., Henrion, M., Pajot, K., Desplanques, Y., & Dufrenoy, P. (2025). Implications of operating condition changes on thermal and thermomechanical behavior, affecting tribological performance, wear and emissions in railway friction braking. *Tribology International*, *212*(May), 110822. https://doi.org/10.1016/j.triboint.2025.110822

Fruhwirt, D., Nöst, T., Leonhardt, P., Leitner, M., Brunnhofer, P., Bode, G., Michael, S., & Rodler, J. (2025). Emission characteristics of railway tread brakes. *Atmospheric Environment: X*, *25*, 100320. https://doi.org/https://doi.org/10.1016/j.aeaoa.2025.100320

Furuya, K., Kudo, Y., Okinaga, K., Yamuki, M., Takahashi, S., Araki, Y., & Hisamatsu, Y. (2001). Seasonal variation and their characterization of suspended particulate matter in the air of subway stations. *Journal of Trace and Microprobe Techniques*, *19*(4), 469–485. https://doi.org/10.1081/TMA-100107583

Garg, B. D., Cadle, S. H., Mulawa, P. A., Groblicki, P. J., & Laroo, C. (2000). *Brake Wear Particulate Matter Emissions*. 4463–4469.

Gensch, M., & Weber, A. P. (2017). Rebound behavior of nanoparticle-agglomerates. *Advanced Powder Technology*, *28*(8), 1930–1942. https://doi.org/https://doi.org/10.1016/j.apt.2017.05.003

Godet, M. (1984). The third-body approach: A mechanical view of wear. *Wear*, *100*(1), 437–452. https://doi.org/https://doi.org/10.1016/0043-1648(84)90025-5

Gong, Y., Wei, Y., Cheng, J., Jiang, T., Chen, L., & Xu, B. (2017). Health risk assessment and personal exposure to Volatile Organic Compounds (VOCs) in metro carriages — A case study in Shanghai, China. *Science of the Total Environment*, *574*(1239), 1432–1438. https://doi.org/10.1016/j.scitotenv.2016.08.072

Grass, D., Ross, J. M., Family, F., Barbour, J., Simpson, H. J., Coulibaly, D., Hernandez, J., Chen, Y., Slavkovich, V., Li, Y., Graziano, J. H., Santella, R. M., Brandt-Rauf, P. W., & Chillrud, S. N. (2010). Airborne particulate metals in the New York City subway: a pilot study to assess the potential for health impacts. *Environmental Research*, *110 1*, 1–11.

Grigoratos, T., Mamakos, A., Arndt, M., Lugovyy, D., Anderson, R., Hafenmayer, C., Moisio, M., Vanhanen, J., Frazee, R., Agudelo, C., & Giechaskiel, B. (2023). Characterization of Particle Number Setups for Measuring Brake Particle Emissions and Comparison with Exhaust Setups. *Atmosphere*, *14*(1). https://doi.org/10.3390/atmos14010103

Grigoratos, T., & Martini, G. (2014). Non-exhaust traffic related emissions - Brake and tyre wear PM: Literature review. *EUR - Scientific and Technical Research Series*, 1–53. https://doi.org/doi:10.2790/21481

Grigoratos, T., & Martini, G. (2015). Brake wear particle emissions: a review. *Environmental Science and Pollution Research*, *22*(4), 2491–2504. https://doi.org/10.1007/s11356-014-3696-8

Guarnieri, M., & Balmes, J. R. (2014). Outdoor air pollution and asthma. *Lancet (London, England)*, *383*(9928), 1581–1592. https://doi.org/10.1016/S0140-6736(14)60617-6

Hagino, H., Oyama, M., & Sasaki, S. (2016). Laboratory testing of airborne brake wear particle emissions using a dynamometer system under urban city driving cycles. *Atmospheric Environment*, *131*, 269–278. https://doi.org/10.1016/J.ATMOSENV.2016.02.014

Haut Conseil pour la Santé Publique. (2019).

Hernández-Castillo, O., Mugica-Álvarez, V., Castañeda-Briones, M. T., Murcia, J. M., García-Franco, F., & Falcón Briseño, Y. (2014). Aerobiological study in the Mexico City subway system. *Aerobiologia*, *30*(4), 357–367. https://doi.org/10.1007/s10453-014-9334-6

Houston, D., Wu, J., Yang, D., & Jaimes, G. (2013). Particle-bound polycyclic aromatic hydrocarbon concentrations in transportation microenvironments. *Atmospheric Environment*, *71*, 148–157. https://doi.org/10.1016/j.atmosenv.2013.02.002

Huang, H., Wang, Z., Dai, C., Guo, J., & Zhang, X. (2022). Volatile organic compounds emission in the rubber products manufacturing processes. *Environmental Research*, *212*(PC), 113485. https://doi.org/10.1016/j.envres.2022.113485

Iijima, A., Sato, K., Yano, K., Tago, H., Kato, M., Kimura, H., & Furuta, N. (2007). Particle size and composition distribution analysis of automotive brake abrasion dusts for the evaluation of antimony sources of airborne particulate matter. Atmospheric Environment, 41(23), 4908–4919. https://doi.org/10.1016/j.atmosenv.2007.02.005

International Agency for Research on Cancer. (n.d.). *Agents classified by the IARC monographs, volumes 1–129.* IARC. Retrieved March 15, 2023, from http://monographs.iarc.fr/ENG/Classification/index.php

Johansson, C., & Johansson, P. Å. (2003). Particulate matter in the underground of Stockholm. *Atmospheric Environment*, *37*(1), 3–9. https://doi.org/10.1016/S1352-2310(02)00833-6

Kam, W., Cheung, K., Daher, N., & Sioutas, C. (2011). Particulate matter (PM) concentrations in underground and ground-level rail systems of the Los Angeles Metro. *Atmospheric Environment*, *45*(8), 1506–1516. https://doi.org/10.1016/j.atmosenv.2010.12.049

Kamani, H., Hoseini, M., Seyedsalehi, M., Mahdavi, Y., & Safari, G. (2014). Concentration and Characterization of Airborne Particles in Tehran's Subway System. *Environmental Science and Pollution Research International*, *21*. https://doi.org/10.1007/s11356-014-2659-4

Karlsson, H. L., Nilsson, L., & Möller, L. (2005). Subway particles are more genotoxic than street particles and induce oxidative stress in cultured human lung cells. *Chemical Research in Toxicology*, *18*(1), 19–23. https://doi.org/10.1021/tx049723c

Křístková, M., Filip, P., Weiss, Z., & Peter, R. (2004). Influence of metals on the phenol-formaldehyde resin degradation in friction composites. *Polymer Degradation and Stability*, *84*(1), 49–60. https://doi.org/10.1016/j.polymdegradstab.2003.09.012

Kukutschová, J., Moravec, P., Tomášek, V., Matějka, V., Smolík, J., Schwarz, J., Seidlerová, J., Šafářová, K., & Filip, P. (2011). On airborne nano/micro-sized wear particles released from low-metallic automotive brakes. *Environmental Pollution*, *159*(4), 998–1006. https://doi.org/10.1016/J.ENVPOL.2010.11.036

Lamaison, L. (2006). *Caractérisation des particules atmosphériques et identification de leurs sources dans une atmosphère urbaine sous influence industrielle*. http://www.theses.fr/2006LIL10071

Lansdown, A. R., & Price, A. L. (1986). *Materials to resist wear*. Pergamon Books Inc.,Elmsford, NY. https://www.osti.gov/biblio/5679944

Lee, C. M., Kim, Y. S., Nagajyoti, P. C., Park, W., & Kim, K. Y. (2011). Pattern Classification of Volatile Organic Compounds in Various Indoor Environments. *Water, Air, & Soil Pollution*, *215*(1), 329–338. https://doi.org/10.1007/s11270-010-0481-2

Lee, H. W. (2020). Generation characteristics of the airborne wear particles emitted from the wheel–rail contact for various train velocities and their generation relation with the train

velocity. *Atmospheric Environment: X*, *5*, 100068. https://doi.org/10.1016/j.aeaoa.2020.100068

Li, T.-T., Bai, Y.-H., Liu, Z.-R., Liu, J.-F., Zhang, G.-S., & Li, J.-L. (2006). Air quality in passenger cars of the ground railway transit system in Beijing, China. Science of The Total Environment, 367(1), 89–95. https://doi.org/https://doi.org/10.1016/j.scitotenv.2006.01.007

Liati, A., Schreiber, D., Lugovyy, D., Gramstat, S., & Dimopoulos Eggenschwiler, P. (2019). Airborne particulate matter emissions from vehicle brakes in micro- and nano-scales: Morphology and chemistry by electron microscopy. *Atmospheric Environment*, *212*(March), 281–289. https://doi.org/10.1016/j.atmosenv.2019.05.037

Lim, J., Jeong, J., Jung, B., Lee, J., Moon, J., Chung, Y.-S., & Kim, K.-H. (2011). Characteristics of the elemental compositions of particulate matter at a subway platform using INAA and XRF. *Proceedings in Radiochemistry*, *1*, 313–318. https://doi.org/10.1524/rcpr.2011.0054

Lundström, S. L., Levänen, B., Nording, M., Klepczynska-Nyström, A., Sköld, M., Haeggström, J. Z., Grunewald, J., Svartengren, M., Hammock, B. D., Larsson, B. M., Eklund, A., Wheelock, Å. M., & Wheelock, C. E. (2011). Asthmatics exhibit altered oxylipin profiles compared to healthy individuals after subway air exposure. *PLoS ONE*, *6*(8). https://doi.org/10.1371/journal.pone.0023864

Lyu, Y., Varriale, F., Malmborg, V., Ek, M., Pagels, J., & Wahlström, J. (2024). Tribology and airborne particle emissions from grey cast iron and WC reinforced laser cladded brake discs. Wear, 556–557(June). https://doi.org/10.1016/j.wear.2024.205512

Malachova, K., Kukutschova, J., Rybkova, Z., Sezimova, H., Placha, D., Cabanova, K., & Filip, P. (2016). Toxicity and mutagenicity of low-metallic automotive brake pad materials. Ecotoxicology and Environmental Safety, 131, 37–44. https://doi.org/10.1016/j.ecoenv.2016.05.003

Mamakos, A., Kolbeck, K., Arndt, M., Schröder, T., & Bernhard, M. (2021). Particle emissions and disc temperature profiles from a commercial brake system tested on a dynamometer under real-world cycles. *Atmosphere*, *12*(3). https://doi.org/10.3390/atmos12030377

Martins, V., Moreno, T., Minguillón, M. C., Amato, F., de Miguel, E., Capdevila, M., & Querol, X. (2015). Exposure to airborne particulate matter in the subway system. *Science of The Total Environment*, *511*, 711–722. https://doi.org/https://doi.org/10.1016/j.scitotenv.2014.12.013

Matti Maricq, M. (2007). Chemical characterization of particulate emissions from diesel engines: A review. *Journal of Aerosol Science*, *38*(11), 1079–1118. https://doi.org/https://doi.org/10.1016/j.jaerosci.2007.08.001

Menapace, C., Leonardi, M., Secchi, M., Bonfanti, A., Gialanella, S., & Straffelini, G. (2019). Thermal behavior of a phenolic resin for brake pad manufacturing. *Journal of Thermal Analysis and Calorimetry*, *137*(3), 759–766. https://doi.org/10.1007/s10973-019-08004-2

Moreno, T., Pérez, N., Reche, C., Martins, V., de Miguel, E., Capdevila, M., Centelles, S., Minguillón, M. C., Amato, F., Alastuey, A., Querol, X., & Gibbons, W. (2014). Subway platform air quality.Assessing the influences of tunnel ventilation, train piston effect and station design. *Atmospheric Environment*, *92*, 461–468. https://doi.org/10.1016/j.atmosenv.2014.04.043

Moreno, T., Reche, C., Rivas, I., Cruz Minguillón, M., Martins, V., Vargas, C., Buonanno, G., Parga, J., Pandolfi, M., Brines, M., Ealo, M., Sofia Fonseca, A., Amato, F., Sosa, G., Capdevila, M., de Miguel, E., Querol, X., & Gibbons, W. (2015). Urban air quality comparison for bus, tram, subway and pedestrian commutes in Barcelona. *Environmental Research*, *142*, 495–510. https://doi.org/10.1016/J.ENVRES.2015.07.022

Mosleh, M., Blau, P. J., & Dumitrescu, D. (2004). Characteristics and morphology of wear particles from laboratory testing of disk brake materials. Wear, 256(11–12), 1128–1134. https://doi.org/10.1016/j.wear.2003.07.007

Namgung, H.-G., Kim, J.-B., Woo, S.-H., Park, S., Kim, M., Kim, M.-S., Bae, G.-N., Park, D., & Kwon, S.-B. (2016). Generation of Nanoparticles from Friction between Railway Brake Disks and Pads. *Environmental Science & Technology*, *50*(7), 3453–3461. https://doi.org/10.1021/acs.est.5b06252

NIOSH. (2003). *Elemental carbon (diesel particulate) using thermal-optical analysis.* https://www.cdc.gov/niosh/docs/2003-154/pdfs/5040.pdf

Nogueira, A. P. G., Leonardi, M., Straffelini, G., & Gialanella, S. (2020). Sliding Behavior and Particle Emissions of Cu-Free Friction Materials with Different Contents of Phenolic Resin. *Tribology Transactions*, *63*(4), 770–779. https://doi.org/10.1080/10402004.2020.1753870

Nosko, O., Vanhanen, J., & Olofsson, U. (2017). Emission of 1.3–10 nm airborne particles from brake materials. *Aerosol Science and Technology*, *51*(1), 91–96. https://doi.org/10.1080/02786826.2016.1255713

Octau, C. (2019). *Contribution to the study of the generation and dynamics of particles emitted during braking: Application to railway braking*.

Octau, C., Meresse, D., Watremez, M., Schiffler, J., Lippert, M., Keirsbulck, L., & Dubar, L. (2020). Characterization of particulate matter emissions in urban train braking - An investigation of braking conditions influence on a reduced-scale device. *Environmental Science and Pollution Research*, *27*(15), 18615–18631. https://doi.org/10.1007/s11356-020-08337-8

Onat, B., & Stakeeva, B. (2013). Personal exposure of commuters in public transport to PM2.5 and fine particle counts. *Atmospheric Pollution Research*, *4*(3), 329–335. https://doi.org/10.5094/APR.2013.037

Onat, B., & Stakeeva, B. (2014). Assessment of fine particulate matters in the subway system of Istanbul. *Indoor and Built Environment*, *23*(4), 574 – 583. https://doi.org/10.1177/1420326X12464507

Österle, W., Dörfel, I., Prietzel, C., Rooch, H., Cristol-Bulthé, A. L., Degallaix, G., & Desplanques, Y. (2009). A comprehensive microscopic study of third body formation at the interface between a brake pad and brake disc during the final stage of a pin-on-disc test. *Wear*, *267*(5–8), 781–788. https://doi.org/10.1016/j.wear.2008.11.023

Pachy, Y. (2023). *Evaluation of the performance of gas and liquid chromatography methods to quantify the emission of VOCs emitted from construction materials*.

Pang, X., & Mu, Y. (2007). Characteristics of carbonyl compounds in public vehicles of Beijing city: Concentrations, sources, and personal exposures. *Atmospheric Environment*, *41*(9), 1819–1824. https://doi.org/https://doi.org/10.1016/j.atmosenv.2006.10.057

Park, D.-U., & Ha, K.-C. (2008). Characteristics of PM10, PM2.5, CO2 and CO monitored in interiors and platforms of subway train in Seoul, Korea. *Environment International*, *34*(5), 629–634. https://doi.org/https://doi.org/10.1016/j.envint.2007.12.007

Patel, A., Aggarwal, S., Bard, L., Durif, O., Introna, M., Juárez-Facio, A. T., Tu, M., Elihn, K., Nozière, B., Olofsson, U., & Steimer, S. S. (2024). Gaseous emissions from brake wear can form secondary particulate matter. *Scientific Reports*, *14*(1), 23253. https://doi.org/10.1038/s41598-024-74378-5

Perraud, V., Blake, D. R., Wingen, L. M., Barletta, B., Bauer, P. S., Campos, J., Ezell, M. J., Guenther, A., Johnson, K. N., Lee, M., Meinardi, S., Patterson, J., Saltzman, E. S., Thomas, A. E., Smith, J. N., & Finlayson-Pitts, B. J. (2024). Unrecognized volatile and semi-volatile organic compounds from brake wear. *Environmental Science: Processes and Impacts*, *26*(5), 928–941. https://doi.org/10.1039/d4em00024b

Perrino, C., Marcovecchio, F., Tofful, L., & Canepari, S. (2015). Particulate matter concentration and chemical composition in the metro system of Rome, Italy. *Environmental Science and Pollution Research*, *22*(12), 9204–9214. https://doi.org/10.1007/s11356-014-4019-9

Pitz, M., Cyrys, J., Karg, E., Wiedensohler, A., Wichmann, H.-E., & Heinrich, J. (2003). Variability of Apparent Particle Density of an Urban Aerosol. *Environmental Science & Technology*, *37*(19), 4336–4342. https://doi.org/10.1021/es034322p

Plachá, D., Vaculík, M., Mikeska, M., Dutko, O., Peikertová, P., Kukutschová, J., Mamulová Kutláková, K., Růžičková, J., Tomášek, V., & Filip, P. (2017). Release of volatile organic compounds by oxidative wear of automotive friction materials. *Wear*, *376–377*, 705–716. https://doi.org/10.1016/j.wear.2016.12.016

Qiao, T., Xiu, G., Zheng, Y., Yang, J. J., Wang, L., Yang, J. J., & Huang, Z. (2015). Preliminary investigation of PM1, PM2.5, PM10 and its metal elemental composition in tunnels at a subway station in Shanghai, China. *Transportation Research Part D: Transport and Environment*, *41*, 136–146. https://doi.org/https://doi.org/10.1016/j.trd.2015.09.013

Querol, X., Moreno, T., Karanasiou, A., Reche, C., Alastuey, A., Viana, M., Font, O., Gil, J., de Miguel, E., & Capdevila, M. (2012). Variability of levels and composition of PM$_{10}$ and PM$_{2.5}$ in the Barcelona metro system. *Atmospheric Chemistry and Physics*, *12*(11), 5055–5076. https://doi.org/10.5194/acp-12-5055-2012

RATP. (2023). *Améliorer la qualité de l'air dans les enceintes ferroviaires souterraines, août 2023, 24 pages*. https://ratpgroup.com/api/media/202308-DOSSIER-QUALITE-DE-LAIR_MEL.pdf

Raut, J. C., Chazette, P., & Fortain, A. (2009). Link between aerosol optical, microphysical and chemical measurements in an underground railway station in Paris. *Atmospheric Environment*, *43*(4), 860–868. https://doi.org/10.1016/J.ATMOSENV.2008.10.038

Renouf, M., & Saulot, A. (2015). *THIRD-BODY FLOW DURING WHEEL-RAIL INTERACTION THIRD-BODY FLOW DURING WHEEL-RAIL INTERACTION*. *July*.

Richardson, K., Steffen, W., Lucht, W., Bendtsen, J., Cornell, S. E., Donges, J. F., Drüke, M., Fetzer, I., Bala, G., Bloh, W. Von, Feulner, G., Fiedler, S., Gerten, D., Gleeson, T., Hofmann, M., Huiskamp, W., Kummu, M., Mohan, C., Nogués-bravo, D., … Rockström, J. (2023). *Earth beyond six of nine planetary boundaries*. 1–16. https://doi.org/10.1126/sciadv.adh2458

Robache, A., Mathé, F., Galloo, J., & Guillermo, R. (2016). *Multi-element analysis by inductively coupled plasma optical emission spectrometry of airborne particulate matter collected with a low-pressure cascade impactor Multi-element analysis by inductively coupled plasma optical emission spectrometry of airborne*. *November 2000*. https://doi.org/10.1039/b003048l

Salma, I., & Maenhaut, W. (2007). Time-resolved mass concentration, composition and sources of aerosol particles in a metropolitan underground railway station. *Atmospheric Environment*, *41*, 8391–8405. https://doi.org/10.1016/j.atmosenv.2007.06.017

Salma, I., Pósfai, M., Kovács, K., Kuzmann, E., Homonnay, Z., & Posta, J. (2009). Properties and sources of individual particles and some chemical species in the aerosol of a metropolitan underground railway station. *Atmospheric Environment*, *43*(22), 3460–3466. https://doi.org/https://doi.org/10.1016/j.atmosenv.2009.04.042

Sanders, P. G., Xu, N., Dalka, T. M., & Maricq, M. M. (2003). Airborne Brake Wear Debris: Size Distributions, Composition, and a Comparison of Dynamometer and Vehicle Tests. Environmental Science & Technology, 37(18), 4060–4069. https://doi.org/10.1021/es034145s

Seinfeld, John H and Pandis, S. N. (2016). *Atmospheric chemistry and physics: from air pollution to climate change*. John Wiley \& Sons.

Shiohara, N., Fernández-Bremauntz, A. A., Blanco Jiménez, S., & Yanagisawa, Y. (2005). The commuters' exposure to volatile chemicals and carcinogenic risk in Mexico City. *Atmospheric Environment*, *39*(19), 3481–3489. https://doi.org/https://doi.org/10.1016/j.atmosenv.2005.01.064

Shorowordi, K. . M., Haseeb, A. S. M. A., & Celis, J. P. (2009). Tribo-Chemical Degradation of Phenolic Resin in Automotive Brake Pad During Dry Sliding Against Mmc. *Tribopedia.Com*, *May*, 4–5. https://www.tribopedia.com/paper/ntc2009/NTC-2009-009.pdf

Shorowordi, K. M., & Celis, A. (2009). Tribo-Chemical Degradation of Phenolic Resin in Automotive Brake Pad During Dry Sliding Against Mmc. Tribopedia.Com, May, 4–5.

Singh, R. (2016). *Applied Welding Engineering (Second Edition)* (pp. 65–81). https://doi.org/https://doi.org/10.1016/B978-0-12-804176-5.00007-4.

Son, Y. S., Kang, Y. H., Chung, S. G., Park, H. J., & Kim, J. C. (2011). Efficiency evaluation of adsorbents for the removal of VOC and NO2 in an Underground subway station. *Asian Journal of Atmospheric Environment*, *5*(2), 113–120. https://doi.org/10.5572/ajae.2011.5.2.113

Son, Y.-S., Dinh, T.-V., Chung, S.-G., Lee, J., & Kim, J.-C. (2014). Removal of Particulate Matter Emitted from a Subway Tunnel Using Magnetic Filters. *Environmental Science & Technology*, *48*(5), 2870–2876. https://doi.org/10.1021/es404502x

Standard Reference Material 1648a. (n.d.). https://tsapps.nist.gov/srmext/certificates/1648a.pdf

Tagiyeva, N., & Sheikh, A. (2014). Domestic exposure to volatile organic compounds in relation to asthma and allergy in children and adults. *Expert Review of Clinical Immunology*, *10*(12), 1611–1639. https://doi.org/10.1586/1744666X.2014.972943

Tang, X., Misztal, P. K., & Goldstein, A. H. (2016). *Volatile Organic Compound Emissions from Humans Indoors*. https://doi.org/10.1021/acs.est.6b04415

The Future of Rail (2019). https://www.oecd.org/content/dam/oecd/en/publications/reports/2019/02/the-future-of-rail_g1g9f609/9789264312821-en.pdf

Tokarek, S., & Bernis, A. (2006). An exemple of particle concentration reduction in Parisian subway stations by electrostatic precipitation. *Environmental Technology*, *27*(11), 1279–1287. https://doi.org/10.1080/09593332708618746

Tranchant, J. (1982). *Chromatographie en phase gazeuse*. I Ed. Techniques Ingénieur.

Tu, M., Cha, Y., Wahlström, J., & Olofsson, U. (2019). Towards a two-part train traffic emissions factor model for airborne wear particles. *Transportation Research Part D: Transport and Environment*, *67*, 67–76. https://doi.org/10.1016/J.TRD.2018.11.006

UBA. (2020).

Vakis, A. I., Yastrebov, V. A., Scheibert, J., Nicola, L., Dini, D., Minfray, C., Almqvist, A., Paggi, M., Lee, S., Limbert, G., Molinari, J. F., Anciaux, G., Aghababaei, R., Echeverri Restrepo, S., Papangelo, A., Cammarata, A., Nicolini, P., Putignano, C., Carbone, G., … Ciavarella, M. (2018). Modeling and simulation in tribology across scales: An overview. *Tribology International*, *125*, 169–199. https://doi.org/10.1016/j.triboint.2018.02.005

Vinzents, P. S., Møller, P., Sørensen, M., Knudsen, L. E., Hertel, O., Jensen, F. P., Schibye, B., & Loft, S. (2005). Personal exposure to ultrafine particles and oxidative DNA damage. *Environmental Health Perspectives*, *113*(11), 1485–1490. https://doi.org/10.1289/ehp.7562

Von Der Weiden, S. L., Drewnick, F., & Borrmann, S. (2009). Particle Loss Calculator - A new software tool for the assessment of the performance of aerosol inlet systems. *Atmospheric Measurement Techniques*, *2*(2), 479–494. https://doi.org/10.5194/amt-2-479-2009

Von Uexküll, O., Skerfving, S., Doyle, R., & Braungart, M. (2005). Antimony in brake pads-a carcinogenic component? Journal of Cleaner Production, 13(1), 19–31. https://doi.org/10.1016/J.JCLEPRO.2003.10.008

Wahlström, J., Gventsadze, D., Olander, L., Kutelia, E., Gventsadze, L., Tsurtsumia, O., & Olofsson, U. (2011). A pin-on-disc investigation of novel nanoporous composite-based and conventional brake pad materials focussing on airborne wear particles. *Tribology International*, *44*(12), 1838–1843. https://doi.org/10.1016/j.triboint.2011.07.008

Wahlström, J., Leonardi, M., Tu, M., Lyu, Y., Perricone, G., Gialanella, S., & Olofsson, U. (2020). A Study of the Effect of Brake Pad Scorching on Tribology and Airborne Particle Emissions. *Atmosphere 2020, Vol. 11, Page 488*, *11*(5), 488. https://doi.org/10.3390/ATMOS11050488

Wahlström, J., Olander, L., & Olofsson, U. (2010). Size, shape, and elemental composition of airborne wear particles from disc brake materials. *Tribology Letters*, *38*(1), 15–24. https://doi.org/10.1007/s11249-009-9564-x

Wang, B. Q., Liu, J. F., Ren, Z. H., & Chen, R. H. (2016). Concentrations, properties, and health risk of PM2.5 in the Tianjin City subway system. *Environmental Science and Pollution Research*, *23*(22), 22647–22657. https://doi.org/10.1007/s11356-016-7444-0

Wang, B., Zhu, J., & Lin, Z. (2016). A theoretical framework for multiphysics modeling of methane fueled solid oxide fuel cell and analysis of low steam methane reforming kinetics. *Applied Energy*, *176*, 1–11. https://doi.org/10.1016/J.APENERGY.2016.05.049

Wang, Y., Yin, H., Yang, Z., Su, S., Hao, L., Tan, J., Wang, X., Niu, Z., & Ge, Y. (2022). Assessing the brake particle emissions for sustainable transport: A review. *Renewable and Sustainable Energy Reviews*, *167*(June), 112737. https://doi.org/10.1016/j.rser.2022.112737

Woo, S. H., Kim, J. B., Bae, G. N., Hwang, M. S., Tahk, G. H., Yoon, H. H., Kwon, S. B., Park, D., & Yook, S. J. (2018a). Size-dependent characteristics of diurnal particle concentration variation in an underground subway tunnel. *Environmental Monitoring and Assessment*, *190*(12). https://doi.org/10.1007/s10661-018-7110-8

Woo, S. H., Kim, J. B., Bae, G. N., Hwang, M. S., Tahk, G. H., Yoon, H. H., Kwon, S. B., Park, D., & Yook, S. J. (2018b). Size-dependent characteristics of diurnal particle concentration variation in an underground subway tunnel. *Environmental Monitoring and Assessment*, *190*(12). https://doi.org/10.1007/s10661-018-7110-8

Xu, B., & Hao, J. (2017). Air quality inside subway metro indoor environment worldwide: A review. *Environment International*, *107*(May), 33–46. https://doi.org/10.1016/j.envint.2017.06.016

Yan, C., Zheng, M., Yang, Q., Zhang, Q., Qiu, X., Zhang, Y., Fu, H., Li, X., Zhu, T., & Zhu, Y. (2015). Commuter exposure to particulate matter and particle-bound PAHs in three transportation modes in Beijing, China. *Environmental Pollution (Barking, Essex : 1987)*, *204*, 199—206. https://doi.org/10.1016/j.envpol.2015.05.001

Yang, J., Fan, X., Zhang, H., Zheng, W., & Ye, T. (2023). A review on characteristics and mitigation strategies of indoor air quality in underground subway stations. *Science of The Total Environment*, *869*(December 2022), 161781. https://doi.org/10.1016/j.scitotenv.2023.161781

Yao, P., Holzinger, R., Materić, D., Oyama, B. S., de Fátima Andrade, M., Paul, D., Ni, H., Noto, H., Huang, R. J., & Dusek, U. (2023). Methylsiloxanes from Vehicle Emissions Detected in Aerosol Particles. *Environmental Science and Technology*, *57*(38), 14269–14279. https://doi.org/10.1021/acs.est.3c03797

Zhang, Q., Yin, J., Fang, T., Guo, Q., Sun, J., Peng, J., Zhong, C., Wu, L., & Mao, H. (2024). Regenerative braking system effectively reduces the formation of brake wear particles. *Journal of Hazardous Materials*, *465*, 133350. https://doi.org/10.1016/j.jhazmat.2023.133350

Zhang, Y., Li, C., Wang, X., Guo, H., Feng, Y., & Chen, J. (2012). Rush-hour aromatic and chlorinated hydrocarbons in selected subway stations of Shanghai, China. *Journal of Environmental Sciences*, *24*(1), 131–141. https://doi.org/https://doi.org/10.1016/S1001-0742(11)60736-5

Appendices

Appendix 1 Transfer function of the tribometer at LaMcube

1. Introduction

The aim of these tests was to investigate the transfer function of the tribometer bench at LaMcube. The transfer function is the response of the system to a given signal. that is to understand how gas and particles escaped the tribometer box once emitted at a braking event.

2. Experimental conditions

A series of tests were performed using CO_2 and ammonium nitrate (NH_4NO_3) particles injected directly in the braking zone (between the pad and the disc), aiming at simulating brake gas and particle emissions. The tribometer box was continuously flushed by filtered air at a flow of 300 L/min (humidity around 30%).

2.1. Set-up

Pure CO_2 was injected from a cylinder at a regulated flow of 2 L/min while ammonium nitrate particles were produced in an ATM 228 (Topas GmbH) aerosol generator (using a solution of 5 mM of NH_4NO_3) before being injected at a flow of 2 L/min. The aerosol generator produces monodisperse particles centred at around 45 nm with a Full Width at Half Maximum (FWHM) of about 60 nm (Figure A1.1).

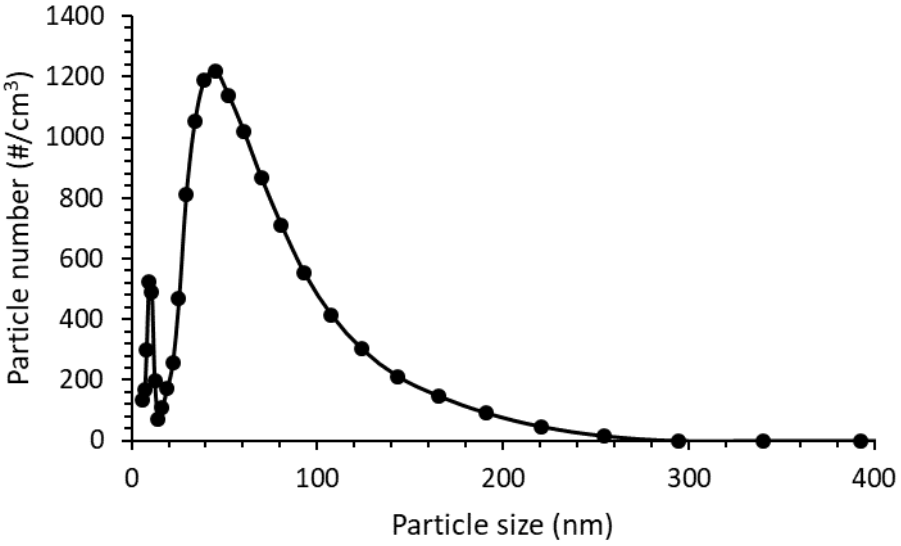

Figure A1.1 Typical size distribution measured at the exit of the tribometer with ammonium nitrate.

CO_2 and particles can be injected independently (2 L/min each) or together (4 L/min total) via a Teflon line going through a drilled aluminium pad up to the braking zone (Figure A1.2a and Figure A1.2 b). Note that the hole in the pad was made at one end of the pad corresponding to the exit of the flow.

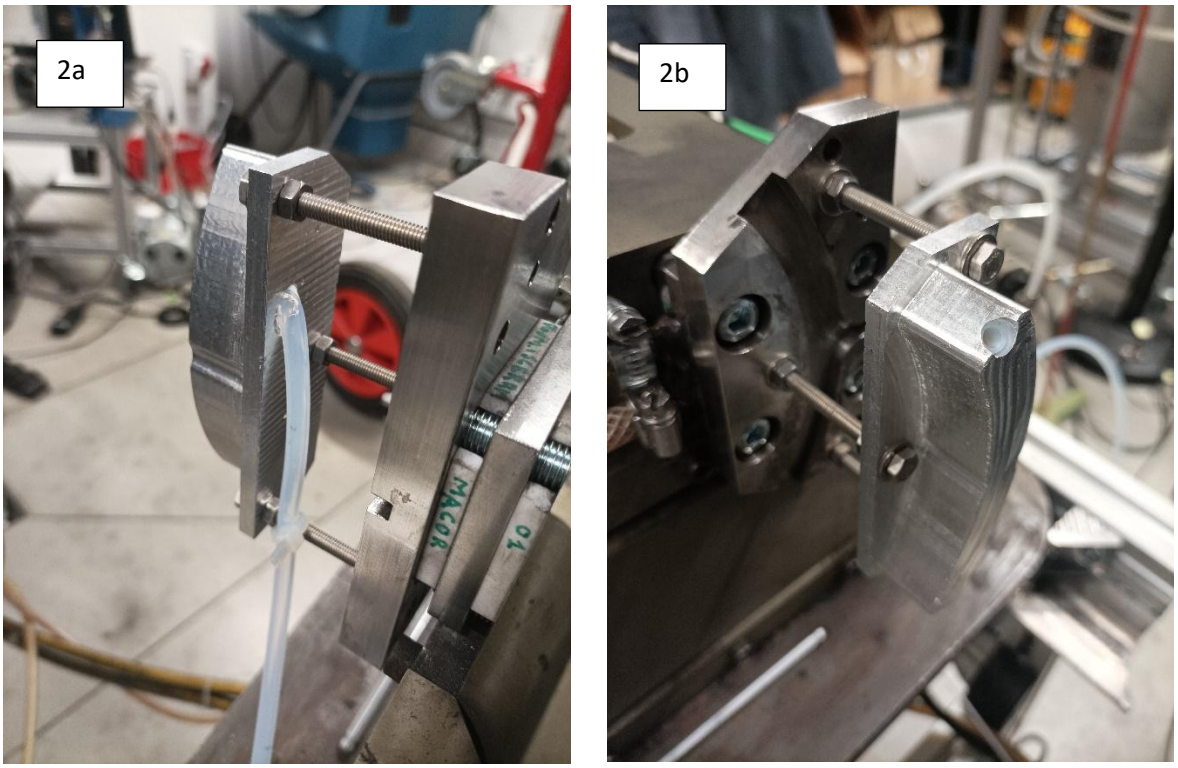

Figure A1.2 Photos of the ¼" Teflon tube going through the pad and allowing CO2 and particles to be injected between the disc and the pad, at the exit flow; a) rear view of the pad; b) front view of the pad.

The exit of the box consisted of a ~1-m long stainless-steel tube (diameter of 74 mm) allowing the flushing air to be evacuated. CO_2 was sampled via a hole in the exit tube (approximately 30 cm away from the box). The particles were collected through an isokinetic nozzle set in the middle of the exit tube at about 23 cm away from the box. CO_2 was recorded by a Licor 840A and particle concentrations were monitored by an Ultrafine Condensation Particle Counter (CPC TSI 3756) and an Engine Exhaust Particle Sizer (EEPS TSI 3090). The transfer times (between the exit of the box and the entrance of the sampling) are short and similar, about 0.26 s for the CO_2 and 0.20 s for the particles at a total flow of 300 L/min.

2.2. Methodology

Two series of tests were carried out: 1) CO_2 injected alone, with varying the rotation of the disc (from 0 to 1500 tr/min) and at increasing injection times (from a pulse of about 1 s to a pulse of 20 s); 2) CO_2 and particles injected together, again with varying the rotation of the disc and at increasing injection times (same ranges as with CO_2 alone). These tests are summarized in Table A1. 1 . Each injection was performed at least 5 times with inter-injection times between 30 s and 1 min. Before starting the tests, blank experiments were conducted, where only filtered air was flushed through the bench at different disc rotation speeds (from 0 to 1500 tr/min) to determine the backgrounds of CO_2 and particles. For CO_2 a background of about 2110 ppm was obtained, while about 60 particles/cm^3 were observed for particles.

Table A1. 1 Experimental conditions of the tests

	Tests with 1) CO_2 alone and 2) with CO_2 + particles															
Disc rotation speed (tr/min)	0				500				1000				1500			
Pulse duration (s)	1	5	10	20	1	5	10	20	1	5	10	20	1	5	10	20

3. Results

3.1 CO_2 alone

A global view of all the injections of CO_2 with and without disc rotation and at different pulse durations is displayed on Figure A1.3. Considering a flow of 2 L/min of pure CO_2 injected into a flushing air flow of 300 L/min already containing about 2110 ppm CO_2 yields a theoretical maximum CO_2 concentration of 8719 ppm in the outflow of the tribometer, if we assume a constant injection of CO_2 (which was not the case). The highest CO_2 value observed is about 7400 ppm (20 s pulse, 1500 tr/min), which is 15% less than the expected concentration. Two reasons may be invoked: 1) some CO_2 molecules are lost from the box through leaks, or 2) CO_2 is not well injected into the box (real CO_2 flow lower than the set-up one).

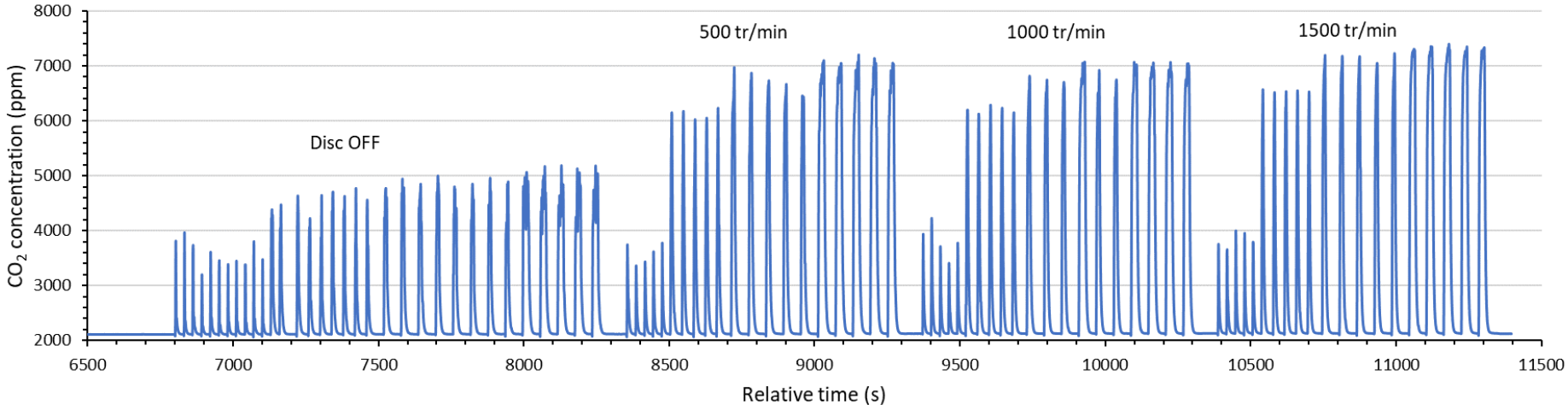

Figure A1.3 Global view of the results of the tests carried out with CO2 alone. Each peak represents an injection of CO2 (pulses of 1 s, 5 s, 10 s or 20 s) at different disc rotation speeds (disc off, 500 tr/min, 1000 tr/min and 1500 tr/min) following the conditions in Table 1. In general, five injections were repeated for each condition (for each pulse time and rotation speed), except at the beginning of the tests (disc off), where eleven pulses of 1 s were done, followed by nine pulses of 5 s, eight pulses of 10 s and five pulses of 20 s. Under a rotation speed of 1000 tr/min, a pulse of 20 s was inserted between the third and the fourth pulses of 10 s (at around 9900 s).

Repeatability. When the disc is not running, the repeatability of the successive pulses is rather poor (Figure A1.4 and Figure A1.5), with large fluctuations in the CO_2 appearing time (especially for 1-s pulses) and in the maxima. These fluctuations may reflect turbulences inside the box implying variable residence times for CO_2. Conversely, when the disc is on, the repeatability is considerably improved (Figure A1.6 and Figure A1.7).

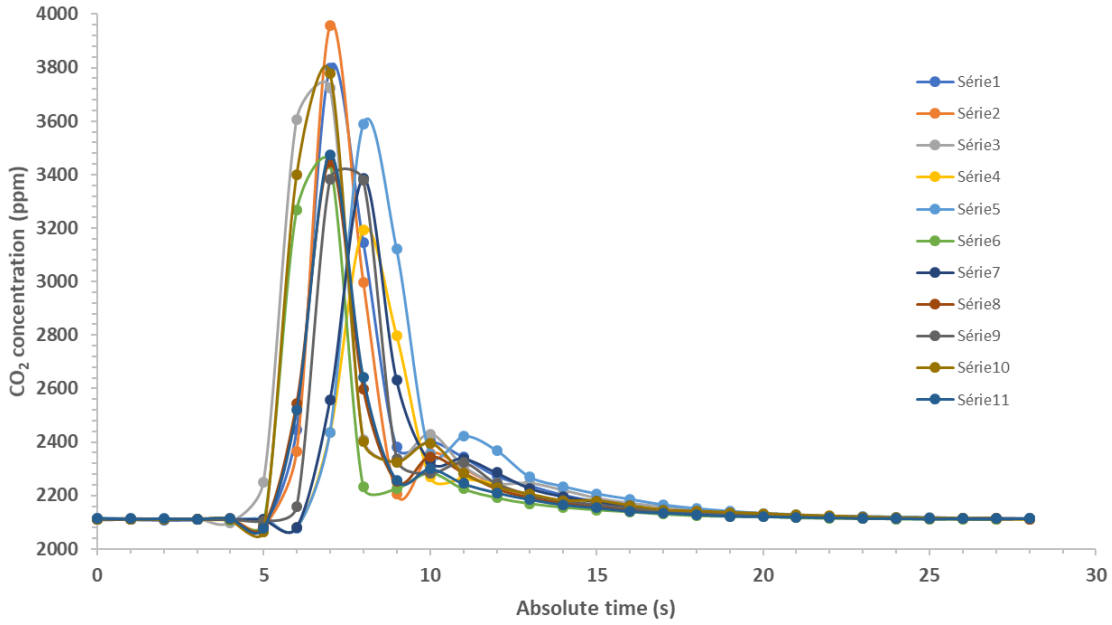

Figure A1.4 Repeatability of 11 CO2 injections of 1-s pulses without particles, disc rotation off. Time zero corresponds to turning on the CO2 valve.

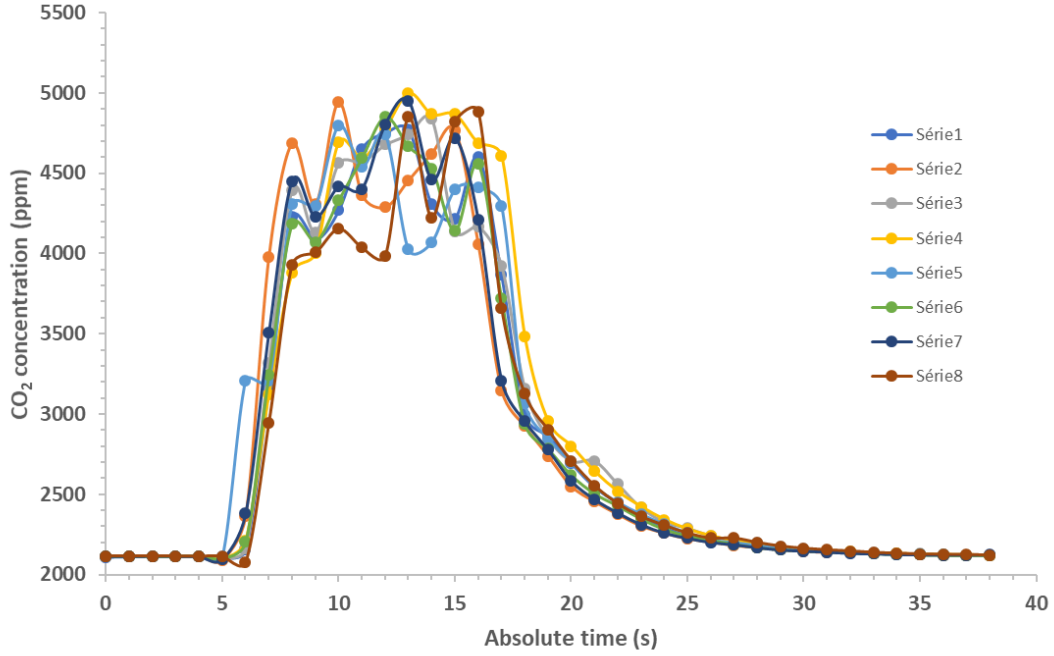

Figure A1.5 Repeatability of eight 10-s injection pulses of CO2 without particles, disc rotation off. Time zero corresponds to turning on the CO2 valve.

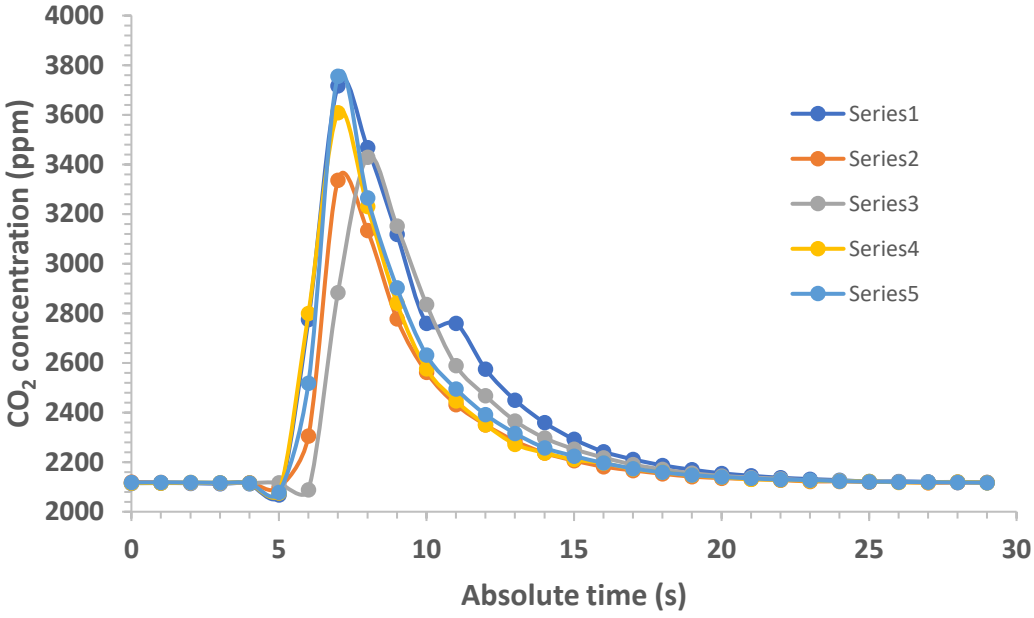

Figure A1.6 Repeatability of 5 CO2 injections of 1-s pulses without particles, disc rotation at 500 tr/min. Time zero corresponds to turning on the CO2 valve.

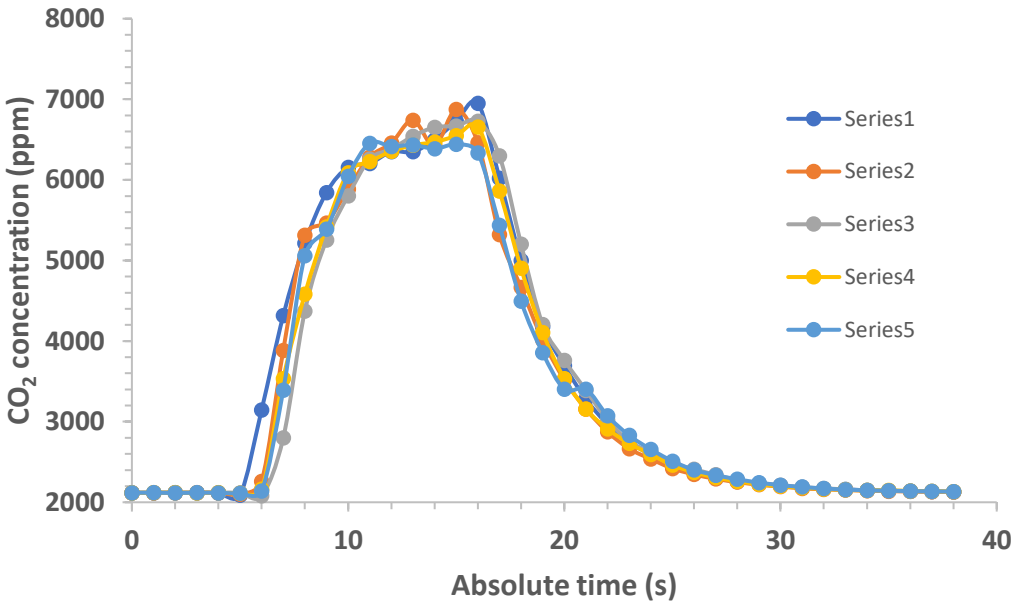

Figure A1.7 Repeatability of 5 CO2 injections of 10-s pulses without particles, disc rotation at 500 tr/min. Time zero corresponds to turning on the CO2 valve.

It is noteworthy that a more or less constant delay of about 6 s is observed between the injection of CO_2 and its detection by the Licor 840A. The reason for this delay will be discussed later.

Effect of disc rotation speed: first, we observed a significant increase (~50%) of the maximal CO_2 concentration when the disc was "on" compared to disc "off", which was particularly true for the 5 s, 10 s and 20 s pulses (see Figure A1.6 as an example). Note that this effect largely vanished when

particles are injected together with CO_2 (see Figure A1.12 after). Note also that, since the area under the curve in Figure A1.8. is proportional to the number of CO_2 molecules entering the box, the rotation of the disc seems to largely favor the injection of the CO_2 flow. We may thus invoke two effects: 1) a 'suction' effect of the rotating disc on the CO_2 flow (the rotating disc is fairly close to the CO_2 Teflon tube exit; the interspace is about 1 mm), thus locally reducing the pressure at the exit of the Teflon tube and 'helping' the CO_2 flow to enter the box; 2) an overpressure effect inside the box, due to the 300 L/min flushing air, enhancing CO_2 losses through leaks, this effect being (supposedly) reduced by the rotation of the disc that may push both CO_2 and particle flows into the flushing air.

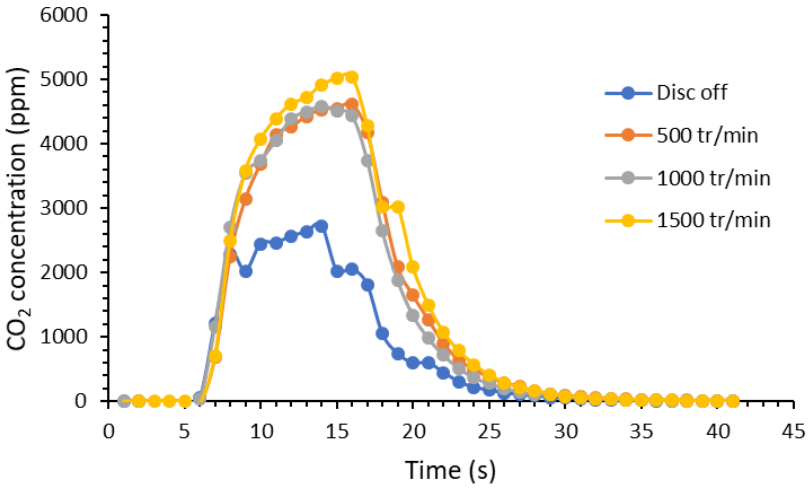

Figure A1.8 Effect of disc rotation on the outflow concentrations of CO2 (background subtracted) for a pulse of 10 s. Time 0 corresponds to the injection of CO2.

Transfer function: considering the volume of the box (~13 L) and the flushing flow (300 L/min) leads to a theoretical residence time of 2.6 s, assuming a perfectly mixed box. Looking at the CO_2 concentration decays after stopping the injection and trying to simulate these decays by an exponential law ($[CO_2]_{max} \times \exp(-\beta t)$) shows that this law is confirmed over the decay (see Figure A1.9 as examples). The characteristic time β of the decays is around 3.2 s, which is slightly higher than the theoretical residence time of 2.6 s, meaning that the chamber is not simply flushed by the air flow but that the air stays some time inside the box before leaving. Figure A1.9 also shows that the characteristic time is not dependent on the speed of the disc. Regarding the increase of CO_2 concentrations inside the box, an exponential law ($[CO_2]_{max} \times [1-\exp(-\alpha t)]$) can also be applied, leading to more dispersed characteristic times α, 2.1 and 2.6 s in the examples shown in Figure A1.9. Figure A1.15 shows that the addition of a flow of particles does not change the time profile (and thus neither the characteristic times).

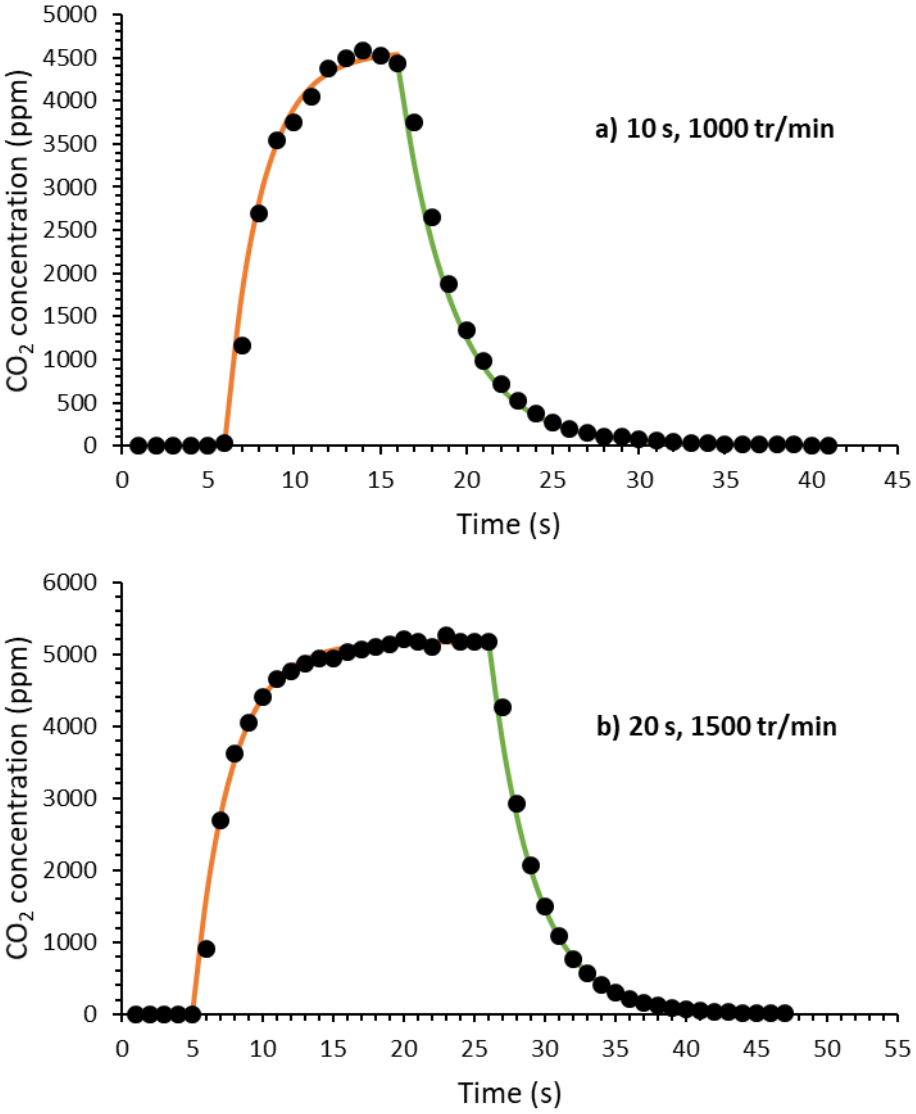

Figure A1.9 Examples of CO2 time profile (a: pulse duration = 10 s, disc rotation speed = 1000 tr/min; b: pulse duration = 20 s, disc rotation speed = 1500 tr/min). The colored lines correspond to exponential simulation (orange: with a function of type $[CO2]_{max} \times [1-\exp(-\alpha t)]$; green: with a function of type $[CO2]_{max} \times \exp(-\beta t)$; α and β represent the characteristic times of filling and emptying the box, respectively). The characteristic times are 2.1 and 2.6 s (filling time for a) and b), respectively) and 3.2 s (same emptying time for a) and b)). Time 0 corresponds to the injection of CO2. Background is subtracted.

Response time of the system to a change in the CO_2 concentration: the expected total delay between a change in the CO_2 concentration and its detection can be approximated by a summation of the individual delays and the residence time into the box. Table A1.2 presents the estimation of the individual delays for CO_2. The expected total delay is about 5.3 s, which is close to the observed 6 s delay.

Table A1.2 Estimated delays of the system's response to a change in the CO2 concentration.

Source of the delay	Delay time (s)
Residence time into the box (washout time)	3.2
Transfer time from the exit of the box, through the exit duct, to the sampling point	0.3
Transfer time from the duct sampling point, through the tubing, to the CO_2 analyzer	0.9
Response time of the CO_2 analyzer	0.9
Total expected delay	5.3

3.2 CO_2 and particles

The tests were almost identically repeated with particles added to CO_2 (total injection flow now of 4 L/min). A global view of all the injections of CO_2 is displayed on Figure A1. 10 , while Figure A1.11 displays the simultaneous particle injections.

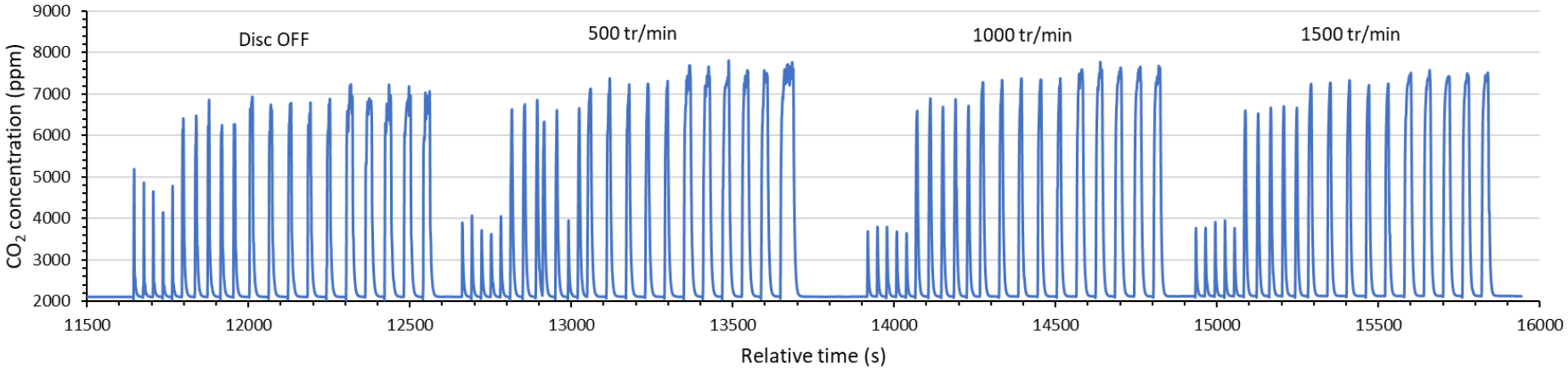

Figure A1. 10 Global view of the results of the tests carried out with injection of CO2 and particles. Each peak represents an injection of CO2 (pulses of 1 s, 5 s, 10 s or 20 s) at different disc rotation speeds (disc off, 500 tr/min, 1000 tr/min and 1500 tr/min). In general, five injections were repeated for each condition (for each pulse time and rotation speed). Under a rotation speed of 500 tr/min, a pulse of 1 s was inserted between the fifth and the sixth pulses of 5 s (at around 13000 s). The last pulse at 500 tr/min (at around 13650 s) was a 40 s duration pulse. Under a rotation speed of 1000 tr/min, the second '5 s' (around 14100 s) pulse lasted actually 6 s.

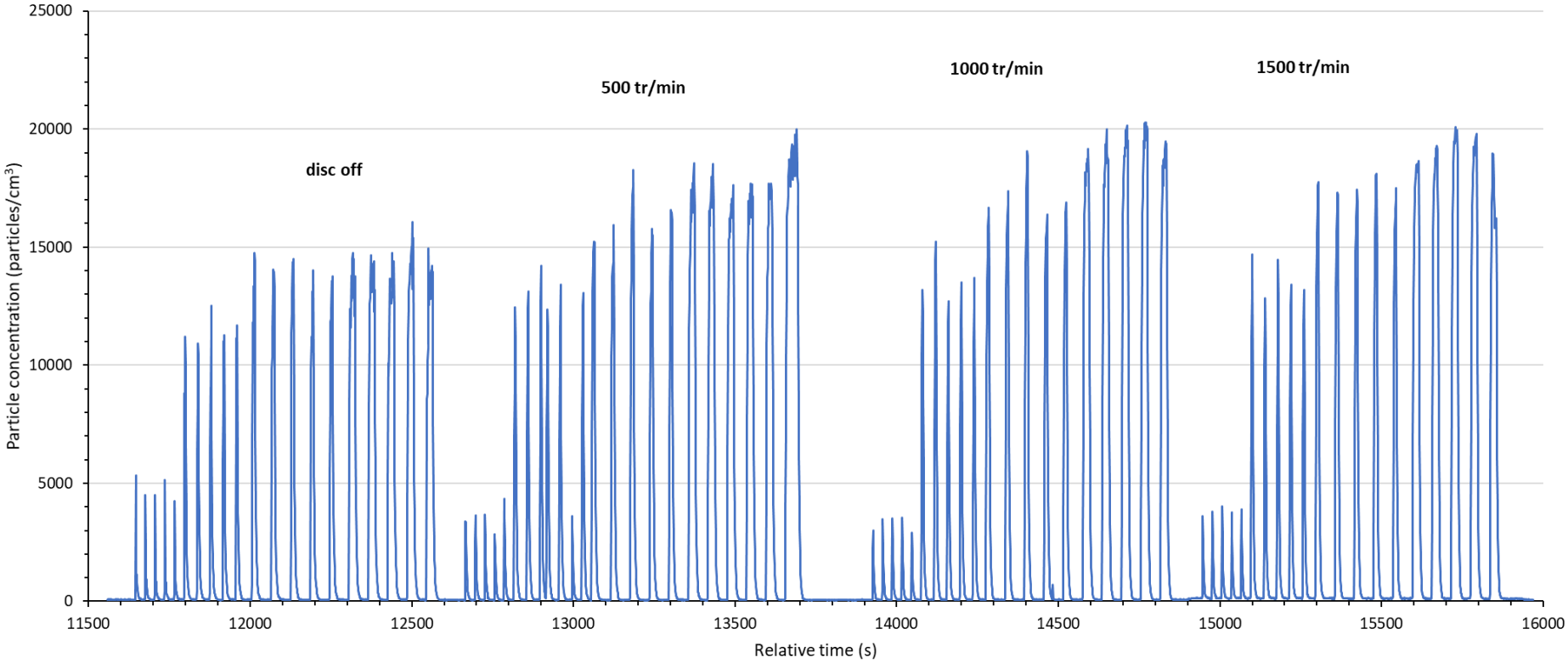

Figure A1.11 Global view of the results of the tests carried out with injection of CO2 and particles. Each peak represents an injection of ammonium nitrate particles (pulses of 1 s, 5 s, 10 s or 20 s) at different disc rotation speeds (disc off, 500 tr/min, 1000 tr/min and 1500 tr/min). In general, five injections were repeated for each condition (for each pulse time and rotation speed). Under a rotation speed of 500 tr/min, a pulse of 1 s was inserted between the fifth and the sixth pulses of 5 s (at around 13000 s). The last pulse at 500 tr/min (at around 13650 s) was a 40 s duration pulse. Under a rotation speed of 1000 tr/min, the second '5 s' (around 14100 s) pulse lasted actually 6 s.

Again, considering a flow of 2 L/min of pure CO_2 plus a flow of 2 L/min of particles in air injected into a flushing air flow of 300 L/min already containing about 2110 ppm CO_2 yields a theoretical CO_2 concentration of 8661 ppm in the outflow of the tribometer (assuming a constant injection of CO_2). The highest CO_2 value observed is about 7800 ppm, which is only 10% less than the expected concentration.

As with CO_2 injections alone (section 3.1), the pulses were fairly well reproducible both for CO_2 and particles, even for the 1 s pulses (probably also more experience in the manual handling of the valve that controls the injection). This is illustrated on Figure A1.12 for particles with disc rotating speed of 1500 tr/min and 1 s pulse duration.

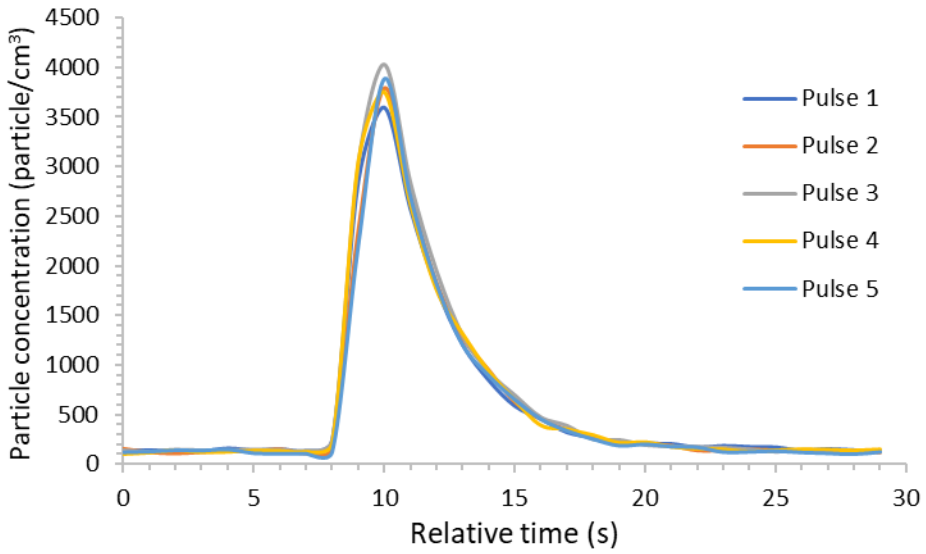

Figure A1.12 Reproducibility of the 1-s pulse injection of particles with a disc rotating speed of 1500 tr/min (5 successive pulses with 30 s time intervals). Time zero is arbitrary, since the CPC was not synchronized.

Effect of disc rotation speed: first, as already noticed, it is noteworthy that, when the disc is not rotating, the maximal CO_2 concentrations are much higher when CO_2 is injected together with particles than without (Figure A1.13). Indeed, the surface areas under the curves (representing the total amount of CO_2 injected) should *a priori* be the same.

Thus, the additional flow of particle (of 2 L/min) may help reducing the pressure effect of the large flushing air flow. Note that this effect is not relevant for real brake experiments (no additional flows). Again, as for CO_2 alone, the effect of turning on the disc seems to suck the CO_2 and particle flows into the flushing air flow and homogenize the concentrations inside the box (see Figure A1.14 as an example).

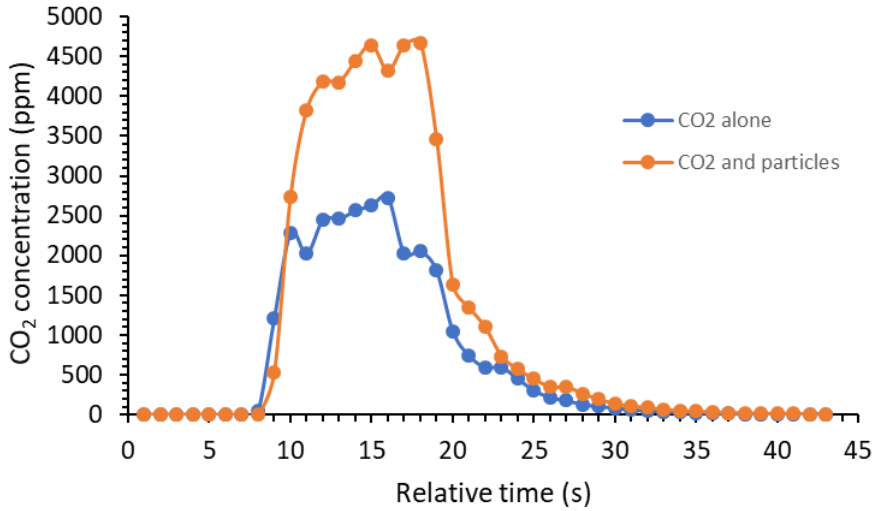

Figure A1.13 Comparison of a 10-s pulse of CO2 alone and a pulse of CO2 together with particles, in the case of disc off.

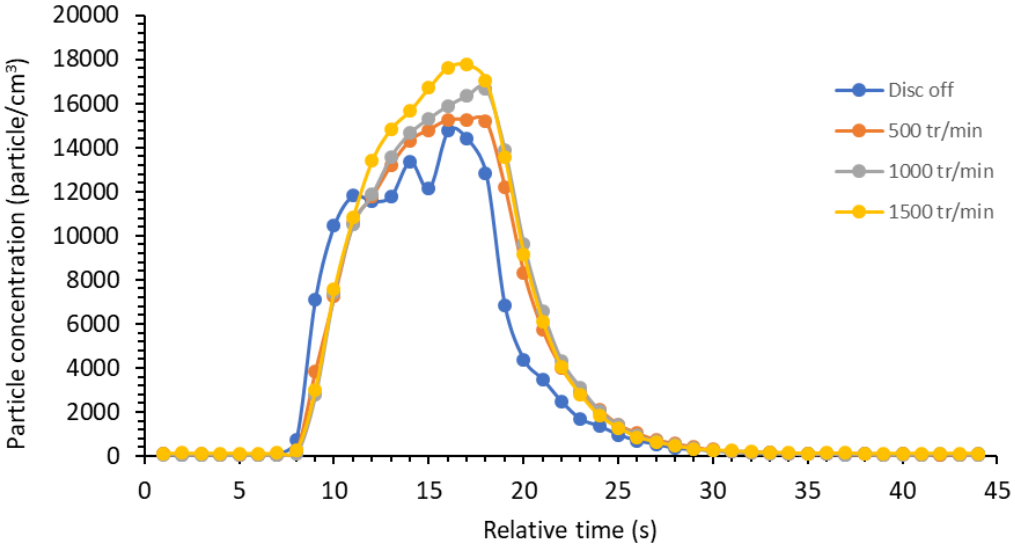

Figure A1.14 Effect of disc rotation on the outflow concentrations of particles for a pulse of 10 s.

Transfer function: the decay profiles obtained for the particles are very similar to those of CO_2 (Figure A1.15) and the same characteristic times of the transfer function determined previously are expected from the particle time profiles.

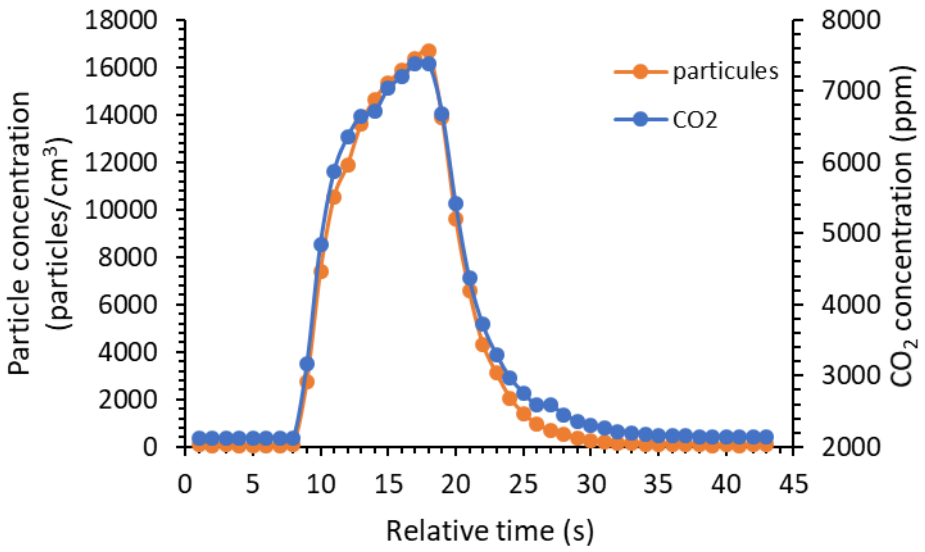

Figure A1.15 Comparing decay profiles of CO2 and particles at a disc rotation speed of 1000 tr/min for a pulse of 10 s.

4. Conclusion

The series of tests carried out in the present work allowed highlighting the following results:

- Turning on the disc enables a better homogenization of the gas and particles emitted inside the box;
- The tribometer box can be considered as a perfectly mixed box, each gas and particle pulses being evacuated through an exponential function; thus, the gas and particles emitted during a braking event will quit exponentially the box;
- The characteristic time of the box is fairly constant with a value of about 3.2 s, either for gas or for particles (at least for ammonium nitrate particles);
- This characteristic time is consistent with the mean residence time of a chamber flushed by air at 300 L/min.
- Leaks from the box are significant, especially when the disc is off, which is the case at the end of a breaking event.

Acknowledgments to the people involved in these experiments: Marina Jamar and Alexandre Tomas (IMT Nord Europe) and Laurent Coustenoble, Edouard Davin, Yannick Desplanques (Centrale Lille – University of Lille)

Appendix 2 Cut-off aerodynamic diameters of the 3-stage impactor

The original stages of the Dekati 3-stage impactor are designed to have 50% cut-off aerodynamic diameters of 10 µm (stage 1), 2.5 µm (stage 2), and 1 µm (stage 3). The backup filter, which is placed under the 1-µm stage (stage 3), collects particles with aerodynamic diameters < 1 µm (PM1). The original version is presented in Table A2..

For this study, as braking particles can be in the ultrafine range (< 0.1 µm, $PM_{0.1}$), the stages have been modified in an attempt to lower the cut-off sizes of the last stage (stage 3) and to collect $PM_{0.1}$ on the backup filter, in order to analyze the chemical composition of this fraction, which is potentially hazardous to health.

To this end, at the position of stage 2, the 2.5-µm stage (the original stage 2) was removed and replaced by the 1-µm stage (the original stage 3). At the position left vacant of stage 3, it was placed the "stage No. 3" of a 13-stage Dekati Low Pressure Impactor (DLPI, a former version of the current 14-stage DLPI+), with a 50% cut-off aerodynamic diameter of 0.1 µm (Robache et al., 2016). The modified version with its target cut-off sizes are presented Table A2.1.

Table A2.1 Cut-off aerodynamic diameters for each stage of the Dekati PM10 Impactor (original version of the 3-stage impactor) and its modified version

Stages	50% cut-off aerodynamic diameters [µm] of the 3-stage impactor	
	Original version	Modified version: Target cut-off diameters
Stage 1	10	10
Stage 2	2.5	1.0
Stage 3	1.0	0.108
Backup filter	PM1	PM0.1

This modified version was used in a previous study on urban particles (ANR MEGATOX), which usually have effective densities of 1- 2 g/cm^3 (Pitz et al., 2003). According to this study, the apparent cut-off aerodynamic diameter of stage 3 in the modified version was around 0.3 µm.

In contrast to the previous study, several factors influenced the actual cut-off size of the modified impactor, including particle characteristics (such as quantity, density, shape and adhesion properties) and the type of filter used, which can affect particle rebound behavior (Garg et al., 2000). The present work probably involves dense braking particles, between 2 to 6 g/cm^3 ((Fruhwirt et al., 2025). Due to their higher impact velocity, these particles may be more prone to rebound (Gensch & Weber, 2017). Upon hitting the impaction surface, they may bounce from their intended stage into downstream stages, leading to misclassification in size distribution (Dekati, Technical Documentation). While surface coatings (such as a surface layer of oil on the impaction stage) could have reduced the bouncing, they were avoided in this study to prevent introducing uncertainty in the metal analysis.

And although a greater particle load improves the reliability of metal quantification, it also intensifies the rebound effect. In this case, when the impaction surface becomes overloaded, the incoming particles hit the collected particles, leading to more bouncing and thus mixing between the upper and lower impactor

stages. The recommended maximum loading on one impactor stage by Dekati is 1 mg. However, due to the 8-h long samplings performed in the present study, many filter masses exceeded this limit, with only the emissions from soft pad braking remaining below the threshold. These exceedances are more numerous for the 3-stage impactor (compared to the 14-stage impactor) due to the lower number of stages. Thus, it is likely that bouncing has influenced the stage No. 3 of the 3-stage impactor.

However, to better estimate the apparent cut-off size of the last stage (stage No. 3) in the modified version of the 3-stage impactor, the size-resolved elemental compositions of particles, sampled during the Normal pathway (NP), using both the modified 3-stage impactor and the 14-stage impactor (DLPI+), were compared. The apparent cut-off size of stage No. 3 is calculated based on the assumption that the backup filter should have the same metal mass composition as the combined lower stages (e.g. stages 2–9) of the 14-stage impactor, with masses normalized by the sampling volumetric flow rate of each impactor (Figure A2.1).

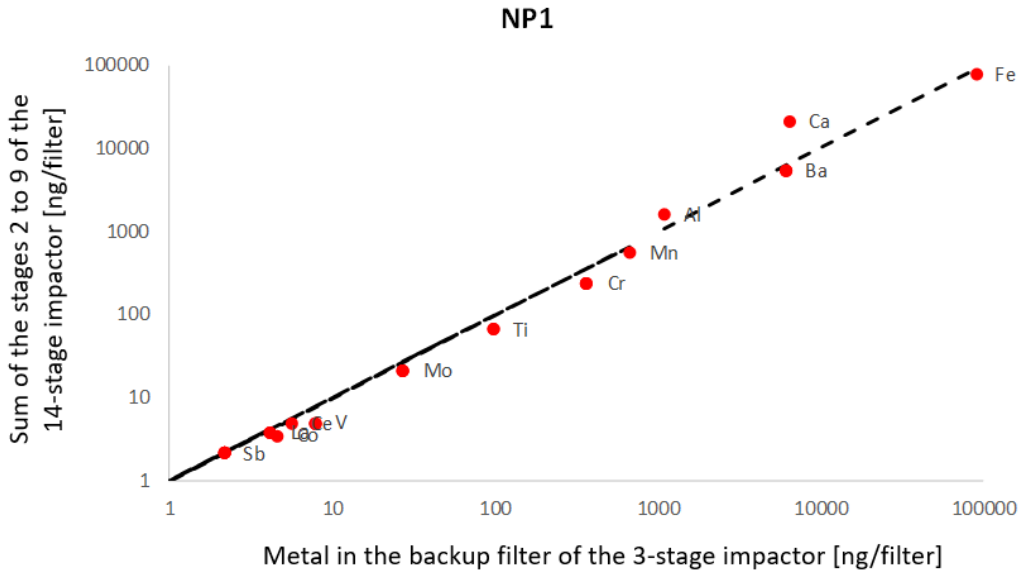

Figure A2.1 Correlation of the cumulated metal masses of the stages 2 to 9 (0.0157 to 0.943 µm) of the 14-stage impactor with the metal masses on the backup filter of the 3-stage impactor. The dashed line corresponds to equality (slope =1). For each impactor, the masses have been normalized by the sampling flow rate, in order to compare both impactors on a common flow rate basis.

Figure A2.1 the cumulated elements' masses of the eight lower stages (No. 2 to 9) of the 14-stage impactor (DLPI+), ranging from 0.016 to 0.94 µm. From the results presented in Figure A2.1, it can be stated that the apparent cut-off aerodynamic diameter of the stage No. 3 of the modified 3-stage impactor is about 1 µm. Thus, particles on the backup filter predominantly comprise submicron particles (<1 µm), therefore equivalent to PM_1.

The same procedure was applied to the replicated NP (NP2), leading to the same cut-off diameter for the stage No. 3, but with more scattered data. For HP1 and HP2, the procedure was not applicable because the mass determination for the 14-stage impactor (total mass and the mass size distribution) was too uncertain, due to a high overloading of some stages and the loss of loose particles during the manipulation of the filters for weighing.

Based on the NP1's comparison, the knowledge of the cut-off diameter of stage No. 3 enables to estimate the cut-off diameter of stage No. 2 to be around 2.6 µm (Table A2.2). However, in the following of this research, only the backup filter (equivalent to PM_1) will be used, because the cut-off sizes of the stages 1 and 2 are too variable depending on the occurrence and intensity of the rebound effect, as previously discussed.

Table A2.2 Apparent cut-off diameters of the stages of the modified 3-stage impactor for NP1.

Stages	Apparent effective size ranges [µm] of the modified 3-stage impactor
Stage 1	>10
Stage 2	2.6 – 10
Stage 3	1.0 – 2.6
Backup filter	< 1.0

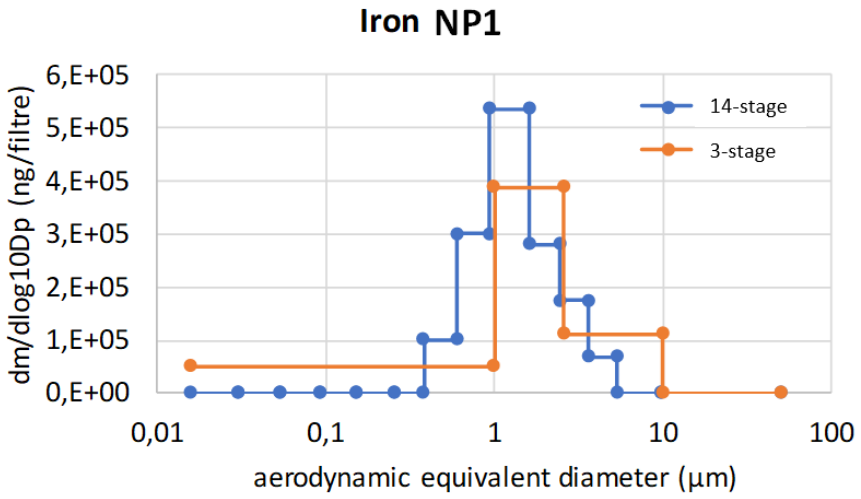

Figure A2.2 Superimposition of the mass size distributions for iron, obtained with both impactors, considering the cut-off sizes of Table A2.2 (For each impactor, the mass of each stage has been normalized by the sampling flow rate, in order to compare both impactors).

References:

Fruhwirt, D., Nöst, T., Leonhardt, P., Leitner, M., Brunnhofer, P., Bode, G., Michael., S., Rodler, J., Emission characteristics of railway tread brakes; ATMOSPHERIC ENVIRONMENT: X 25 (2025) 100320

Gensch, M., Weber, A.P., Rebound behavior of nanoparticle-agglomerate Advanced Powder Technology, Volume 28, Issue 8, 2017, Pages 1930-1942, https://doi.org/10.1016/j.apt.2017.05.003.

Pitz, M., Cyrys, J., Karg, E., Wiedensohler, A., Wichmann, H.-E., Heinrich, J., Variability of Apparent Particle Density of an Urban Aerosol, Environ. Sci. Technol. 2003, 37, 19, 4336–4342, https://doi.org/10.1021/es034322p

Appendix 3 Validation of the mineralization protocol using certified reference materials (Table A3.1 & Table A3.2)

Table A3.1 Recovery rate from MRC, NIST SRM 1648a (Minor)

Elements	Recovery (n=9) (%)
	Av ± SD
Ag	101.0 ± 14.0
As	116.7 ± 6.2
Ba	113.6 ± 4.3
Cd	108.1 ± 9.7
Ce	98.7 ± 5.5
Co	97.9 ± 3.4
Cr	102.7 ± 9.5
Cu	103.7 ± 6.0
La	104.5 ± 8.8
Mn	107.8 ± 2.8
Ni	106.0 ± 11.0
Pb	112.4 ± 4.8
Sb	104.1 ± 8.9
Se	108.0 ± 35.4
Sr	99.8 ± 4.2
Ti	105.8 ± 4.0
V	111.3 ± 5.7
Zn	109.9 ± 6.1

Table A3.2 Recovery rate from MRC, NIST SRM 1648a (Major)

Elements	Recovery (n=9) (%)
	Av ± SD
Al	100.3 ± 2.3
Ca	93.8 ± 3.5
Fe	97.4 ± 2.2
Mg	88.4 ± 1.9
S	275.1 ± 5.5
Si	73.0 ± 4.2

Appendix 4 Evaluation of blanks and limits of detection & quantification (Table A4.1 & Table A4.2)

Table A4.1 Limits of detection and quantification of 32 elements (minor) analyzed by ICP-MS

Elements	Teflon filters 47 mm (n=20)		Teflon filters 25 mm (n=100)	
	LD (ng/filter)	LQ (ng/filter)	LD (ng/filter)	LQ (ng/filter)
Ag	1.8	6.1	1.9	6.3
As	1.1	3.5	1.1	3.8
Ba	304.3	1014.2	77.3	257.7
Be	0.03	0.1	0.1	0.4
Ce	0.3	1.1	0.2	0.7
Co	1.2	4.1	1.0	3.4
Cr	167.2	557.5	86.2	287.2
Cu	997.8	3326.0	85.4	284.7
Hf	7.7	25.6	7.7	25.8
Ge	0.1	0.2	0.1	0.3
La	0.5	1.6	0.1	0.3
Li	0.2	0.5	0.2	0.6
Mn	48.9	163.0	21.5	71.7
Mo	10.8	35.9	16.6	55.5
Ni	45.7	152.3	67.0	223.5
Pb	4.2	14.1	2.5	8.3
Sb	0.5	1.8	0.4	1.5
Se	1.2	4.1	1.3	4.4
Sn	81.3	270.9	4.6	15.2
Sr	3.8	12.6	0.6	2.1
Th	0.1	0.2	0.0	0.1
Ti	108.5	361.6	9.0	30.0
U	0.0	0.1	0.0	0.1
V	2.3	7.6	0.6	1.8
Zn	57.0	189.9	87.0	289.9
Zr	222.3	741.1	141.6	472.0

Table A4.2 Limits of detection and quantification of 32 elements (major) analyzed by ICP-MS/AES

Elements	Teflon filters 47 mm (n=20)		Teflon filters 25 mm (n=100)	
	LD (ng/filter)	LQ (ng/filter)	LD (ng/filter)	LQ (ng/filter)
Al	179.9	599.7	41.9	139.7
Ca	1310.3	4367.6	1241.1	4136.8
Fe	8997.7	29992.3	1070.5	3568.2
Mg	81.8	272.7	106.2	354.1
Si	850.9	2836.2	909.2	3030.8
S	1096.7	3655.8	1136.0	3786.5

Appendix 5 Evaluation of the method: accuracy and intermediate precision (Table A5.1, Table A5.2, Table A5.3 & Table A5.4)

Table A5.1 Repeatability and accuracy of the method evaluated using certified reference solutions (QC: Quality Control) at ICP-MS (minor elements)

Elements	QC 33 (400 ppt, n=9)				QC 4 (400 ppt, n=9)			
	Average	Srept.	CV r %	Recovery %	Average	Srept.	CV r %	Recovery %
Ag	419	21	4.9	105 ± 5	427	25	5.8	107 ± 6
As	406	20	5.0	102 ± 5	433	12	2.7	108 ± 3
Ba	449	32	7.2	112 ± 8	442	32	7.2	111 ± 8
Be	420	30	7.2	105 ± 8	419	32	7.7	105 ± 8
Cd	428	24	5.6	107 ± 6	425	23	5.4	106 ± 6
Ce	438	25	5.8	109 ± 6	447	22	4.8	112 ± 5
Co	429	26	6.1	107 ± 7	409	26	6.3	102 ± 6
Cr	450	24	5.4	113 ± 6	439	27	6.1	110 ± 7
Cu	434	23	5.2	108 ± 6	420	31	7.3	105 ± 8
Hf	-	-	-	-	-	-	-	-
Ge	-	-	-	-	456	26	5.6	114 ± 6
La	454	20	4.4	114 ± 5	448	20	4.5	112 ± 5
Li	439	37	8.4	110 ± 9	471	33	7.0	118 ± 8
Mn	431	25	5.7	108 ± 6	416	24	5.7	104 ± 6
Mo	446	18	4.1	111 ± 5	429	33	7.8	107 ± 8
Ni	431	33	7.7	108 ± 8	414	21	5.0	103 ± 5
Pb	459	22	4.7	115 ± 5	440	37	8.4	110 ± 9
Sb	408	18	4.5	102 ± 5	411	23	5.6	103 ± 6
Se	483	46	9.5	121 ± 11	440	50	11.4	110 ± 13
Sn	445	27	6.0	111 ± 7	-	-	-	-
Sr	426	23	5.3	107 ± 6	459	24	5.3	115 ± 6
Th	0	0		0	459	29	6.4	115 ± 7
Ti	494	54	11.0	124 ± 14	496	45	9.2	124 ± 11
U	462	32	6.9	116 ± 8	464	32	6.9	116 ± 8
V	439	22	5.1	110 ± 6	430	24	5.5	107 ± 6
Zn	513	61	11.9	128 ± 15	425	22	5.3	106 ± 6
Zr	-	-	-	-	447	28	6.2	112 ± 7

Table A5.2 Repeatability and accuracy of the method evaluated using certified reference solutions (QC: Quality Control) at ICP-MS/AES (major elements)

Elements	QC 33 (20 ppb, n=8)				QC 4 (20 ppb, n=9)			
	Average	Srept.	CV r %	Recovery %	Average	Srept.	CV r %	Recovery %
Al	19	1	2.6	94 ± 2	18	1	3.9	88 ± 3
Ca	22	5	22.5	111 ± 25	-	-	-	-
Fe	18	1	1.9	92 ± 2	17	1	3.7	87 ± 3
Mg	18	1	3.0	89 ± 3	17	1	4.0	86 ± 3
S*	28	5	17.5	111 ± 20	-	-	-	-
Si	18	4	22.2	92 ± 20	29	4	14.0	145 ± 20

*Sulfur is analyzed by AES, of QC: 25 ppb

Table A5.3 Internal reproducibility (intermediate precision) of the method evaluated using certified reference solutions (QC: Quality Control) at ICP-MS (minor elements)

Elements	QC 33 (400 ppt, n=35)				QC 4 (400 ppt, n=35)			
	Average	Srepr.	CV_F %	Recovery %	Average	Srepr.	CV_F %	Recovery %
Ag	405	22	5.3	101 ± 5	405	43	10.7	101 ± 11
As	397	19	4.7	99 ± 5	412	46	11.0	103 ± 11
Ba	435	33	7.6	109 ± 8	417	54	13.0	104 ± 14
Be	409	29	7.1	102 ± 7	402	49	12.3	100 ± 12
Bi	434	24	5.6	108 ± 6	434	25	5.9	108 ± 6
Cd	419	25	5.9	105 ± 6	405	40	10.0	101 ± 10
Ce	421	25	5.9	105 ± 6	423	45	10.5	106 ± 11
Co	415	24	5.9	104 ± 6	392	42	10.7	98 ± 11
Cr	433	28	6.4	108 ± 7	413	50	12.2	103 ± 13
Cu	414	27	6.4	103 ± 7	396	49	12.4	99 ± 12
Ge	-	-	-	-	429	47	10.9	107 ±12
La	439	23	5.2	110 ± 6	425	47	11.1	106 ± 12
Li	417	30	7.1	104 ± 7	444	51	11.5	111 ± 13
Mn	418	25	6.0	104 ± 6	399	49	12.4	100 ± 12
Mo	424	23	5.4	106 ± 6	402	48	11.9	100 ± 12
Ni	414	26	6.4	103 ± 7	393	45	11.5	98 ± 11
Pb	448	30	6.6	112 ± 7	422	50	11.8	106 ± 12
Rb	415	18	4.3	104 ± 5	421	16	3.8	105 ± 4
Sb	402	22	5.6	100 ± 6	390	42	10.6	98 ± 10
Se	457	54	11.9	114 ± 14	427	71	16.6	107 ± 18
Sr	394	46	11.7	99 ± 12	422	70	16.5	105 ± 17
Th	-	-	-	-	440	52	11.8	110 ± 13
Ti	443	62	14.1	111 ±16	442	80	18.1	111 ± 20
Tl	429	30	7.0	107 ± 7	413	31	7.5	103 ± 8
U	454	33	7.3	113 ± 8	449	50	11.0	112 ± 12
V	423	25	6.0	106 ± 6	408	46	11.3	102 ± 12
W	-	-	-	-	471	17	3.7	118 ± 4
Zn	462	92	19.8	116 ± 23	424	91	21.6	106 ± 23
Zr	-	-	-	-	420	46	11.0	105 ± 12

Table A5.4 Internal reproducibility (intermediate precision) of the method evaluated using certified reference solutions (QC: Quality Control) at ICP-MS/AES (major elements)

Elements	QC 33 (20 ppb, n=35)				QC 4 (20 ppb, n=35)			
	Average	Srepr.	CV_F %	Recovery %	Average	Srepr.	CV_F %	Recovery %
Al	18	1	4.2	92 ± 4	18	1	4.5	90 ± 4
Ba	18	1	5.5	91 ± 5	18	1	6.1	92 ± 6
Ca	23	6	26.1	114 ± 30	-	-	-	-
Fe	18	1	3.5	92 ± 3	18	1	4.5	90 ± 4
K	19	1	3.7	94 ± 3	-	-	-	-
Mg	18	1	6.2	89 ± 6	17	1	5.6	87 ± 5
Na	18	0	2.0	91 ± 2	19	1	3.8	94 ± 4
S**	30	8	25.5	120 ± 31	-	-	-	-
Si	22	6	25.2	110 ± 28	30	5	16.7	152 ± 25

**Sulfur is analyzed by AES, of QC: 25 ppb and n=31

Appendix 6 X-ray diffraction analysis of disc and pad

The powder X-ray diffraction (XRD) analysis was carried out with a Bruker Phaser II diffractometer using a copper Kα radiation, at the CERI MP of IMT Nord Europe (M. Guillaume Dhainaut). The diffractograms were analyzed using the Diffrac.Eva V3.1 software.

The XRD analysis of chips of the cast iron disc (Figure A6.1), obtained by drilling the material, shows a high-intensity peak of ferrite (α-Fe) at 2θ angles around 44.9° (I/Imax = 100) and 65.2° (I/Imax = 16.1) (https://www.phase-trans.msm.cam.ac.uk/2003/Lattices/ferrite.data.txt), and a minor peak of graphite at 26.5° (https://rruff.info/graphite), as expected for a grey cast iron disc with lamellar graphite flakes.

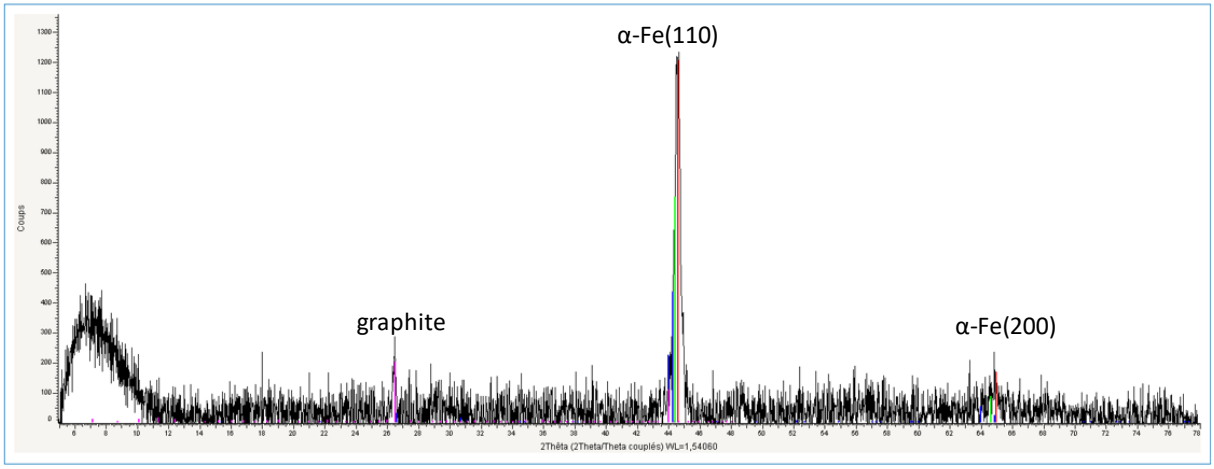

Figure A6.1 XRD diffractogram of cast iron chips.

The XRD diffraction pattern of the reference pad (Figure A6.2) shows a variety of peaks corresponding to baryte ($BaSO_4$), aluminosilicates (possibly clays such as kaolinite, illite, montmorillonite) and silicate (wollastonite), iron and iron oxide, zinc species (oxide, carbide).

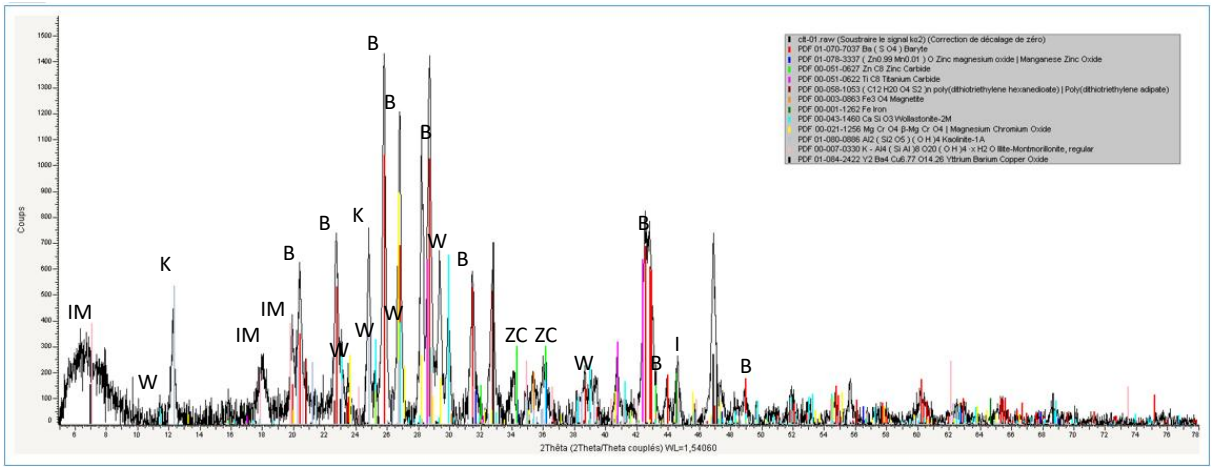

Figure A6.2 XRD diffractogram of milled organic pad (B: baryte; I: iron; IM: illite-montmorillonite; K: kaolinite; W: wollastonite; ZC: zinc carbide).

Baryte and clays may be used as fillers, wollastonite as fibers or powder (Singh et al.; 2017), iron as fibers, and zinc species as modifier.

References:

https://rruff.info/barite

https://rruff.info/kaolinite

https://rruff.info/wollastonite

Singh, Tej; Tiwari, Avinash; Patnaik, Amar; Chauhan, Ranchan; Ali, Sharafat . (2017). *Influence of wollastonite shape and amount on tribo-performance of non-asbestos organic brake friction composites. Wear, 386-387(), 157–164.* doi:10.1016/j.wear.2017.06.011

Appendix 7 Masses collected using 14-stage impactor

Table A7.1 presents the mass collected during the normal pathway at each plate of the 14-stage impactor, corresponding to a specific aerodynamic diameter (**D50**). Notably, six out of the fourteen measurements were below the limit of quantification.

Table A7.1 Masses weighed in each plate for the NP using the 14-stage impactor

D50 [µm]	Mass collected [µg]
9.84	7
5.34	7
3.64	30
2.46	69
1.62	124
0.943	287
0.600	180
0.38	47
0.254	14
0.154	10
0.0943	5
0.0541	5
0.0303	4
0.0157	4

Appendix 8 TSP Metal concentrations and weight content during NP and HP using the reference pad (Table A8.1 & Table A8.2)

Table A8.1 Metals concentration with uncertainties of particles collected on filter holders of normal and heavy pathways using the reference pad

	Reference							
	NP1		NP2		HP1		HP2	
	Conc.	U	Conc.	U	Conc.	U	Conc.	U
	ng/m³	ng/m³	ng/m³	ng/m³	ng/m³	ng/m³	ng/m³	ng/m³
Ag	<LQ		<LQ		<LQ		<LQ	
Al	802.6	49.1	793.8	48.6	19709.9	1206.0	20584.1	1259.5
As	2.3	0.2	2.6	0.2	33.6	2.7	36.8	3.0
Ba	4409.5		4277.6		128943.7		131889.3	
Be	0.3		0.1		3.8		3.6	
Bi	NA		NA		2.0		1.1	
Ca	4348.3	567.5	4756.0	620.7	138539.2	18079.4	145238.6	18953.6
Cd	NA		NA		0.4		0.6	
Ce	4.5	0.3	4.3	0.3	102.8	8.0	110.7	8.6
Co	3.4	0.2	4.0	0.3	37.6	2.7	41.0	2.9
Cr	268.5	26.0	293.8	28.5	2991.7	290.1	2973.4	288.3
Cu	447.5	37.1	451.4	37.4	4688.7	388.3	4561.9	377.8
Fe	65663.9	4022.4	73222.5	4485.5	726592.9	44509.6	743563.5	45549.2
Ge	1.0		0.9		39.4		41.2	
Hf	<LQ		1.8		2.4		2.5	
K	NA		NA		793.3		883.7	
La	3.2	0.3	3.1	0.3	76.8	7.0	82.8	7.6
Li	<LD		<LD		6.4		6.5	
Mg	125.5	7.9	155.8	9.7	3743.5	232.0	4073.2	252.5
Mn	490.4	36.8	563.2	42.3	7987.2	599.4	8122.6	609.5

Mo	21.1		18.4		NA		NA	
Na	NA		NA		1056.2		1085.8	
Ni	35.1	3.5	36.7	3.7	301.9	30.3	315.9	31.7
Pb	<LQ		<LQ		10.6	0.8	10.5	0.8
Pd	NA		NA		3.6		3.7	
Rb	NA		NA		3.7		4.2	
Ru	NA		NA		<LQ		<LQ	
S	3890.1	504.1	2879.9	373.2	32132.9	4164.3	34836.9	4514.7
Sb	1.6	0.1	1.1	0.1	22.6	2.0	22.4	2.0
Se	3.1	0.8	<LD		NA		NA	
Si	4218.4	551.8	3823.0	500.3	140133.9	18280.4	141185.5	18417.6
Sn	31.8		30.9		1724.8		1788.1	
Sr	27.4	2.4	30.5	2.7	835.4	74.7	873.8	78.1
Te	NA		NA		<LQ		<LQ	
Th	0.5		0.4		10.7		11.3	
Ti	54.9	5.3	57.0	5.5	788.0	75.5	865.4	82.9
Tl	NA		NA		0.1		0.1	
U	0.1		<LD		2.2		2.6	
V	6.4	0.5	5.9	0.5	65.6	5.2	70.9	5.6
W	NA		NA		10.7		11.5	
Zn	<LQ		<LQ		283.2	29.7	190.9	20.0
Zr	<LQ		39.9		121.4		126.1	

Table A8.2 Weight content with uncertainties of particles collected on filter holders of normal and heavy pathways using the reference pad

	CLT 01 ref							
	NP1		NP2		HP1		HP2	
	Concentration	Uncertainty	Concentration	Uncertainty	Concentration	Uncertainty	Concentration	Uncertainty
	µg/mg	µg/mg	µg/mg	µg/mg	µg/mg	µg/mg	µg/mg	µg/mg
Ag	<LQ		<LQ		<LQ		<LQ	
Al	4.3	0.3	5.1	0.3	9.7	0.6	10.1	0.6
As	0.01	0.001	0.02	0.001	0.02	0.001	0.02	0.001
Ba	23.8	1.7	27.7	2.0	63.5	4.6	64.7	4.7
Be	0.0		0.0		0.002		0.002	
Bi	NA		NA		0.001		0.001	
Ca	23.5	3.1	30.8	4.0	68.2	8.9	71.3	9.3
Cd	NA		NA		0.0002		0.0003	
Ce	0.02	0.002	0.03	0.002	0.1	0.004	0.1	0.004
Co	0.02	0.001	0.03	0.002	0.02	0.001	0.02	0.001
Cr	1.5	0.1	1.9	0.2	1.5	0.1	1.5	0.1
Cu	2.4	0.2	2.9	0.2	2.3	0.2	2.2	0.2
Fe	355.0	21.7	474.1	29.0	357.9	21.9	364.8	22.3
Ge	0.0		0.01		0.02		0.02	
Hf	<LQ		0.01		0.001		0.001	
K	NA		NA		0.4		0.4	
La	0.02	0.002	0.02	0.002	0.04	0.003	0.04	0.004
Li	<LD		<LD		0.003		0.003	
Mg	0.7	0.04	1.0	0.1	1.8	0.1	2.0	0.1
Mn	2.7	0.2	3.6	0.3	3.9	0.3	4.0	0.3
Mo	0.1		0.1		NA		NA	
Na	NA		NA		0.5		0.5	
Ni	0.2	0.02	0.2	0.02	0.1	0.01	0.2	0.02
Pb	<LQ		<LQ		0.01	0.0004	0.01	0.0004
Pd	NA		NA		0.002		0.002	
Rb	NA		NA		0.002		0.002	

Ru	NA		NA		<LQ		<LQ	
S	21.0	2.7	18.6	2.4	15.8	2.1	17.1	2.2
Sb	0.01	0.001	0.01	0.001	0.01	0.001	0.0	0.001
Se	0.02	0.004	<LD		NA		NA	
Si	22.8	3.0	24.8	3.2	69.0	9.0	69.3	9.0
Sn	0.2		0.2		0.8		0.9	
Sr	0.1	0.01	0.2	0.02	0.4	0.04	0.4	0.04
Te	NA		NA		<LQ		<LQ	
Th	0.0		0.0		0.0		0.01	
Ti	0.3	0.03	0.4	0.04	0.4	0.04	0.4	0.04
Tl	NA		NA		0.0001		0.00004	
U	0.0		<LD		0.001		0.001	
V	0.0	0.003	0.04	0.003	0.03	0.003	0.03	0.003
W	NA		NA		0.01		0.01	
Zn	<LQ		<LQ		0.1	0.01	0.1	0.01
Zr	<LQ		0.3		0.1		0.1	

Appendix 9 Fraction Metal concentrations and weight content during NP1 and NP2 using the reference pad (Table A9.1 & Table A9.2)

Table A9.1 Metals concentration with uncertainties of particles collected on the 3-stage impactor of normal pathways using the reference pad

	NP1								NP2							
	>10 µm		10-2.6 µm		2.6-1 µm		<1 µm		>10 µm		10-2.6 µm		2.6-1 µm		<1 µm	
	C	U	C	U	C	U	C	U	C	U	C	U	C	U	C	U
	ng/m³	ng/m³	ng/m³	ng/m³	ng/m³	ng/m³	ng/m³	ng/m³	ng/m³	ng/m³	ng/m³	ng/m³	ng/m³	ng/m³	ng/m³	ng/m³
Ag	<LD		<LD		<LD		<LD		<LQ		<LD		<LD		<LD	
Al	<LQ		551.8	33.8	110.5	6.8	287.3	17.6	<LQ		421.7	25.8	89.8	5.5	140.0	8.6
As	<LQ		1.7	0.1	<LQ		1.0	0.1	<LQ		1.5	0.1	<LQ		0.7	0.1
Ba	<LQ		3049.6		659.8		1543.9		<LQ		2153.6	0.0	483.6		769.1	
Be	0.01		0.1		0.1		0.0		<LQ		0.0	0.0	0.0		<LQ	
Bi	NA		NA		NA		NA		NA		NA		NA		NA	
Ca	<LQ		3006.7	392.7	605.0	79.0	1703.2	222.5	<LD		2252.0	294.2	686.8	89.7	923.3	120.6
Cd	NA		NA		NA		NA		NA		NA		NA		NA	
Ce	<LD		3.0	0.2	0.6	0.05	1.4	0.1	<LD		2.0	0.2	0.5	0.04	0.7	0.1
Co	<LD		2.6	0.2	0.5	0.04	1.2	0.1	<LD		1.9	0.1	0.4	0.03	0.7	0.05
Cr	<LD		175.0	17.0	35.7	3.5	96.4	9.3	<LD		144.1	14.0	32.9	3.2	<LQ	
Cu	<LD		271.4	22.5	51.6	4.3	<LQ		<LD		219.5	18.2	48.3	4.0	<LD	
Fe	<LQ		44799.5	2744.3	9007.3	551.8	22901.5	1402.9	<LQ		40831.5	2501.3	7924.2	485.4	13015.6	797.3
Ge	<LQ		0.4		0.1		0.1		<LQ		0.4		0.1		0.2	
Hf	<LD		<LD		<LD		<LD		0.9		<LD		<LD		<LD	
K	NA		NA		NA		NA		NA		NA		NA		NA	
La	<LD		2.1	0.2	0.5	0.04	1.1	0.1	<LQ		1.6	0.1	0.3	0.03	0.6	0.1
Li	<LQ		0.1		<LQ		<LD		<LD		<LD		<LD		<LD	
Mg	<LD		92.3	5.8	<LQ		58.9	3.7	<LD		67.0	4.2	<LQ		32.0	2.0
Mn	<LQ		334.1	25.1	66.7	5.0	172.3	12.9	<LQ		278.5	20.9	62.3	4.7	98.8	7.4
Mo	<LD		13.8		2.9		7.3		<LQ		8.8		2.2		<LQ	

Na	NA		NA		NA		NA		NA		NA		NA		NA	
Ni	<LD		21.6	2.2	<LQ		24.5	2.5	<LD		17.6	1.8	<LQ		<LQ	
Pb	<LD		0.4	0.03	<LD		<LD		<LD		0.3	0.0	<LD		<LD	
Pd	NA		NA		NA		NA		NA		NA		NA		NA	
Rb	NA		NA		NA		NA		NA		NA		NA		NA	
Ru	NA		NA		NA		NA		NA		NA		NA		NA	
S	<LQ		2592.9	336.0	606.2	78.6	1307.3	169.4	<LQ		1032.7	133.8	740.8	96.0	755.9	98.0
Sb	<LD		1.0	0.1	0.3	0.02	0.6	0.1	<LQ		0.7	0.1	<LQ		0.2	0.0
Se	<LQ		<LD		<LD		<LQ		<LD		<LD		<LD		<LD	
Si	<LQ		2685.5	351.3	<LQ		1079.8	141.3	<LQ		1768.7	231.4	<LQ		1099.8	143.9
Sn	<LD		20.1		4.4		<LQ		<LD		15.1	0.0	3.4		<LD	
Sr	<LQ		20.6	1.8	2.9	0.3	9.9	0.9	<LQ		15.5	1.4	3.0	0.3	5.1	0.5
Te	NA		NA		NA		NA		NA		NA		NA		NA	
Th	<LD		0.3		0.1		0.2		<LD		0.2		0.1	0.0	0.1	
Ti	<LQ		39.1	3.8	7.7	0.7	<LQ		<LQ		28.3	2.7	6.6	0.6	<LD	
Tl	NA		NA		NA		NA		NA		NA		NA		NA	
U	<LQ		0.1		<LQ		<LD		<LQ		<LD		<LQ		<LD	
V	<LQ		4.0	0.3	0.8	0.1	2.1	0.2	<LQ		3.1	0.2	0.7	0.1	1.5	0.1
W	NA		NA		NA		NA		NA		NA		NA		NA	
Zn	<LD		<LD		<LD		<LQ		<LQ		<LQ		<LQ		<LD	
Zr	<LD		<LQ		<LD		<LD		17.6		<LQ		<LD		<LD	

Table A9.2 Weight content with uncertainties of particles collected on the 3-stage impactor of normal pathways using the reference pad

	NP1								NP2							
	>10 µm		10-2.6 µm		2.6-1 µm		<1 µm		>10 µm		10-2.6 µm		2.6-1 µm		<1 µm	
	C	U	C	U	C	U	C	U	C	U	C	U	C	U	C	U
	µg/mg	µg/mg	µg/mg	µg/mg	µg/mg	µg/mg	µg/mg	µg/mg	µg/mg	µg/mg	µg/mg	µg/mg	µg/mg	µg/mg	µg/mg	µg/mg
Ag	<LD		<LD		<LD		<LD		<LQ		<LD		<LD		<LD	
Al	<LQ		5.8	0.4	5.4	0.3	5.5	0.3	<LQ		5.4	0.3	5.4	0.3	3.0	0.2
As	<LQ		0.02	0.002	<LQ		0.02	0.002	<LQ		0.02	0.002	<LQ		0.01	0.001
Ba	<LQ		32.3	2.4	32.2	2.4	29.7	2.2	<LQ		27.7	2.0	28.9	2.1	16.3	1.2
Be	0.02		0.001		0.003		0.0002		<LQ		0.001		0.002		<LQ	
Bi	NA		NA		NA		NA		NA		NA		NA		NA	
Ca	<LQ		31.9	4.2	29.6	3.9	32.7	4.3	<LD		29.0	3.8	41.1	5.4	19.6	2.6
Cd	NA		NA		NA		NA		NA		NA		NA		NA	
Ce	<LD		0.03	0.002	0.03	0.002	0.03	0.002	<LD		0.03	0.002	0.03	0.002	0.02	0.001
Co	<LD		0.03	0.002	0.03	0.002	0.02	0.002	<LD		0.02	0.002	0.02	0.002	0.01	0.001
Cr	<LD		1.9	0.2	1.7	0.2	1.9	0.2	<LD		1.9	0.2	2.0	0.2	<LQ	
Cu	<LD		2.9	0.2	2.5	0.2	<LQ		<LD		2.8	0.2	2.9	0.2	<LD	
Fe	<LQ		474.6	29.1	440.2	27.0	440.3	27.0	<LQ		525.1	32.2	474.2	29.0	276.3	16.9
Ge	<LQ		0.0		0.0		0.003		<LQ		0.005		0.01		0.0	
Hf	<LD		<LD		<LD		<LD		1.1		<LD		<LD		<LD	
K	NA		NA		NA		NA		NA		NA		NA		NA	
La	<LD		0.02	0.002	0.02	0.002	0.02	0.002	<LQ		0.02	0.002	0.02	0.002	0.01	0.001
Li	<LQ		0.002		<LQ		<LD		<LD		<LD		<LD		<LD	
Mg	<LD		1.0	0.1	<LQ		1.1	0.1	<LD		0.9	0.1	<LQ		0.7	0.04
Mn	<LQ		3.5	0.3	3.3	0.2	3.3	0.2	<LQ		3.6	0.3	3.7	0.3	2.1	0.2
Mo	<LD		0.1		0.1		0.1		<LQ		0.1		0.1		<LQ	
Na	NA		NA		NA		NA		NA		NA		NA		NA	
Ni	<LD		0.2	0.02	<LQ		0.5	0.05	<LD		0.2	0.02	<LQ		<LQ	
Pb	<LD		0.004	0.0003	<LD		<LD		<LD		0.003	0.0003	<LD		<LD	
Pd	NA		NA		NA		NA		NA		NA		NA		NA	
Rb	NA		NA		NA		NA		NA		NA		NA		NA	

Ru	NA		NA		NA		NA		NA		NA		NA		NA	
S	<LQ		27.5	3.6	29.6	3.8	25.1	3.3	<LQ		13.3	1.7	44.3	5.7	16.0	2.1
Sb	<LD		0.01	0.001	0.01	0.001	0.01	0.001	<LQ		0.01	0.001	<LQ		0.005	0.0004
Se	<LQ		<LD		<LD		<LQ		<LD		<LD		<LD		<LD	
Si	<LQ		28.5	3.7	<LQ		20.8	2.7	<LQ		22.7	3.0	<LQ		23.3	3.1
Sn	<LD		0.2		0.2		<LQ		<LD		0.2		0.2		<LD	
Sr	<LQ		0.2	0.02	0.1	0.01	0.2	0.02	<LQ		0.2	0.02	0.2	0.02	0.1	0.01
Te	NA		NA		NA		NA		NA		NA		NA		NA	
Th	<LD		0.004		0.003		0.004		<LD		0.003		0.003		0.001	
Ti	<LQ		0.4	0.04	0.4	0.04	<LQ		<LQ		0.4	0.03	0.4	0.04	<LD	
Tl	NA		NA		NA		NA		NA		NA		NA		NA	
U	<LQ		0.001		<LQ		<LD		<LQ		<LD		<LQ		<LD	
V	<LQ		0.04	0.003	0.04	0.003	0.04	0.003	<LQ		0.04	0.003	0.04	0.003	0.03	0.002
W	NA		NA		NA		NA		NA		NA		NA		NA	
Zn	<LD		<LD		<LD		<LQ		<LQ		<LQ		<LQ		<LD	
Zr	<LD		<LQ		<LD		<LD		23.2		<LQ		<LD		<LD	

Appendix 10 Fraction Metal concentrations and weight content during NP1 and NP2 using the reference pad (Table A10.1 & Table A10.2)

Table A10.1 Metals concentration with uncertainties of particles collected on the 3-stage impactor of heavy pathways using the reference pad

	HP1								HP2							
	>10 µm		10-2.6 µm		2.6-1 µm		<1 µm		>10 µm		10-2.6 µm		2.6-1 µm		<1 µm	
	C	U	C	U	C	U	C	U	C	U	C	U	C	U	C	U
	ng/m³	ng/m³	ng/m³	ng/m³	ng/m³	ng/m³	ng/m³	ng/m³	ng/m³	ng/m³	ng/m³	ng/m³	ng/m³	ng/m³	ng/m³	ng/m³
Ag	<LD		0.4		<LQ		3.5		<LD		0.3		<LQ		<LQ	
Al	23.3	1.4	10603.4	649.7	1372.2	84.1	5282.8	323.7	<LQ		9678.3	593.0	1519.0	93.1	4849.2	297.1
As	<LD		19.6	1.6	2.3	0.2	8.3	0.7	<LD		17.1	1.4	2.3	0.2	8.9	0.7
Ba	132.7		69596.8		9184.7		33706.0		29.7		63300.7		10033.1		29269.8	
Be	<LD		1.7		0.2		0.8		<LD		1.9		0.2		0.9	
Bi	0.0		1.1		0.1		0.6		<LD		0.6		0.1		0.3	
Ca	<LD		74786.2	9768.3	9323.8	1217.8	36505.5	4768.2	<LD		68672.0	8969.7	10514.1	1373.3	33838.9	4419.9
Cd	<LD		0.3		<LQ		0.1		<LD		0.3		<LD		0.1	
Ce	0.1	0.01	56.1	4.4	7.0	0.5	26.9	2.1	<LQ		51.7	4.0	8.3	0.6	25.9	2.0
Co	<LQ		21.5	1.5	2.6	0.2	9.9	0.7	<LQ		19.8	1.4	2.8	0.2	9.3	0.7
Cr	<LD		1641.7	159.2	197.6	19.2	796.9	77.3	<LD		1437.6	139.4	201.3	19.5	693.3	67.2
Cu	<LD		2594.1	214.8	282.9	23.4	1182.9	98.0	<LD		2223.3	184.1	297.3	24.6	1030.7	85.4
Fe	1189	723	398323	24401	51618	3162	194489	11914	<LQ		358264	21950	54659	3348	173663	10638
Ge	0.1		21.1		2.7		10.4		<LD		19.5		3.2		9.8	
Hf	<LD		1.3		<LD		<LD		<LD		1.3		<LD		<LD	
K	<LD		438.9		46.2		207.9		<LD		399.0		56.6		196.8	
La	0.1	0.01	42.1	3.8	5.2	0.5	20.1	1.8	0.03		39.2	3.6	6.1	0.6	19.1	1.7
Li	<LD		3.6		0.4		1.7		<LD		3.1		0.5		1.5	
Mg	<LD		2048.9	128.4	252.3	15.8	960.0	60.2	<LD		1928.1	120.8	272.6	17.1	904.9	56.7
Mn	7.6	0.6	4328.6	324.9	558.8	41.9	2152.5	161.6	<LD		3870.2	290.5	589.5	44.2	1914.7	143.7
Mo	NA		NA		NA		NA		NA		NA		NA		NA	

Na	<LD		570.0		63.3		284.9		<LD		505.4		72.1		262.2	
Ni	<LD		175.1	17.6	23.3	2.3	83.1	8.4	<LD		162.8	16.4	22.7	2.3	74.2	7.5
Pb	<LQ		5.4	0.4	0.7	0.1	2.8	0.2	<LD		5.3	0.4	0.9	0.1	2.7	0.2
Pd	<LD		1.8		0.2		0.9		<LD		1.7		0.3		0.8	
Rb	<LD		2.0		0.2		1.0		<LD		1.9		0.3		1.0	
Ru	<LD		<LQ		<LD		<LD		<LD		0.04		<LD		<LQ	
S	<LD		17528.0	2271.5	2740.6	355.2	8271.7	1072.0	550.9	71.4	15973.2	2070.0	2793.0	362.0	7730.8	1001.9
Sb	<LD		12.0	1.1	1.5	0.1	6.4	0.6	<LD		11.0	1.0	1.7	0.2	5.4	0.5
Se	NA		NA		NA		NA		NA		NA		NA		NA	
Si	<LD		55756.9	7293.8	7159.6	936.6	35811.4	4684.6	<LD		65144.1	8521.8	7045.9	921.7	28435.5	3719.8
Sn	2.2		920.2		119.8		458.4		<LD		834.5		131.9		423.8	
Sr	<LD		462.8	41.4	50.7	4.5	214.2	19.1	<LD		421.9	37.7	58.4	5.2	195.0	17.4
Te	<LD		<LD		<LD		<LD		<LD		<LD		<LD		<LD	
Th	0.03		5.9		0.6		2.8		0.02		5.4		0.8		2.5	
Ti	<LD		562.9	54.0	<LD		182.9	17.5	<LD		401.3	38.5	<LD		178.8	17.1
Tl	<LD		0.1		0.01		0.0	0.0	<LQ		0.0		<LQ		0.02	
U	<LQ		1.2		0.2		0.6	0.0	<LQ		1.1		0.2		0.6	
V	<LQ		36.5	2.9	4.7	0.4	17.1	1.4	<LQ		33.4	2.6	5.1	0.4	16.5	1.3
W	<LD		6.5		0.8		2.8		<LD		5.5		0.8		2.7	
Zn	<LQ		129.9	13.6	36.1	3.8	110.7	11.6	<LD		53.9	5.7	11.8	1.2	32.4	3.4
Zr	<LD		65.3		8.2		<LQ		<LD		61.0		9.2		<LQ	

Table A10.2 Weight content with uncertainties of particles collected on the 3-stage impactor of heavy pathways using the reference pad

	HP1								HP2							
	>10 µm		10-1 µm		1-0.2 µm		<0.2 µm		>10 µm		10-1 µm		1-0.2 µm		<0.2 µm	
	C	U	C	U	C	U	C	U	C	U	C	U	C	U	C	U
	µg/mg	µg/mg	µg/mg	µg/mg	µg/mg	µg/mg	µg/mg	µg/mg	µg/mg	µg/mg	µg/mg	µg/mg	µg/mg	µg/mg	µg/mg	µg/mg
Ag	<LD		<LD		<LQ		<LD		<LD		<LD		<LQ		<LQ	
Al	5.7	0.3	10.2	0.6	9.7	0.6	9.9	0.6	<LQ		10.9	0.7	10.0	0.6	10.0	0.6
As	<LD		0.02	0.002	0.02	0.001	0.02	0.001	<LD		0.02	0.002	0.02	0.001	0.02	0.002
Ba	32.2	2.3	67.2	4.9	65.1	4.7	63.0	4.6	9.5	0.7	71.5	5.2	66.3	4.8	60.5	4.4
Be	<LD		0.002		0.001		0.001		<LD		0.002		0.002		0.002	
Bi	0.0		0.001		0.001		0.001		<LD		0.001		0.001		0.001	
Ca	<LD		72.2	9.4	66.1	8.6	68.3	8.9	<LD		77.6	10.1	69.5	9.1	69.9	9.1
Cd	<LD		0.0002		<LQ		0.0		<LD		0.0003		<LD		0.0003	
Ce	0.03	0.003	0.1	0.004	0.05	0.004	0.1	0.004	<LQ		0.1	0.005	0.1	0.004	0.1	0.004
Co	<LQ		0.0	0.001	0.02	0.001	0.02	0.001	<LQ		0.02	0.002	0.02	0.001	0.02	0.001
Cr	<LD		1.6	0.2	1.4	0.1	1.5	0.1	<LD		1.6	0.2	1.3	0.1	1.4	0.1
Cu	<LD		2.5	0.2	2.0	0.2	2.2	0.2	<LD		2.5	0.2	2.0	0.2	2.1	0.2
Fe	288.5	17.7	384.5	23.6	365.8	22.4	363.7	22.3	<LQ		404.6	24.8	361.4	22.1	358.7	22.0
Ge	0.0		0.02		0.02		0.0		<LD		0.02		0.02		0.02	
Hf	<LD		0.001		<LD		<LD		<LD		0.001		<LD		<LD	
K	<LD		0.4		0.3		0.4		<LD		0.5		0.4		0.4	
La	0.02	0.002	0.04	0.004	0.04	0.003	0.04	0.003	0.0		0.04	0.004	0.04	0.004	0.04	0.004
Li	<LD		0.004		0.003		0.003		<LD		0.004		0.003		0.003	
Mg	<LD		2.0	0.1	1.8	0.1	1.8	0.1	<LD		2.2	0.1	1.8	0.1	1.9	0.1
Mn	1.9	0.1	4.2	0.3	4.0	0.3	4.0	0.3	<LD		4.4	0.3	3.9	0.3	4.0	0.3
Mo	NA		NA		NA		NA		NA		NA		NA		NA	
Na	<LD		0.6		0.4		0.5		<LD		0.6		0.5		0.5	
Ni	<LD		0.2	0.02	0.2	0.02	0.2	0.02	<LD		0.2	0.02	0.1	0.02	0.2	0.02

Pb	<LQ		0.01	0.0004	0.005	0.0004	0.01	0.0004	<LD		0.01	0.0005	0.006	0.0005	0.006	0.0004
Pd	<LD		0.002		0.001		0.002		<LD		0.002		0.002		0.002	
Rb	<LD		0.002		0.002		0.002		<LD		0.002		0.002		0.002	
Ru	<LD		<LQ		<LD		<LD		<LD		0.00005		<LD		<LQ	
S	<LD		16.9	2.2	19.4	2.5	15.5	2.0	176.0	22.8	18.0	2.3	18.5	2.4	16.0	2.1
Sb	<LD		0.01	0.001	0.01	0.001	0.01	0.001	<LD		0.01	0.001	0.01	0.001	0.01	0.001
Se	NA		NA		NA		NA		NA		NA		NA		NA	
Si	<LD		53.8	7.0	50.7	6.6	67.0	8.8	<LD		73.6	9.6	46.6	6.1	58.7	7.7
Sn	0.5		0.9		0.8		0.9		<LD		0.9		0.9		0.9	
Sr	<LD		0.4	0.04	0.4	0.03	0.4	0.04	<LD		0.5	0.04	0.4	0.03	0.4	0.04
Te	<LD		<LD		<LD		<LD		<LD		<LD		<LD		<LD	
Th	0.0		0.0		0.0		0.01		0.01		0.01		0.01		0.01	
Ti	<LD		0.5	0.1	<LD		0.3	0.03	<LD		0.5	0.04	<LD		0.4	0.04
Tl	<LD		0.0001		0.0001		0.0001		<LQ		0.00005		<LQ		0.00005	
U	<LQ		0.001		0.001		0.001		<LQ		0.001		0.001		0.001	
V	<LQ		0.04	0.003	0.03	0.003	0.03	0.003	<LQ		0.04	0.003	0.03	0.003	0.03	0.003
W	<LD		0.01		0.01		0.01		<LD		0.01		0.01		0.01	
Zn	<LQ		0.1	0.01	0.3	0.03	0.2	0.02	<LD		0.1	0.01	0.1	0.008	0.1	0.01
Zr	<LD		0.1		0.1		<LQ		<LD		0.1		0.1		<LQ	

Appendix 11 Results of the source apportionment based on the metal analysis of particles: application to NP and HP routes for the reference pad and disc.

The estimated relative mass contributions of the brake pad and disc to the emitted total suspended particles (TSP) for both normal (NP) and harsh (HP) braking routes are presented in Table A11.1, based on the previously identified metal tracers.

Table A11.1 Calculation of the relative mass contribution of the pad and disc to TSP based on each metal tracer, for NP and HP routes.

	Pad metal tracers			**Disc metal tracers**			
	Al	**Ba**	**Ca**	**Cr**	**Cu**	**Fe**	
Pad and disc : metal weight content in a first body (µg metal /mg first body)							
Pad	13,91	68,76	82,90	0,06	0,40	199,05	
Disc	0,01	0,00	0,07	4,06	6,38	894,79	
Total Suspended Particles (TSP) : metal weight content in TSP (µg metal/mg TSP)							
NP1	4,34	23,84	23,51	1,45	2,42	354,98	
NP2	5,14	27,70	30,79	1,90	2,92	474,11	
HP1	9,71	63,51	68,24	1,47	2,31	357,87	
HP2	10,10	64,71	71,26	1,46	2,24	364,81	
Estimated relative contribution of pad to TSP: pad % w/w in TSP, from each pad metal tracer							**Average pad %**
NP1	31%	35%	28%	Not applicable			31% ± 3%
NP2	37%	40%	37%				38% ± 2%
HP1	70%	92%	82%				81% ± 11%
HP2	73%	94%	86%				84% ± 11%
Estimated relative contribution of disc to TSP: disc % w/w in TSP, from each disc metal tracer							**Average disc %**
NP1	Not applicable			36%	38%	40%	38%± 2%
NP2				47%	46%	53%	49%± 4%
HP1				36%	36%	40%	38%± 2%
HP2				36%	35%	41%	37%± 3%

For a given first body (pad or disc) and a given pathway (NP or HP), the calculated average mass contributions to TSP are similar whatever the metal tracer, with a maximum coefficient of variation (= standard deviation divided by the mean) of 14% for the pad metal tracers for HP1. This result tends to validate the choice of the metal tracers, as they behave similarly. Nevertheless, concerning the disc metal tracers, Cr and Cu show closer disc contribution values than the ones of Fe which are always higher. This overestimation of the disc contribution using Fe is probably due to the fact that the Fe content in the pad is ignored in this approach, while in reality the pad may also contribute to Fe in TSP.

Moreover, the sum of the mass contributions of the pad and the disc to TSP does not give the expected value of 100%, the error on the sum varying from -31% to + 21% (Table A11.2). This lack of precision may

be due to the combination of uncertainties in the analysis of the metals in pad, disc and TSP. Another cause may be the failure to comply with the hypotheses. Among them, the hypothesis that all the components of the heterogeneous pad have the same 8h-averaged contribution to the TSP is maybe not realistic. In fact, the emission behavior of the pad metal tracers coming from fillers components (such as aluminum powder (Al), calcium carbonate (Ca) or barite (Ba)), which are initially fine-grained powders, may be similar. But this is maybe not the case for fibers made of iron oxide, which are likely to generate wear particles with higher density and different sizes, not necessarily emitted in the same way as the fillers' particles.

Table A11.2 Summary of the relative mass contributions of the pad and disc to TSP, for NP and HP routes.

Route	Average pad mass % to TSP	Average disc mass % to TSP	Sum of the percentages	Error of the sum
NP1	31%	38%	69% ± 4%	-31%
NP2	38%	49%	87% ± 4%	-13%
HP1	81%	38%	119% ± 12%	19%
HP2	84%	37%	121% ± 11%	21%

Despite these limitations of the method, the calculated average mass contributions of pad and disc to TSP show a rather similar contribution of pad and disc to NP (pad % ≈ disc %), and a higher contribution of the pad to HP (pad % >> disc %). These trends are consistent with the measurements of the volumetric losses of pad and disc made by Frangieh (2025).

Finally, using the average pad and disc mass contributions to TSP calculated for each pathway, it is possible to check if the mass balance of Mn, which is a metal present in both pad and disc, is fulfilled (Table A11.3). These calculations show that the mass balance of Mn is satisfactorily fulfilled for both HP1 and HP2, with errors around 15-16%, and less well verified for NP1 and NP2 but remains acceptable.

Table A11.3 Mass balance of Mn using the raw pad and disc mass contributions to TSP from Table A11.1.

	Mn (µg Mn/mg pad or disc)		
Pad	2,02		
Disc	7,74		
	Calculated Mn (µg Mn/mg TSP)	**Measured Mn** (µg Mn/mg TSP)	**Error**
NP1	3,56	2,65	34%
NP2	4,53	3,65	24%
HP1	4,55	3,93	16%
HP2	4,58	3,99	15%

About the tracers' method applicability to the emitted particles, one may conclude that it provides rough results with large uncertainties but nevertheless plausible and informative, in terms of the trends they indicate when comparing NP with HP.

Appendix 12 Pad & disc mass fractions calculated by the metal tracers' method in particles collected by the 3-stage impactor tracers

Pad tracers: Al, Ba, Ca

Disc tracers: Cr, Cu

Table A12.1 Pad and disc mass fraction (NP1)

	NP1		
	mean pad %w pad	mean disc %w	sum %w
stage 1: < 10 µm	n.a.	n.a.	n.a.
stage 2: 2.6 - 10 µm	42%	45%	88%
stage 3: 1 - 2.6 µm	40%	41%	82%
backup filter (< 1 µm)	41%	46%	86%

Table A12.2 Pad and disc mass fraction (NP1)

	NP2		
	mean pad %w pad	mean disc %w	sum %w
stage 1: < 10 µm	n.a.	n.a.	n.a.
stage 2: 2.6 - 10 µm	38%	45%	83%
stage 3: 1 - 2.6 µm	43%	47%	90%
backup filter (< 1 µm)	23%	n.a.	n.a.

Table A12.3 Pad and disc mass fraction (HP1)

	HP1		
	mean pad %w pad	mean disc %w	sum %w
stage 1: < 10 µm	n.a.	n.a.	n.a.
stage 2: 2.6 - 10 µm	86%	39%	125%
stage 3: 1 - 2.6 µm	81%	33%	114%
backup filter (< 1 µm)	82%	36%	117%

Table A12.4 Pad and disc mass fraction (HP2)

	HP2		
	mean pad %w pad	mean disc %w	sum %w
stage 1: < 10 µm	n.a.	n.a.	n.a.
stage 2: 2.6 - 10 µm	92%	40%	132%
stage 3: 1 - 2.6 µm	84%	32%	116%
backup filter (< 1 µm)	81%	34%	116%

n.a.: not available

Appendix 13 Chromatograms (Figure A13.1, Figure A13.2, Figure A13.3, Figure A13.4, Figure A13.5, Figure A13.6, Figure A13.7, Figure A13.8 & Figure A13.9)

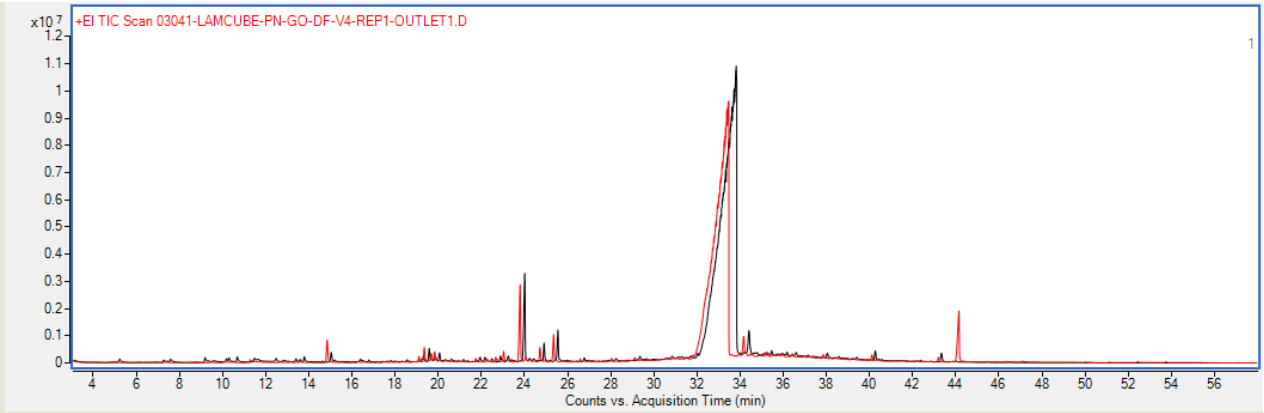

Figure A13.1 TIC from GC/MS analysis of NP 1 test outlet in red and NP2 test outlet in black

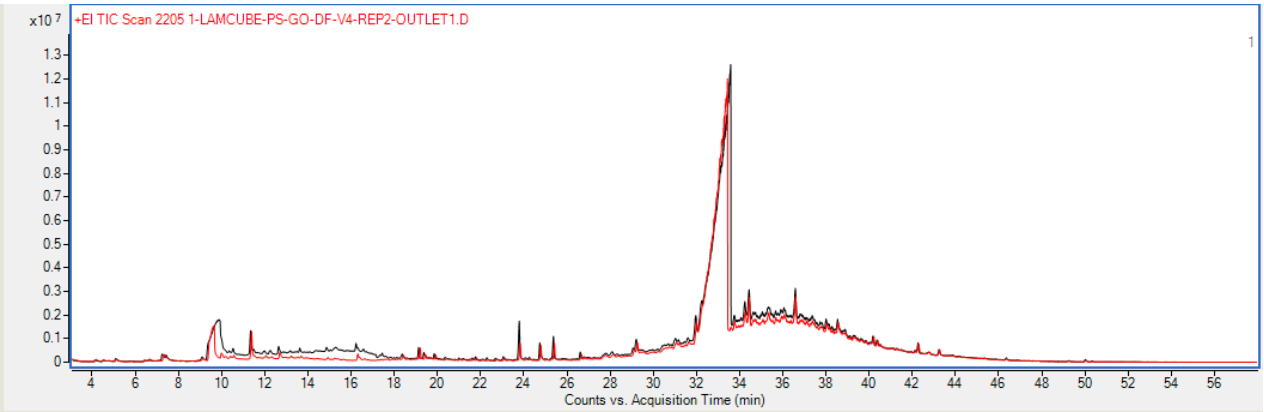

Figure A13.2 TIC from GC/MS analysis of HP1 test outlet in black and HP2 test outlet in red

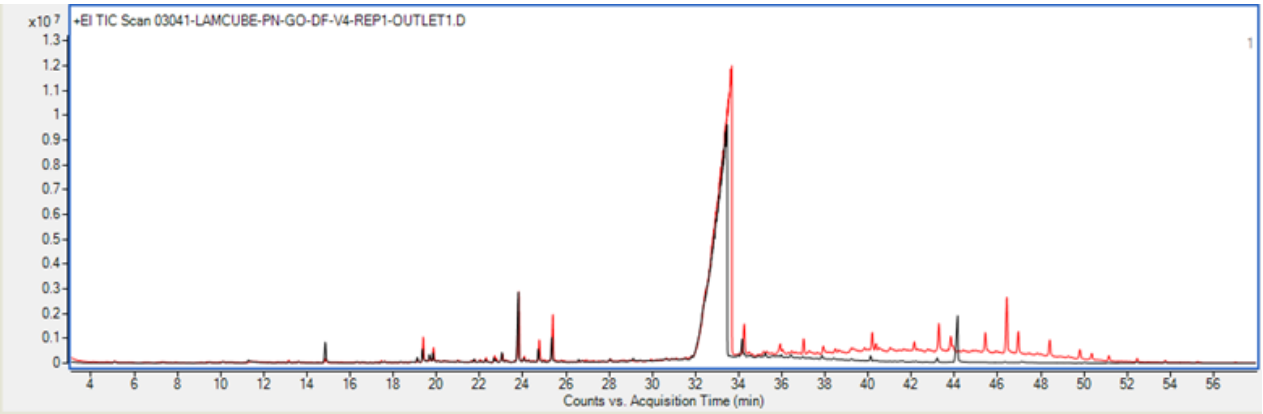

Figure A13.3 TIC from GC/MS analysis of NP1, test outlet in black and test inlet in red

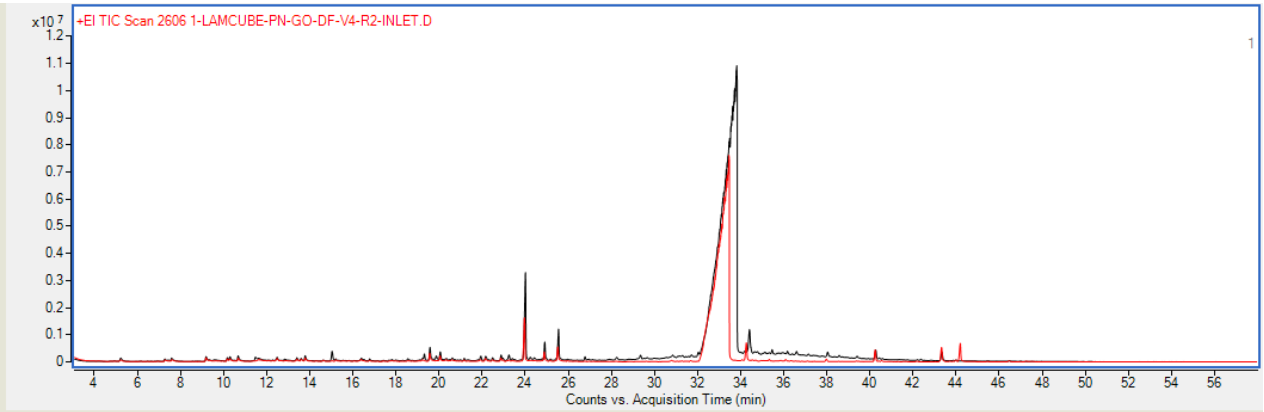

Figure A13.4 TIC from GC/MS analysis of NP2, test outlet in black and test inlet in red

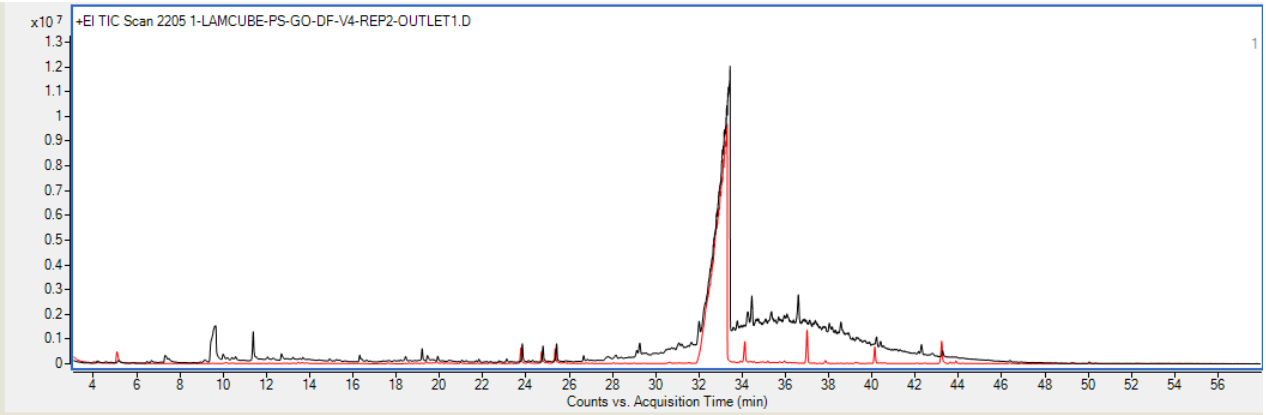

Figure A13.5 TIC from GC/MS analysis of HP2 test outlet in black and HP2 test inlet in red

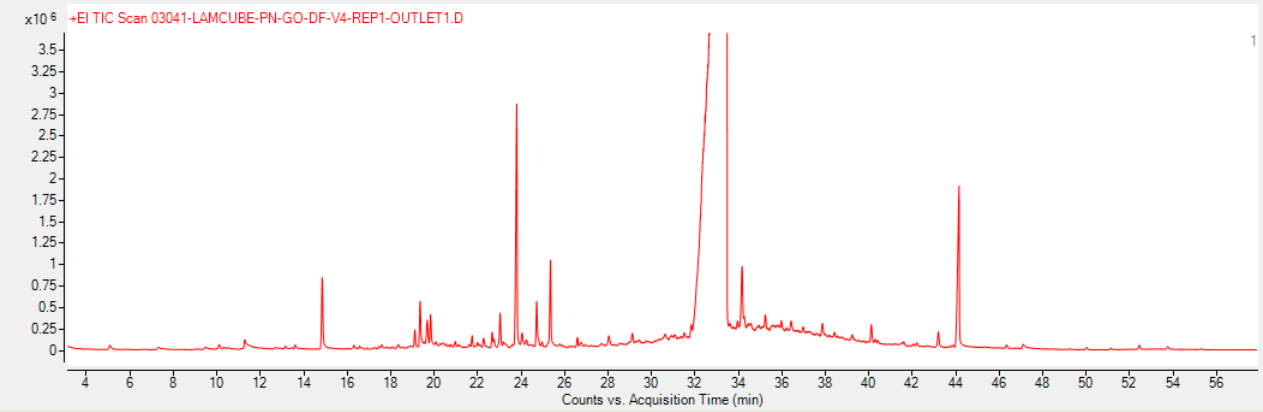

Figure A13.6 Zoomed TIC from GC/MS analysis of NP 1 test outlet

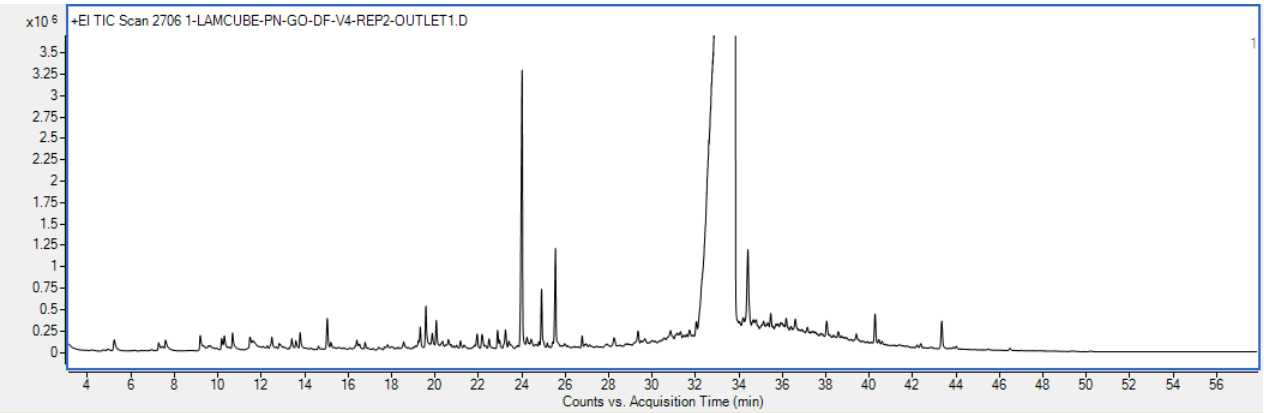

Figure A13.7 Zoomed TIC from GC/MS analysis of NP 2 test outlet

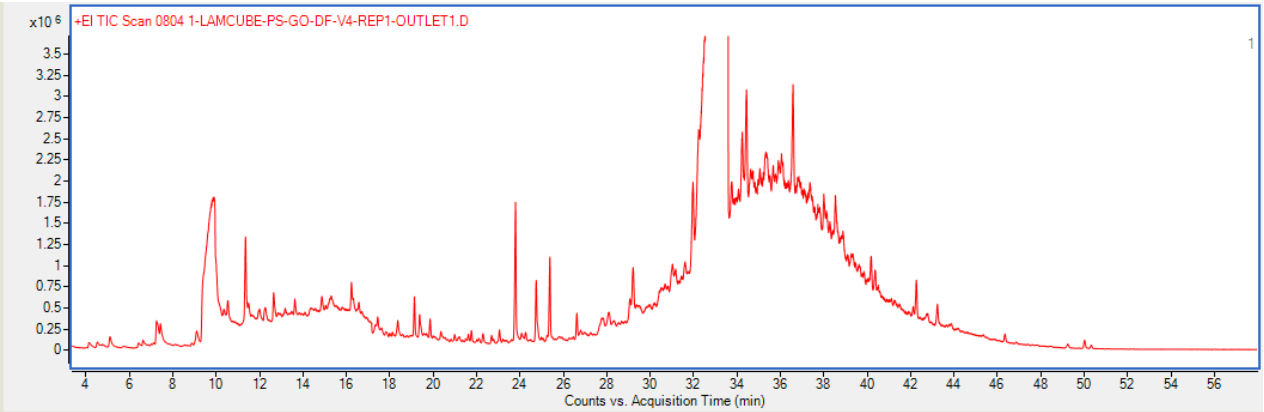

Figure A13.8 Zoomed TIC from GC/MS analysis of HP 1 test outlet

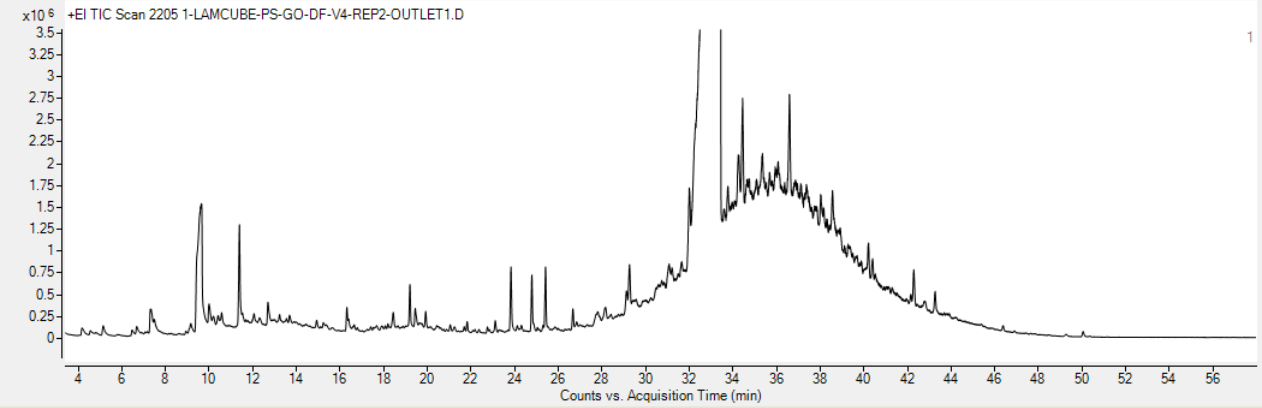

Figure A13.9 Zoomed TIC from GC/MS analysis of HP 2 test outlet

Appendix 14 TSP using different sampling supports across different pads

Figure A14.1 summarizes the TSP mass concentrations found for the NP and HP using different particle sampling devices. Among the measurement methods, the filter holder recorded the highest values due to its reliance on filtration as a sampling technique and the collection onto one simple filter. In contrast, the 3-stage and 14-stage impactors utilize impaction for sampling with many filters in series.

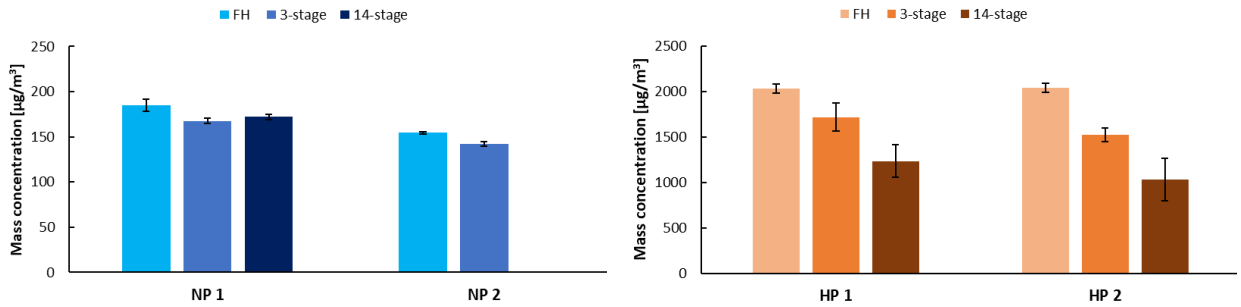

Figure A14.1 TSP across different sampling supports in the Normal Pathway (a) and Heavy Pathway (b) using a reference pad and the cast iron disc

The TSP across different sampling supports for the soft and rigid pad is shown in Figure A14.2. The **14-stage impactor consistently captures the highest mass concentrations** for the soft pad, followed by the filter holder and then the 3-stage impactor.

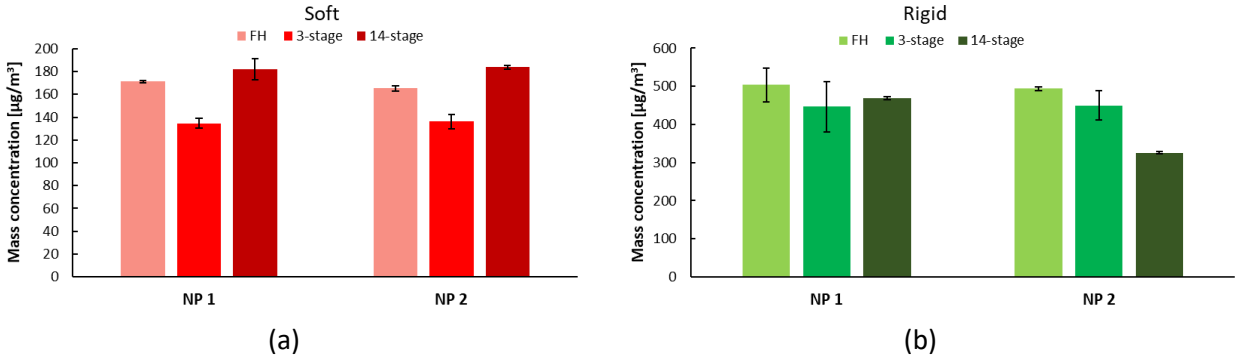

Figure A14.2 Across Different Sampling Supports using (a) the soft pad, and (b) the rigid pad

Appendix 15 Sum of metals from the tests using different sampling devices

Sum of all detected metals except sulfur and silicon. These graphs (Figure A15.1) show a similar trend to that of particles.

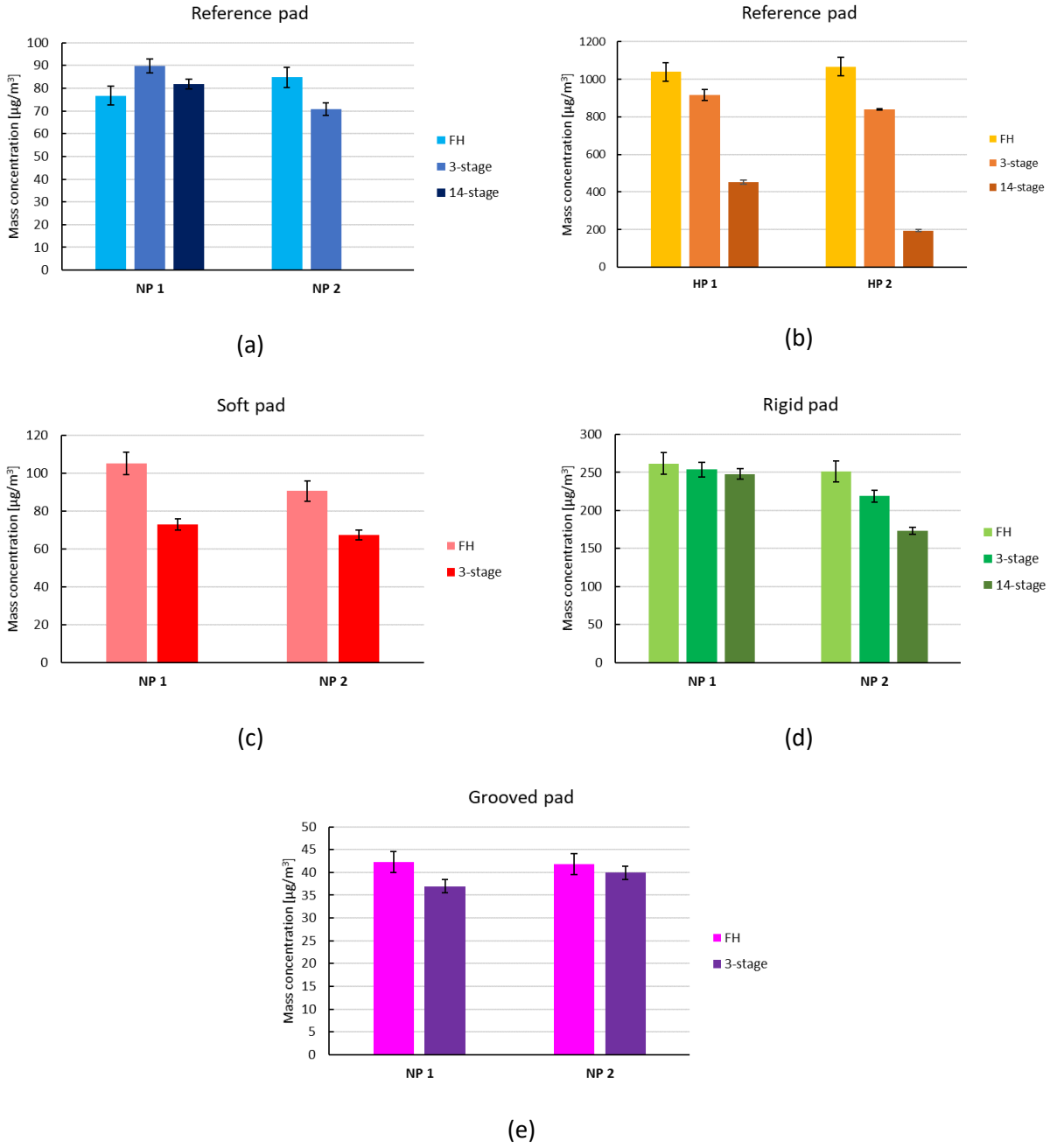

Figure A15.1 Sum of all detected metals (excluding sulfur and silicon) across all sampling supports (FH, 3-stage, and 14-stage) for each braking condition: (a) reference pad – normal pathway, (b) reference pad – heavy pathway, (c) soft pad – normal pathway, (d) rigid pad – normal pathway, and (e) grooved pad – normal pathway

The emissions from braking are influenced by the elemental composition of the primary bodies (the brake pad and disc). Under heavy braking (HP), the wear is predominantly concentrated on the pad rather than the disc (Figure A15.2).

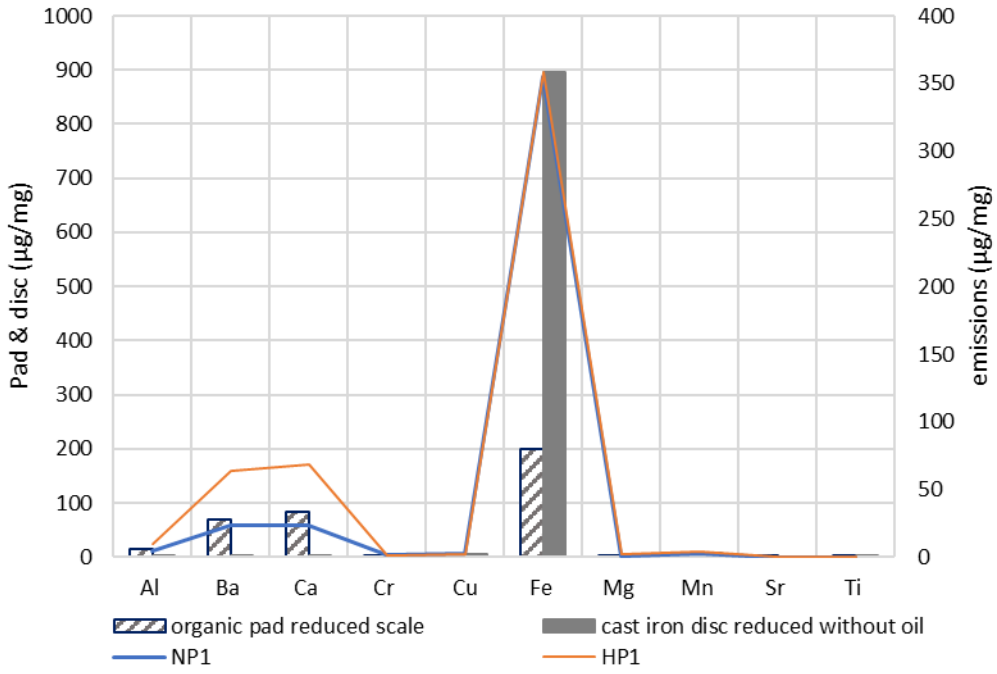

Figure A15.2 Composition of the pad and disc vs the particles: The relationship between raw materials and emissions

Appendix 16 Metal concentrations and weight content during NP using the modified pads (Table A16.1 & Table A16.2)

Table A16.1 TSP Metals concentration with uncertainties of the normal pathways using the soft, rigid, and grooved pad

	Soft				Rigid				Grooved			
	NP1		NP2		NP1		NP2		NP1		NP2	
	Conc.	U	Conc.	U	Conc.	U	Conc.	U	Conc.	U	Conc.	U
	ng/m³	ng/m³	ng/m³	ng/m³	ng/m³	ng/m³	ng/m³	ng/m³	ng/m³	ng/m³	ng/m³	ng/m³
Ag	<LQ		<LD		<LQ		<LQ		<LD		<LD	
Al	620.7	38.0	525.3	32.2	2049.6	125.4	1943.4	118.9	415.2	25.4	413.1	25.3
As	3.2	0.3	3.1	0.3	9.2	0.7	10.1	0.8	2.1	0.2	1.4	0.1
Ba	2137.6		1843.7		8507.0		8141.6		1809.9		1822.1	
Be	NA		NA		0.3		0.3		NA		NA	
Bi	0.2		0.1		NA		NA		<LQ		0.2	
Ca	1543.4	201.6	<LQ		8850.7	1155.0	8225.5	1073.5	1699.6	222.0	1939.7	253.3
Cd	<LQ		<LD		NA		NA		<LD		<LD	
Ce	0.5	0.0	0.4	0.03	10.6	0.8	10.6	0.8	2.4	0.2	2.2	0.2
Co	4.7	0.3	4.3	0.3	14.3	1.0	13.4	1.0	2.6	0.2	2.1	0.2
Cr	364.9	35.4	322.8	31.3	1128.0	109.4	1086.7	105.4	<LQ		<LQ	
Cu	<LQ		<LQ		1728.0	143.1	1768.2	146.4	<LD		<LD	
Fe	98904.4	6058.7	86584.0	5304.0	236155.7	14466.4	226517.7	13876.0	37855.6	2319.0	36984.8	2265.6
Ge	0.8		0.8		2.8		2.6		0.3		0.7	
Hf	<LD		<LD		<LQ		0.6		<LD		<LD	
K	154.7		115.4		NA		NA		<LD		<LQ	
La	<LQ		<LQ		8.5	0.8	8.6	0.8	1.9	0.2	1.7	0.2
Li	0.3		<LQ		0.7		<LD		0.2		<LQ	
Mg	153.9	9.6	118.6	7.4	289.5	18.0	274.6	17.1	<LQ		117.9	7.4
Mn	708.7	53.2	654.8	49.1	2498.7	187.5	2418.4	181.5	274.6	20.6	286.4	21.5

Mo	19.4		17.1		69.8		68.2		<LQ		<LQ	
Na	106.6		69.4		NA		NA		<LQ		<LQ	
Ni	<LQ		<LQ		126.7	12.7	115.5	11.6	<LQ		<LQ	
Pb	<LD		<LD		<LQ		<LQ		<LD		<LD	
Pd	<LD		<LD		NA		NA		<LD		<LD	
Rb	0.7		0.6		NA		NA		<LD		<LD	
Ru	<LD		<LD		NA		NA		<LD		<LD	
S	NA		NA		6142.6	796.1	4452.4	577.0	NA		NA	
Sb	0.6	0.1	<LD		2.5	0.2	2.7	0.2	1.0	0.1	1.0	
Se	<LQ		<LQ		<LQ		<LQ		<LD		<LD	
Si	NA		NA		13826.5	1804.1	13514.6	1763.4	NA		NA	
Sn	225.1		210.4		134.9		141.7		207.0		188.1	
Sr	40.8	3.6	36.8	3.3	164.7	14.7	156.0	13.9	15.4	1.4	15.7	1.4
Te	NA		NA		NA		NA		NA		NA	
Th	0.1		<LQ		1.7		1.9		0.3		0.3	
Ti	<LQ		<LD		98.1	9.4	93.2	8.9	<LQ		<LQ	
Tl	NA		NA		NA		NA		NA		NA	
U	<LD		<LD		0.2		0.2		0.1		0.1	
V	5.9	0.5	5.0	0.4	20.0	1.6	19.1	1.5	4.1	0.3	4.4	0.3
W	NA		NA		NA		NA		NA		NA	
Zn	<LD		<LD		<LQ		<LQ		<LD		<LQ	
Zr	<LD		<LD		<LQ		21.3		<LD		<LD	

Table A16.2 TSP metal weight content with uncertainties of the normal pathways using the soft, rigid, and grooved pad

	soft				rigid				grooved			
	NP1		NP2		NP1		NP2		NP1		NP2	
	Conc.	**U**	**Conc.**	**U**	**Conc.**	**U**	**Conc.**	**U**	**Conc.**	**U**	**Conc.**	**U**
	µg/mg	**µg/mg**	**µg/mg**	**µg/mg**	**µg/mg**	**µg/mg**	**µg/mg**	**µg/mg**	**µg/mg**	**µg/mg**	**µg/mg**	**µg/mg**
Ag	<LQ		<LD		<LQ		<LQ		<LD		<LD	
Al	3.6	0.2	3.2	0.2	4.1	0.2	3.9	0.2	4.8	0.3	3.6	0.2
As	0.02	0.002	0.02	0.002	0.02	0.001	0.02	0.002	0.02	0.002	0.01	0.001
Ba	12.5	0.9	11.2	0.8	16.9	1.2	16.5	1.2	20.9	1.5	15.8	1.2
Be	NA		NA		0.001		0.0		NA		NA	
Bi	0.001		0.001		NA		NA		<LQ		0.002	
Ca	9.0	1.2	<LQ		17.6	2.3	16.6	2.2	19.6	2.6	16.8	2.2
Cd	<LQ		<LD		NA		NA		<LD		<LD	
Ce	0.003	0.0002	0.002	0.0002	0.02	0.002	0.02	0.002	0.03	0.002	0.02	0.001
Co	0.03	0.002	0.03	0.002	0.03	0.002	0.03	0.002	0.03	0.002	0.02	0.001
Cr	2.1	0.2	2.0	0.2	2.2	0.2	2.2	0.2	<LQ		<LQ	
Cu	<LQ		<LQ		3.4	0.3	3.6	0.3	<LD		<LD	
Fe	577.5	35.4	523.7	32.1	469.2	28.7	458.4	28.1	436.5	26.7	321.1	19.7
Ge	0.005		0.005		0.01		0.01		0.004		0.01	
Hf	<LD		<LD		<LQ		0.001		<LD		<LD	
K	0.9		0.7		NA		NA		<LD		<LQ	
La	<LQ		<LQ		0.02	0.002	0.02	0.002	0.02	0.002	0.02	0.001
Li	0.001		<LQ		0.001		<LD		0.003		<LQ	
Mg	0.9	0.1	0.7	0.05	0.6	0.04	0.6	0.03	<LQ		1.0	0.1
Mn	4.1	0.3	4.0	0.3	5.0	0.4	4.9	0.4	3.2	0.2	2.5	0.2
Mo	0.1		0.1		0.1		0.1		<LQ		<LQ	
Na	0.6		0.4		NA		NA		<LQ		<LQ	
Ni	<LQ		<LQ		0.3	0.03	0.2	0.02	<LQ		<LQ	
Pb	<LD		<LD		<LQ		<LQ		<LD		<LD	

Pd	<LD		<LD		NA		NA		<LD		<LD	
Rb	0.004		0.004		NA		NA		<LD		<LD	
Ru	<LD		<LD		NA		NA		<LD		<LD	
S	NA		NA		12.2	1.6	9.0	1.2	NA		NA	
Sb	0.004	0.0003	<LD		0.01	0.0005	0.01	0.0005	0.01	0.001	0.01	
Se	<LQ		<LQ		<LQ		<LQ		<LD		<LD	
Si	NA		NA		27.5	3.6	27.3	3.6	NA		NA	
Sn	1.3		1.3		0.3		0.3		2.4		1.6	
Sr	0.2	0.02	0.2	0.02	0.3	0.03	0.3	0.03	0.2	0.02	0.1	0.01
Te	NA		NA		NA		NA		NA		NA	
Th	0.0004		<LQ		0.003		0.004		0.003		0.002	
Ti	<LQ		<LD		0.2	0.02	0.2	0.02	<LQ		<LQ	
Tl	NA		NA		NA		NA		NA		NA	
U	<LD		<LD		0.0004		0.0004		0.001		0.001	
V	0.03	0.003	0.03	0.002	0.04	0.003	0.04	0.003	0.05	0.004	0.04	0.003
W	NA		NA		NA		NA		NA		NA	
Zn	<LD		<LD		<LQ		<LQ		<LD		<LQ	
Zr	<LD		<LD		<LQ		0.04318		<LD		<LD	

Appendix 17 Fraction Metal concentrations and weight content during NP using the modified pads (Table A17.1, Table A17.2 & Table A17.3)

Table A17.1 Metals concentration with uncertainties of particles collected on the 3-stage impactor of normal pathways using the soft pad

	soft											
	NP1						NP2					
	10-2.6 µm		2.6-1 µm		<1 µm		10-2.6 µm		2.6-1 µm		<1 µm	
	C	U	C	U	C	U	C	U	C	U	C	U
	ng/m³	ng/m³	ng/m³	ng/m³	ng/m³	ng/m³	ng/m³	ng/m³	ng/m³	ng/m³	ng/m³	ng/m³
Ag	<LD		<LD		<LD		<LD		<LD		<LD	
Al	149.2	9.1	<LQ		230.7	14.1	158.4	9.7	<LQ		184.2	11.3
As	0.8	0.1	<LD		1.2	0.1	0.9	0.1	<LD		1.1	0.1
Ba	521.4		156.7		781.8		538.8		165.9		635.2	
Be	NA		NA		NA		NA		NA		NA	
Bi	0.0		<LQ		0.2		0.04		<LQ		0.1	
Ca	<LQ		<LQ		464.0	60.6	<LQ		<LQ		419.6	54.8
Cd	<LD		<LD		<LD		<LD		<LD		<LQ	
Ce	<LQ		<LQ		0.3	0.0	<LQ		<LD		0.2	0.01
Co	1.2	0.1	0.4	0.0	1.9	0.1	1.2	0.1	<LQ		1.7	0.1
Cr	90.1	8.7	<LQ		145.9	14.2	93.4	9.1	<LQ		115.8	11.2
Cu	<LQ		<LD		<LQ		<LQ		<LD		<LQ	
Fe	23849.4	1461.0	6981.7	427.7	38579.6	2363.3	26200.5	1605.0	6801.0	416.6	31038.6	1901.4
Ge	0.2		0.1		0.4		0.3		0.1		0.4	
Hf	<LD		<LD		<LD		<LD		<LD		<LD	
K	<LQ		<LD		49.0		29.8		<LQ		47.2	
La	<LQ		<LD		0.2		<LQ		<LD		<LQ	
Li	0.1		<LQ		0.1		0.1		<LD		0.1	
Mg	<LQ		<LQ		47.1	3.0	<LQ		<LQ		41.0	2.6
Mn	176.9	13.3	54.6	4.1	297.2	22.3	191.2	14.3	55.6	4.2	242.8	18.2

Mo	<LQ		<LQ		7.3		5.1		<LQ		6.0	
Na	<LQ		<LD		38.8		<LQ		<LQ		27.6	
Ni	<LQ		<LD		<LQ		<LQ		<LD		<LQ	
Pb	<LD		<LD		<LD		<LD		<LD		<LD	
Pd	<LD		<LD		<LQ		<LD		<LD		<LD	
Rb	0.1		<LD		0.2		0.2		<LD		0.2	
Ru	<LQ		<LD		<LD		<LQ		<LQ		<LD	
S	NA		NA		NA		NA		NA		NA	
Sb	<LD		<LD		0.3	0.0	<LD		<LD		0.3	0.02
Se	<LD		<LD		<LD		<LD		<LD		<LD	
Si	NA		NA		NA		NA		NA		NA	
Sn	56.3		<LQ		93.5		61.6		<LQ		76.0	
Sr	10.7	1.0	2.7	0.2	15.9	1.4	11.4	1.0	2.7	0.2	12.7	1.1
Te	NA		NA		NA		NA		NA		NA	
Th	0.0		<LD		0.0		0.03		<LD		0.03	
Ti	<LD		<LD		<LQ		<LD		<LD		<LQ	
Tl	NA		NA		NA		NA		NA		NA	
U	<LD		<LD		<LQ		<LD		<LD		<LD	
V	1.4	0.1	<LQ		2.4	0.2	1.5	0.1	<LQ		2.0	0.2
W	NA		NA		NA		NA		NA		NA	
Zn	<LD		<LD		<LQ		<LD		<LD		<LD	
Zr	<LD		<LD		<LD		<LD		<LD		<LD	

Table A17.2 Metals concentration with uncertainties of particles collected on the 3-stage impactor of normal pathways using the rigid pad

	rigid															
	NP1								NP2							
	>10 µm		10-2.6 µm		2.6-1 µm		<1 µm		>10 µm		10-2.6 µm		2.6-1 µm		<1 µm	
	C	U	C	U	C	U	C	U	C	U	C	U	C	U	C	U
	ng/m³	ng/m³	ng/m³	ng/m³	ng/m³	ng/m³	ng/m³	ng/m³	ng/m³	ng/m³	ng/m³	ng/m³	ng/m³	ng/m³	ng/m³	ng/m³
Ag	<LD		<LQ		<LD		<LD		<LD		<LQ		<LD		<LD	
Al	29.5	1.8	1156.3	70.8	232.5	14.2	630.5	38.6	33.1	2.0	937.2	57.4	219.6	13.5	1097.2	67.2
As	<LD		5.0	0.4	0.9	0.1	2.5	0.2	<LD		5.2	0.4	1.0	0.1	2.4	0.2
Ba	33.2		4697.0		915.0		2489.9		<LQ		3954.0		881.7		2089.9	
Be	0.03		0.1		0.03		0.03		0.03		0.03		0.03		0.1	
Bi	NA		NA		NA		NA		NA		NA		NA		NA	
Ca	<LQ		4612.0	602.4	874.4	114.2	2657.8	347.2	<LQ		4125.8	538.9	763.1	99.7	2176.4	284.3
Cd	NA		NA		NA		NA		NA		NA		NA		NA	
Ce	<LQ		6.0	0.5	1.2	0.1	3.2	0.2	<LD		4.8	0.4	1.1	0.1	2.8	0.2
Co	<LQ		7.2	0.5	1.4	0.1	3.7	0.3	<LQ		6.2	0.4	1.3	0.1	3.8	0.3
Cr	<LQ		622.7	60.4	120.5	11.7	323.0	31.3	<LD		513.1	49.8	118.2	11.5	296.2	28.7
Cu	<LD		908.5	75.2	171.6	14.2	486.0	40.2	<LD		795.3	65.9	176.4	14.6	481.6	39.9
Fe	853.0	52.3	132632.9	8124.8	26091.8	1598.3	70766.8	4335.0	<LQ		112170.5	6871.4	25287.1	1549.0	59792.2	3662.8
Ge	<LQ		1.4		0.2		0.7		<LQ		1.3		0.2		0.7	
Hf	<LD		<LD		<LD		<LD		<LD		<LD		<LD		<LD	
K	NA		NA		NA		NA		NA		NA		NA		NA	
La	<LQ		4.7	0.4	0.9	0.1	2.4	0.2	<LQ		3.8	0.4	0.8	0.1	2.0	0.2
Li	<LQ		0.3		<LQ		0.2		<LQ		0.2	0.0	<LQ		<LD	
Mg	<LQ		138.8	8.7	49.4	3.1	93.6	5.9	<LQ		129.6	8.1	44.4	2.8	91.8	5.8
Mn	8.8	0.7	1380.8	103.6	264.2	19.8	719.9	54.0	<LQ		1213.9	91.1	261.1	19.6	659.7	49.5
Mo	<LQ		38.4		7.9		21.9		<LD		37.0		7.7		18.4	
Na	NA		NA		NA		NA		NA		NA		NA		NA	
Ni	<LD		58.6	5.9	11.5	1.2	34.9	3.5	<LD		53.4	5.4	11.5	1.2	39.4	4.0
Pb	<LD		1.1	0.1	<LQ		<LQ		<LD		1.1	0.1	0.2	0.01	<LQ	
Pd	NA		NA		NA		NA		NA		NA		NA		NA	

Rb	NA		NA		NA		NA		NA		NA		NA		NA	
Ru	NA		NA		NA		NA		NA		NA		NA		NA	
S	<LQ		2983.6	386.7	872.7	113.1	1573.3	203.9	<LQ		2576.5	333.9	718.1	93.1	1454.4	188.5
Sb	<LD		1.2	0.1	0.2	0.02	0.6	0.1	<LD		1.1	0.1	0.2	0.02	0.5	0.05
Se	<LD		<LD		<LQ		<LQ		<LD		<LD		<LD		<LQ	
Si	<LQ		5682.4	743.3	1358.7	177.7	3564.2	466.3	<LQ		6636.7	868.2	1256.4	164.4	3639.3	476.1
Sn	<LD		71.7		13.8		38.7		<LD		71.0		14.8		38.5	
Sr	0.5	0.04	89.1	8.0	17.6	1.6	47.6	4.3	<LQ		75.7	6.8	17.6	1.6	41.3	3.7
Te	NA		NA		NA		NA		NA		NA		NA		NA	
Th	<LD		1.0		0.2		0.5		<LD		0.9		0.2		0.5	
Ti	<LD		51.9	5.0	11.2	1.1	<LQ		<LQ		46.9	4.5	10.8	1.0	<LQ	
Tl	NA		NA		NA		NA		NA		NA		NA		NA	
U	<LD		0.1	0.0	<LD		<LD		<LD		0.1	0.0	<LD		0.1	
V	<LQ		10.4	0.8	2.1	0.2	5.8	0.5	<LD		9.9	0.8	2.1	0.2	5.1	0.4
W	NA		NA		NA		NA		NA		NA		NA		NA	
Zn	<LD		19.3	2.0	<LQ		25.8	2.7	<LD		20.3	2.1	<LQ		<LQ	
Zr	<LD		8.2		<LQ		<LD		<LQ		7.8		<LQ		<LD	

Table A17.3 Metals concentration with uncertainties of particles collected on the 3-stage impactor of normal pathways using the grooved pad

	Grooved											
	NP1						NP2					
	10-2.6 µm		2.6-1 µm		<1 µm		10-2.6 µm		2.6-1 µm		<1 µm	
	C	U	C	U	C	U	C	U	C	U	C	U
	ng/m³	ng/m³	ng/m³	ng/m³	ng/m³	ng/m³	ng/m³	ng/m³	ng/m³	ng/m³	ng/m³	ng/m³
Ag	<LD		<LD		<LD		<LD		<LD		<LD	
Al	175.2	10.7	<LQ		189.9	11.6	191.9	11.8	<LQ		114.9	7.0
As	0.6	0.0	<LD		0.7	0.1	1.0	0.1	<LD		0.5	0.04
Ba	655.3		154.9		822.7		895.1		299.9		521.0	
Be	NA		NA		NA		NA		NA		NA	
Bi	<LQ		<LD		0.02		<LQ		<LD		<LQ	
Ca	726.6	94.9	<LQ		826.0	107.9	890.5	116.3	<LQ		596.1	77.9
Cd	<LD		<LD		<LD		<LD		<LD		<LD	
Ce	1.0	0.1	0.2	0.01	1.2	0.1	1.1	0.1	0.3	0.03	0.6	0.05
Co	1.1	0.1	<LQ		1.0	0.1	1.2	0.1	<LQ		0.8	0.1
Cr	<LQ		<LD		<LQ		63.0	6.1	<LQ		<LQ	
Cu	<LD		<LD		<LD		<LQ		<LD		<LD	
Fe	15706.6	962.2	<LQ		17144.3	1050.2	19348.6	1185.3	5552.7	340.1	10907.6	668.2
Ge	0.2		0.1		0.2		0.2		0.0		0.2	
Hf	<LD		<LD		<LD		<LD		<LD		<LD	
K	<LD		<LD		<LQ		<LQ		<LQ		<LD	
La	2.5	0.2	<LQ		0.9	0.1	0.9	0.1	0.3	0.03	0.5	0.04
Li	<LQ		<LD		0.1		0.1		<LD		<LQ	
Mg	42.3	2.7	<LQ		48.3	3.0	51.5	3.2	<LQ		<LQ	
Mn	115.6	8.7	20.7	1.6	122.8	9.2	151.4	11.4	40.8	3.1	98.0	7.4
Mo	5.1		<LD		6.0		5.5		<LQ		<LQ	
Na	<LQ		<LD		<LQ		<LQ		<LQ		<LQ	
Ni	<LQ		<LD		<LQ		<LQ		<LD		<LQ	
Pb	<LD		<LD		<LD		<LD		<LD		<LD	
Pd	<LD		<LD		<LQ		<LQ		<LD		<LD	

Rb	<LD		<LD		<LD		<LD		<LD		<LD	
Ru	<LD		<LQ		<LQ		<LD		<LD		<LD	
S	NA		NA		NA		NA		NA		NA	
Sb	0.6	0.1	<LD		0.6	0.1	0.7	0.1	<LD		0.5	0.04
Se	<LD		<LD		<LD		<LD		<LD		<LD	
Si	NA		NA		NA		NA		NA		NA	
Sn	87.4		<LQ		92.8		102.4		<LQ		64.3	
Sr	5.7	0.5	<LQ		7.1	0.6	7.5	0.7	2.2	0.2	4.7	0.4
Te	NA		NA		NA		NA		NA		NA	
Th	0.1		0.02		0.1		0.1		0.03		0.1	
Ti	<LQ		<LD		<LQ		<LQ		<LD		<LD	
Tl	NA		NA		NA		NA		NA		NA	
U	0.02		<LD		0.02		0.02		<LD		<LQ	
V	1.8	0.1	<LQ		1.8	0.1	1.9	0.1	<LQ		1.4	0.1
W	NA		NA		NA		NA		NA		NA	
Zn	<LD		<LD		<LQ		<LD		<LD		<LD	
Zr	<LD		<LD		<LD		<LD		<LD		<LD	

Appendix 18 Mass size distribution of rigid pad

Elemental size distribution for NP1 using the rigid pad for the selected metals, showing the same mode as NP2 at 1.62 and 2.46 µm, is shown in Figure A18.1.

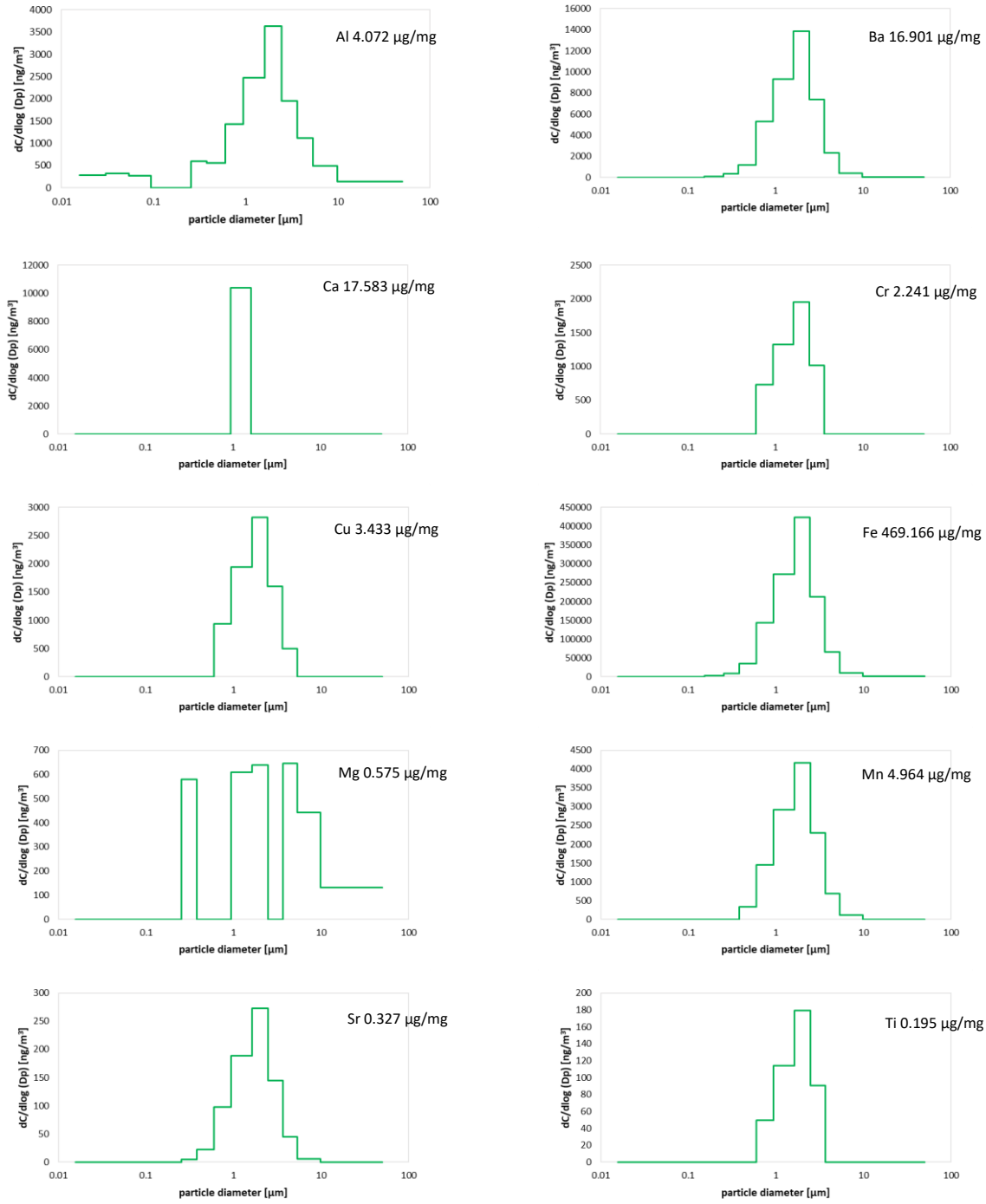

Figure A18.1 Mass concentration size distribution of selected metals using the rigid pad during the normal pathway 1

Appendix 19 Particle number size distribution

The number size distribution of particles has been studied by means of an FMPS (electrical mobility diameter from 5.6 to 560 nm) and an OPS (optical diameter from 0.3 to 10 µm). Results are presented for the heavy pathway (HP), as it generates more particles than the normal pathway (NP), using the reference pad, and for both reduced scale and full-scale experiments.

1. Reduced-scale

1.1. FMPS data

The results presented for the reduced scale refer to the HP1 test carried out on 8/03/2024. The evolution of the total number of particles (expressed as the number concentration of particles for all sizes per cm^3 of air) with time shows multiple peaks corresponding to the braking events (Figure A19.1). Between braking events, the total number of particles drops to the background level, which increases with time but remains inferior than 1E4 #/cm^3.

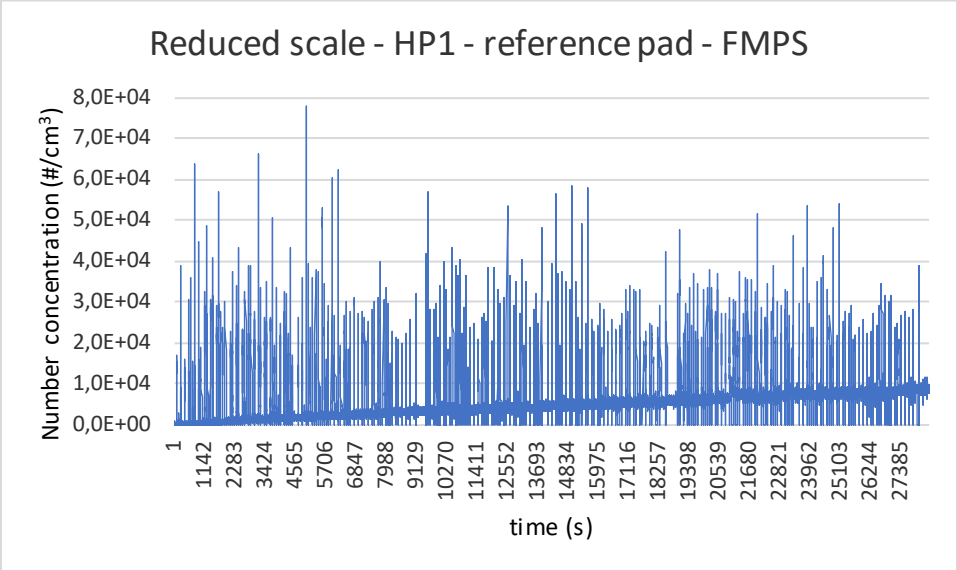

Figure A19.1 Total number of particles (#/cm^3) measured by FMPS with the reference pad for HP1 at reduced scale

The normalized particle size distribution measured by FMPS shows a number size mode at 191.1 nm, related to particles emitted by braking (Figure A19.2).

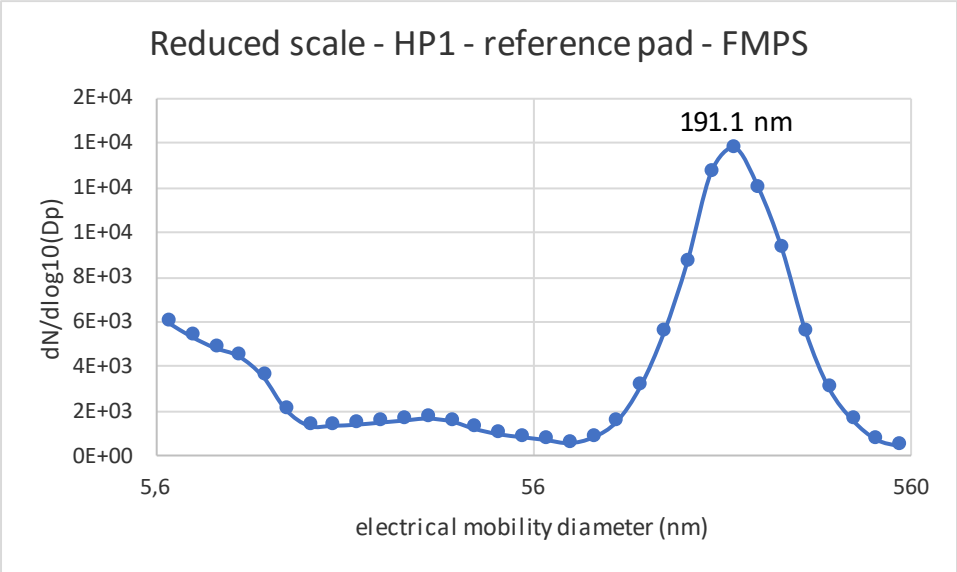

Figure A19.2 Normalized particle size distribution (#/cm³) measured by FMPS with the reference pad for HP1 at reduced scale

1.2. OPS data

As for the FMPS data, the total number of particles increases for each braking event (Figure A19.3). Between braking events, the total number of particles drops to the background level, which increases with time but remains inferior than 1E4 #/cm³.

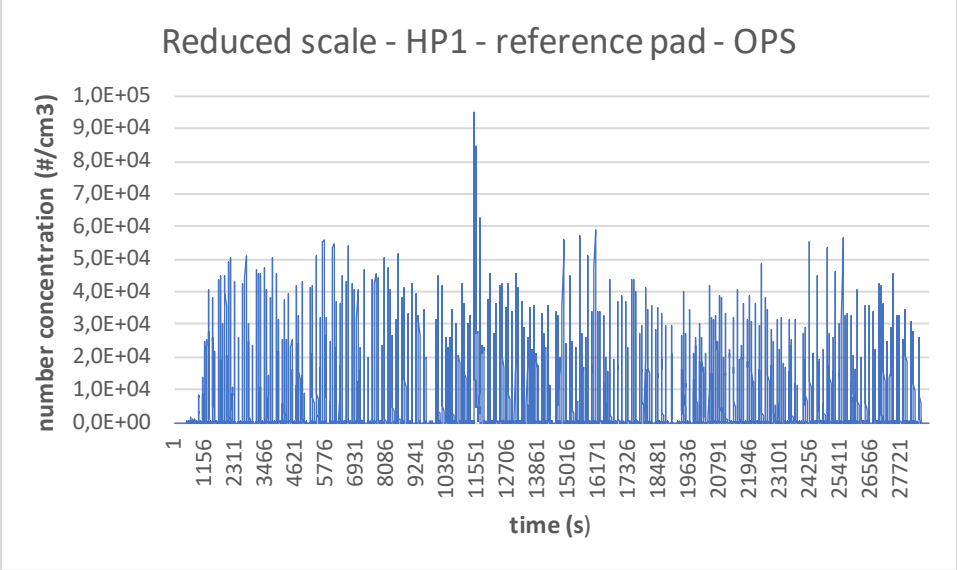

Figure A19.3 Total number of particles (#/cm3) measured by OPS with the reference pad for HP1 at reduced scale

The normalized particle size distribution measured by OPS shows a number size mode at 419 nm (0.419 µm), related to particles emitted by braking (Figure A13.4).

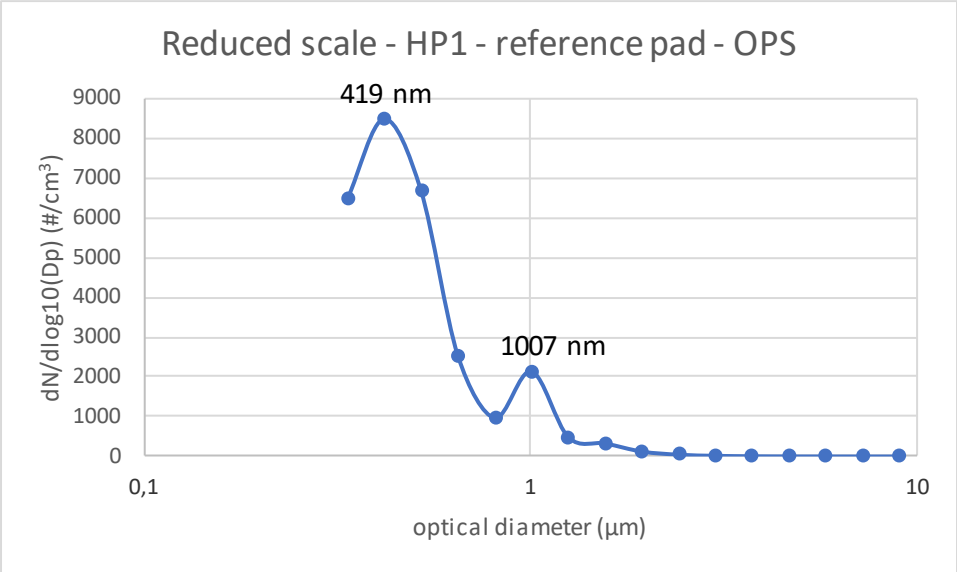

Figure A19.4 Normalized particle size distribution (#/cm³) measured by OPS with the reference pad for HP1 at reduced scale

1.3. Combined FMPS and OPS data

The normalized particle size distributions measured by FMPS and OPS present distinct size modes with different number concentrations (Figure A19.5):
- for FMPS, a mode at 191.1 nm with a concentration of almost 1.4E4 #/cm³.
- for OPS, a mode at 419 nm with a concentration of about 0.9E4 #/cm³.

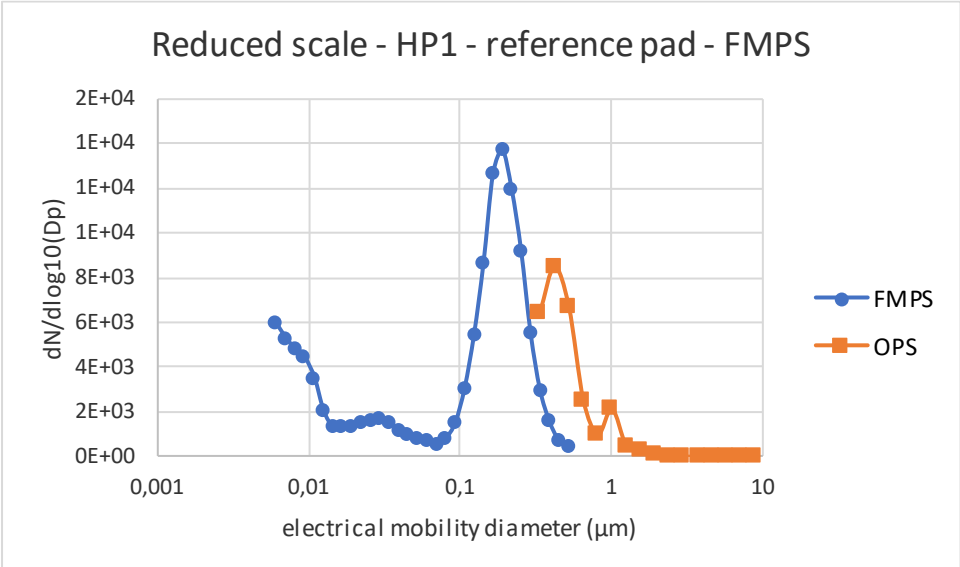

Figure A19.5 Normalized particle size distributions (#/cm³) measured by both FMPS and OPS with the reference pad for HP1 at reduced scale

According to previous works dealing with the comparison of FMPS with reference particle sizers, Jeong and Evans (2009) found that the FMPS size distribution was accurate only for diameters less than 100 nm, while Zimmerman et al. (2015) found that the accuracy was limited to diameters less than 80 nm. Above

this range of 80-100 nm, the FMPS under-sizes the diameters. Therefore, it is probable that the mode diameter observed at 191.1 nm with the FMPS is in reality higher, and could correspond to the mode diameter of 419 nm observed with the OPS. The correspondence of the FMPS number size distribution with the OPS one is also made difficult by the difference in the measured diameters: electrical mobility diameter for FMPS and optical diameter for OPS. The difference in number concentration for the size modes may be related to the different techniques used and their respective measurement artifacts. Particularly, the FMPS particle counting is sensitive to particles carrying multiple electrical charges instead of only one.

2. Full-scale

The results presented for the full scale refer to the HP2 test carried out on 26/09/2024 with the reference pad. Prior to the realization of the HP2, a "blank" test was performed, consisting in a 1h-long measurement of the particle number concentration with a constant disc rotation of 80 km/h (maximum disc rotation for HP is 110 km/h) without any braking event, carried out the same day as HP2. This "blank" test is useful to determine the background level of particles.

2.1 FMPS data

The evolution of the total number of particles with time shows several peaks with a high amplitude, up to 380,000 #/cm^3 (Figure A19.6). At this scale, the effect of the 216 braking events on the particle levels is not clearly visible.

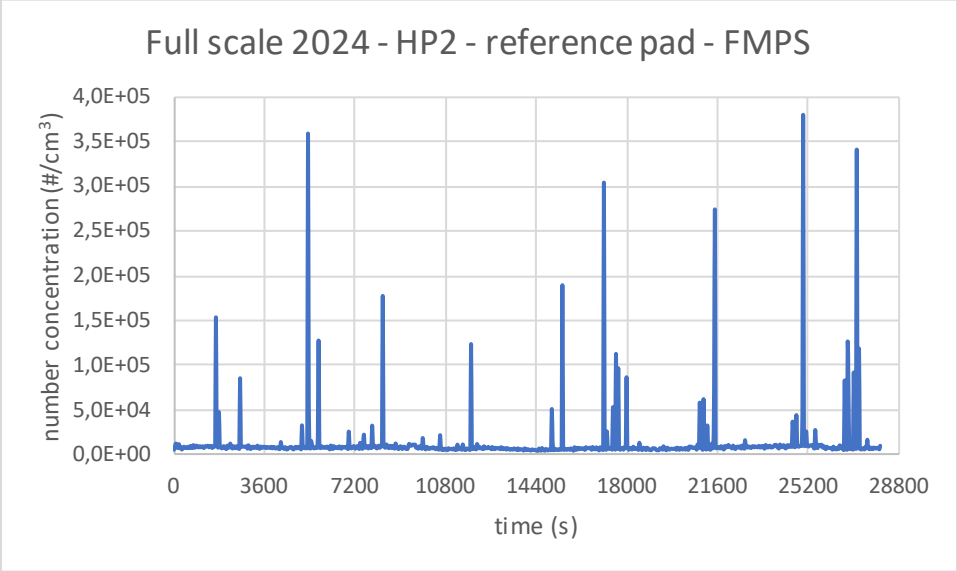

Figure A19.6 Total number of particles (#/cm3) measured by FMPS with the reference pad for HP2 at full scale

When zooming on the first trip (among 6 trips for the whole HP) and for a lower number concentration range between 4000 and 10,000 #/cm^3, it is visible that each braking event results in an increase of the particle concentration, but with a limited amplitude of about 1000 or 2000 #/cm^3, probably due to the high air flow rate circulating in the full-scale dynamometer (Figure A13.7). Its is also noticeable that the baseline (particle number concentration in the interbraking periods) fluctuates with time, contrary to the linear increase observed at the reduced scale.

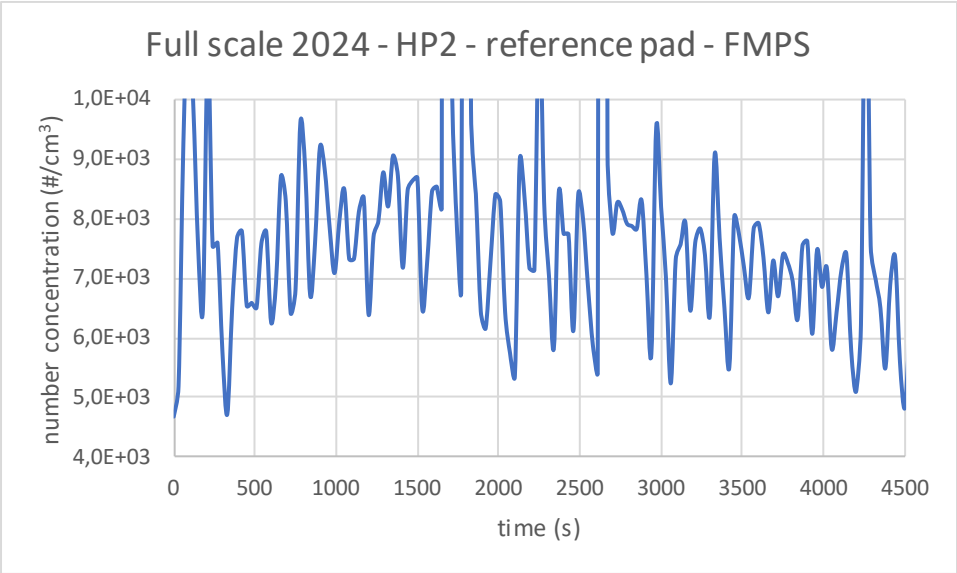

Figure A19.7 Total number of particles (#/cm3) measured by FMPS with the reference pad for the first trip of HP2 at full scale

The normalized particle size distribution measured by FMPS shows a number size mode at 10.8 nm (Figure A13.8). As the baseline is variable, the size distribution for HP2 is superimposed to the size distribution of the "blank" experiment. The "blank" experiment shows the same sizes but with lower concentrations (roughly, half), highlighting the effect of the braking events on the number concentration.

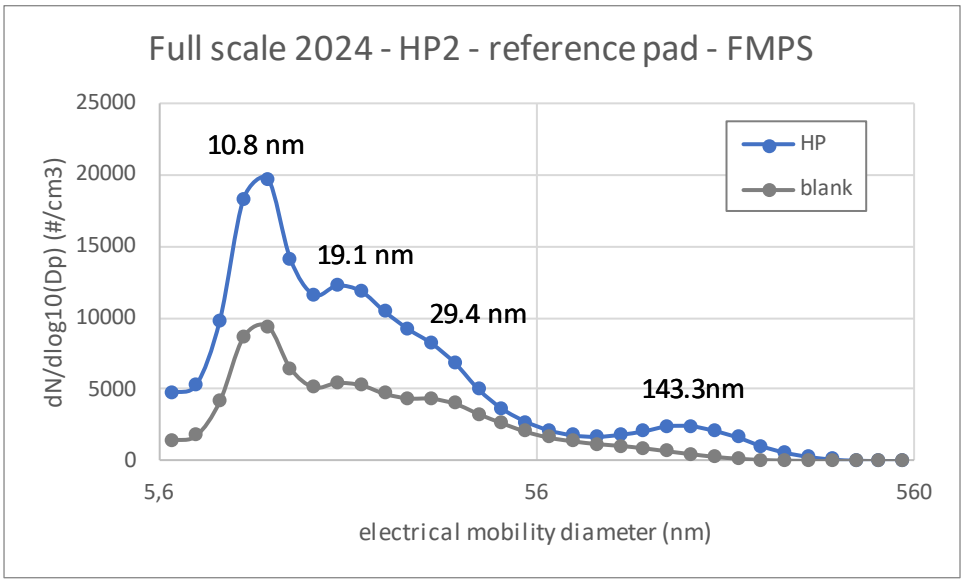

Figure A19.8 Normalized particle size distribution measured by FMPS with the reference pad for HP2 at full scale

2.2. OPS data

Contrary to the FMPS, the effect of the braking events on the levels of particles is clearly visible on the OPS data (Figure A19.9).

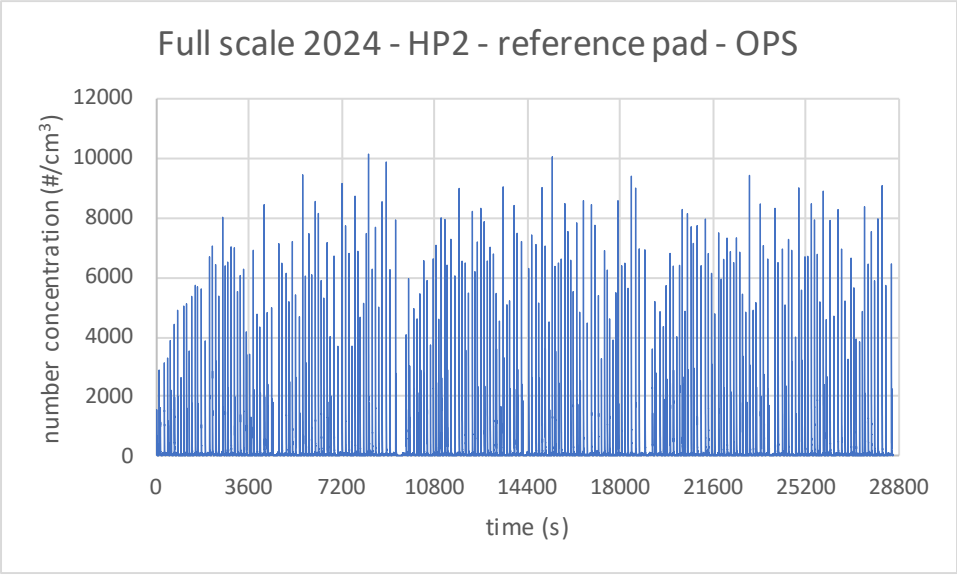

Figure A19.9 Total number of particles (#/cm³) measured by OPS with the reference pad for HP2 at full scale

The normalized particle size distribution measured by OPS shows a number size mode at 419 nm (0,419 µm). Contrary to the FMPS, the "blank" experiments shows that the background levels of particles in the OPS size range are negligible (Figure A19.10).

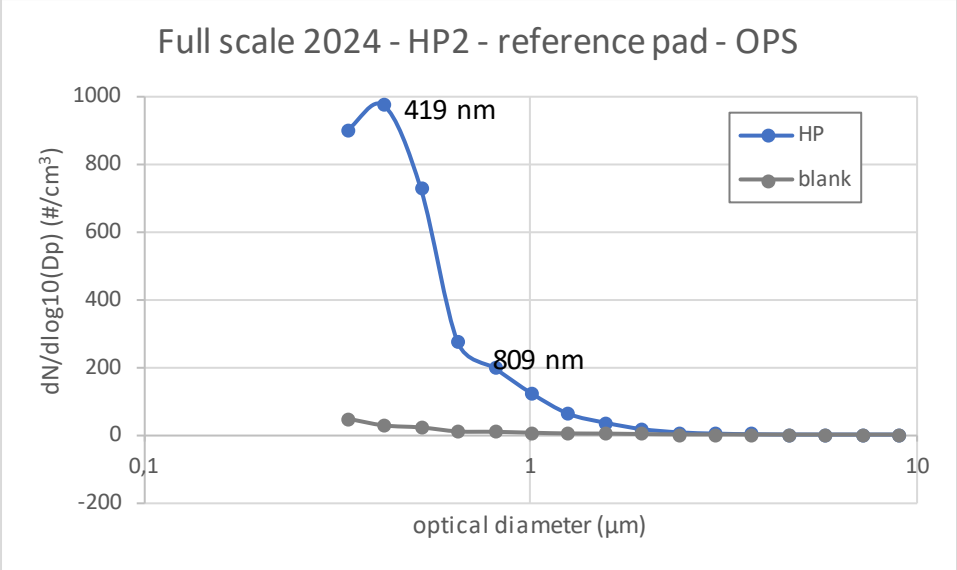

Figure A19.10 Normalized particle size distribution measured by OPS with the reference pad for HP2 at full scale

2.3. Combined FMPS and OPS data

As the background levels of particles in the FMPS size range are important, these background levels are subtracted from the FMPS number size distribution obtained of HP2, prior to present both the FMPS and OPS size distributions of HP2 on the same graph. Also, the size range is limited to particles higher than 50 nm to better highlight the comparison of the FMPS with the OPS (Figure A19.11).

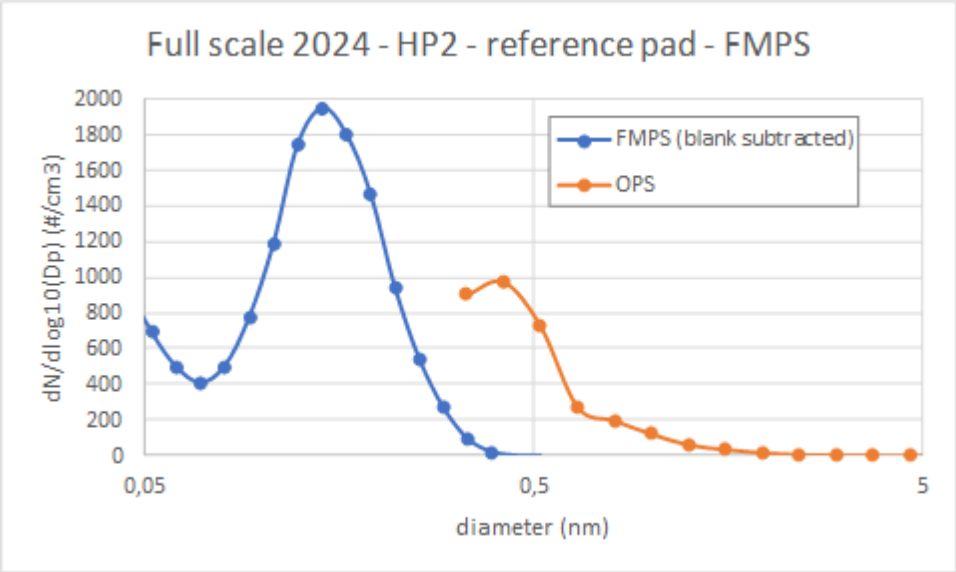

Figure A19.11 Normalized particle size distribution measured by both FMPS (blank subtracted) and OPS with the reference pad for HP2 at full scale

The normalized particle size distributions measured by FMPS and OPS present distinct size modes with different number concentrations:

- for FMPS, a mode at 143.3 nm with a concentration of almost 1945 #/cm^3.
- for OPS, a mode at 419 nm with a concentration of about 975 #/cm^3.

As discussed previously for the reduced scale, it is probable that the mode diameter observed at 143.3 nm with the FMPS is in reality higher, and could correspond to the mode diameter of 419 nm observed with the OPS.

3. Comparison of particle size distribution at both scales

The main characteristics of the particle size distributions are summarized in Table A19.1 Table A19..

Table A19.1 Main characteristics of the particle size distributions at both scales observed with both FMPS and OPS

Scale	Particle size distribution	FMPS	OPS
Reduced scale	Mean number concentration (#/cm^3)	7479	2692
	% of particles with size less than 50 nm	32%	-
	Particle size mode (nm)	191.1	419
Full scale	Mean number concentration (#/cm^3)	10897	268
	% of particles with size less than 50 nm	87%	-
	Particle size mode (nm)	10.8	419

The common observation at both scales is the emission of particles with an optical size mode of 419 nm measured by the OPS. These particles are the ones which contribute mostly to the mass of the particles.
Concerning particles with an electrical mobility diameter less than 50 nm (considered here as a proxy of ultrafine particles), they are predominant in the particle size distribution at full scale (87%), possibly due to their high background level in the full-scale facility, contrary to the reduced scale (32%). Considering that braking with an organic pad emits VOCs, it is likely that ultrafine particles may nucleate and growth. Based on the cleaner conditions of the reduced scale set-up, the ultrafine particles may represent one third of the total number of particles emitted by braking.

Appendix 20 Valorization of thesis work

Publications:

- J. Frangieh, A. Griria, E. Davin, F. Brunel, **R. Al Kaderi,** E. Perdrix, A. Tomas, M. Henrion, R. Mann, Y. Desplanques, P. Dufrenoy (2025). Railway braking wear dynamics and particle emissions: Relationship between tribological circuit and pad design. Wear. https://doi.org/10.1016/j.wear.2025.205854

Conferences:

- **R. Al Kaderi**, A. Grira, J. Frangieh, M. Jamar, B. Malet, et al.. Gas and Particle Emissions from Representative Railway Braking Systems: A Comprehensive Study at Two Scales. Compola, Oct 2024, Ben Guerir, Morocco.

- **R. Al Kaderi**, A. Grira, J. Frangieh, B. Malet, L. Alleman, et al.. Particle Emissions from Representative Railway Braking Systems: A Comprehensive Study of Size Distribution and Chemical Composition at Two Scales, **Oral presentation**, European Aerosol Conference, Aug 2024, Tampere, Finland.

- A. Grira, J. Frangieh, **R. Al Kaderi**, E. Davin, B. Malet, et al.. Effect of operating conditions on particulates emitted from the friction between railway brake pads and discs. Eurobrake, FISITA, Jun 2024, Rheingoldhalle, Germany.

- **R. Al Kaderi**, A. Grira, M. Jamar, L. Alleman, E. Perdrix, et al.. Characterization of Volatile Organic Compounds (VOCs) in the emissions of representative railway braking systems. Eurobrake, Sep 2023, Barcelone, Spain.

- Y. Desplanques, M. Briatte, A. Grira, J. Frangieh, **R. Al Kaderi**, et al.. Processus d'usure en freinage par friction : quelle clé pour atténuer à la source les émissions de particules ?. Journées Tribologie et Traitements de surface, Nov 2023, Senlis, France.

- **R. Al Kaderi**, A. Grira, M. Jamar, L. Alleman, E. Perdrix, et al.. Characterization of Volatile Organic Compounds (VOCs) in the emissions of railway braking system: exploratory study at reduced scale. Journées Internationales Francophones de Tribologie, May 2023, Lille, France.